A Cumulative Dissertation approved by the Department of Materials Science
in fulfillment of the requirements for the Degree of Doktor-Ingenieur (Dr.-Ing.)

Single-Source-Precursor Synthesis and Electromagnetic Properties of SiCN-Based Ceramic Nanocomposites Modified with Carbon Nanofillers from 1D CNTs to 3D RGO/CNTs

M. Sc. Xingmin Liu

From Qingzhou, Shandong, China

Matrikel-Nr. 2337221

TECHNISCHE
UNIVERSITÄT
DARMSTADT

Referee: Prof. Dr. Ralf Riedel

Co-referee: Prof. Dr. Nahum Travitzky

Fachbereich Material- und Geowissenschaften

Technische Universität Darmstadt

Date of submission: 19. 02. 2018

Date of oral examination: 06. 04. 2018

February 2018-Darmstadt-D 17

M. Sc. Xingmin Liu
Alarich-Weiss-Str. 2
64287 Darmstadt

Declaration

This work described in this thesis was carried out at the Department of Materials Science, Technische Universität Darmstadt during the period October 2014 to February 2018. This thesis represents the author's original work and no part of it has been submitted for a degree at any other university. Prior to the submission of this thesis, some work has been published as described in the relevant chapters herein.

Eidesstattliche Erklärung
Hiermit erkläre ich an Eides statt, dass ich die vorliegende Dissertation selbstständig und nur mit den angegebenen Hilfsmitteln angefertigt habe. Von mir wurde weder an der Technischen Universität Darmstadt noch einer anderen Hochschule ein Promotionsversuch unternommen.

Darmstadt, den 10. 02. 2018

Xingmin Liu

Acknowledgements

I would like to acknowledge all the people who supported me during my PhD period:

- My deep thanks and respect to Prof. Dr. Ralf Riedel, who gave me this opportunity to work in his group. Many thanks for his supervision, constant support and encouragement during my PhD study.
- My warm thanks to Prof. Dr. Zhaoju Yu for her outstanding scientific supervision, productive discussions and encouragement during my entire PhD period, which improved my work and working discipline.
- My heartfelt gratitude to Prof. Dr. Xiaowei Yin who led me into the field of electromagnetic materials. Thanks for the convenience that being provided by him for the measurement of my samples during my PhD work.
- Many thanks to PD Dr. Emanuel Ionescu for the revision of my research proposal which was used for the application of my scholarship from Chinese Scholarship Council (CSC).
- Thanks to Dipl.-Ing. Claudia Fasel for the glove box instruction, TG/MS measurements and lots of technical help in daily lab work.
- Thanks to M. Sc. Lingqi Chen for the help of SEM measurements.
- Thanks to Dr. Wenyan Duan for the help of electrical conductivity measurements.
- Thanks to Dr. Xiaofei Liu for the help of dielectric measurements.
- Thanks to Dr. Ryo Ishikawa and Prof. Yuichi Ikuhara for the measurement of STEM.
- Thanks to M. Sc. Hailong Xu for the establishment of 3D electromagnetic performance figures.
- Thanks to Dr. Wenjie Li, Dr. Jia Yuan, Dr. Qingbo Wen and Dr. Cong Zhou for their constant help in my experiment.
- Thanks to Dr. Meng Hu for the help of TEM images.
- Thanks to M. Sc Nan Chai for the help of chemicals.
- Thanks to all the DF members for the great time we spend together during my PhD.
- Thanks to all the friends I met here in Darmstadt for sharing great time with you guys on beer, party, journey and everything.
- I would like to greatly acknowledge the CSC and Deutscher Akademischer Austauschdienst (DAAD) for their financial support.

- Lastly my thanks to my beloved parents, brother and family for their loving consideration, constant supporting and great confidence in me all through these years. A special thanks to my wife, Baojuan Zhang, for all her support and my son, Yinuo Liu who brings me enthusiasm and confidence when I felt frustrated and was lack of confidence.

Dedicated to my parents, wife, son and beloved friends:

“Where there is a will there is a way”

“有志者，事竟成”

The presented cumulative dissertation summarizes the essential scientific findings, which were reported to the scientific community in the following peer-reviewed journals. The reports itself [1]–[3] are enclosed in the Chapter Cumulative Publications of this thesis.

[1] Liu X, Yu Z, Chen L, et al., Role of single-source-precursor structure on microstructure and electromagnetic properties of CNTs-SiCN nanocomposites. *Journal of the American Ceramic Society*, 100 (**2017**) 4649-4660.

[2] Liu X, Yu Z, Ishikawa R, et al., Single-source-precursor synthesis and electromagnetic properties of novel RGO-SiCN ceramic nanocomposites. *Journal of Materials Chemistry C*, 5 (**2017**) 7950-7960.

[3] Liu X, Yu Z, Ishikawa R, et al., Single-source-precursor derived RGO/CNTs-SiCN ceramic nanocomposite with ultra-high electromagnetic shielding effectiveness. *Acta Materialia*, 130 (**2017**) 83-93.

Table of contents

List of abbreviations

EM	Electromagnetic
EMW	Electromagnetic wave
HIRF	High-intensity radiated fields
EMC	Electromagnetic compatibility
RAM	Radar absorbing materials
EAB	Effective absorption bandwidth
CNTs	Carbon nanotubes
RGO	Reduced graphene oxide
PDCs	Polymer derived ceramics
CB	Carbon black
CF	Carbon fibers
CNCs	Carbon nanocoils
GNs	Graphite nanosheets
1D	One dimensional
SWCNTs	Single-walled carbon nanotube
EMI	Electromagnetic interference
SE	Shielding effectiveness
MWCNTs	Muilt-walled carbon nanotubes
PMMA	Poly(methyl methacrylate)
PS	Polystyrene
2D	Two dimensional
SSA	Specific surface areas
LPB	Liquid phase blending

CVD	Chemical vapor deposition
PDMS	Poly (dimethylsiloxane)
RC	Reflection coefficient
3D	Three dimensional
SSP	Single-source-precursor
SiCN	Silicon carbonitride
NC	Nano carbon
ε	Complex permittivity
ε'	Real part of the permittivity
ε''	Imaginary part of the permittivity
Tan δ	Dielectric loss tangent
SiO_2	Silica
ε'_p	Relative permittivity of porous materials
ε'_0	Relative permittivity of dense materials
P	Porosity
ε'_c	Relative permittivity of the composite
V_i	Volume fractions
ε'_i	Relative permittivity of phase i
η	Admittance of the propagating medium
Z	Intrinsic impedance
E	Electric field vectors
H	Magnetic field vectors
μ_o	Permeability of free space
ε_o	Permittivity of free space
RC_{min}	Minimum reflection coefficient

P_A	Absorption power
P_R	Reflection power
P_I	Incident power
λ	Wavelength of microwave
d	Sample thickness
c	Light velocity in vacuum
P_t	Transmitted power
SE_R	Reflection shielding effectiveness
SE_A	Absorption shielding effectiveness
SE_{MR}	Multiple reflections shielding effectiveness
δ	Skin depth
f	Frequency
σ	Electrical conductivity
σ_{AC}	Alternate current conductivity
σ_{dc}	Direct current conductivity
dB	Decibel
R	Reflection power
A	Absorption power
T	Transmission power
S	Scattering parameters
A_{eff}	Effective absorbance
SiOC	Silicon oxycarbide
PDC-NCs	Polymer-derived ceramic nanocomposites
PCS	Polycarbosilanes
PBSZ	Polyborosilazane

PSN	Polysilazane
PSO	Polysiloxane
CNTs-COOH	Carboxylic carbon nanotubes
Zinc chloride	$ZnCl_2$
CNTs-NH_2	Amino functionalized CNTs
G_G	Graphitization grade
VNA	Vector network analyzer
XRD	X-ray diffraction
FTIR	Fourier transformed infrared spectroscopy
SEM	Scanning electron microscopy
HRTEM	High-resolution transmission electron microscopy
TEM	Transmission electron microscopy

1. Introduction and motivation

Electromagnetic (EM) microwaves are a form of microwaves with wavelengths ranging from one meter to one millimeter and frequencies ranging between 300 MHz (1 m) and 300 GHz (1 mm) [1,2]. In recent decades, with the wide application of electronic devices and wireless communication technology, a phenomenon called electromagnetic radiation (EMR) is becoming more and more serious, which exposes our living space in a deteriorating electromagnetic environment [3-5]. Electromagnetic radiation refers to the waves (or their quanta, photons) of EM field propagating (radiating) through space carrying electromagnetic radiant energy. It is reported that EMR has become the fourth severe pollution after that of water, air and noise pollution since the radiation of electromagnetic waves from electric devices can not only interfere the functioning of other electronic devices but also can affect the system of living species and promote the growth of tumor in human body [6-10]. To reduce the pollution of EMR, electromagnetic materials (EMMs) that can absorb, attenuate or block electromagnetic waves from radiation are playing increasing role in a large variety of applications including aerospace and aeronautics, electromagnetic protection from lightning and intentional interference [11,12], high-intensity radiated fields (HIRF) protection [13], nuclear physics, shields adopted in particle accelerators [14], nuclear EM pulses (NEMP) protection [15], electromagnetic compatibility (EMC), equipment level shielding [16,17], anechoic chambers for the realizations of wedges and pyramidal arrays [18], and human exposure mitigation [19].

The research activity on EMMs can be dated back to 1940s during the World War II, when electromagnetic absorption materials were employed on the aircraft by Germans in response to the detecting of radarsets from Allies [19, 20]. As the first-generation artificially conceived radar absorbing materials (RAM), a ferrite-based radar absorbing paint was developed at that time [19-29]. Typically, light weight and high efficiency are two key factors that drive the practical application for EM wave attenuation materials [30-35]. However, these ferrite-based materials suffered from some intrinsic disadvantages including high density, poor absorption efficiency and low effective absorption bandwidth, which cannot well meet the high requirement in the practical application [30]. To overcome these drawbacks, various species of EM materials have been developed. Among them, the most widely investigated electromagnetic absorbents are the hybrids of ferroferric oxide, cobalt oxide, or nickel ferrite nanocrystals and nanocarbon fillers including carbon nanotubes (CNTs), reduced graphene oxide (RGO) modified polymer based materials [23-26]. Even though the EM performances of

these materials were improved significantly, these materials are always limited by the Curie temperature [30]. Besides that, in some applications EM materials have to be operated in high temperature and oxidizing environments and/or under high mechanical loadings [36-40]. For example, when EM materials are used on the outer surface of hypersonic vehicles, combined properties of good electromagnetic interference shielding, mechanical strength and thermal resistance will have to be considered [36-40]. In this circumstance, the currently reported carbon nanofiller, metal fiber or particles modified polymer [41-44], foam [45, 46] or film [47-50] based EM materials lose their superiority and a substitute of these materials will have to be developed.

Polymer derived ceramics (PDCs) owning to their outstanding physical, chemical and functional properties as well as their easily accessible to be shaped via a wide variety of processing approaches such as warm pressing and electrospinning, have found wide applications in many key fields including defense technology, transport, energy as well as environmental systems, biomedical components and micro- or nanoelectromechanical systems since their emergence in 1960s [51, 52]. Recently, investigations have shown that the intrinsic advantages of PDCs including relatively low density, good oxidation resistance, relatively high hardness, thermal-chemical stability, good machinability, high creep resistance, and high thermal shock resistance make them promising matrix candidate for EM materials for high temperature applications [53-59]. Moreover, the insulating and electrically conductive phases in PDCs endow them with tunable dielectric properties, which may vary from EM wave transparent to absorption and shielding [40, 60, 61]. However, owing to their high brittleness and relatively low electrical conductivity, ceramics alone are usually not sufficient to meet the high requirements for practical applications [60, 61, 62].

Carbon based materials including carbon black (CB), carbon fibers (CF), CNTs, carbon nanocoils (CNCs), graphite nanosheets (GNs) and graphene due to their excellent functional properties have been widely used in EM materials [63-74]. Among them, CNTs as one of the most widely investigated one dimensional (1D) carbon nanomaterials have been widely used as absorbent in dielectric materials due to their outstanding property such as high electrical conductivity (~10^6 S/m), strong mechanical strength and high aspect ratio (>1000) since their emergence in 1991[75-78]. For example, Ning Li and coauthors reported single-walled carbon nanotubes (SWCNTs) modified epoxy based electromagnetic interference shielding composites. When the content of SWCNTs is 15.0 wt.% in the epoxy matrix, the electromagnetic interference shielding effectiveness (EMI SE) of the resulting EM materials reached 49 dB [79]. In 2004, Geim and Novoselov extracted single carbon atom layer which were named as graphene through mechanical exfoliation from bulk graphite which found new

avenue for EM materials [80]. As the thinnest two dimensional (2D) material in the carbon family, graphene, which possesses extremely high specific surface areas (SSA) and carrier mobilities, has been proven to be outstanding candidates for obtaining higher loss tangent and high-efficiency EMI shielding[31, 81-87]. Zongping Chen and coauthors fabricated lightweight and flexible graphene foam composites for high-performance electromagnetic interference shielding. When the thickness of samples is 1 mm, the graphene foam exhibited an EMI SE of 23 dB [31]. Bo Wen and coauthors introduced chemically reduced graphene oxide (RGO) into SiO_2 xerogel nanopowders. With 20.0 wt.% RGO in the composite, the resulting material exhibited an EMI SE of ~38 dB [30]. Recently, it is reported that compared with their individual component, three dimensional (3D) hybrids of Graphene and CNTs hybrids (G/CNTs) is suggested to be more promising in functional application according to the theoretical predication and experimental results [88-97]. To take the advantage of G/CNTs hybrids, plenty of strategies have been explored, including postorganization methods through layer-by-layer self-assembly, electrodeposition, liquid phase blending (LPB), and direct chemical vapor deposition (CVD) growth routes through growing CNTs on graphene layers and in situ growth of G/CNTs hybrids on Cu foil coated with Fe catalyst layer [92, 94, 98-106]. For example, Luo Kong and coauthors fabricated CNTs modified graphene foam with CVD method and introduced the hybrids into poly(dimethylsiloxane) (PDMS). When the filler loading is 5 wt.% and the thickness is 2.75 mm, the minimal reflection coefficient (RC_{min}) of CNTs-PDMS and RGO-PDMS is 10 and 14 dB, and the RC_{min} of CNT/G-PDMS reaches 55 dB, which exhibits the advantage of G/CNTs as EM absorbent [95].

By now, nanocarbon absorbents from 1D CNTs to 3D G/CNTs have been widely used in polymer, film or foam based EM materials [43, 46-48, 79, 85, 86, 95]. However, reports on carbon nanofiller modified PDCs based EM materials are still very limited. Especially for the 3D G/CNTs hybrids modified ceramic based EM materials, no report has been found. When the carbon nanofillers were introduced into ceramics, at least two different architectures can be conceived: a) carbon nanofillers can be used as absorbent to improve the permittivity; b) ceramic matrices can adjust the impedance matching and protect the carbon fillers from harsh environment [107]. Even though, the introduction of carbon nanofillers into ceramic matrix can lead to the formation of beneficial micorsturcture, the homogeneous dispersion of carbon nanofillers in ceramics is still an insurmountable challenge. Due to the strong van der Waals interactions between each individual nanofiller and poor wettability between the host precursor and nanofillers, a homogeneous distribution of carbon nanofillers in PDC matrices by blending or mechanical mixing is still challenging, since agglomeration of nanofillers will

unavoidably occur during the polymer-to-ceramic transformation from liquid to solid when the ultrasonic force is removed [108, 109]. The agglomeration of nanofillers will lead to a decreased interface polarization and relaxation, and thus will result in an inferior EM performance [108]. Unfortunately, by now mechanical dispersion is still the exclusively employed method and no breakthrough in the dispersion approaches has been developed.

It is reported that one of the most facile and effective preparative routes in preparing homogeneous nanocomposite ceramics is the single-source-precursor (SSP) route [110-112]. Firstly, the preceramic single-source precursors can be tailored at the molecular level to design ceramic nanocomposites with unique phase/chemical compositions and microstructures [112]. Secondly, the grafted molecular preceramic polymer can not only change the wettability and compatibility between the nanofillers and polymer but also impart the nanofillers solubility, which can guarantee excellent homogeneity of the nanocomposites [113,114]. Thus, in this Ph.D. work, the working objective is settled, namely single-source-precursor synthesis and electromagnetic properties of carbon nanofillers (from 1D to 3D) modified silicon carbonitride (SiCN) ceramic nanocomposites. The single-source-precursor route is employed to prepare nano carbon (NC=CNTs, RGO, RGO/CNTs) containing ceramic nanocomposites as novel and prospective EM materials for EM absorption and shielding application. Therefore, SiCN-based materials are synthesized by means of varying the type of absorbent and content. The microstructure of the nanocomposites is detailedly analyzed and correlated with the permittivity and EM performance of the resultant materials.

2. Fundamentals

In this Chapter, the fundamentals and basic principles underlying the scientific findings in this thesis are introduced, with respect to the latest research developments.

2.1. Electromagnetic materials

Electromagnetic materials are a class of materials that can modify electromagnetic fields when interacting with them in specific or intentional ways [115-117]. Typically, the purpose of electromagnetic materials is to redirect, absorb, attenuate, or to block the electromagnetic waves [115-117]. When an electromagnetic wave is incident into a material, it undergoes reflection, absorption and transmission [118-120]. According to the capability of a material that can absorb, reflect and transmit the electromagnetic waves, the electromagnetic materials can be divided into three categories, which are known as electromagnetic transparent, absorption and interference shielding materials (Fig. 1) [121, 122]. Electromagnetic materials have wide applications in both civilian and military, such as antenna designs and protection against high power transient in densely packed printed circuits [121]. For certain applications, the materials are required to possess special frequency or polarization response to meet the components or system specification [121]. An in-depth understanding of the response of materials to electromagnetic waves will enable us better design and fabricate materials with satisfying performance.

The electromagnetic properties of non-magnetic materials can be characterized with complex permittivity (ε), which can be expressed as follows [115, 116, 121, 122]:

$$\varepsilon = \varepsilon' + j\varepsilon'' \qquad \text{Eq. 1}$$

Where ε' is the real part of the permittivity and ε'' is the imaginary part of the permittivity. The electromagnetic properties of composites can be explicated by the Debye theory, the ε' and ε'' of permittivity are shown as follows [115-122]:

$$\varepsilon' = \varepsilon_\infty + \frac{\varepsilon_s - \varepsilon_\infty}{1+\omega^2\tau^2} \qquad \text{Eq. 2a}$$

$$\varepsilon'' = \frac{\varepsilon_s - \varepsilon_\infty}{1+\omega^2\tau^2}\omega\tau + \frac{\sigma}{\omega\varepsilon_0} \qquad \text{Eq. 2b}$$

According to the above equations, the relationship between ε' and ε'' without the second part of the Eq. 2b can be deduced as [121]:

$$\left(\varepsilon' - \frac{\varepsilon_s - \varepsilon_\infty}{2}\right)^2 + (\varepsilon'')^2 = \left(\frac{\varepsilon_s - \varepsilon_\infty}{2}\right)^2 \quad \text{Eq. 3}$$

Typically, EM transparent materials should possess extremely low ε' and ε", which allows for the transmitting of EM waves. However, EM absorption materials should possess intermediate ε' and ε". Table 1 reviews the requirements on the permittivity of EM transmission, absorption and shielding in the frequency range of 8.2-12.4 GHz (X-band).

Table 1 Requirements on dielectric properties of non-magnetic materials for different applications in X-band [121]

Appilcations	Required properties		Example			
	ε'	ε"	Materials	ε'	ε"	Conductivity (S/cm)
EM transmission	1-5	Tanδ ≤ 0.01	Polymer:Teflon	2.1	$<2.0\times10^{-4}$	10^{-16}-10^{-15}
			Ceramic:Quartz	4.5–4.6	$<3.0\times10^{-4}$	10^{-15}-10^{-12}
EM absorption	5-20	1-10	Polymer:CNTs and graphene/polyaniline	~7 ~9.7	~4 ~4.2	- -
			Ceramic:SiC/Si_3N_4			
EM shielding	>20	>10	Metal: platinum	-	-	9.7×10^6
			Polymer:graphene/PDMS	-	-	60-200
			Ceramic: Ti_3SiC_2	-	-	$\sim4.5\times10^6$

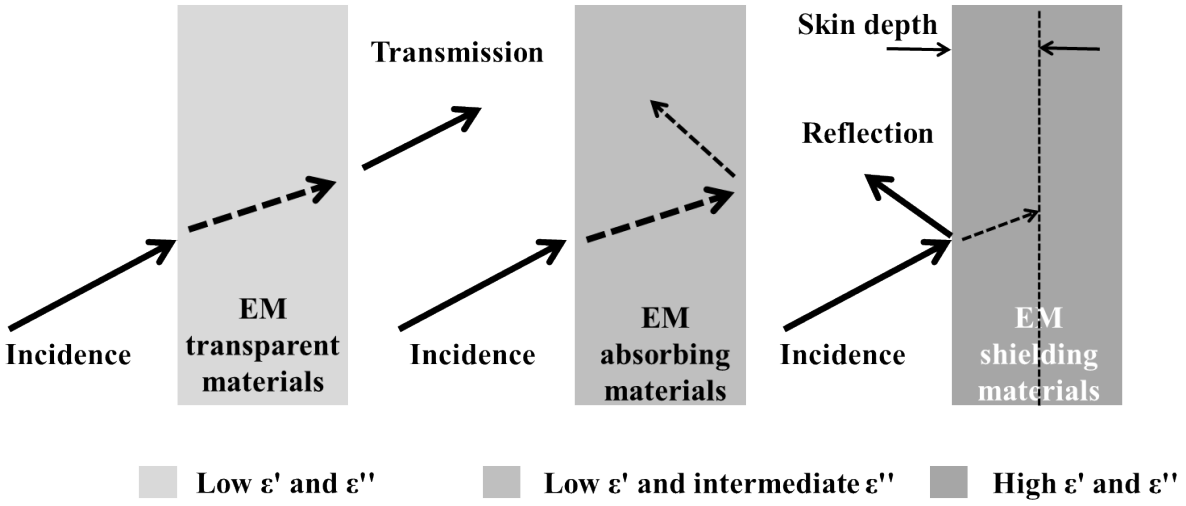

Fig. 1 Schematic illustrations of EM transparent, absorption and shielding materials [121]

Experimentally, the permittivity can be measured with a vector network analyzer (VNA). Fig. 2 shows the optical image and schematic illustration of a VNA.

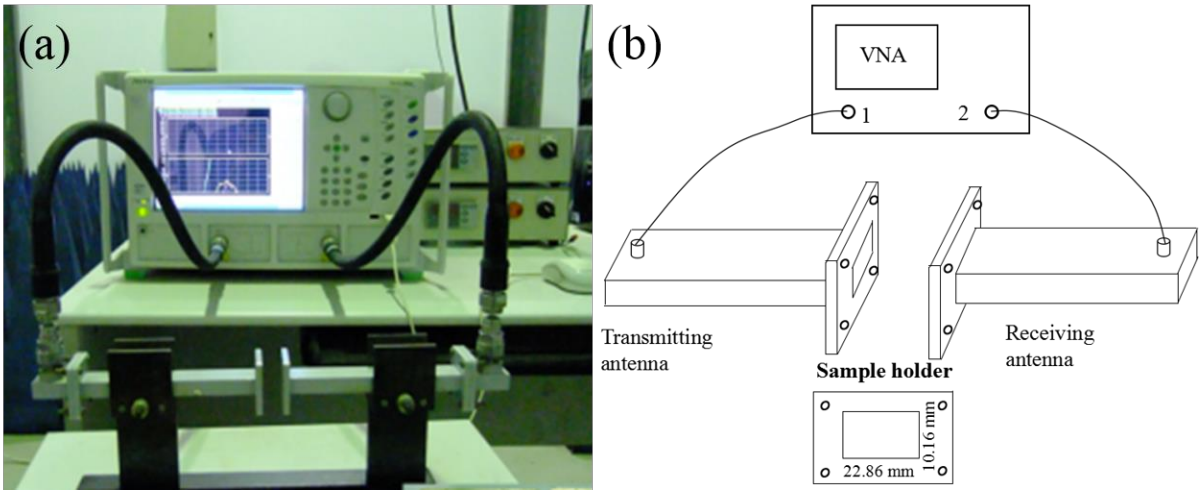

Fig. 2 (a) Optical image and (b) schematic illustration of a VNA [62]

2.1.1. EM transparent materials

2.1.1.1. Definition of EM transparent materials

In the electromagnetic field, transparency is a physical property which allows the EM wave to transmit the material without scattering or with extremely low scattering [121, 123]. Typically, EM transparent materials are employed to fabricate antenna housings or radomes, which can protect the antennas from the effects of the surrounding medium or harsh environments. The transparency of EM materials to EM waves can be achieved through designing the materials to possess low dielectric loss tangent ($\tan\delta \leq 0.01$) and low real part of the permittivity ($\varepsilon' = 1\text{-}5$) as listed in Table 1. By now, commercially available radome materials are electrically insulating materials such as polymers or insulating ceramics such as silica (SiO_2). For example, ε' and $\tan\delta$ of polytetrafluoroethylene are 2.1×10^{-4} and 4.2×10^{-4}, while the ε' and $\tan\delta$ of SiO_2 are 3.9×10^{-4} and 3.0×10^{-4} [121], which can well fufill the requirements of EM transparent materials for practical application.

2.1.1.2. Principle to design EM transparent materials

High quality EM transparent materials must simultaneously fulfill several requirements, such as low permittivity and permeability, good temperature and broadband frequency stability as well as low dielectric loss to minimize capacitive coupling and signal delay, and prevent signals from attenuation [121, 123].

The complex permittivity, permeability and scattering parameters of EM transparent materials can be measured with a resonant cavity method while those of EM absorption and shielding materials are typically measured with a wave-guide chamber since the resonant cavity method is more suitable for the accseement of materials with low dielectric loss, which can provide a better accuracy [121]. According to the working mechanism of EM transparent materials, this class of materials should possess extremely low permittivity and permeability [121]. To get low permittivity, the EM transparent materials must possess low electrical conductivity. The variation in ε' is attributed to the frequency dependence of the polarization mechanisms (i.e. electron and dipole) that contribute to the permittivity [124]. An effective approach to lower ε' of a dielectric is to reduce the number of polarizable groups in per unit volume. Another approach is to design composites composed of phases with low ε'. For a statistic mixture, Lichtenecker and Rother developed a logarithmic law of mixing, which can be mathematically expressed as [125]:

$$\log \varepsilon'_c = \sum_{1}^{i} V_i \log \varepsilon'_i \qquad \text{Eq. 4}$$

Where ε'_c is the relative permittivity of the composite, V_i and ε'_i are the volume fractions and the relative permittivity of phase *i*. In the materials, pores can effectively act as a phase with low ε and tanδ [126]. For porous composites, the Lichtenecker-Rother equation can be expressed as [121]:

$$\log \varepsilon'_P = (1-P) \log \varepsilon'_0 \qquad \text{Eq. 5}$$

Where ε'_p and ε'_0 are the relative permittivity of porous and dense materials, and *P* is the porosity of composite.

2.1.2. EM absorption materials

2.1.2.1. Attenuation mechanism

The function of EM absorption materials is to attenuate the EM waves and prevent the EM waves from reflection. In practical applications, there are three factors that can decrease the reflection [116].

To minimize the reflection of EM waves from a material, it is necessary to take the physical equations which represent RC into consideration. The first equation of interest is that describes *RC* at an interface [116,127]:

$$RC = \frac{\eta_M - \eta_O}{\eta_M + \eta_O} = \frac{Z_M - Z_O}{Z_M + Z_O} \qquad \text{Eq. 6}$$

$$\eta = \sqrt{\frac{j\omega\mu}{\sigma + j\omega\beta}} \qquad \text{Eq. 7}$$

Where η is the admittance of the propagating medium (subscript O for incident medium or air and M for the substrate), σ is electrical conductivity, ω is angular frequency, and μ and ε are permeability and permittivity, respectively. The admittance in this equation can be replaced with the intrinsic impedance ($Z = 1/\eta$). The intrinsic impedance of free space can be expressed as follows [127-129]:

$$Z_0 = \frac{\hat{E}}{\hat{H}} = \sqrt{\frac{\mu_0}{\varepsilon_0}} \qquad \text{Eq. 8}$$

Where $\hat{E}$ and $\hat{H}$ are the electric and magnetic field vectors and μ_o and ε_o are the permeability and permittivity of free space.

The second factor that can influence the RC is impedance matching. Perfect impedance matching can be established through designing the materials to possess equal permittivity and permeability. The normalized intrinsic impedance can be expressed as follows [127-129]:

$$\frac{Z_M}{Z_O} = \sqrt{\frac{\mu^*_r}{\varepsilon^*_r}} \qquad \text{Eq. 9}$$

Where $\varepsilon_r^* = \frac{\varepsilon' - i\varepsilon''}{\varepsilon_o}$ and $\mu_r^* = \frac{\mu' - i\mu''}{\mu_o}$, the prime and double prime superscripts represent the real and imaginary parts of the complex numbers, respectively. If the real and imaginary parts of the permittivity and permeability are equal, then there will be no reflections from the surface of material.

The third factor is the absorption coefficient of the material [121]. In physics, absorption of EM waves inside the materials is a process in which the energy of photons is taken by the electrons of absorbents. Finally, the energy of EM waves is transformed into internal energy by absorbent, typically, thermal energy.

The power of the EM waves propagating inside the materials decays exponentially with the thickness (d) of absorption materials, by the factor $e^{-\alpha d}$, where α is the attenuation constant of the material. Mathematically, α can be expressed as follows [127-129]:

$$\alpha = -\sqrt{\varepsilon_o \mu_o}\,\omega\left(a^2 + b^2\right)^{1/4} \sin\left(\frac{1}{2}\tan^{-1}\left(-\frac{a}{b}\right)\right) \qquad \text{Eq. 10}$$

Where $a = (\varepsilon_r' \mu_r' - \varepsilon_r'' \mu_r'')$ and $b = (\varepsilon_r' \mu_r' + \varepsilon_r'' \mu_r'')$

To get a large specific absorption (absorption devided by sample thickness), α should be as large as possible, which requires large values of permeability and permittivity. However, the attenuation constant should also be compatible with the first factor in Eq. 6, where large values of permittivity and permeability would lead to strong reflections [128, 130].

Based on the transmission-line theory and metal back panel model, RC can be calculated with the relative complex permeability and permittivity [121, 131-134]:

$$RC = 20 \log_{10} \left| \frac{Z_{in} - 1}{Z_{in} + 1} \right| \qquad \text{Eq. 11}$$

$$Z_{in} = \sqrt{\frac{\mu}{\varepsilon}} \tanh\left(j 2\pi \frac{\sqrt{\mu\varepsilon} f d}{c}\right) \qquad \text{Eq. 12}$$

where Z_{in}, $\varepsilon=\varepsilon'-j\varepsilon''$ and $\mu=\mu'-j\mu''$ is the normalized input impendence, permittivity and permeability of the material, d and c represent thickness (m) and the light velocity in vacuum (3×10^8 m/s). Here μ_r was taken equal to 1 because in this paper the materials exhibit negligible magnetic properties.

Fig. 3 is the schematic illustration of the metal back plane model. Accordingly, when the EM wave is propagating inside the material, one part of the incident EMW is absorbed, the other is reflected on the two surfaces. When the thickness of EM absorbing materials is approximately a quarter of the propagating wavelength, that is,

$$d = \left(\frac{n}{4}\right)\lambda \qquad \text{Eq.13}$$

Where n is an odd number ($n= 1, 3, 5, 7, 9 \ldots$), the signal reflected by the left surface ($x=0$) has a phase opposite to the signal reflection coming from the right surface ($x=d$), resulting in destructive inter.

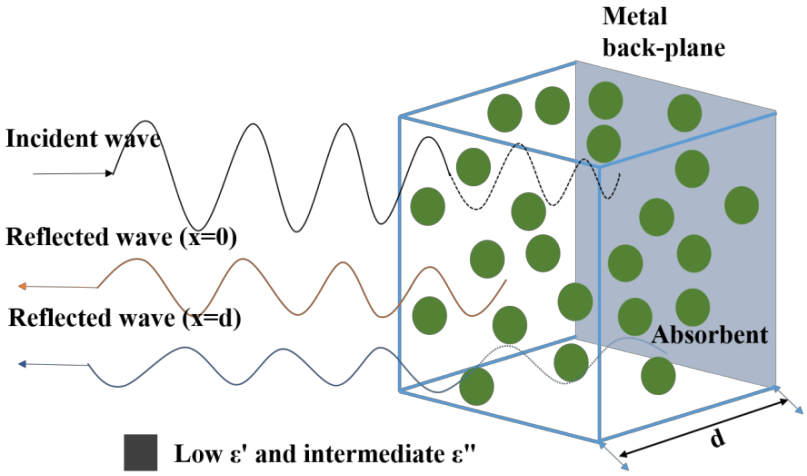

Fig. 3 Schematic illustration of metal back plane model

2.1.2.2. Principle to design electromagnetic absorption materials

The performance of EM absorption materials can be characterized with RC and effective absorption bandwidth (EAB) [121]. When the value of RC is lower than -10 dB (>90 EM wave is attenuated), the RC values are called effective absorption values and the bandwidth of RC curve which is lower than -10 dB is defined as EAB [121,131]. The lower is the RC value; the better is the performance of an EM absorption material. Therefore, the designing principle for EM absorption materials is to try to enhance EAB and minimize the RC value. Typically, excellent EM absorbing materials should be composed of an EM transparent matrix and no less than one electrical and/or magnetic lossy phase(s) [121]. The function of EM transparent matrix is to change the impedance mismatching while lossy phases are used to attenuate the EM waves that propogates inside the materials. When the EM wave comes to the surface of absorption materials, the EM transparent matrix can help to provide a good impedance matching, which could reduce the reflection of EM waves from the surface of materials. When the EM wave is incident into the materials, energy loss will occur through the interactions of the photons with the electrons and dipoles and be transformed into heat by electrically lossy phases [121]. The generated heat is related to the conductivity and dielectric losses of materials. In order to obtain improved EM absorption properties, absorbing materials may have dielectric loss by polarization, and an appropriately high conductivity to attenuate the incident electromagnetic wave [121]. Typically, CB, CF, CNTs, RGO and RGO/CNTs hybrids are ideal absorbents in EM absorption materials [121].

2.1.2.3. Typical types of EM absorption material

The research activity on electromagnetic-wave absorbers can be dated back to the last century 1940s during World War II by Germans in response to detecting aircrafts with the early radar sets [19, 20]. Ferrite based painting was designed as the first generation EM absorption material. After that, a wide range of EM absorption materials were developed by researchers in the worldwide. Among them, the most commonly known type of EM absorption material is iron ball paint composed of tiny spheres coated with carbonyl iron or ferrite [135,136]. The alternating EM field from the radarsets can induce oscillations of the iron atoms, which converts the EM wave energy into heat. Another kind of electromagnetic absorption material is the conductive fillers such as CB, CF, CNTs, RGO and RGO/CNTs modified foam based materials, which is used as lining of anechoic chambers for the measurements of electromagnetic radiation. These kinds of materials typically are composed of a fireproofed urethane foam modified with conductive fillers or iron spherical particles [137-139]. In recent decades, various species of EM materials have been developed. The most widely investigated electromagnetic absorbents are the hybrids of ferroferric oxide, cobalt oxide, or nickel ferrite nanocrystals and nanocarbon fillers [23-26]. One practical application is to paint them together with certain kinds of polymers onto the surface of aircraft to hide from the detection of radar. By now, plenty of studies have been performed to investigate the electromagnetic absorption property of CNTs based absorbers as stealth technology on aircraft [16, 17, 140-143]. Recently, RGO has been widely reported as EM absorbent in EM field due to the excellent electrical conductivity and high specific surface area [95].

2.1.3. Electromagnetic Interference shielding materials

2.1.3.1. Definition of EMI shielding materials

Electromagnetic interference is a disturbance generated by external signals from intentional or natural source that can affect an electrical circuit by electromagnetic induction, electrostatic coupling, or conduction [121]. The EMI can influence the function of the circuit or even stop it from working [121]. Both intentional and natural sources that are able to generate alternative electrical currents can cause EMI, such as automobile ignition systems, mobile phones, thunderstorms, the Sun, and the Northern Lights [144]. EMI shielding is a practice that blocks the power of EM field in a space through blocking the EM field with shielding materials made of electrically conductive, magnetic or both electrically conductive and magnetic materials [121, 145]. The basic requirement for the EMI shielding material is to possess as high as shielding performance.

The capability of a material to block the electromagnetic waves is defined as shielding effectiveness (SE) [144-146]. The unit of SE is decibel (dB).

Mathematically, SE can be calculated with the ratio of the magnitude of the electric field that is incident on the material to the magnitude of the electric field that transmits through the material, which can be expressed as follows [145,146]:

$$SE = 10\log\frac{\hat{E}_i}{\hat{E}_t} \qquad \text{Eq. 14}$$

Where $\hat{E}_i$ represents the incident electric field and $\hat{E}_t$ represents the transmitted electric field. The value of SE is always a positive result as the incident field is not lower than the field that exits in the shielding material. For example, an SE value of 60 dB means that the magnitude of $\hat{E}_t$ is reduced from the magnitude of $\hat{E}_i$ by a factor of 10^6, which represents 99.9999% of EM wave is shielded.

2.1.3.2. Shielding mechanism of EM materials

There are three mechanisms that can contribute to the shielding effectiveness, which are known as shielding by reflection (SE_R), shielding by absorption (SE_A) and shielding by multiple reflections (SE_{MR}) (Fig. 4) [113, 121, 128, 130, 133, 144-146]. The primary mechanism of EMI shielding is reflection as shielding materials always possess high electrical conductivity. For reflection of EM waves, the materials need to possess mobile charge carriers (electron or holes), which can interact with the electromagnetic fields in the radiation. As a result, the shield tends to be electrically conducting, even though conductivity is not required. Shielding does not require good electrical conductivity, however, good electrical conductivity can absolutely improve the EM shielding performance [147, 148].

The secondary mechanism of EM material is absorption. For significant absorption of electromagnetic waves, the shielding material should possess electric and/or magnetic dipoles, which interacts with the electromagnetic fields in the radiation [131, 133, 138, 148]. The electric dipoles can be provided by materials such as CNTs and RGO that possess a high value of dielectric constant. However, the magnetic dipoles are provided by the materials possessing a high value of magnetic permeability such as Fe, Co, Ni and their oxides [84, 85, 96, 97, 121].

Besides shielding by reflection and absorption, the third mechanism of shielding is multiple reflections, which refer to the reflections at various interfaces in the shield [30, 31, 38, 40-42, 121, 146]. This mechanism requires the presence of large amount of interfaces inside the material [121]. In this circumstance, porous or foam materials typically possess higher SE_{MR} than dense

materials. The multiple reflections are the internal reflections of the shielding material. In cases where the SE_A is higher than 10 dB or the sample thickness is larger than the skin depth (δ), which means most of the multi-reflected waves will be attenuated within the material, the multi-reflected power can be ignored [40-42].

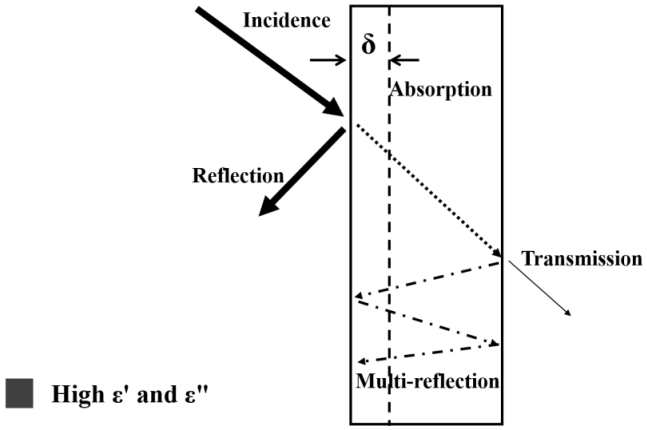

Fig. 4 Schematic illustration of EM shielding

The skin depth is the distance at which the strength of electromagnetic field drops to *1/e* of the incident strength [40-42]. Mathematically, it can be calculated as follows [40-42]:

$$\delta = \left(\sqrt{\pi f \mu \sigma}\right)^{-1} \qquad \text{Eq. 15}$$

Where f is the frequency, μ is the magnetic permeability ($\mu = \mu_o \mu_r$), $\mu_o = 4\ \pi \times 10^{-7}$ Hm^{-1}, μ_r is the relative magnetic permeability and σ is the electrical conductivity of the shield. In the calculations, the μ_r is assumed to be 1.

The alternate current (AC) conductivity (σ_{AC}) can be calculated with the imaginary part of permittivity and the frequency as follows [41, 42, 146]:

$$\sigma_{AC} = 2\pi f \varepsilon_o \varepsilon'' \qquad \text{Eq. 16}$$

Where f is the frequency in Hz and ε_o is the permittivity of free space ($\varepsilon_o = 8.854 \times 10^{-12}$ Fm^{-1}).

The sum of SE_R, SE_A and SE_{MR} is the total shielding effectiveness (SE_T) of a shield [40-42, 121, 146, 149].

For electrically conductive materials, EMI SE can be calculated with Simon formalism [146, 149]:

$$SE = 50 + 10\log\left(\frac{\sigma}{f}\right) + 1.7d\sqrt{\sigma f} \qquad \text{Eq. 17}$$

Where σ is the electrical conductivity, f is the frequency in Hz and d is the thickness of shield. From Eq. 17, we can get to know that the EMI SE is strongly determined by their electrical conductivity. When EM waves are incident into shielding materials, mobile charge carriers

inside the absorbent can interact with incident EM waves, which prevents EM waves from transmitting [147, 148].

Experimentally, EMI SE can be directly obtained with the logarithmic ratio of incoming power (P_I) to transmitted power (P_T) as follows [40-42, 121, 146, 148]:

$$SE(dB) = 10\log(\frac{P_I}{P_T}) \quad \text{Eq. 18}$$

The sum of reflection power (R), absorption power (A), and transmission power (T) is 1, which can be expressed as [40-42, 121, 146, 148]:

$$R + A + T = 1 \quad \text{Eq. 19}$$

The reflection and transmission power can be calculated with scattering parameters (S_{ij}). Here, "i" represents the network analyzer port receiving the EM wave signal and "j" represents the port that is giving EM wave signal. VNA directly gives the outputs of scattering parameters (S_{11}, S_{12}, S_{21}, S_{22}), which can be used to calculate the R and T coefficients as follows [40-42, 121, 146, 148]:

$$R = |S_{11}|^2 = |S_{22}|^2 \quad \text{Eq. 20}$$

$$T = |S_{12}|^2 = |S_{21}|^2 \quad \text{Eq. 21}$$

When the value of SE_A is higher than 10 dB which means more than 90 % of incident waves are absorbed or the sample thickness is larger than δ, most of the multi-reflected waves will be attenuated within the material. In this circumstance, the contribution of SE_{MR} can be ignored. Then the SE_T can be written as follows [40-42, 121, 146, 148]:

$$SE_T = SE_R + SE_A \quad \text{Eq. 22}$$

SE_R and SE_A can be calculated in terms of reflection and absorption considering the power of the incident electromagnetic waves inside the shielding material as follows [40-42, 121, 146, 148]:

$$SE_R = 10\log\left(\frac{1}{1-R}\right) \quad \text{Eq. 23}$$

$$SE_A = 10\log\left(\frac{1-R}{T}\right) \quad \text{Eq. 24}$$

2.1.3.3. Typical types of EM shielding material

By now, the most traditional materials used for EMI shielding are metals including metal sheet, metal screen, and metal foam [115, 116, 121, 128]. For example, copper, aluminum or nickel

films are used as radio frequency shielding because they can reflect and absorb EM waves. These kinds of films were typically prepared through spraying inks of corresponding small metal particles onto the enclosure to form a continuous conductive layer. However, the biggest disadvantage of these kinds of materials is that metals suffer from poor chemical stability. Polymer-matrix composites modified with carbon fillers are the second generation EM shielding materials. Conductive fillers such as CB, CFs, CNCs, CNTs or RGO modified polymer based composites are attractive for shielding due to their processability (e.g., moldability) [41, 42, 121]. In practical application, seams are commonly encountered when metal sheets are used as the shield, which may cause leakage of the radiation and diminish the effectiveness of the shield. The polymer based shielding materils can overcome this drawback easily due to their relative flexibility. Moreover, the polymer based EM materials are also attractive for their relatively low density compared with metals [121]. However, the polymer matrix is usually electrically insulating and cannot contribute to shielding. Although some polymers are conductive, these kinds of polymers tend to be poor in processability and mechanical properties [95]. In some cases, cements can also work as the matrix of shielding materials due to the intrinsic advantages including good processibility and mechanical strength [150-152]. Compared with insulating polymers, cement is slightly conductive which endows cement-matrix composites higher shielding effectiveness than corresponding polymer matrix composites with the same content of conductive fillers. However, cement-matrix based composites typically encounter poor dispersion of conductive fillers. Typically, cement based EM materials are always used for the shielding in buildings [151, 152].

2.2. Polymer-derived ceramics

2.2.1. General background

PDCs are a class of ceramic materials that can be prepared through thermal pyrolysis of different polymer precursors under protection atmospheres such as Ar or N_2 [51-53]. Thus, PDCs are differed by following the chemical routes rather than the traditional sintering routes, which have found promising applications in the production of technologically important ceramic components such as fibers, coatings, infiltrated porous media or complex-shaped bulk parts. The most commonly known classes of PDCs by now are binary systems such as Si_3N_4, SiC, BN, and AlN, ternary systems such as SiCN, SiOC, and BCN as well as quaternary systems such as SiCNO, SiBCN, SiBCO, SiAlCN, and SiAlCO [153]. In recent years, several quinary systems such as transition metals such as Ta and Hf modified PDCs have been

reported as well [51, 52, 154-157]. In this PhD thesis, we mainly concentrate our attention on carbon nanofillers modified silicon-based PDCs. Other classes of PDCs will not be introduced. Compared with the traditional process of ceramic powders sintered under high temperatures, PDC approach is a relatively new technology. The origination of PDC materials can be dated back to last century in 1960s when Ainger and Herbert, Chantrell and Popper reported the synthesis of nonoxide ceramics through pyrolysis of molecular precursors [158, 159]. One decade later, the PDC approach was further developed by Verbeek and colleagues through fabrication of Si_3N_4/SiC ceramic fibers for high-temperature applications via thermal pyrolysis of polysilazanes, polysiloxanes, and polycarbosilanes [160-162]. At the end of 1970s, based on the work of Fritz and the early work of Yajima, PDC SiC was reported to be synthesized through thermolysis of polycarbosilazanes [163-165]. After that, significant improvements had been achieved in the development of novel synthesis routes to preceramic polymers with controlled molecular structure and flexible processing behavior. When the time went into 1980s, further advancements were achieved by the development of new synthesis routes for preceramics with better controlled molecular structure and chemical compositions [166-168]. In 1990s, Riedel et al. reported high temperature stable boron-containing SiCN ceramics with respect to decomposition reaching 2200°C [53]. In the last two decades, the synthesis and properties of PDC nanocomposites (PDC-NCs) were investigated intensively [51].

The intrinsic advantages of PDCs such as covalent bonds and amorphous structures endow them a unique combination of remarkable properties including high temperature, structural and functional properties [51]. The strong bonds between silicon, carbon, oxygen and nitrogen enable the successful synthesis of Si-contained PDCs such as Si-C, Si-N, Si-O-N, Si-C-N and Si-B-C-N. Generally, PDCs such as SiC and Si_3N_4 possess good high temperature stability, excellent high temperature resistance towards oxidation, corrosion and creep resistance and enhanced thermo-mechanical strength, which makes them excellent thermal structural materials [51]. Moreover, the tunable electrical conductivity of PDCs from insulating to conductive enables PDCs being promising functional materials, including electrode materials and thermoelectric materials [52, 121, 169, 170]. Recently, due to their tunable EM properties from EM transparent to EM shielding, PDCs were reported to find promising application in EM field [121].

2.2.2. Synthesis of preceramic Si-based precursors

Synthesis of the preceramic precursors is a crucial step for the preparation of PDCs since the molecular structure and type of the preceramic polymer can influence not only the

composition but also the phase numbers and distribution as well as the morphology (such as porosity) of the resultant ceramic material [51, 52, 171]. The polymer-to-ceramic conversion process is always accompanied by the evaporation of gaseous byproducts, mass loss and volume shrinkages, which could lead to the formation of pores, cracks or even destroying of bulk materials. Thus, the most important issue for the designing of polymer precursors is that the mass loss of preceramics during pyrolysis should be as low as possible in the prerequisite of without sacrificing the processability and reactivity of the precursors [171].

Fig. 5 shows the general oversimplified schematic illustration of the molecular structure of silicon-based polymers [52]. Generally, there are two methods to modify and design the chemistry and the architecture of the preceramic precursors: firstly, the atom (X) of the polymer backbone, secondly, the substituent R_1 and R_2 attached to silicon [52]. The alteration of X can result in the formation of different classes of Si-based polymers such as polycarbosilanes (PCS), polyborosilazane (PBSZ), polysilazane (PSN), and polysiloxane (PSO) [52, 172]. R_1 and R_2 attached to silicon atoms are functional groups including hydrogen, aliphatic or aromatic groups. Through adjusting R_1 and R_2, the chemical and thermal stability, solubility and fusibility as well as electronic, optical and rheological properties of the polymer precursors can be modified [52, 172]. Moreover, the carbon content within the PDCs can also be affected by the R groups [173].

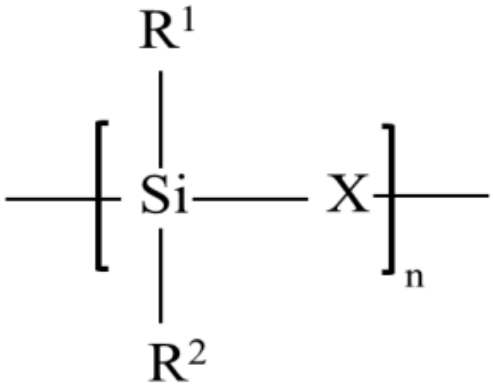

Fig. 5 Schematic illustration of oversimplified representation of the molecular structure of silicon-based polymer

In this Ph.D. work, a poly(organo)silazane is used as a precursor for the synthesis of SiCN-based ceramics. Thus, the detailed introduction in this part focuses mainly on the synthesis of poly(organo)silazane. Synthesis of poly(organo)silazane can be made starting from chlorosilanes by means of ammonolysis reactions with ammonia or aminolysis with different

amines [174,175], as shown in Fig. 6. These types of reactions normally yield a mixture of oligomers and low molecular weight polymers which can easily volatilize and depolymerize giving low ceramic yields. Therefore, cross-linking must be performed prior to pyrolysis [175-178].

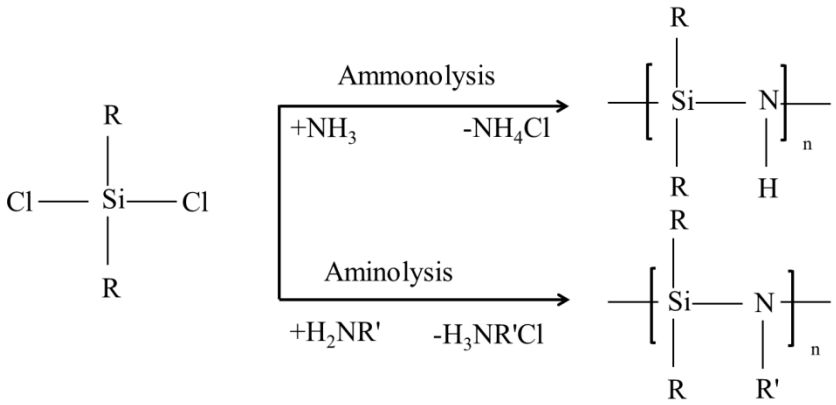

Fig. 6 Synthesis routes to polycarbosilazanes starting from chlorosilanes [174]

By now, one of the most successful commercially available poly(organo)silazane is HTT 1800 (Merck), which is the precursor of all the SiCN based ceramics in this Ph.D work. Fig. 7 shows the general formula of HTT 1800. The HTT 1800 is synthesized by coammonolysis of dichloromethylvinylsilane (H_2C=$CHSi(CH_3)Cl_2$) and dichloromethylsilane (CH_3SiHCl_2) [179].

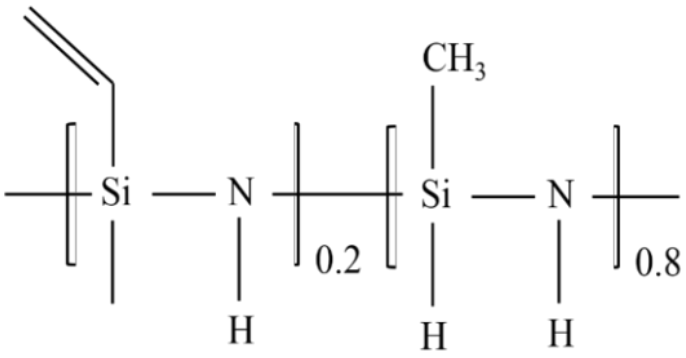

Fig.7 General formula of poly(organo)silazane HTT 1800

2.2.3. Functional properties of PDCs

In this part, typical functional properties of PDCs are introduced mainly from electrical and magnetic.

Electrical conductivity is one of the most commonly investigated functional property of PDCs. Electrical conductivity of polycarbosilane-derived SiC as a function of pyrolysis temperature was firstly investigated by Yajima at the early discovery of PDC materials [180]. After that, plenty of investigations on the electrical conductivity of PDCs have been reported by the research colleagues [180-188]. Investigations showed that preceramic molecular structure, composition, pyrolysis and annealing temperature, heating program and atmosphere can all have influence on the electrical conductivity of the resultant PDCs. The electrical conductivity of PCDs at room temperature can vary by more than 10 orders of magnitudes [52]. Typically, there are three approaches that can be empolyed to improve the electrical conductivity of PDCs, namely, a) increasing the pyrolysis or annealing temperature; b) in-situ formation of nanowire, nanotube or nanowires in the closed pores in the matrix [121]; c) incorporation of conductive fillers [52,185-187]. Increasing of pyrolysis temperature could lead to loss of organic bonds and increase in the sp^2/sp^3 ratio of the carbon atoms or separation of conductive phase while incorporation and in-situ formation of nano fillers can establish more conductive networks inside the PDC matrix, which helps to provide better conductive pathways in same cross section [185-187]. By now, introduction of conductive nanofillers is the most effective way to improve the conductive since the content of fillers can be easily controlled [121]. However, the disadvantage of this approach is the poor dispersion of the nanofillers at high filler content.

Magnetic property of PDC materials mainly refers to the composites containing Fe, Co and Ni elements [189-194]. The magnetic property of PDCs based materials is mainly determained by the content of magnetizable elements inside the PDCs. For example, composites consisting of iron particles dispersed in SiCN was fabricated either by introduction of Fe_3O_4 powders into polysilazane precursor followed by reduction during the pyrolysis or starting from Fe powder followed by thermal annealing at 1100ºC in Ar atmosphere [189]. PDC SiOC with magnetic propety was reported to be fabricated through pyrolysis of the mixture of a preceramic polymer and iron silicide fillers [190]. One of the most serious drawbacks of these works is the difficulty in homogeneous dispersion of magnetizable elements inside the matrix due to the intrinsic disadvantages of physical blending approach. A more efficient approach to produce PDC based materials with magnetic functionalities is to graft metallic iron atoms in the backbone of the polymeric precursor with single-source-precursor route.

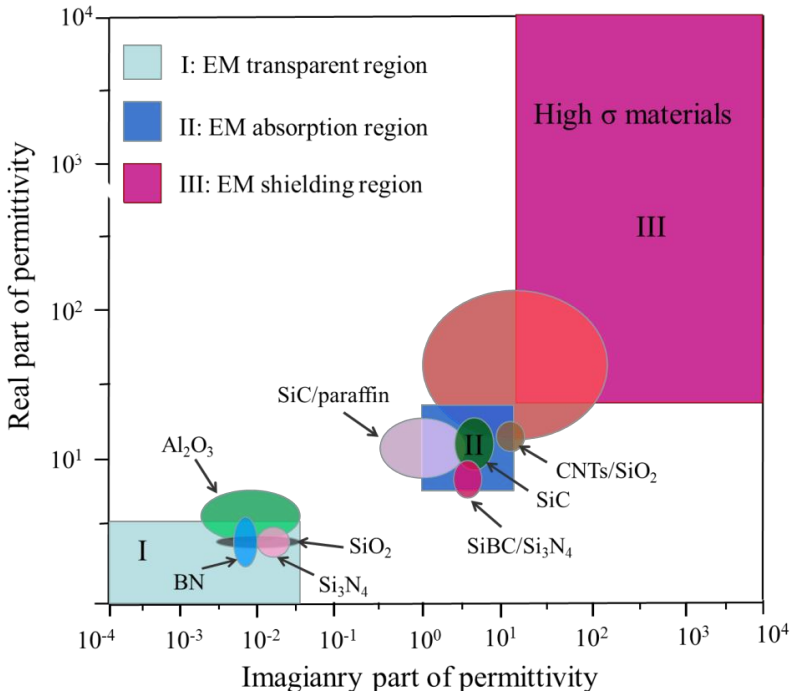

Fig. 8 Chart of permittivity of typical dielectric ceramics, SiO_2, BN, Si_3N_4, SiC/paraffin, SiCN, $SiBC/Si_3N_4$, Ti_3SiC_2/Al_2O_3, $CNTs/SiO_2$ and Al_2O_3 [121]

2.2.4. PDCs based nanocompoistes towards EMMs

PDC based materials are natural candidates for EM materials due to their easily accessible in designing of microstructure and properties from EM transparent to EM shielding. For example, due to the intrinsic insulating property of some ceramics such as SiO_2, Si_3N_4, Si_3N_4-SiO_2, Si_3N_4-BN, and Si_3N_4-SiO_2-BN, they have been proven to be promising EM wave transparent materials for applications and excellent matrix candidates for EM absorption materials [121,198,202,205]. Fig. 8 shows a schematic review of different ceramic based EM materials from EM transparent to EM shielding [121]. As shown in Fig. 8, ceramics are good candidates for EM transparent materials due to their low σ. However, when it comes to EM absorption and shielding, ceramics alone cannot well meet the basic requirement for practical application. There are two approaches that can improve the attenuation capability of ceramic based EM materials, which are a) in-situ formation of conductive or semiconductive fillers including amorphous or graphitic carbon, carbon nanofibers, CNTs, SiC nanophase or nanowires through in-situ formation or phase separation [196-201], b) incorporation of absorbents into the ceramic matrix [108,202]. According to the designing principle of EM absorption materials, excellent EM absorbing materials should be composed of an electrically insulating matrix and suitable amount of electrically lossy phase(s) [121]. The content of electrically lossy phase(s) is typically lower than 20 wt.%. However, for EM shielding

materials, compared with the EM absorption materials, the content of electrically lossy phase should be as high as possible or consist of an electrically phase, such as metal film based EM shielding materials [121,203,204]. In PDC composites, the insulating phase can work as matrix, the glass or graphite carbon, carbon nanofibers, CNTs, SiC nanophase or nanowires and magnetic phases can all be employed as absorbents. For example, Duan and coauthors had improved the EM absorption property of SiOC based PDCs through in-situ formation of SiC nanowires in the pores with the assistance of Fe catalyst and annealing [205]. The results showed that with increasing catalyst content and annealing temperature, the amount of in-situ formed SiC NWs increased accordingly while the real permittivity and the imaginary permittivity increased from 3.63 and 0.14 to 10.72 and 12.17, respectively, the RC_{min} decreased from -1.22 dB to -20.01 dB and the EMI SE increased from from 2.6 dB to 18.0 dB. Li et al. improved the EM absorption property of SiCN PDCs through phase separation of SiC nanophase and carbon graphite ribbons with the assistance of heat treatment [198]. When the annealing temperature increased from 1000ºC to 1500ºC, the average real permittivity, imaginary permittivity and loss tangent increased from 4.4, 0.2 and 0.05 to 13.8, 6.3 and 0.46, respectively and the RC_{min} and the frequency bandwidth below -10 dB for SiCN annealed at 1500ºC were -53 dB and 3.02 GHz, indicating good microwave absorption properties. For absorption application, widely investigations have also been reported. For example, Zhang et al. improved the EM absorption property of PDCs-SiBCN through introducing multi-walled carbon nanotubes [202]. Han et al. improved the EM absorption property of SiOC ceramics through introducing RGO and in-situ formation of SiC nanowires [108]. Table 2 summarizes the state of the art of various ceramic based electromagnetic materials. For comparison, the chemical composition, amount of absorbent, RC_{min} and EAB are listed.

Table 2 Summary of the state of the art of various ceramic based electromagnetic materials. For comparison, the chemical composition, amount of absorbent, RC_{min} and EAB are listed.

Materials	Matrix	Absorbent	ε'	ε''	RC_{min}	EAB (GHz)	Ref.
PDC-SiC	SiC,C	SiC, C	3.6-8.4	0.17-10.1	-9.9	0	196
	SiCTi	SiC, C	～11.9	～4.5	-	-	197
	SiC(Fe)	SiC	4.4-38.9	0.7-39.6	-22	3.45	198
	SiC(Co)	SiC, C, Co	5.8-10.0	0.2-3.5	-42	2.4	199
PDC-SiBCN	SiBCN	SiC	2.7-10.4	0.03-5.6	-15.8	3.6	200
	SiBCN	SiC nanoparticles	2.7-7.0	0.1-1.0	-17	0.9	201
	SiBCN	CNTs	2.7-15.6	0.1-15.6	-32	3	202
PDC-SiCN	SiCN	SiC, C	4.3-14.1	0.2-6.5	-53	3.02	203
	Si_3N_4	SiC, C	3.7-8.9	0.004-1.8	-	-	204
PDC-SiOC	SiOC	SiC, C	3.6-5.6	0.1-1.3	-10	0.06	205
	SiOC	C, SiC nanowires	3.6-10.7	0.1-12.7	-17	3.57	206
	SiOC	C, Nano Si	3.2-13.0	0.1-10.8	-61	3.5	207
	SiOC	C,SiC	3.0-28.2	0.0-46.3	-46	3.0	208
	SiC(N)O	RGO	4.0-11	2.0-9.5	-43.4	3.0	209

Although this summary gives a comprehensive overview of EM property of various ceramic based composites, it cannot describe the correlation between the microstructure, chemical composition and EM properties of each single materials in detail.

3. Cumulative part of the thesis

With the cumulative part of this thesis the major scientific findings, which are reported in publication [1]-[3] are summarized and correlated.

The initial work presented in Chapter 3.1 relates to the synthesis, characterization of microstructure, dielectric and electromagnetic absorption property of CNTs containing silicon carbonitride (CNTs-SiCN) ceramic nanocomposites derived from chemical modification of carboxylic carbon nanotubes (CNTs-COOH) modified poly(organo)silazane HTT 1800. In this work, a systematic synthesis of CNTs-COOH modified HTT 1800 single-source-precursor route was developed with the assistance of zinc chloride ($ZnCl_2$). The following Chapters 3.2 and 3.3 focus on RGO-SiCN and RGO/CNTs-SiCN nanocomposites, in which the influence of absorbent content on the microstructure, dielectric, electromagnetic absorption and electromagnetic shielding properties were investigated in detail. The study of the composites follows two major objectives: *i*) the characterization of microstructures, *ii*) the influence of the microstructure on the dielectric, electromagnetic absorption and shielding properties. In Chapter 3.3, chemically bonded GO/CNTs hybrids were synthesized with GO and amino functionalized CNTs (CNTs-NH_2) prior to the synthesis of CNTs/GO-HTT 1800 single-source-precursor. In this case, a structural stable CNTs/GO is available to be used as precursor of CNTs/RGO hybrids in order to study the synergetic effect of CNTs/RGO hybrids, in terms of their electromagnetic performance.

3.1. Microstructure and electromagnetic properties of CNTs-SiCN nanocomposites derived from single-source-precursor

The content of this Chapter is published in:

[1] Liu X, Yu Z, Chen L, et al. Role of single-source-precursor structure on microstructure and electromagnetic properties of CNTs-SiCN nanocomposites. Journal of the American Ceramic Society, 100 (2017) 4649-4660.

In the present Chapter, the correlation between the microstructural development and electromagnetic properties of as-prepared CNTs-SiCN ceramic nanocomposites is presented. The dispersion state of CNTs-COOH with respect to synthesis approach including physical blending and single-source-precursor route is investigated in detail. The morphology of carbon backbones of incorporated CNTs in each fabrication stage is characterized and investigated. In addition, the influence of CNTs content on the permittivity and electromagnetic properties is presented and the performance of the resulting CNTs-SiCN ceramic nanocomposites was optimized. Finally, the electromagnetic absorption performance of different samples with varying sample thickness is discussed.

3.1.1. Results and discussion

The carboxylic functionalized multi-walled carbon nanotubes (MWCNTs-COOH) (Outer Diameter: 20~30 nm, Length: 10~30 μm, Special surface area (SSA) >110 m^2/g, Electrical conductivity >100 s/m, -COOH content: 1.23 wt%, Xianfeng Nano, China) were dispersed into N, N-Dimethylformamide (DMF) (Sigma-Aldrich, Munich, Germany) with a weight ratio of 1:100 in a flask. After ultra-sonication of the obtained mixture for 4 h, $ZnCl_2$ catalyst and poly(methylvinyl)silazane HTT 1800 (KiON Specialty Polymers) with a weight ratio of 2:98 was added. Then the reaction mixture was heated up to 70°C for 72 h under argon flow with magnetic stirring. Subsequently, the as-synthesized SSPs were cross-linked at 120°C for 4 h. After the evaporation of the DMF, black solid powders were isolated. After ball milling for 3 hours under the protection of Ar atmosphere, the SSP powders were warm-pressed into green bodies with a dimension of 50.0×40.0×3.0 mm^3 under a pressure of 60 KN while maintaining the temperature at 245 °C for 2 h. The green bodies were pyrolyzed in an Ar atmosphere at 1000°C using the heating program shown in Fig. 9, and machined into samples with a dimension of 22.86×10.16×2.00 mm^3 by wire cutting. The synthesis procedure of monolithic

CNTs-SiCN nanocomposites is shown in Fig. 10.

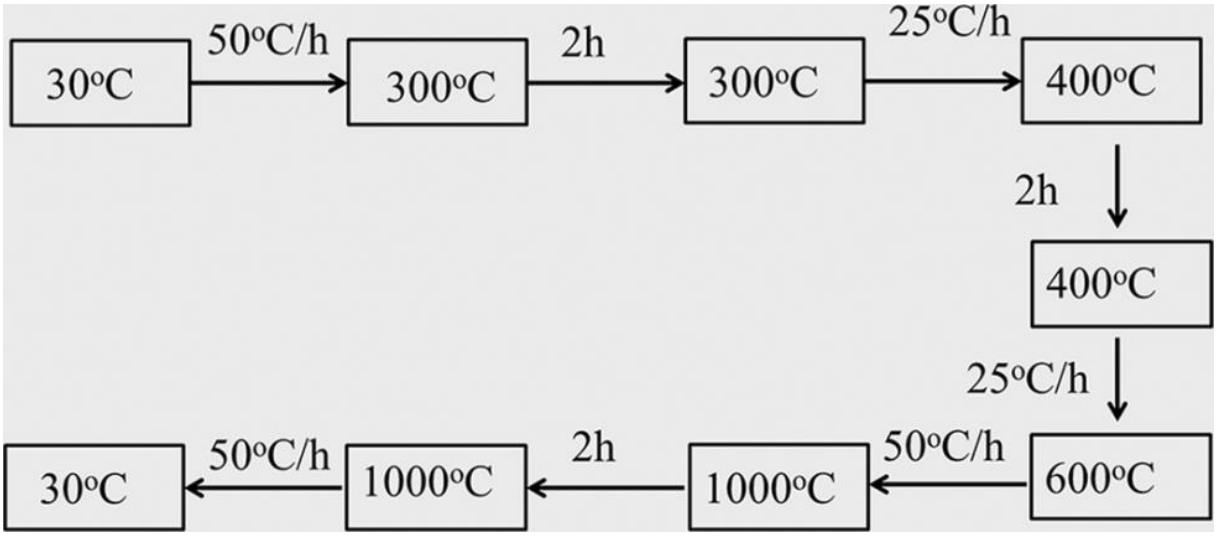

Fig. 9 Schematic illustration of the heating program

To investigate the influence of the CNT content on the EM properties of the final ceramic composites, a series of CNTs-SiCN nanocomposites with different CNT content in the feed were prepared (see Table 3). With 2.5 wt%, 4.5 wt% and 8.0 wt% CNTs in the feed and with $ZnCl_2$ as catalyst, the obtained SSPs were denoted as HTT 1800-2.5, HTT 1800-4.5a and HTT 1800-8.0, respectively. To make a comparison with the SSP, a control test containing 4.5 wt% CNTs without catalyst was performed under the same condition and the resultant physically-blended-precursor was denoted as HTT 1800-4.5b. After pyrolysis of the preceramic precursors HTT-1800, HTT 1800-2.5, HTT 1800-4.5a, HTT 1800-4.5b and HTT 1800-8.0 under the same condition, the resultant CNTs-SiCN samples were denoted as S-0.0, S-2.5, S-4.5a, S-4.5b and S-8.0, respectively.

Table 3 Content of catalyst and CNTs in the feed

Ceramics	Precursors	CNT content (wt.%)	$ZnCl_2$ content (wt.%)
S-0.0	HTT 1800-0.0	0.0	0.0
S-2.5	HTT 1800-1.0	1.0	2.0
S-4.5 b[1]	HTT 1800-4.5b	4.5	0.0
S-4.5 a	HTT 1800-4.5a	4.5	2.0
S-8.0	HTT 1800-8.0	8.0	2.0

[1] S-4.5 b was obtained by pyrolysis of a physically blended CNTs/HTT 1800 mixture

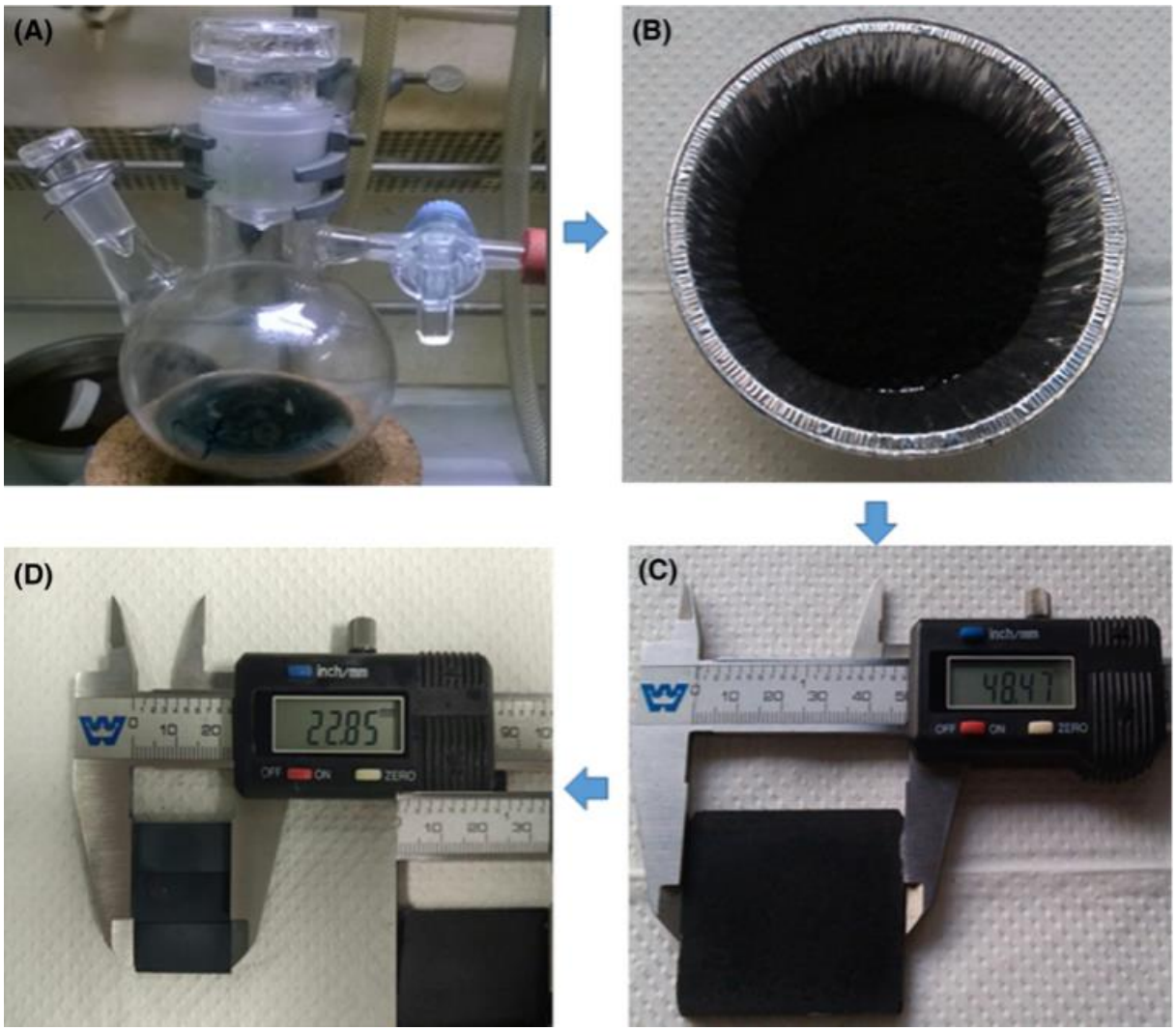

Fig. 10 (A) As-synthesized single-source-precursor in DMF, (B) single-source-precursor powders after removal of DMF, (C) green body of single-source-precursor after warm-pressing at 245ºC and (D) CNTs-SiCN ceramic sample after machining by wire cutting (insert shows the monolithic CNTs-SiCN ceramic after pyrolysis at 1000ºC).

Fourier transform infrared (FT IR) spectra were collected using a Bruker Vertex 70 FT IR instrument (Bruker, Billerica, MA) in attenuated total reflectance geometry. X-ray diffraction (XRD) was employed to conduct phase analysis (X'Pert Pro; Philips, Netherlands). Raman spectra were recorded from 100 to 4000 cm^{-1}employing a micro-Raman HR8000 spectrometer (Horiba Jobin Yvon, Bensheim, Germany) using a laser wavelength of 514.5 nm.

The microstructure of the samples was analyzed by scanning electron microscopy (SEM; S-4799, Hitachi, Tokyo, Japan). TEM studies were conducted on ground powder samples using a JEM-2100 microscope (JEOL Ltd., Tokyo, Japan) at an acceleration voltage of 200 kV (wavelength l52.51 pm). The density and open porosity of final ceramics were measured

using Archimedes method. The values of scattering parameters (S-parameters; S_{11}, S_{12}, S_{21} and S_{22}) of the as-prepared samples with dimensions of 22.86×10.16×2.00 mm^3were measured by waveguide method using a vector network analyzer (VNA, MS4644A; Anritsu, Japan) from 8.2 to 12.4 GHz (X-band). To diminish the influence of the air-gap, at least three samples for each CNT content were prepared, and the measured values of S-parameters were compared to confirm that the errors caused by sample measurement are less than 3%.

In this study, a series of preceramic precursors were synthesized by adjusting the CNT content in feed. The CNT contents are 0.0 wt%, 2.5 wt%, 4.5 wt% and 8.0 wt%, and the resultant polymers are abbreviated as HTT 1800-0.0, HTT 1800-2.5, HTT 1800-4.5a, HTT 1800-4.5b (physically-blended-precursor), and HTT 1800-8.0, respectively. The FT IR spectra of the SSPs and physically-blended-precursor crossed-linked at 120°C were measured and the results are shown in Fig.11. In the FT IR spectrum of HTT 1800-0.0, typical absorption bands related to C–H (2960 and 2965 cm^{-1}), Si–N–H (1160 cm^{-1}), and Si–N (930 cm^{-1}) groups were observed [210]. With the spectra of the SSPs, additional absorption bands at ν=1332 cm^{-1} (amide C–N), ν=1646 cm^{-1} (amide C=O), ν=1590 cm^{-1} (amide C–N) appeared, due to the formed amide groups derived from the amidation reaction between –COOH groups of CNTs and -N-H groups of HTT 1800 [211-214]. However, for the spectrum of HTT 1800-4.5b prepared by physical blending without catalyst, no absorption bands from amide groups were found, indicating that the amidation reaction did not take place in the absence of $ZnCl_2$ catalyst [215,216]. According to the literature, esterification and dehydrogenative coupling reactions can be effectively catalyzed by Lewis acid such as $FeCl_3$ and $ZnCl_2$ [217, 218]. A possible reaction mechanism were proposed for the present amidation reaction. Accordingly, the $ZnCl_2$ serves as a Lewis acid catalyst and activates the carboxylic group by the coordination of the Zn atom at the O atom of the C=O group. Then, the -NH groups of the polysilazane react with the activated carboxylic C by a nucleophilic attack.

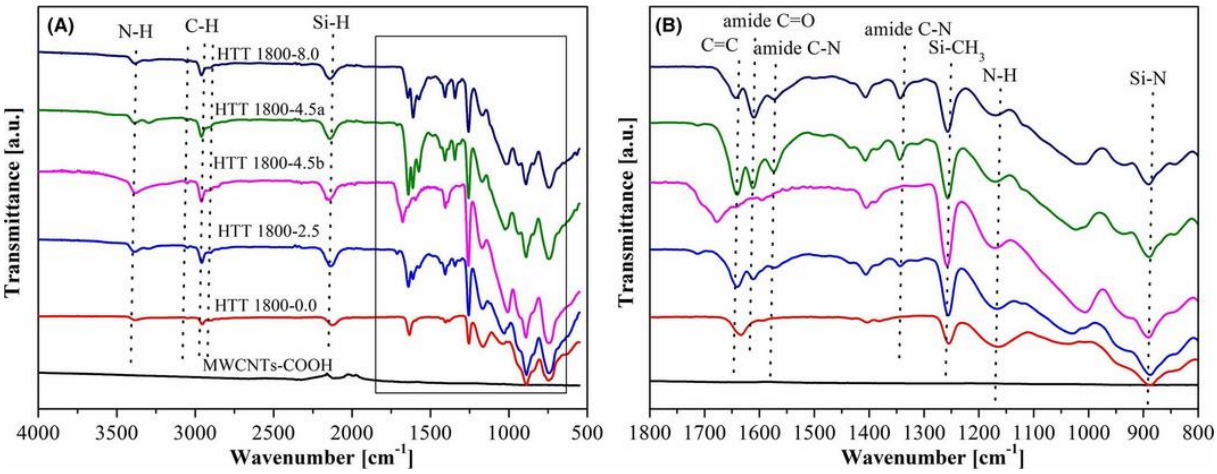

Fig. 11 (A) FT IR spectra of physically-blended-precursor, MWCNTs-COOH and single-source-precursors with different CNT content in the feed, and the region from 800 to 1800 cm^{-1} is shown magnified in (B).

To investigate the morphology of CNTs before and after reaction with HTT 1800, TEM was employed and the results are shown in Fig.12. Fig.12A and 12B are the TEM images of original CNTs-COOH. The diameter of CNTs is about 15~30 nm. From the high-resolution TEM image (Fig.12B), we can clearly observe that the number of CNT walls in this area is about 10~15 and the outside walls of carbon backbones were seriously disrupted (white arrows) due to the attachment of -COOH groups [218]. Fig. 12C is the low resolution TEM image of SSP, which shows that the CNTs were separated by the hosting HTT 1800 matrix. To make a comparison, for the physically blended CNTs/HTT 1800 sample, the serious agglomeration and entangling of CNTs did occur inside the HTT 1800 matrix (Fig.12E). From the high-resolution TEM image of SSP (Fig.12D), an amorphous film with a thickness of ~3 nm was found to attach on the surface of CNTs. However, the high-resolution TEM image of physically-blended-precursor unambiguously shows that, noamorphous film was attached on the surface of CNTs (Fig.12F), which is consistent with the reported literature that during the functionalization of CNTs, the amorphous carbon layer of CNTs was removed by the strong attack of HNO_3 before the attachment of -COOH groups on the graphite layers [107]. Based on the findings shown in Fig.12D and 12F, the amorphous film on the surface of CNTs is due to HTT 1800 polymers attached on the CNTs after amidation reaction.

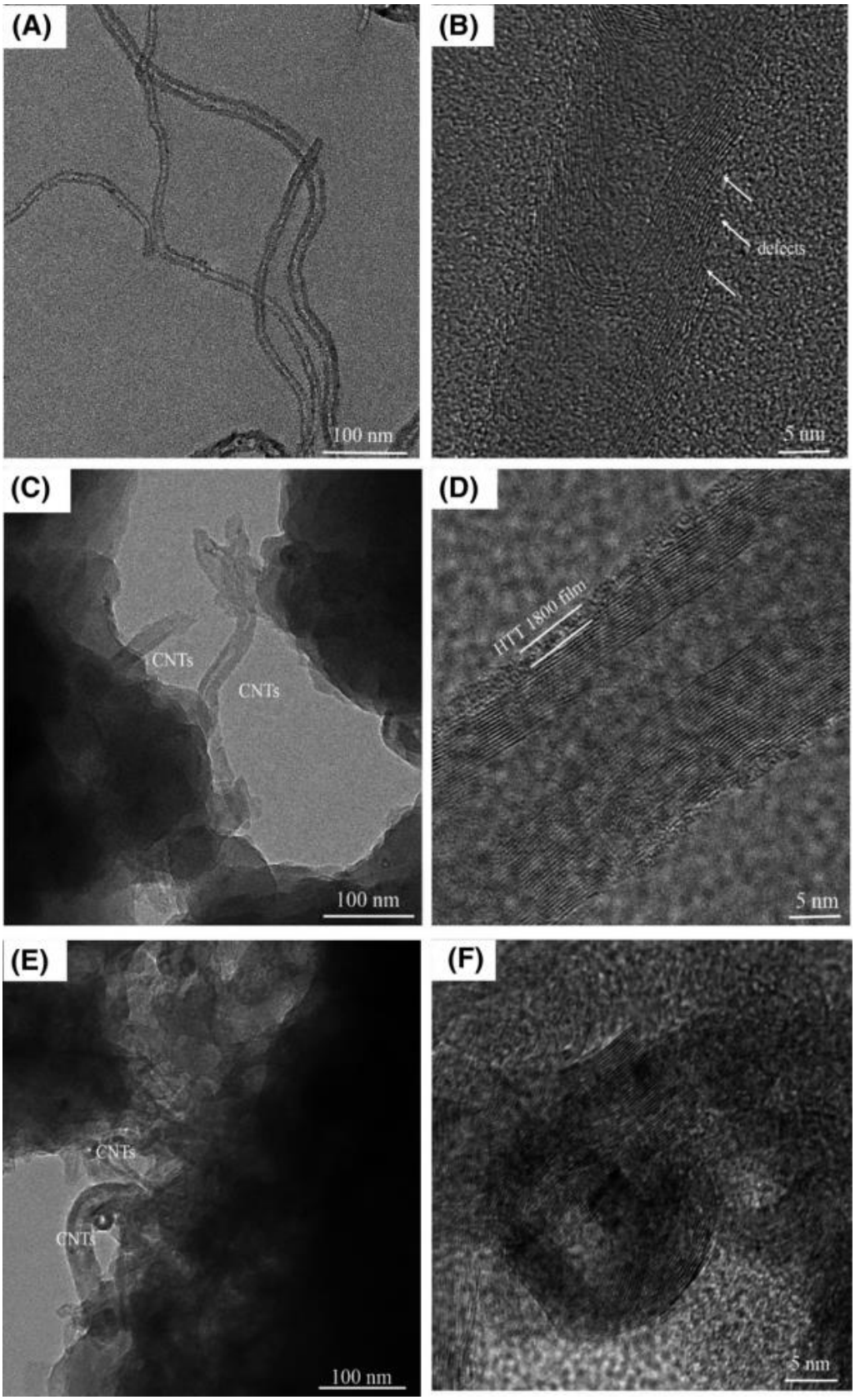

Fig. 12 Low resolution TEM images of (A) original CNTs, (C) single-source-precursor, (E) physically-blended-precursor, and high resolution TEM images of (B) original CNTs, (D) single-source-precursor, (F) physically-blended-precursor.

Therefore, the TEM results are consistent with the FT IR results, which further confirm the successful formation of SSPs. Based on the FT IR and TEM results, Fig.13 shows the chemical reaction between the CNTs-COOH and the HTT 1800.

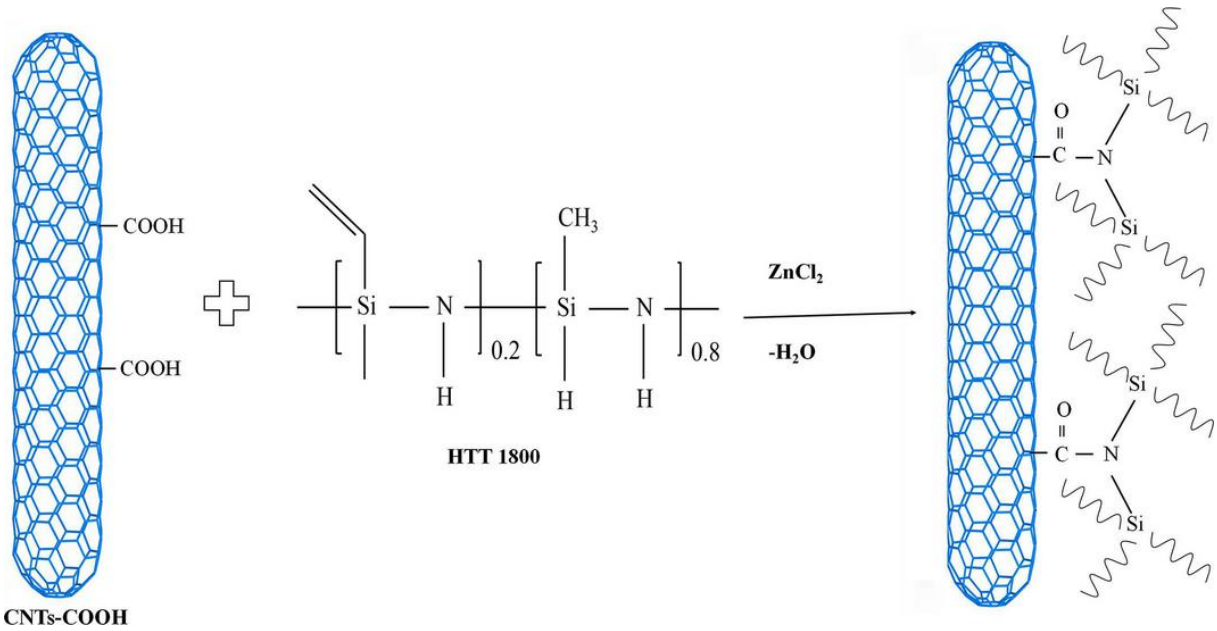

Fig. 13 Reaction between CNT-COOH and HTT 1800 to synthesize single-source-precursors

Fig. 14A shows the XRD patterns of HTT 1800-derived SiCN and CNTs-SiCN ceramic nanocomposites. The pristine SiCN shows a complete amorphous feature which agrees well with the previous reports [51]. As for the CNTs-SiCN ceramic nanocomposites, only a weak characteristic peak of C (0 0 2) plane from graphitic carbon at 2θ of 26.5 is observed. Though $ZnCl_2$ was used as catalyst of chemical synthesis, no signal from Zn was finally found in the XRD pattern. As reported, at the temperature of 1000°C, the $ZnCl_2$ catalyst can be reduced into gaseous Zn by carbon (CNTs) or CO and H_2 released by the decomposition of precursors and evaporates out of the ceramic nanocomposites [220, 221]. Fig. 14B shows the Raman spectra of pristine SiCN and CNTs-SiCN samples, indicating the presence of both disorder-induced (D) and graphite-like (G) bands. The graphitization grade (G_G) of a carbon-based material can be calculated as follows: $I_G/(I_G+I_D)\times100\%$, where I_G and I_D represent the intensity of G and D-bands, respectively [181, 222]. The graphitization grade of resultant CNTs-SiCN (sample S-4.5a) with 4.5 wt% CNT content in the feed amounts 51.6%, higher than that of pristine SiCN (46.7%), due to the introduction of CNTs into the SiCN matrix.

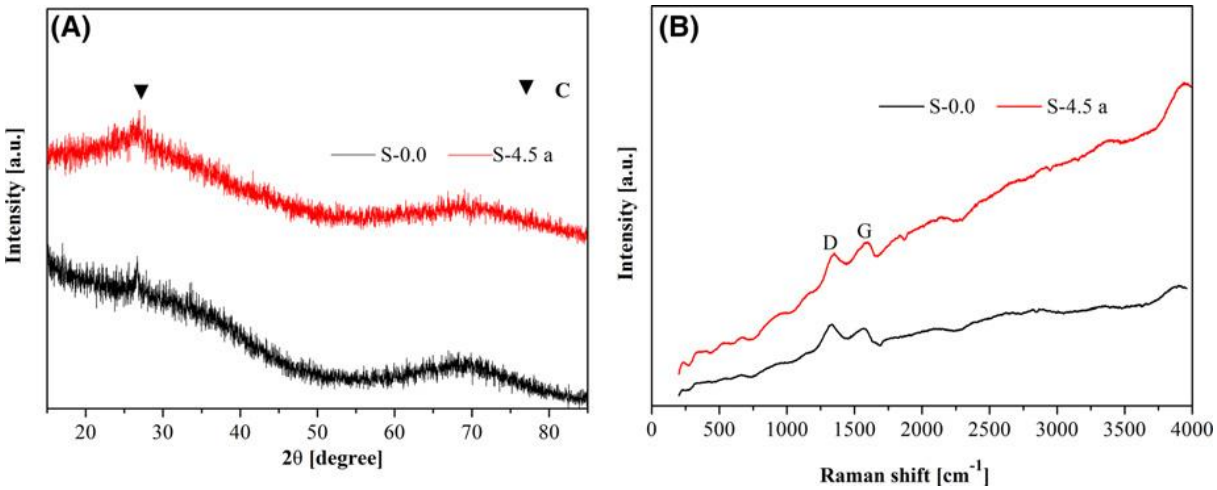

Fig. 14 (A) XRD patterns and (B) Raman spectra of pristine SiCN (sample S-0.0) and CNTs-SiCN nanocomposites (sample S-4.5a)

As shown in Fig. 10, the obtained monolithic CNTs-SiCN ceramic sample shows a totally crack free morphology though it suffered from ca. 30% linear and ca. 66% volume shrinkage. With the CNT content increasing from 2.5 wt% to 8.0 wt% in the feed, the open porosity of resultant CNTs-SiCN composites increased from 4.22% to 4.53% while the density of final ceramic samples decreased from 2.10 g/cm^3 to 2.02 g/cm^3. To further investigate morphology of ceramic samples, the fracture surface of monolithic CNTs-SiCN ceramics derived from SSP and physically-blended-precursor was analyzed with SEM. In general, representative SEM images reveal relatively dense microstructure and no obvious pores were found on the fracture surface. For the SSP-derived sample S-4.5a exhibits uniform distribution of CNT tips in the ceramic matrix (Fig. 15A, D). To make a comparison, in the case of the physically-blended-precursor derived ceramic sample S-4.5b, Fig. 15B (low magnification) and Fig.15E (high magnification) images both show serious aggregation and entangling of CNTs in the ceramic matrix. Despite increasing amount of CNTs in the feed from 2.5 wt% (S-2.5) to 8.0 wt% (S-8.0), no obvious agglomeration of the carbon nanofillers in the ceramic matrix was found (as shown in Fig. 15C, D and F), which further confirms that the CNTs are homogeneously distributed in the SiCN matrix. The SEM results show significant difference in the morphology of the SSP and physically-blended-precursor derived ceramics.

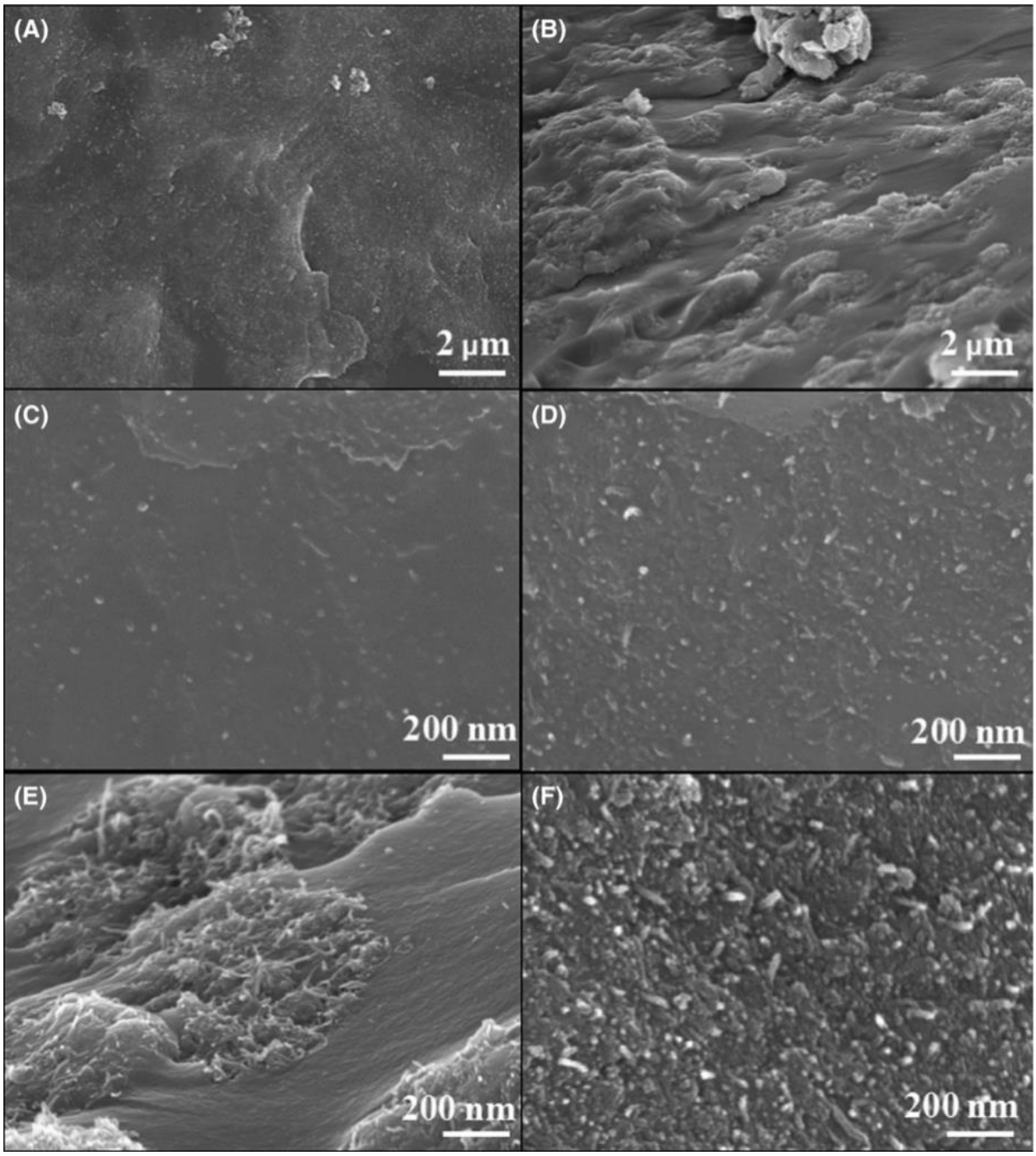

Fig. 15 Low magnification SEM images of (A) S-4.5a and (B) S-4.5b and high magnification SEM images of (C) S-2.5, (D) S-4.5a, (E) S-4.5b and (F) S-8.0

Fig.16 shows the TEM images of CNTs-SiCN ceramic nanocomposites derived from SSP and physically-blended-precursor. After pyrolysis of SSP at 1000°C, each individual CNT is well separated by the SiCN matrix, which means the agglomeration of CNTs is effectively prevented (as shown in Fig.16A). However, for the physically-blended-precursor derived sample (Fig. 16C), serious agglomeration and entangling of CNTs was observed. Fig. 16B and D are the high-resolution TEM images of CNTs-SiCN ceramics. Regardless of dispersing

approach, the seriously disrupted carbon backbones of CNTs-COOH (shown in Fig.12B) were found to get recovered after the pyrolysis (Fig. 16B, D), resulting from the self-catalytic behavior of CNTs [223]. As reported [223], defected carbon nanotubes themselves can absorb and install free C_n species at their opening edges or sidewalls and thus to grow axially and "fat" radially. The structural defects on the tube walls can serve as proper sites for the nucleation and development of new graphene layers. During the polymer-to-ceramic conversion, gaseous byproducts including CH_4, CO and other hydrocarbon gases (C_n) evaporated out of precursor [205, 224, 225]. When the gaseous hydrocarbon evaporating out of precursor passed over the CNTs, they were decomposed and installed on the defected CNTs [223]. The recovery of the carbon backbones leads to the improvement of electrical conductivity [219], which is expected to improve the utilization of CNTs in this work.

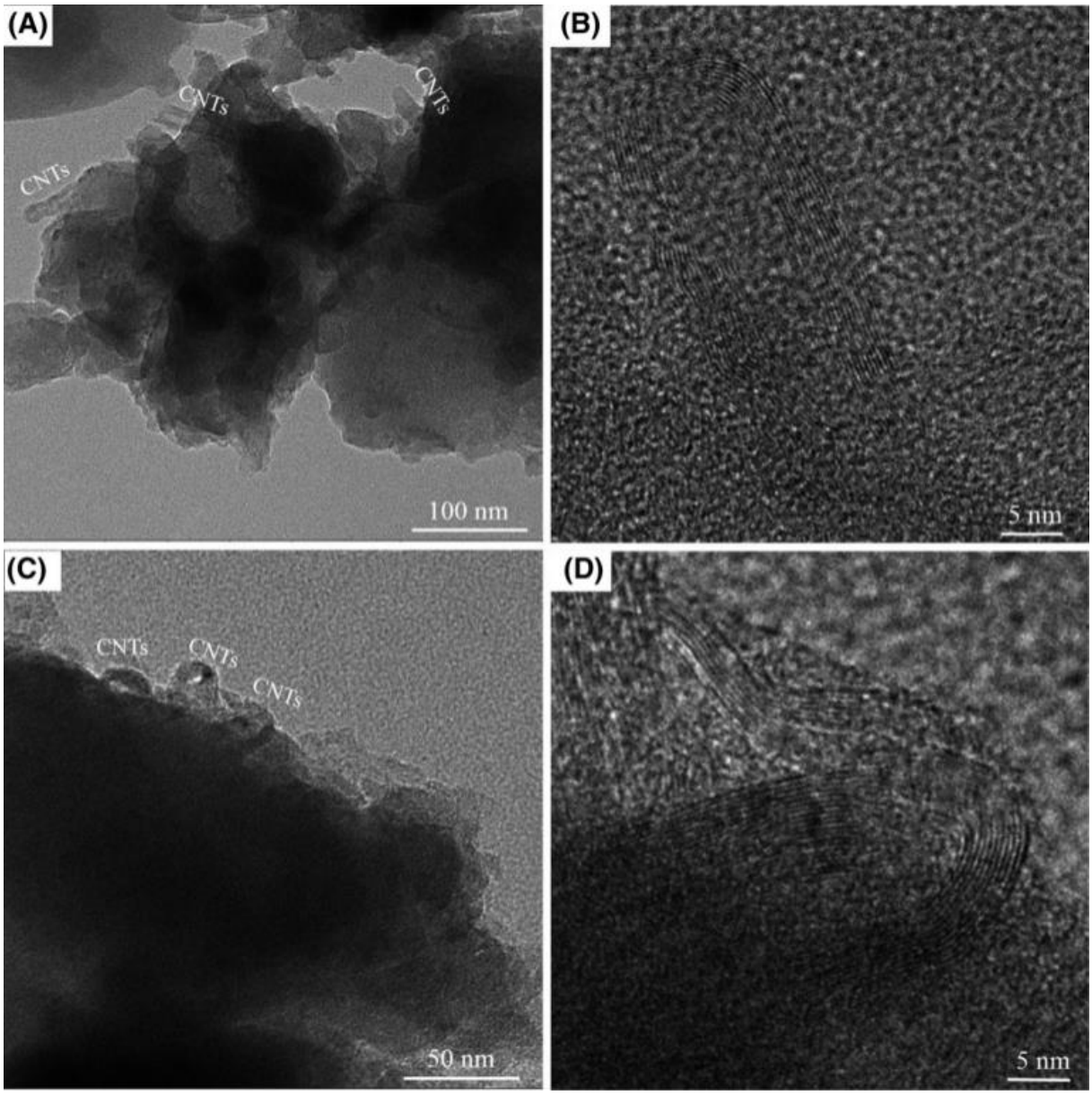

Fig. 16 (A) Low resolution and (B) high-resolution TEM images of singlesource- precursor derived CNTs-SiCN, (C) low resolution and (D) high-resolution TEM images of physically-blended precursor derived CNTs-SiCN.

Based on the FT IR results (Fig. 11) and TEM observation (Fig.12 and 16), Fig. 17 shows microstructural evolution of CNTs-SiCN nanocomposites derived from SSP and single-source-precursor, respectively. Due to the strong van der Waals interactions between each individual CNT and poor compatibility and wettability between the CNTs and HTT 1800, the CNTs exhibit serious agglomeration in the matrix of physically-blended-precursor (Fig.17A) [217, 227] directly leading to an inhomogeneous distribution of CNTs in the SiCN matrix after the polymer-to-ceramic transformation (Fig. 17C). However, Fig. 17B illustrates that in the core of SSP agglomeration of CNTs was avoided. Instead, a homogeneous dispersion of

CNTs was successfully achieved throughout the polymer matrix. Obviously, the HTT 1800 bonded on the surface of CNTs physically blocked the tangling of the CNTs [211, 212, 217, 227]. Due to the formation of SSP, the agglomeration of CNTs is effectively prevented during the cross-linking, warm-pressing and polymer-to-ceramic conversion. Therefore, a homogeneous dispersion is finally obtained in the CNTs-SiCN ceramics (Fig. 17D). Moreover, Fig. 17 shows the recovery of carbon backbones of pristine CNTs-COOH during the polymer-to-ceramic transformation, which is supported by Fig. 16B and D.

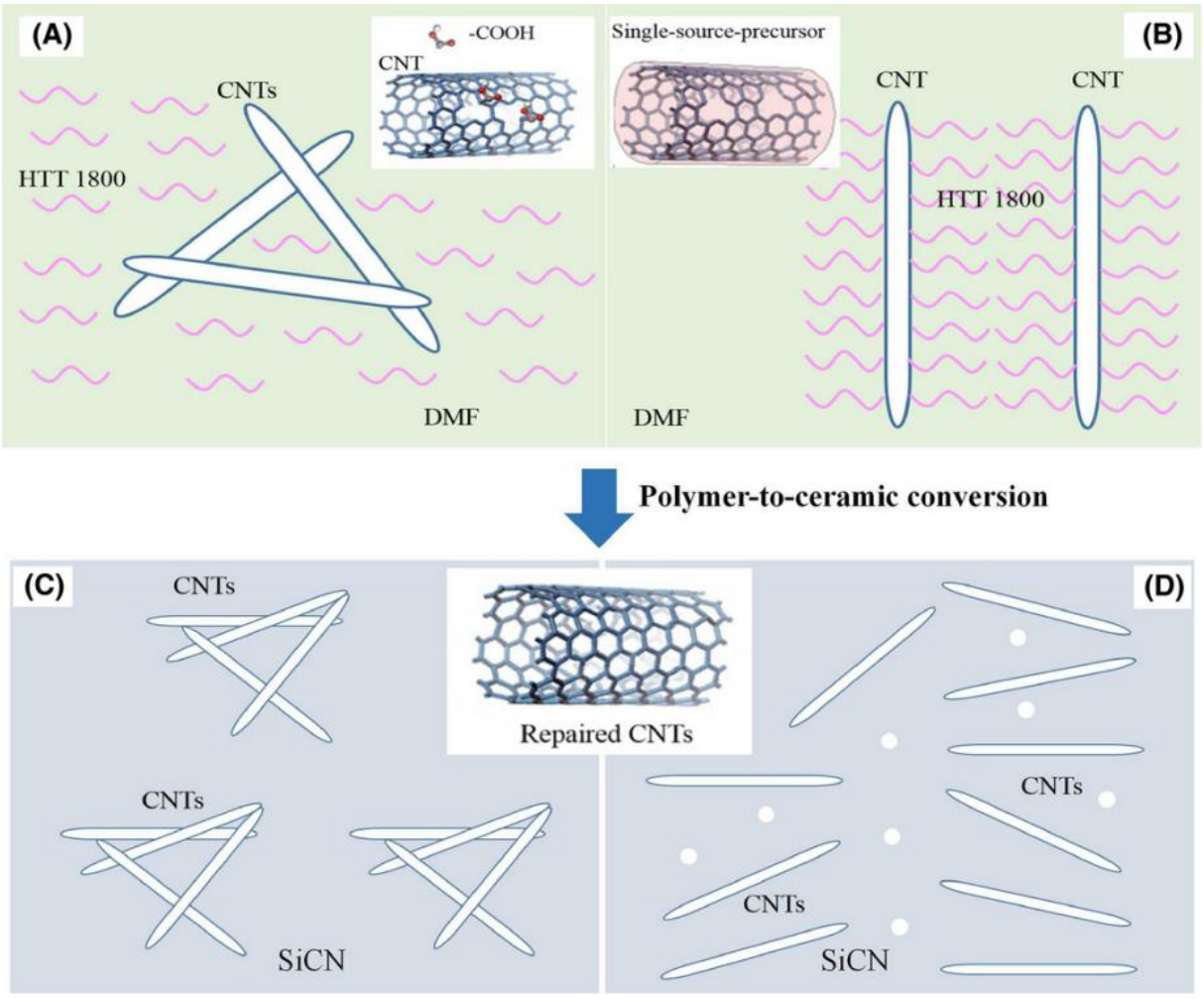

Fig. 17 Schematic illustration of microstructural evolution of (A) physically-blended-precursor and (B) single-source-precursor derived CNTs-SiCN ceramics (C) and (D), respectively.

The relative complex permittivity of the synthesised ceramics was measured in the frequency range of 8.2-12.4 GHz (X band). Fig. 18 shows the ε′ and ε″ of the effective complex permittivity, and the tangent loss of pure SiCN and CNTs-SiCN with different CNT content as a function of frequency. As shown in Fig. 18A, the HTT 1800-derived SiCN ceramic (S-

0.0) presents a relatively low ε' with an average value of 4.87. With the introduction of CNTs into the SiCN ceramic matrix, the ε' value of S-2.5 shows significant enhancement from 4.87 to 9.62. With the increase in CNT content in the ceramics, the value of ε_0 increases gradually. Especially, with the 8.0 wt% CNTs in the feed, the ε′ value of the obtained S-8.0 increases to 23.35. Meanwhile, as shown in Fig. 18B, the ε″ value of SiCN is as low as 1.1×10^{-1}. However, for the samples S-2.5, S-4.5b, S-4.5a and S-8.0, the values of ε" are significantly improved, which are in the range of 1.23~1.27, 1.26~1.30, 4.98~7.08, and 9.18~16.17, respectively. The polarization relaxations induced by the electron motion hysteresis in the dipole under alternating electromagnetic field enhance the dielectric loss, [227, 228] leading to the increasing of ε″. In addition, to the contribution of polarizations, the conductive loss is another factor for the increasing imaginary part, which is caused by the conductive networks constructed by the carbon nanophase [108]. In Fig. 18C, the tangent loss shows an obviously increasing tendency with increasing of CNT content in the SSP-derived ceramics. When the CNT content increases from 0.0 to 8.0 wt%, the tangent loss increases from 0.02 to 0.72. It is worth mentioning that both the ε″and the tangent loss of S-4.5b are significantly lower than those of S-4.5a, due to the decreasing interface polarization and relaxation as well as inferior electrical conductivity in the physically-blended-precursor derived sample S-4.5b compared to the SSP-derived S-4.5a. In conclusion, the dielectric permittivity results indicate the significant advantages of the SSP approach over that of the physical blending method in preparing CNTs-SiCN nanocomposites. This finding is strongly correlated with the microstructure of the CNTs-SiCN.

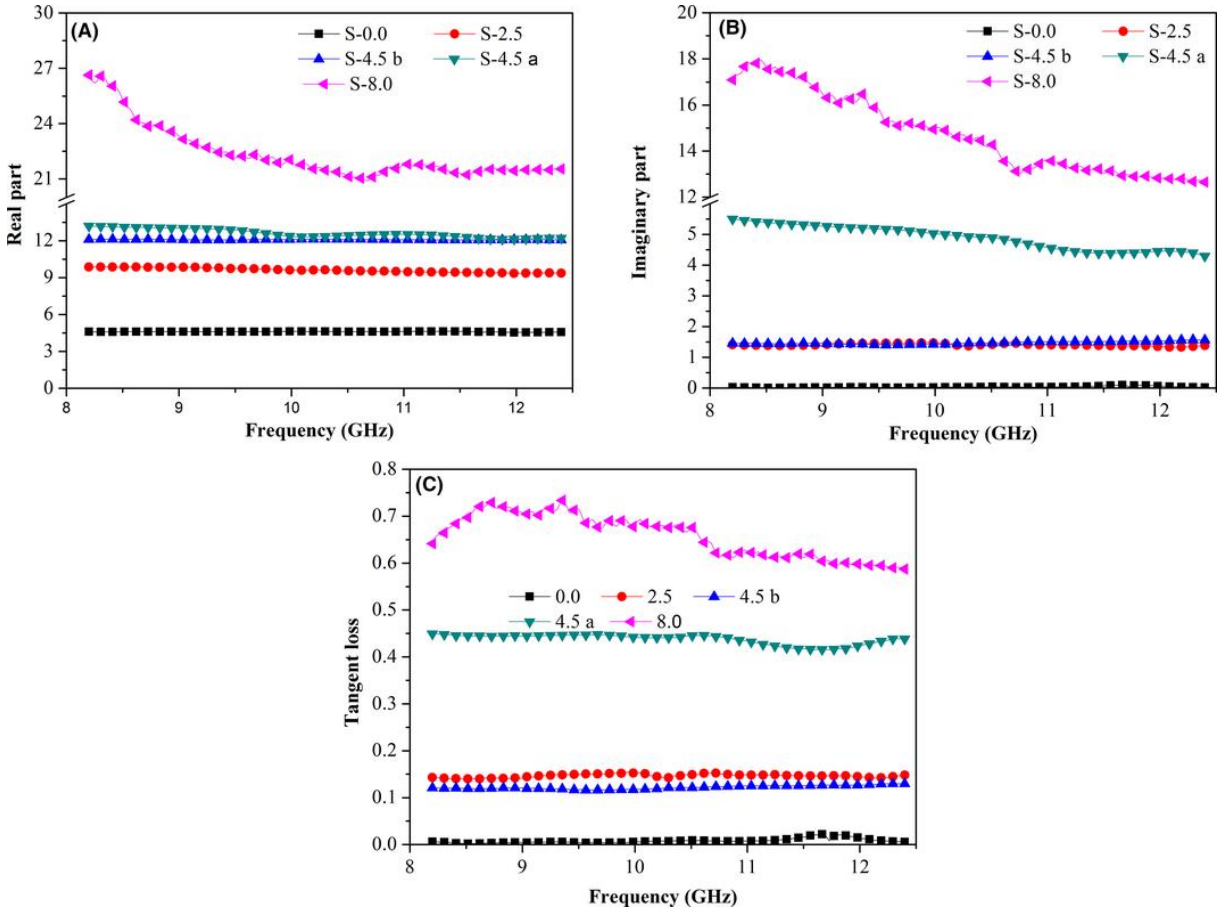

Fig. 18 Real part (A), imaginary part (B) and tangent loss (C) of resultant SiCN and CNTs-SiCN ceramics

The electromagnetic absorbing property was determined by calculating RC [20, 230-232]. Based on the model of metal backplane, RC of the sample is determined from the measured relative complex permeability and permittivity according to Eq.11 and 12 [20, 21, 229, 232, 233].

Fig.19 shows RC of resultant samples as a function of frequency in X-band. The absorption capability of sample S-2.5 is weak at every sample thickness due to the low ε″ (Fig. 19A). With the sample thickness of 3.0 mm, it exhibits a RC_{min}, corresponding to the maximum absorption of -9.1 dB at the frequency of 8.75 GHz. In contrast, the RC_{min} value was significantly improved when the CNT content increases to 4.5 wt%. It can be seen that the RC_{min} of the sample S-4.5a shifts towards a higher frequency with the decreasing sample thickness (Fig.19B). The peak shift was attributed to the phenomena of quarter-wavelength attenuation, in which the absorption meets the phase match conditions [108]. The RC_{min} of the S-4.5a reaches -21.8 dB at 10.2 GHz, and the effective bandwidth (the bandwidth of RC values lower than -10 dB, namely, more than 90% microwaves are attenuated) amounts 3.7 GHz (from 8.7 to 12.4 GHz) with a thickness of 2.2 mm. With the decrease in sample thickness, the RC_{min} exhibits an improved tendency while the effective bandwidth shows a

decreased trend. When the sample thickness decreased to 2.0 mm, the RC_{min} decreased to -26.1 dB with the effective bandwidth of 2.8 GHz (from 9.6 to 11.2 GHz). In contrast, for the sample S-4.5b derived from physically-blended-precursor, the RC_{min} is only -6.4 dB with a sample thickness of 2.2 mm, which is far inferior to that of the SSP-derived sample S-4.5a. This inferior EM property resulted from the low ε" and tangent loss, which is strongly dependent on the poor dispersion of CNTs in the SiCN ceramic matrix [202]. Based on the findings that the ε' and ε" should amount 5~20 and 1~10, respectively for the use as EM absorbing material [121], the EM absorbing performance of the sample S-8.0 is very poor due to the high ε′>20 and ε′′>10 .

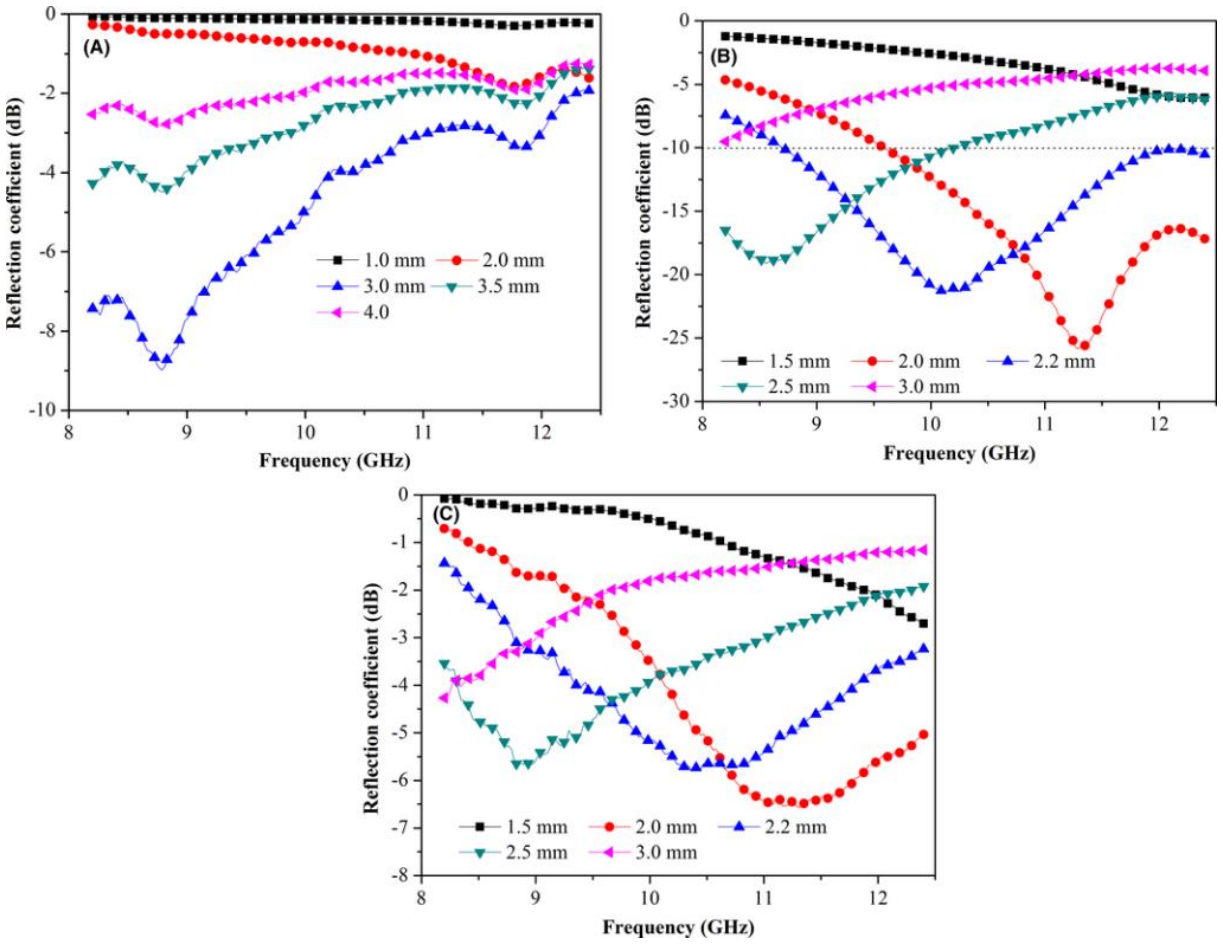

Fig. 19 Reflection coefficient of resultant CNTs-SiCN nanocomposites S-2.5 (A), S-4.5a (B) and S-4.5b (C)

In summary, novel SSPs were prepared through amidation reaction of poly (methylvinyl) silazane HTT 1800 with carboxylic groups functionalized CNTs with the assistance of $ZnCl_2$ catalyst, which was confirmed by FT IR measurements. TEM images of the as-synthesized SSPs reveal that an HTT 1800 film with a thickness of ~3 nm was always attached on the

surface of CNTs, which further indicates the successful formation of the SSPs. Crack-free monolithic CNTs-SiCN ceramic nanocomposites were prepared through pyrolysis of the obtained SSP green bodies at 1000°C. With the same CNT content (4.5 wt%) in the feed, the SSP-derived CNTs-SiCN nanocomposites possess a RC_{min} of -21.8 dB and an effective bandwidth of 3.7 GHz with a sample thickness of 2.2 mm while the physically-blended-precursor derived CNTs-SiCN nanocomposites show a far inferior RC_{min} of -6.4 dB with the same sample thickness. The significant improvement of the EM absorbing property of SSP-derived CNTs-SiCN nanocomposites is due to the microstructural feature characterized by a homogeneous distribution of the CNTs in the SiCN matrix, which issuccessfully achieved by the single-source-precursor-approach.

3.1.2. Statement of personal contribution

[1] Liu X, Yu Z, Chen L, et al. Role of single-source-precursor structure on microstructure and electromagnetic properties of CNTs-SiCN nanocomposites. Journal of the American Ceramic Society, 100 (2017) 4649-4660.

The idea of this work and the design of the experiment was developed by myself. All experimental work related to the material synthesis and preparation was carried out by myself. All applied chemical and microstructural characterization methods were performed by myself, except TEM and permittivity measurement. The TEM measurement was done by Binbin Xu and the permittivity measurement was done by Lingqi Chen. The electromagnetic absorption calculation was accomplished by myself. The manuscript was written by myself and revised and approved by Prof. Zhaoju Yu and Prof. Ralf Riedel.

3.2. Single-source-precursor synthesis and excellent electromagnetic properties of novel RGO-SiCN ceramic nanocomposites

The content of this Chapter is published in:

[2] Liu X, Yu Z, Ishikawa R, et al. Single-source-precursor synthesis and electromagnetic properties of novel RGO–SiCN ceramic nanocomposites. Journal of Materials Chemistry C, 5 (2017) 7950-7960.

In Chapter 3.2, the preparation of RGO/SiCN ceramic nanocomposites derived from thermolysis of GO/HTT 1800 single-source-precursor at 1000°C, is presented. The dispersion state of RGO inside the SiCN matrix prepared with different approaches is investigated and a schematic illustration used to explain the microstructure is established. The influence of the GO in the feed on the microstructure evolution of the composite, as well as permittivity, electromagnetic absorption capacity and electromagnetic shielding effectiveness, is analyzed and discussed.

3.2.1. Results and discussion

Poly(organo)silazane HTT 1800 (KiON Specialty Polymers) was used as precursor for SiCN. The graphene oxide flakes (Xianfeng Nano, China) were firstly blended with DMF (Sigma-Aldrich, Germany) with a weight ratio of 1:500 in a flask. After ultra-sonication for 4 h, the $ZnCl_2$ catalyst (Sigma-Aldrich, Germany) with a weight ratio of 2:98 with respect to the precursor HTT 1800 was added. After ultra-sonication for another 2 h, the HTT 1800 was dropped into the flask. Then the resultant mixture was heated up to 70°C for 72 h under argon flow and magnetic stirring. Subsequently, the as-synthesized SSP was cross-linked at 120 °C before the DMF was finally removed under vacuum. After ball milling for 3 h, the black GO-HTT 1800 powders were warm pressed into green bodies with the dimensions of 50×40×3 mm^2 under a pressure of 60 KN. Then, the as-prepared green bodies were pyrolyzed in an Ar atmosphere at 1000°C and machined into samples with dimensions of 22.86×10.16×2.00 mm^3 with wire cutting.

To investigate the influence of the RGO content on the electromagnetic properties of the ceramic composites, a series of GO-HTT 1800 precursors with different GO contents (0.0 wt.%, 1.0 wt.%, 2.5 wt.%, 6.0 wt.% and 12.0 wt.%) in the feed were prepared (Table 4). With 2.5 wt.% GO in the feed, a control test based on the physical blending method as the reference sample was also performed under the same condition but no $ZnCl_2$ was added.

Table 4 Content of catalyst and graphene oxide in the feed

Ceramics	Precursors	GO (wt.%)	$ZnCl_2$ (wt.%)
S-1	HTT 1800	0.0	0.0
S-2	HTT 1800-1.0	1.0	2.0
S-3[a]	Physically blended HTT 1800-2.5	2.5	0.0
S-4	HTT 1800-2.5	2.5	2.0
S-5	HTT 1800-6.0	6.0	2.0
S-6	HTT 1800-12.0	12.0	2.0

[a] S-3 was obtained by pyrolysis of physically blended GO/HTT 1800 mixture

In the present work, a series of SSPs were synthesized by adjusting the GO content in the feed. The amount of GO was adjusted to 1.0 wt%, 2.5 wt%, 2.5 wt% without catalyst, 6.0 wt% and 12.0 wt%. The resultant preceramic precursors are denoted as HTT 1800-1.0, HTT 1800-2.5, physically blended HTT 1800-2.5, HTT 1800-6.0 and HTT 1800-12.0 (as shown in Table 4), respectively. In the following, the FT IR spectra of the synthesized SSPs crossed-linked at 120°C are discussed and shown in Fig. 20.

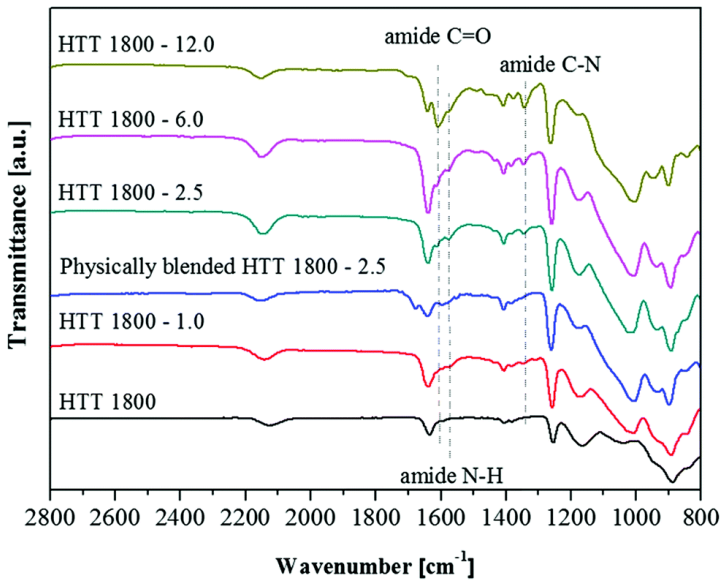

Fig. 20 FT-IR spectra of pristine GO, physically blended HTT 1800/GO mixture and the synthesized SSPs with different GO contents.

In the FT IR spectrum of the sample HTT 1800, typical absorption bands related to C–H (2960 and 2965 cm^{-1}), Si–N–H (1160 cm^{-1}), and Si–N (930 cm^{-1}) groups were analyzed [210]. In the spectra of the GO containing samples HTT 1800-1.0, HTT 1800-2.5, HTT 1800-6.0 and HTT 1800-12.0, additional new absorption bands at ν = 1332 cm^{-1} (amide C–N), ν = 1646 cm^{-1} (amide C=O), ν =

1590 cm^{-1} (amide N–H) appeared [211-214], which are due to the formed amide groups derived from the amidation reaction between –COOH groups of GO and –N–H groups of HTT 1800. In contrast, the spectrum of the sample physically blended HTT 1800-2.5 does not show these new absorption bands, indicating that the amidation reaction did not occur without the presence of $ZnCl_2$. Therefore, the FT IR results confirm that the –COOH groups of GO react with the –N–H groups of HTT 1800 via an amidation reaction to form the SSP, which is shown in Fig. 21. A possible reaction mechanism for the present amidation reaction, as follows: $ZnCl_2$ serves as a Lewis acid catalyst and activates the carboxylic group by the coordination of the Zn atom at the O atom of the C=O group. Then, the –N–H group of polysilazane reacts with the activated carboxylic C by a nucleophilic attack.

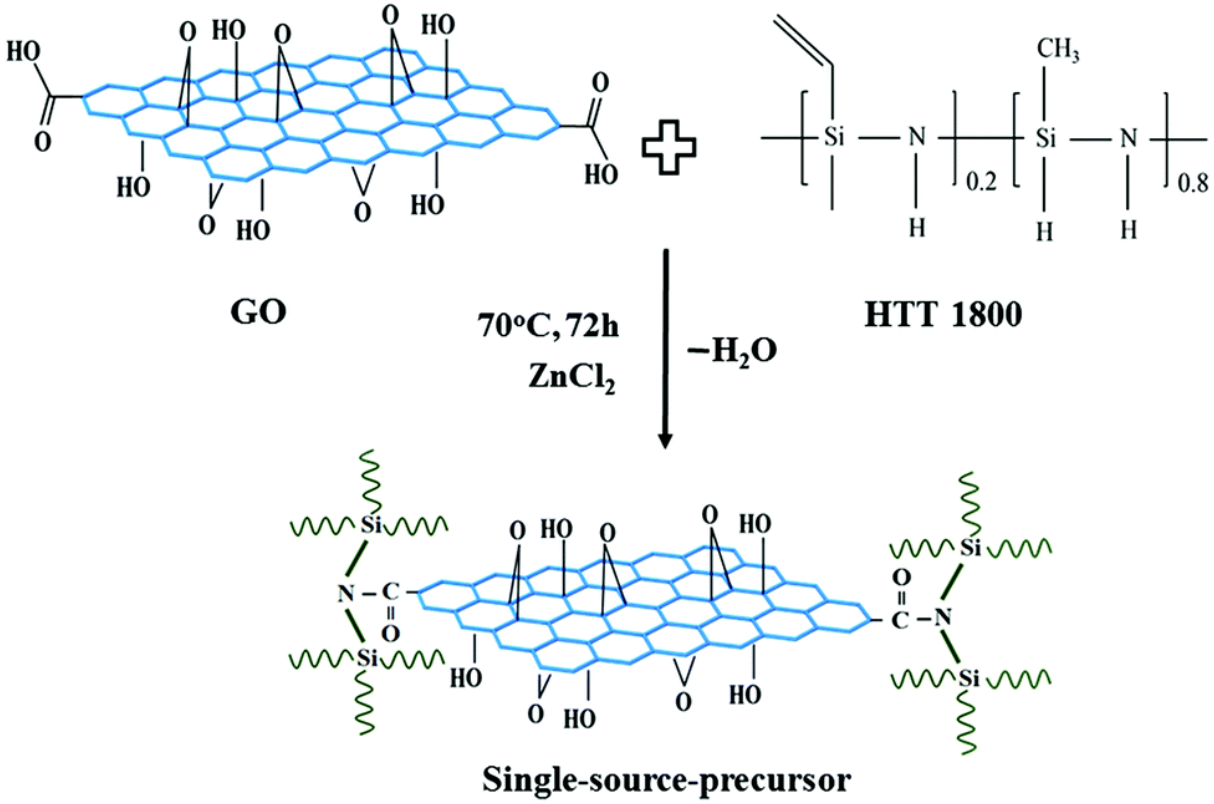

Fig. 21 Synthesis of SSP (GO–HTT 1800) by amidation reaction between GO and HTT 1800.

Raman spectroscopy is a non-destructive method for characterizing carbon-containing materials like graphite, carbon black-based materials, amorphous carbon films, or carbon nanotubes and their composites. Fig. 22a shows the Raman spectra of the HTT 1800-derived SiCN and the resultant RGO–SiCN ceramic nanocomposites. All spectra clearly indicate the presence of both, disorder-induced D and graphite-like G bands. The D-band at 1352 cm^{-1} corresponds to the presence of amorphous carbonaceous products, disordered carbon or defects in graphite and the G-band at

1580 cm^{-1} is related to the signal from graphite [181, 222]. The G_G of a carbon containing material can be calculated as follows: $I_G/(I_G + I_D) \times 100\%$, where I_G and I_D are the intensity of the G and D-bands, respectively [181, 222]. As reported, GO begins to decompose with the desorption of CO, CO_2 and other oxygenated carbon species when the temperature is higher than 200°C, which is known as thermal reduction [234]. During the thermal reduction process, parts of the defective carbon backbones of GO are restored and a higher graphitization grade of the in situ formed RGO should be achieved [222, 234-236]. Based on the findings that the ceramic yield of HTT 1800 is about 70.0 wt% [209] and the GO experiences a mass loss of more than 70.0 wt% with a thermal reduction temperature as high as 1000°C [234]. The RGO content in the resultant RGO–SiCN nanocomposite (with 12.0 wt% GO in the feed) is roughly determined to be less than 5.5 wt%, which accounts for the slight increase of G_G of the resultant ceramic nanocomposites from 46.7% to 53.8% with the GO content increasing from 0.0 wt% to 12.0 wt% in the feed. This finding supports that GO was in situ thermally reduced to RGO during the polymer-to-ceramic transformation of the SSP.

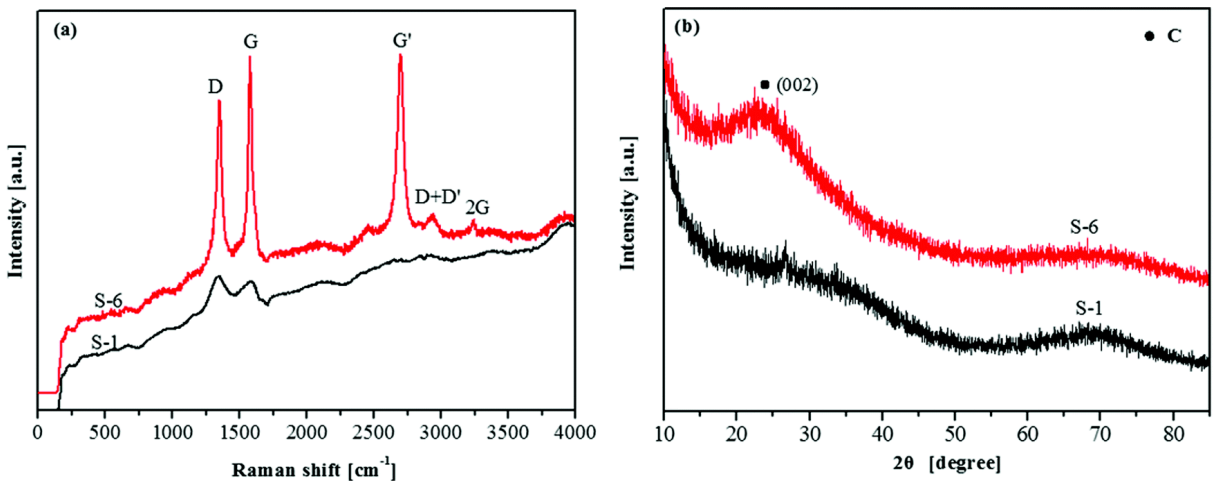

Fig. 22 (a) Raman spectra and (b) XRD patterns of resultant SiCN (sample S-1) and RGO–SiCN ceramic nanocomposite (sample S-6) (according to the Bragg diffraction equation, the interlayer spacing of RGO is calculated as 0.366 nm).

Fig. 22b shows the XRD patterns of pristine SiCN and the obtained RGO–SiCN ceramic nanocomposite. Pure SiCN shows a complete amorphous state which agrees well with the findings reported in the literature [181]. In the pattern of the RGO–SiCN nanocomposite, a weak characteristic peak of C (002) at 2θ of 24.29° refers to the RGO since that of graphite appears at 2θ = 26.5°C. However, no signals related to Zn or Zn compounds were found though $ZnCl_2$ was used as the catalyst. According to the literature [220, 221], this observation is explained by the reduction of

$ZnCl_2$ to metallic Zn by carbon species (thermally reduced GO or H_2, CO released by the decomposition of polysilazane) and metallic Zn evaporates out of the ceramic nanocomposites during the pyrolysis. Therefore, Zn cannot be found in the final nanocomposites, which is also confirmed by the STEM-EDXS elemental images of RGO-SiCN nanocomposites since only Si, C, N and O atoms were found, while no Zn atom was detected (shown in Fig. 25).

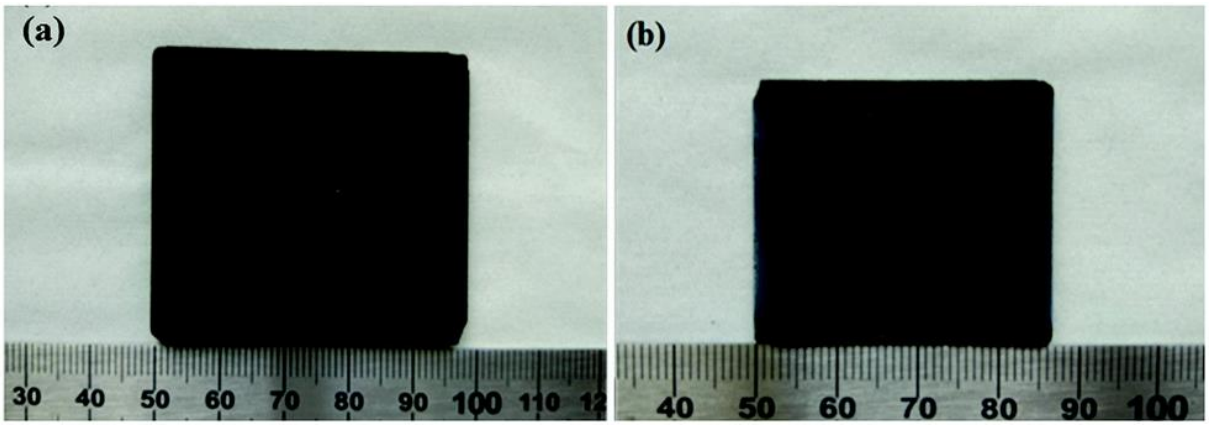

Fig. 23 (a) Optical images of the green body derived from warm pressing of the resultant SSP GO–HTT 1800 at 245°C and (b) monolithic RGO–SiCN nanocomposites obtained after pyrolysis at 1000°C in Ar.

As shown in Fig. 23, the obtained ceramic sample exhibits a linear shrinkage of ca. 30% and volume shrinkage of more than 50% after pyrolysis. However, the monolithic ceramic sample shows a totally crack free morphology though it suffered from large linear and volume shrinkage.

To investigate the morphology of the ceramic samples, the fracture surface of monolithic SiCN (Fig. 24a and c) and RGO–SiCN nanocomposites (Fig. 24b and d) was analyzed by SEM. In general, representative SEM observation images reveal a relatively dense microstructure. In Fig. 24b and d, an obvious and unique network structure (with the width of 50–100 nm) can be clearly identified in the form of a 3D interconnected bright (inter)phase, which was also found in the case of RGO/polymer composites [81]. The formed networks are discussed to result from the in situ formed RGO since such microstructural features were not found inside the pure SiCN matrix.

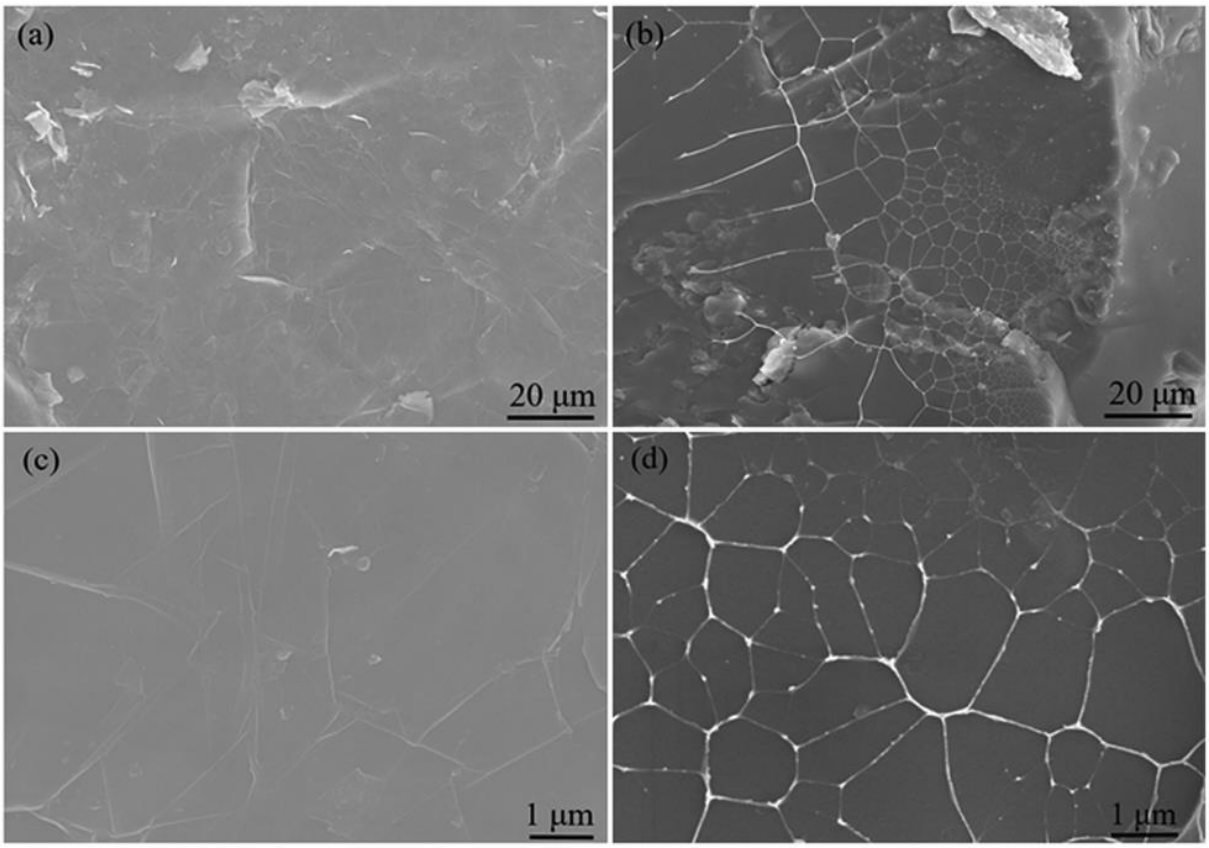

Fig. 24 Low magnification SEM images of fracture surface of (a) SiCN (S-1) and (b) RGO–SiCN (S-6), and high magnification SEM images of fracture surface of (c) S-1 and (d) S-6.

To confirm the chemical composition and microstructure, the bulk SiCN and RGO–SiCN samples were investigated by transmission electron microscopy (TEM). Fig. 25a shows a selected-area diffraction pattern obtained from the network area (Fig. 25b) of the RGO–SiCN sample (GO content is 12.0 wt%). No Bragg reflections but several ring patterns as marked by arrowheads are found, suggesting that both the matrix and the grain boundary interphase (networks) are not crystallized but amorphous. Fig. 25b shows the ADF-STEM image obtained from the network (interphase) regions. The width of the interphase is less than 100 nm and the region exhibits dark-contrast, suggesting that the region consists of light elements. It is noteworthy that the bright contrast in the matrix of Fig. 25b (marked by arrowheads) originates from the supporting carbon thick film of the TEM grid. This carbon grid shows local carbon enrichment (see Fig. 25d). To investigate the elemental distribution in the matrix and the interphase (network), STEM-EDXS mapping was performed and the results are given in Fig. 25c–f, where the used edges are (c) Si–K, (d) C–K, (e) N–K, and (f) O–K, respectively. The Si is basically distributed in the matrix and it becomes poor in the network structure, while carbon has the opposite distribution. The carbon rich phase is segregated in the grain

boundary interphase, denoted as the network. In our observation, the segregated networks will be covered by the matrix, and therefore it is difficult to discuss the accurate composition of the matrix and the segregated phase. It is well accepted that the HTT 1800 precursors were transformed into amorphous SiCN after pyrolysis at 1000°C [209]. Characteristic peaks of graphite are identified by Raman spectra and XRD patterns. Therefore, combining other methods such as Raman and XRD we conclude that the matrix is composed of SiCN and the carbon-rich phase is segregated in the analyzed networks. As reported in the literature, upon pyrolysis at 1000°C, the nanostructure of polysilazane-derived amorphous SiCN ceramics can be generally described as a random network of Si–C–N atoms [237-239]. No segregated carbon was observed by HRTEM in the amorphous SiCN obtained after annealing at 1100°C [238]. With the increase of annealing temperatures to 1400 °C, the amorphous SiCN ceramics experienced phase separation with the formation of Si_3N_4, SiC and graphene-like carbon [238]. In the present work, the carbon-rich phase can only be considered as the in situ formed RGO since no other segregated carbon is formed in the SiCN matrix after heat treatment at a low temperature of 1000°C. The RGO networks form electrically conductive pathways and, therefore, improve the electrical conductivity and dielectric properties.

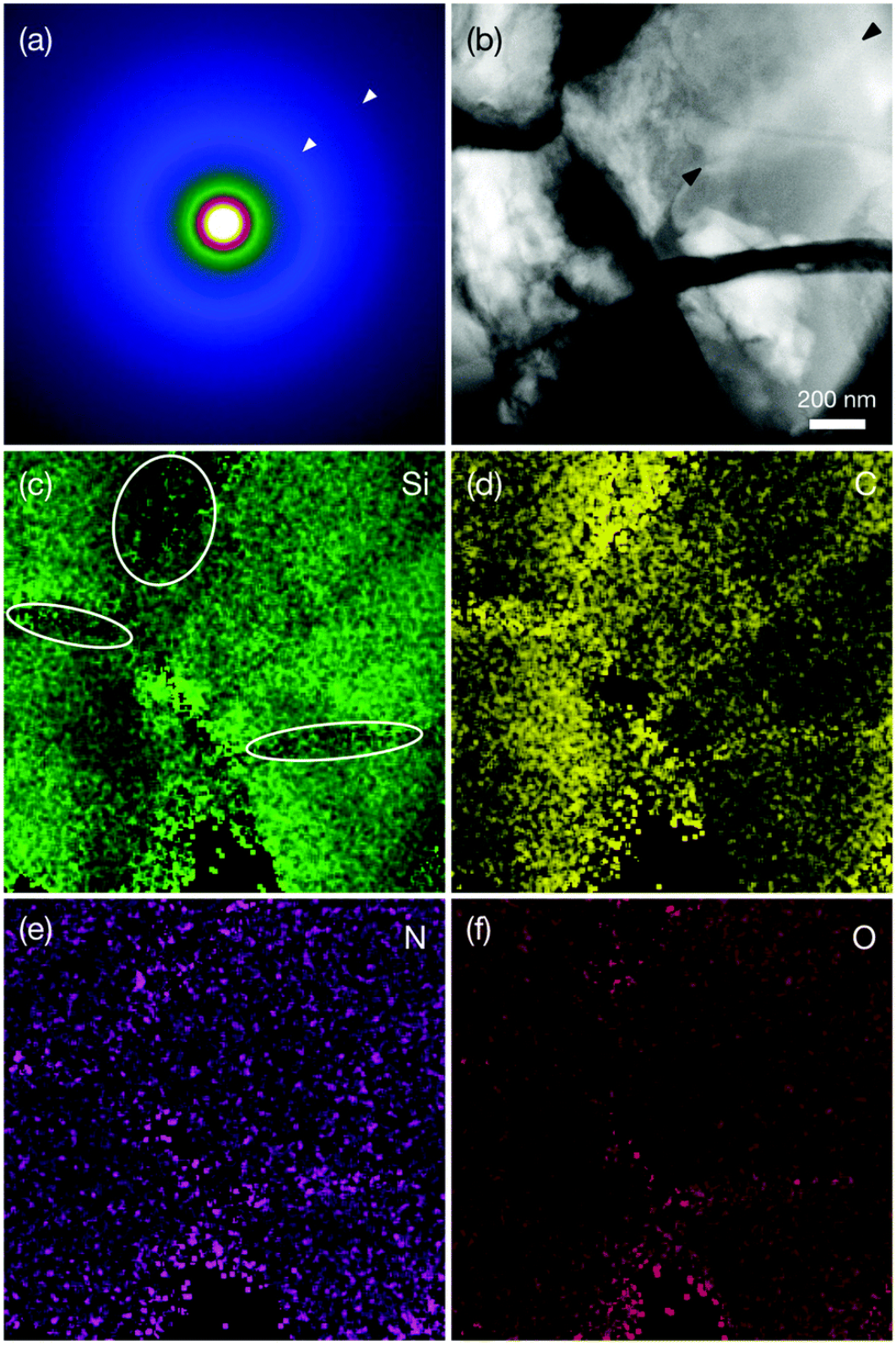

Fig. 25 (a) Electron diffraction pattern obtained from the sample RGO–SiCN (S-6), and (b) ADF-STEM image of the same area of (a). The bright contrast marked with dark arrowheads in (b) refers to the supporting carbon film of the TEM grid. STEM-EDXS elemental images are obtained from the same area of (b), and the images are formed by using the following edges: (c) Si–K, (d) C–K, (e) N–K, (f) O–K, respectively.

To observe the morphology of the in situ formed RGO in the SiCN matrix, representative TEM images of powdered RGO–SiCN nanocomposites derived from a physically-blended-precursor (Fig. 26a) and SSP (Fig. 26c) are shown in Fig. 26. From Fig. 26b, it can be concluded that the RGO layers are seriously restacked in the physically-blended-precursor derived RGO–SiCN. The interlayer distance of the adjacent RGO layers was determined to be ca.0.551 nm, which is larger than that of graphite (*i.e.*, 0.335 nm) and the number of stacked RGO varies from 8 to 12, which is correlated with the results obtained in the literature related to rGO/Si_3N_4 nanocomposites prepared by physical blending of GO and a Si_3N_4 precursor [240]. However, for the sample derived from the SSP (Fig. 26d), the restacking of RGO was significantly reduced since the number of stacked RGO varies between 2 and 3 layers and even single layer RGO (the distance between the adjacent RGO is larger than 1 nm) can be found in some areas. In general, the significantly reduced restacking of RGO is attributed to a physical (steric hindrance) blocking by HTT 1800 grafted on the surface of GO (Fig. 26c), which is consistent with the reported literature [241]. As reported, the layered GO is derived from the exfoliation of graphite with strong chemical attack [234, 242]. During the chemical attack, functional groups including hydroxyl, epoxy groups are attached on their basal planes and carboxyl groups on their edges, which destroies the van der Waals bonds between the adjacent layers. As a result, the interlayer distance of GO is enlarged and is much larger than that of graphite [234,242]. After thermal reduction, the obtained RGO still shows a larger interlayer distance than graphite. With respect to the physically-blended-precursor, the GO layers were dispersed into the HTT 1800 precursor with the assistance of ultrasonication. Due to the strong van der Waals interactions between each adjacent GO layers, they tend to restack when the ultrasonication disappeared (Fig. 26a). However, as shown in Fig. 26c, the HTT 1800 molecules were grafted onto the surface of GO through chemical modification, which blocked GO from restacking and further enlarged their interlayer distance. Therefore, the interlayer distance of RGO in Fig. 26d is even larger than that of RGO in Fig. 26b. After the polymer-to-ceramic conversion, the HTT 1800 transformed into SiCN and inserted into the adjacent RGO, which is strongly supported by the nano/micro-structure shown in Fig. 26d.

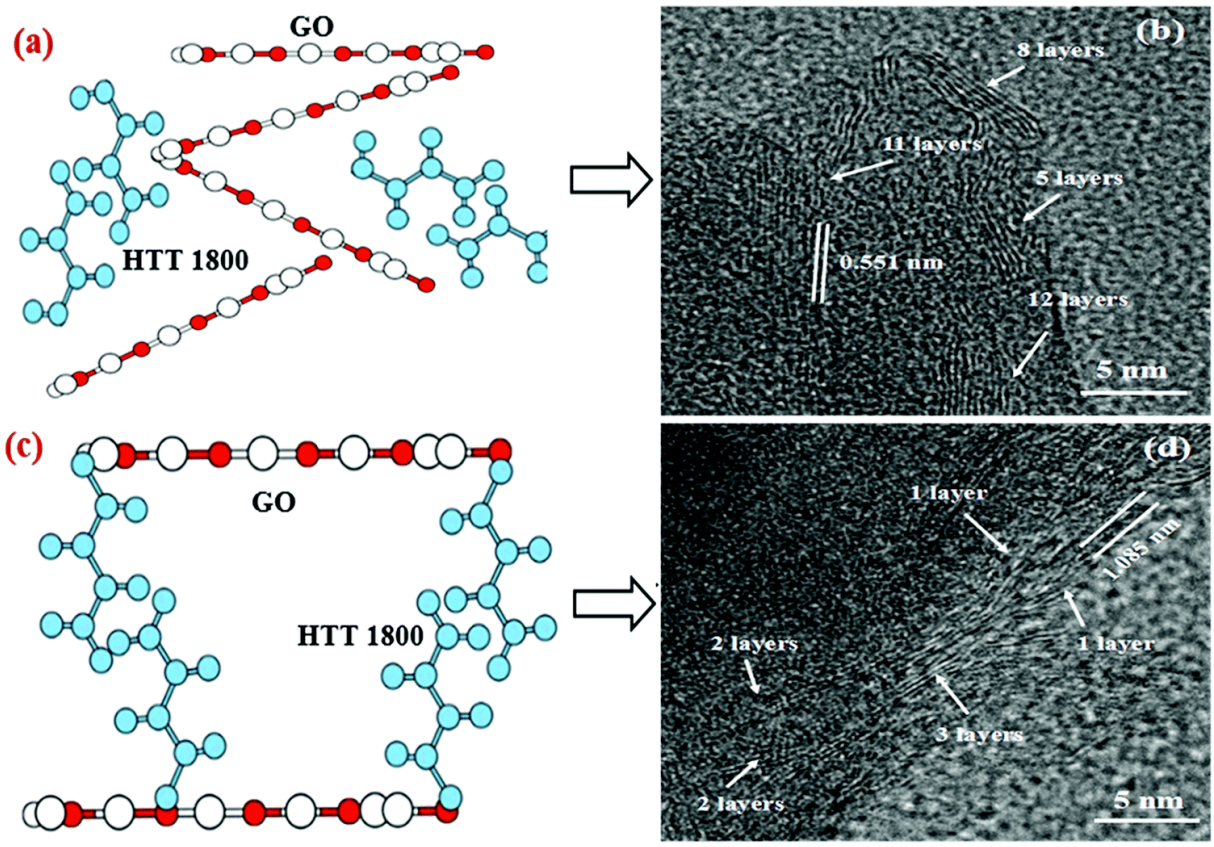

Fig. 26 Schematic illustration of (a) physically-blended-precursor and (c) SSP. TEM images of RGO–SiCN ceramic nanocomposites derived from (b) physically-blended-precursor and from (d) SSP.

The relative complex permittivity of the obtained ceramics was measured in the frequency range of 8.2–12.4 GHz (X band). According to the Debye theory, the real part of the permittivity is related to the polarization relaxation and the imaginary part of the permittivity represents the dielectric loss capability [131, 243, 244].

Fig. 27 shows the ε' and ε'' values of the effective complex permittivity of the resultant SiCN and RGO–SiCN nanocomposites in the X band. The HTT 1800-derived SiCN (S-1) sample exhibits a relatively low ε' with an average value of 4.87. With increasing amount of RGO (corresponding to the increasing amount of GO in the feed), the value of ε' increases gradually as shown in Fig. 28a, which is consistent with the reported literature [108]. Fig. 27b shows that ε'' also increases with increasing RGO content as follows: the ε'' of SiCN is in the range of 0.01–0.02, while those of RGO–SiCN samples S-2, S-3, S-4, S-5 and S-6 are 1.23–1.27, 1.72–1.98, 4.98–7.08, 8.49–10.62 and 9.18–16.17, respectively. An increasing fraction of RGO increases the volume of charge carriers inside the material and improves their electrical conductivity [108]. In addition to the contribution of polarizations, the conductive loss is another factor causing an increasing imaginary part, which originates from the conductive

carbon network formed by RGO [108]. The polarization relaxation induced by the electron motion hysteresis in the dipole under an alternating electromagnetic field enhances the dielectric loss [42, 146]. It is worth mentioning that with the same content of GO in the feed, both the ε' and ε'' values of sample S-4 derived from the SSP are significantly higher than those of sample S-3 obtained by physical blending. With respect to the dielectric performance this result clearly indicates the significant advantage of the SSP approach as compared to that of the physical blending method.

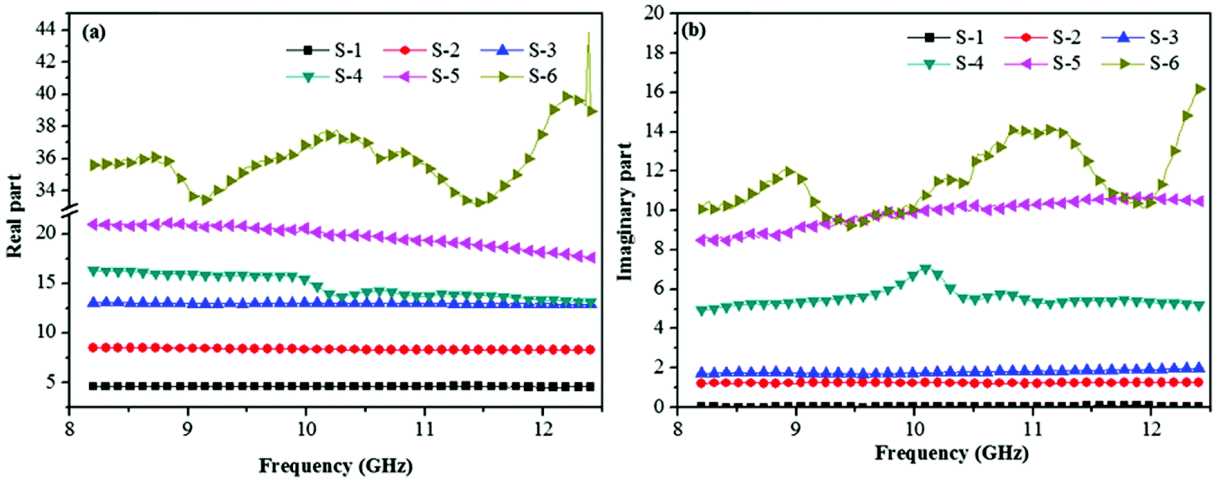

Fig. 27 (a) Real part and (b) imaginary part of the resultant SiCN (S-1) and RGO–SiCN ceramic nanocomposite samples S-2 to S-6 as a function of frequency.

The RC is a comprehensive parameter to evaluate absorption property of an EM material. Based on the metal back-panel model, the RC can be calculated from the relative complex permeability and permittivity according to Eq. 11 and 12 [21, 229].

Fig. 28 shows the RC of the obtained ceramic samples as a function of frequency in the X-band. The absorption capability of S-2 with 1.0 wt% GO in the feed is weak at every sample thickness since it exhibits a RC_{min} of −7 dB. In contrast, the RC value of sample S-4 is significantly improved when the GO content increases to 2.5 wt%. It is worth pointing out that the RC_{min} reaches -61.9 dB at 9.0 GHz and the effective absorption bandwidth (RC values lower than −10 dB) amounts to about 3.0 GHz (from 8.2 to 11.2 GHz). By a comparison of the RC values between samples S-3 and S-4, it unambiguously shows again the significant advantage of the SSP approach over the physical blending method regarding the EM absorption properties: the RC_{min} of the sample S-3 is even higher than −9 dB while the sample S-4 reaches -61.9 dB. The huge difference in the RC_{min} of the samples S-3 and S-4 can be explained by the quality of the dispersion of RGO

in the ceramic matrix as shown in Fig. 26. However, with the GO content in the feed increasing to 6.0 wt%, the value of RC_{min} of the sample S-5 decreases significantly (Fig. 28d). When the RGO content exceeds a certain limit, an impedance mismatching between the sample and air occurs, which leads to a strong reflection. As a result, sample S-4 shows the most excellent absorption capability among all the RGO–SiCN samples.

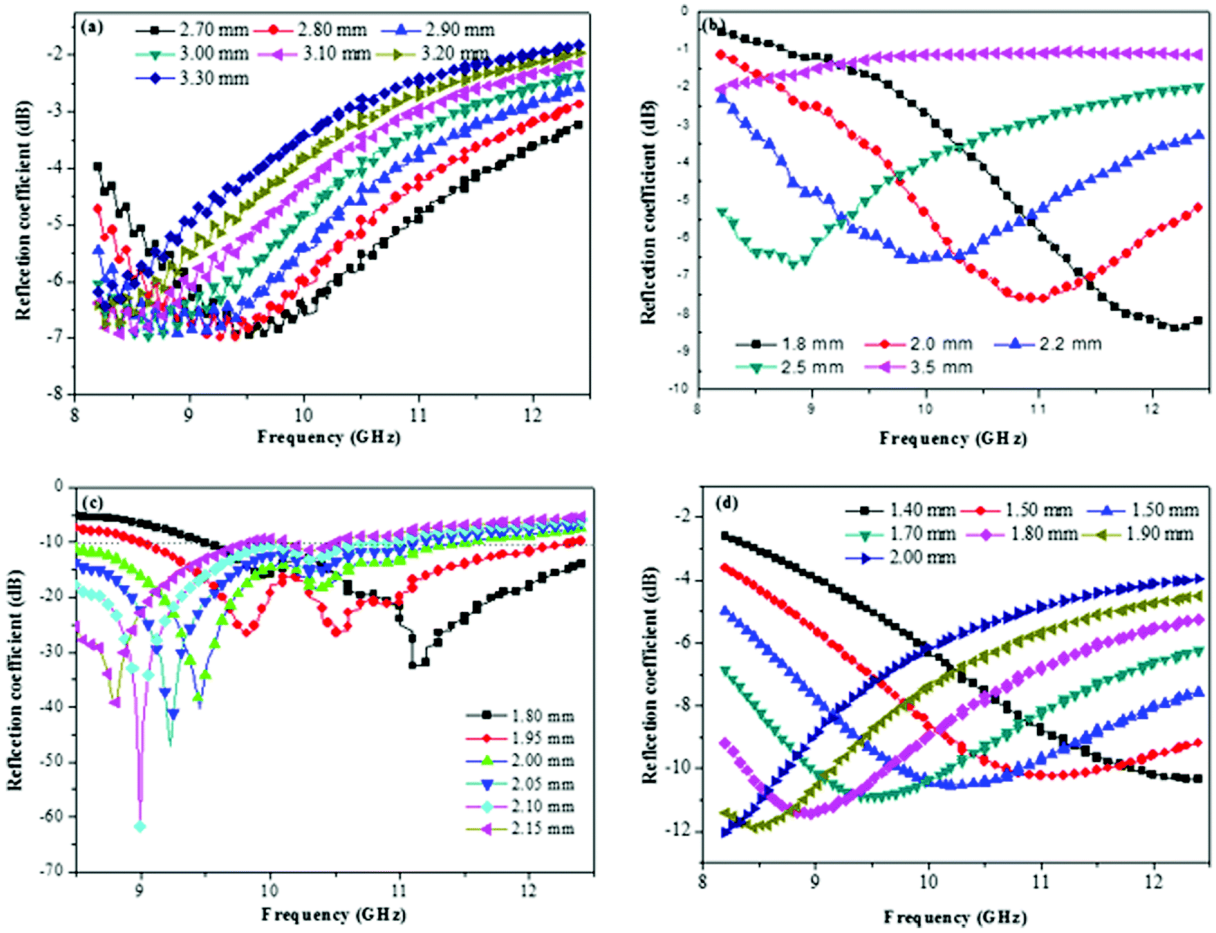

Fig. 28 Reflection coefficients of RGO–SiCN ceramic nanocomposites of the samples (a) S-2, (b) S-3, (c) S-4 and (d) S-5.

As can be seen from each curve calculated from different sample thicknesses, the RC varies with varying frequency and reaches its minimal value only at a certain frequency point. This behavior is explained by the fact that if the sample thickness is the odd multiple of a quarter-wavelength, a sharp destructive interference takes place, which is caused by the inverse phase angle of the reflection EM wave from the upper and bottom surfaces. With decreasing sample thickness, the RC_{min} decreases while the effective bandwidth increases. To better understand the variation of RC as a function of the sample thickness, a two-dimensional colorful map of RC based on sample S-4

is shown in Fig. 29. With the sample thickness of ca. 2.10 mm, the corresponding RC value is much lower than that of their adjacent, indicating better EM absorbing abilities. At a sample thickness beyond 2.10 mm, the EM waves reflected by the upper surface have a phase opposite to that EM wave coming from the back reflection, resulting in the total cancellation of the two waves at the air–material interface [245]. In this case, the thicknesses of the EM absorbing materials are satisfied using the quarter-wavelength law (Eq. 13).

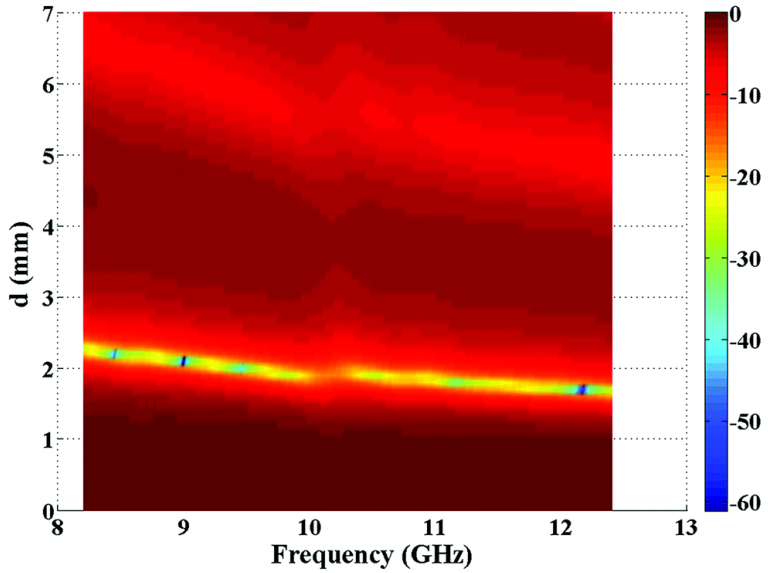

Fig. 29 Two dimensional colorful map of reflection coefficient of sample S-4.

The capability of a shielding material can be expressed by the electromagnetic interference shielding effectiveness or efficiency (EMI SE), indicating how many incident waves are blocked by the shielding material [121]. Theoretically, the EMI SE can be computed using Eq. 16 and 17.

From the Simon formalism, the EMI SE of shielding materials strongly depends on their electrical conductivity. However, the electrical conductivity is not the scientific criterion for the EMI shielding materials since the shielding behavior requires mobile electrons inside the materials to interact with incident EM waves instead of the electrical conductive network [71, 246, 247]. When EM waves are incident into shielding materials, mobile electrons inside the absorbent interact with incident EM waves, which blocks EM waves from transmitting. To make a comparison between the σ_{AC} calculated using Eq.16 and DC conductivity (σ_{DC}) measured using a four-pin probe method, the results showed that the σ_{AC} was remarkably higher than σ_{DC} [42]. Based on the abovementioned drawbacks of Simon formalism, in the present work, the EMI SE is calculated by

S-parameters which can be directly measured by the waveguide method using a vector network analyzer [121, 124, 133].

Shielding mechanisms of a conductive shielding material include reflection, absorption and multiple reflections [42, 229]. Multiple reflections are the internal reflections between the internal surfaces of the shielding material. In the case where the shielding by absorption (*i.e.*, absorption loss) is higher than 10 dB, most of the re-reflected wave will be absorbed within the shield [42, 229]. Thus, multiple reflections can be ignored. Actually, when an electromagnetic wave is incident on a shielding material, the incident power is divided into R, A and T. The SE_T, SE_A, SE_R, R, T and A were calculated based on Eq. 20-24 [4, 248].

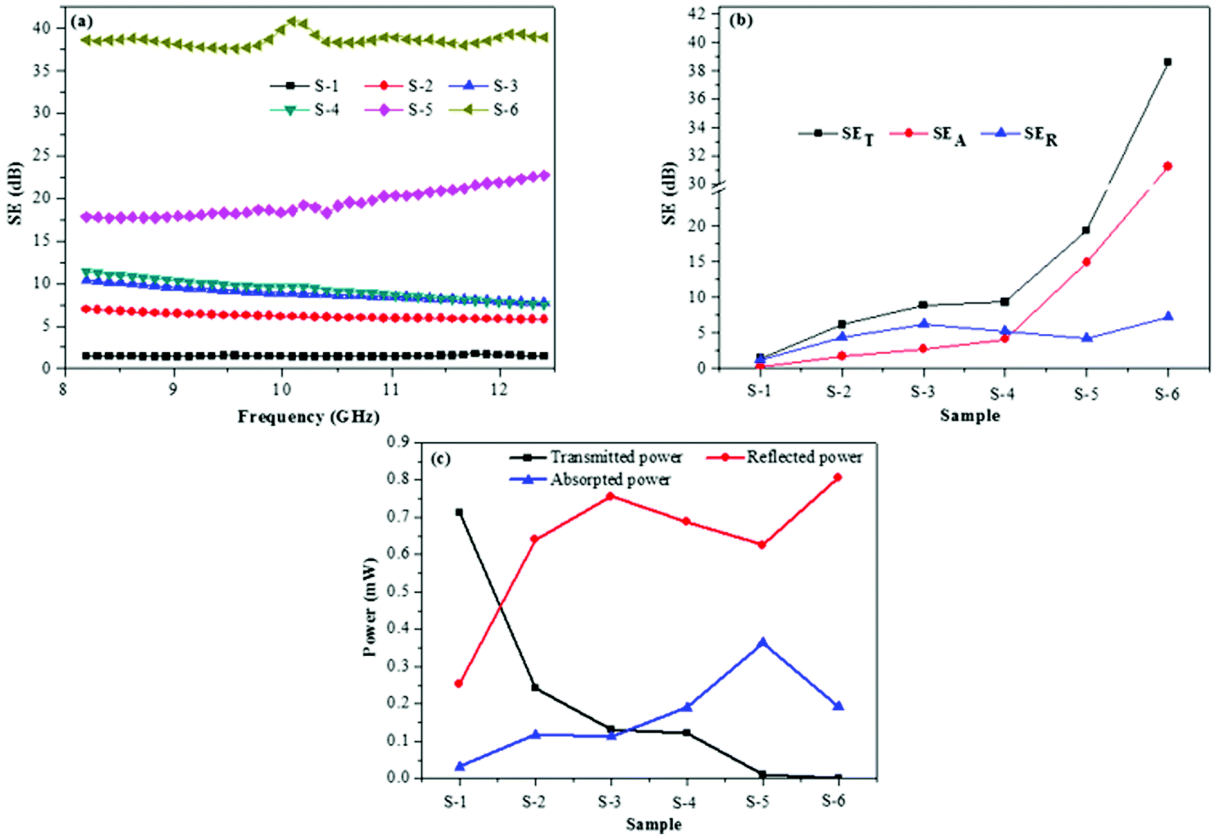

Fig. 30 (a) EMI SE and (b) average SE_T, SE_R and SE_A and (c) power balance of the resultant samples.

Fig. 30 shows the EMI SE and power balance of SiCN and RGO–SiCN ceramic nanocomposites over the frequency range of 8.2–12.4 GHz. As shown in Fig. 30a, the pristine SiCN shows a low SE value of around 1.7 dB, which further demonstrates its role as an impedance matching material. With respect to the RGO–SiCN nanocomposites, the SE value increases gradually with the increasing amount of GO in the feed. The introduction of carbon nanofillers is expected to enhance the electrical conductivity. The fact that the improvement of the electrical conductivity leads to the

improvement of the EMI SE has been proven and reported in the literature [37, 249]. In particular, with the 12.0 wt% GO content in the feed, the maximum EMI SE value of the resultant sample S-6 reaches 41.2 dB, which means that more than 99.99% EM waves are shielded. Fig. 30b shows the change in the mean value of SE_A, SE_R and SE_T of the SiCN and RGO–SiCN nanocomposites. The SE_A increases with increasing GO content in the starting material. When the GO content in the feed is lower than 2.5 wt%, the SE_A is always lower than the SE_R for samples S-2, S-3 and S-4. However, with increasing GO contents, the SE_A of S-5 becomes higher than that of the SE_R of samples S-5 and S-6. In particular, the SE_A of the material S-6 increases to 35.2 dB compared to 9.0 dB of SE_R. As can be seen from Eq.25, the SE_A represents the absorbed ratio of the microwave that reaches the interior part of the material. A high SE_A represents a material possessing a high intrinsic absorption ability. However, a high intrinsic absorption ability is always accompanied by strong reflection [42, 48] which can be proven by its power balance in Fig. 30c. Actually, the reflected power, the absorbed power and the transmitted power represent the capability of a material to reflect, absorb and transmit a microwave, respectively [42, 229]. As shown in Fig. 30c, the power balance reveals a remarkable increase in the reflected power and absorbed power and a decrease in the transmitted power with increasing absorbent content. With the increasing amount of GO in the starting material, the absorbed power exhibits an increasing tendency. However, when the GO content is increased to 12.0 wt%, the absorbed power of sample S-6 is decreased as compared with that of sample S-5. This phenomenon is due to the strong reflection of the material S-6. As reflection occurs before absorption, the microwaves are reflected before they reach the inner part of the material, leading to a decrease of the absorption power. Therefore, the obtained RGO–SiCN nanocomposites (S-6) are not suitable for applications requiring low reflection. However, our materials are useful for applications requiring high thermal resistance and/or high mechanical loads at elevated temperatures [121]. In order to decrease the reflection of a material, a multilayered composite material of graded electrical conductivity has to be designed in future.

3.2.2. Statement of personal contribution

[2] Liu X, Yu Z, Ishikawa R, et al. Single-source-precursor synthesis and electromagnetic properties of novel RGO–SiCN ceramic nanocomposites. Journal of Materials Chemistry C, 5 (2017) 7950-7960.

All experimental work related to material synthesis and preparation was carried out by myself. All applied chemical and microstructural characterization methods were performed by myself, except permittivity and TEM. The calculation of electromagnetic absorption and interference shielding effectiveness were performed by myself. The manuscript was written by myself and revised by Prof. Zhaoju Yu and Prof. Ralf Riedel.

3.3. Single-source-precursor derived RGO/CNTs-SiCN ceramic nanocomposite with ultra-high electromagnetic shielding effectiveness

[3] Liu X, Yu Z, Ishikawa R, et al. Single-source-precursor derived RGO/CNTs-SiCN ceramic nanocomposite with ultra-high electromagnetic shielding effectiveness. Acta Materialia, 130 (2017) 83-93.

In the present Chapter, the synthesis of chemically bonded GO/CNTs hybrids derived from the amidation reaction of GO with amino functionalized CNTs is introduced. RGO/CNTs hybrids modified SiCN ceramic nanocomposites with hybrids finely dispersed within the SiCN ceramic matrix were obtained by chemical modification of HTT 1800 with chemically bonded GO/CNTs by thermolysis. The microstructure of the composites is carefully characterized and materials studied with respect to their electromagnetic properties. The influence of hybrid content and fabrication approach on the dielectric properties is studied. The electromagnetic absorption and interference shielding effectiveness of RGO/CNTs-SiCN ceramic nanocomposite with varying hybrid contents are presented.

3.3.1. Results and discussion

Commercially available CNTs-NH_2 and GO powders employed in this study were purchased from Xianfeng Nano, China. Polysilazane HTT 1800 (KiON Specialty Polymers) was used as precursor for SiCN. The GO and CNTs-NH_2 were separately dispersed in anhydrous ethanol by a weight ratio of 1:1000 in an ultrasonication bath for 4 h before they were blended together with the weight ratio of GO/CNTs of 4:1. Then $ZnCl_2$ (Sigma-Aldrich, Germany) catalyst by a weight percentage of 2.0 wt.% to GO/CNTs/ethanol reaction mixture was added. After ultrasonication at 50°C for 4 h, the obtained GO/CNTs hybrids were separated with the assistance of centrifugation (5000 r/min) and washed with anhydrous ethanol for 5 times. The obtained GO/CNTs hybrids were chosen as the derivative of microwave absorbent and blended into DMF with a weight ratio of 1:500 in a flask. After ultra-sonication for 2 h, the $ZnCl_2$ catalyst was introduced into the GO/CNTs-DMF mixture with a weight ratio of catalyst/HTT 1800 of 2:98. After the reaction solution was heated up to 70ºC for 72 h under argon flow and magnetic stirring, the as-synthesized single-source-precursor was crosslinked at 120ºC before the solvent was removed under vacuum. After ball milling for 3 h, the GO/CNTs-HTT 1800 single-source-precursor powders were warm pressed to rectangular green bodies with dimensions of 50.0 × 40.0 × 2.5 mm^3 under a pressure of 60 KN. After

pyrolysis in Ar atmosphere under the heating program in Fig. 31, the obtained RGO/CNTs-SiCN nanocomposites were machined into samples with dimensions of 22.86×10.16×2.00 mm^3 by wire cutting for the measurement of dielectric properties. The synthesis procedure of RGO/CNTs-SiCN nanocomposites by the SSP approach is shown in Fig. 32.

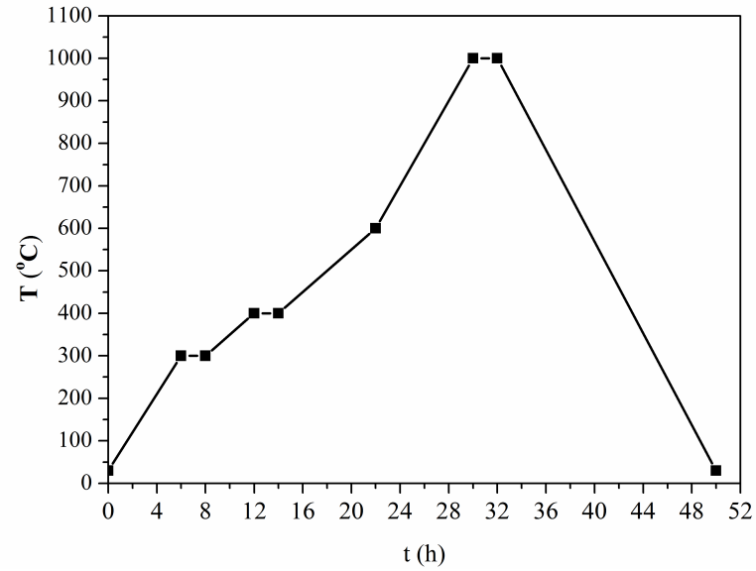

Fig. 31 Heating program of RGO/CNTs-SiCN nanocomposites.

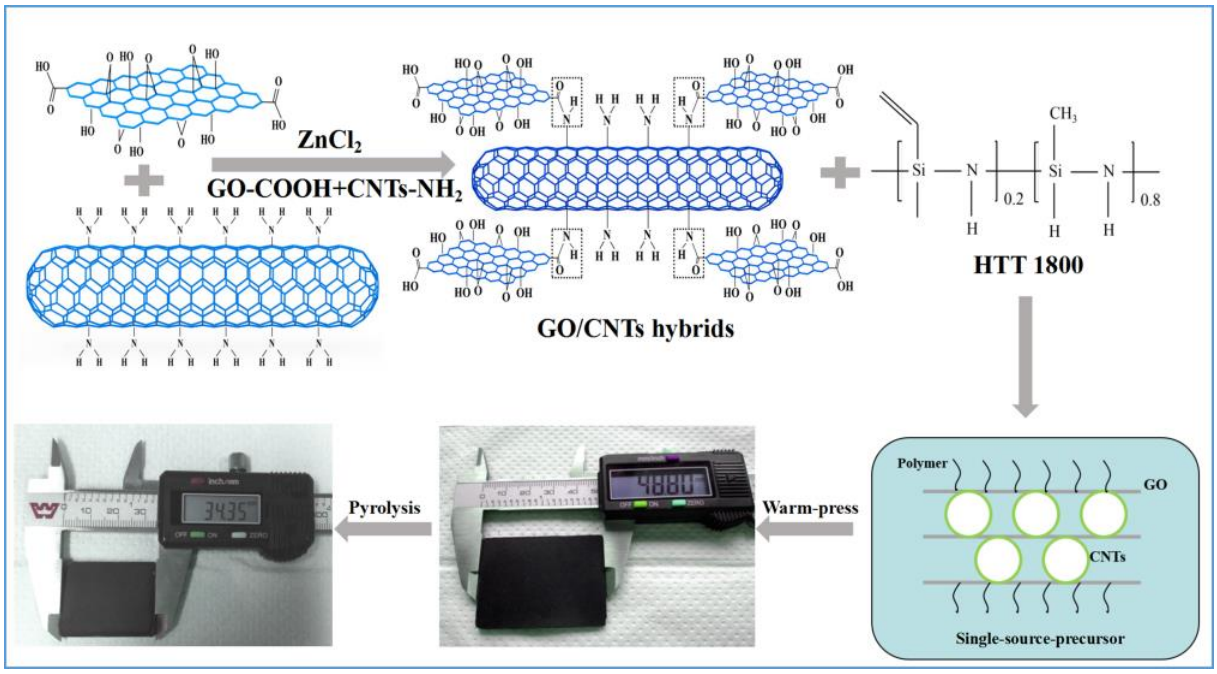

Fig. 32 Synthesis procedure of RGO/CNTs-SiCN nanocomposites.

Table 5 summarizes the starting compositions used to prepare the carbon nanofiller-free SiCN ceramic (sample S1), SiCN-based nanocomposites derived from SSPs and from a physically-blended-precursor (PBP) GO/CNTs/HTT 1800 mixture (sample S3).

Table 5 Content of catalyst and carbon nanofiller in the feed

Ceramic sample	Precursor	Type of carbon nanofiller	GO: CNTs (Weight ratio)	Carbon nanofiller (wt.%)	$ZnCl_2$ (wt.%)
S1	HTT 1800	none	/	0.0	0.0
S2	SSP-GO-2.0	GO	/	2.0	2.0
S3a	PBP-hybrid-2.0	GO/CNTs	4:1	2.0	0.0
S4	SSP-hybrid-2.0	GO/CNTs	4:1	2.0	2.0
S5	SSP-hybrid-10.5	GO/CNTs	4:1	10.5	2.0
S6	SSP-hybrid-15.0	GO/CNTs	4:1	15.0	2.0

[a] S3 was obtained by pyrolysis of physically blended GO/CNTs/HTT 1800 mixture

The pristine GO, CNT-NH_2 and GO/CNTs hybrids were characterized with FT IR (Fig. 33). Fig. 33a shows the FT IR spectra of pristine GO, CNT-NH_2 and GO/CNTs hybrids starting from the CNT-NH_2 with an amino content of 0.45 wt.%. It is worth mentioning that the absorption band corresponding to the C=O of carboxylic groups (1730 cm^{-1}) in GO is partially replaced by new absorption bands (1646 cm^{-1}, assigned to C=O of amide groups) due to the amidation reaction [214, 250]. Besides, the new bands at 1332 cm^{-1} and 1454 cm^{-1} are assigned to the stretching vibrations of amide C-N and N-H bonds, respectively [214, 250-253]. The partial replacement of COOH groups by amide (-CONH-) groups indicates that the amidation reaction between GO-COOH and CNTs-NH_2 did take place. Regardless of the CNT ratio in the feed, remaining COOH groups can always be found in the obtained GO/CNTs hybrids, which can be used to further react with the polysilazane precursor. Fig. 33b exhibits the FT IR spectra of GO, CNTs-NH_2 with a higher amino content of 2~3 wt.%, and the obtained GO/CNTs hybrids with and without $ZnCl_2$ as catalyst. Due to the increase of the amino content in the CNTs from 0.45 to 2~3 wt.%, the intensities of the as-formed amide bands of the GO/CNTs hybrids synthesized with the catalyst significantly increase as compared to those shown in Fig. 33a. However, the FT IR spectrum of GO/CNTs hybrids without $ZnCl_2$ as catalyst shows no changes as compared to that of pristine GO. Again, this finding strongly indicates that $ZnCl_2$ catalyst is necessary for the successful amidation reaction between GO-COOH and CNTs-NH_2. It is worth mentioning that the COOH groups disappear completely, indicating the complete reaction of COOH groups on GO. Since no carboxylic groups were

remained after the amidation reaction, the further reaction of GO/CNTs hybrid with the polysilazane HTT 1800 is impossible. Therefore, in the present work, CNTs-NH_2 with lower amino content (0.45 wt.%) are employed to fabricate GO/CNTs hybrids.

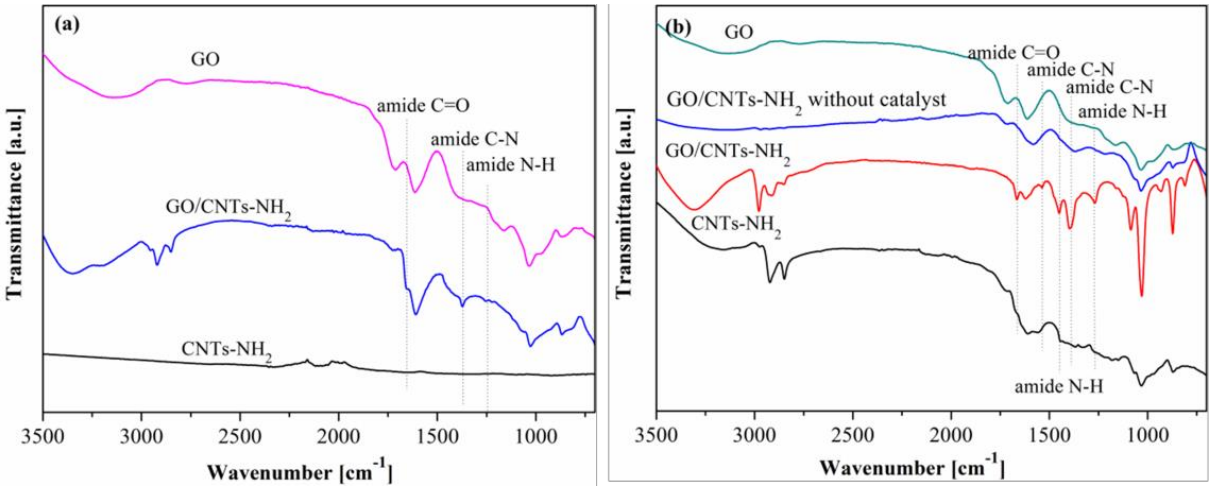

Fig. 33 (a) FT-IR spectra of pristine GO, CNTs-NH_2 and GO/CNTs hybrids starting from the CNTs-NH_2 with an amino content of 0.45 wt.%, (b) FT IR spectra of pristine GO, CNTs-NH_2 and GO/CNTs hybrids starting from the CNTs-NH_2 with an amino content of 2~3 wt.%.

Fig. 34 shows the TEM image and EDXS spectrum of resultant chemically bonded GO/CNTs hybrids. Fig. 34a is a low magnification bright-field scanning transmission electron microscopy (BF-STEM) image of the obtained GO/CNTs hybrids. Though the GO is difficult to be identified because of its weak scattering power (and thin structure), the tubular contrast of CNTs can be seen not isolated but always on the substrate of GO. It is noteworthy that, for the preparation of electron transparent thin specimens, ultrasonic sonication method was employed in ethanol (exposed by 1 h), but CNTs seem to be still well attached onto GO. Fig. 34b shows a high magnification BF-STEM image of single CNT with GO, where the CNT consists of multi-wall nanotubes. We observed a number of different regions, but basically all the CNTs are well attached onto GO, which is most evident in the atomic-resolution ADF-STEM image (annular dark field), as shown in Fig. 34c. Though the used electron probe has a relatively large depth of field (> 5 nm), the observed flat regions are well focused on both CNT edge and GO substrate over the large areas. Therefore, CNTs and GO are chemically bonded between each other. Moreover, we performed energy dispersive x-ray spectroscopy (STEM-EDXS) at few-layer-graphene regions and the spectrum is given in Fig. 34d. The EDX spectrum shows strong oxygen intensity (due to the -COOH and -OH groups of GO) and weak nitrogen intensity (due to amide groups of chemically bonded GO/CNTs). Therefore, our starting material is characterized by the presence of GO/CNTs hybrids and that the

constituents are well-bonded between each other, which agrees well with the FT IR results shown in Fig. 33.

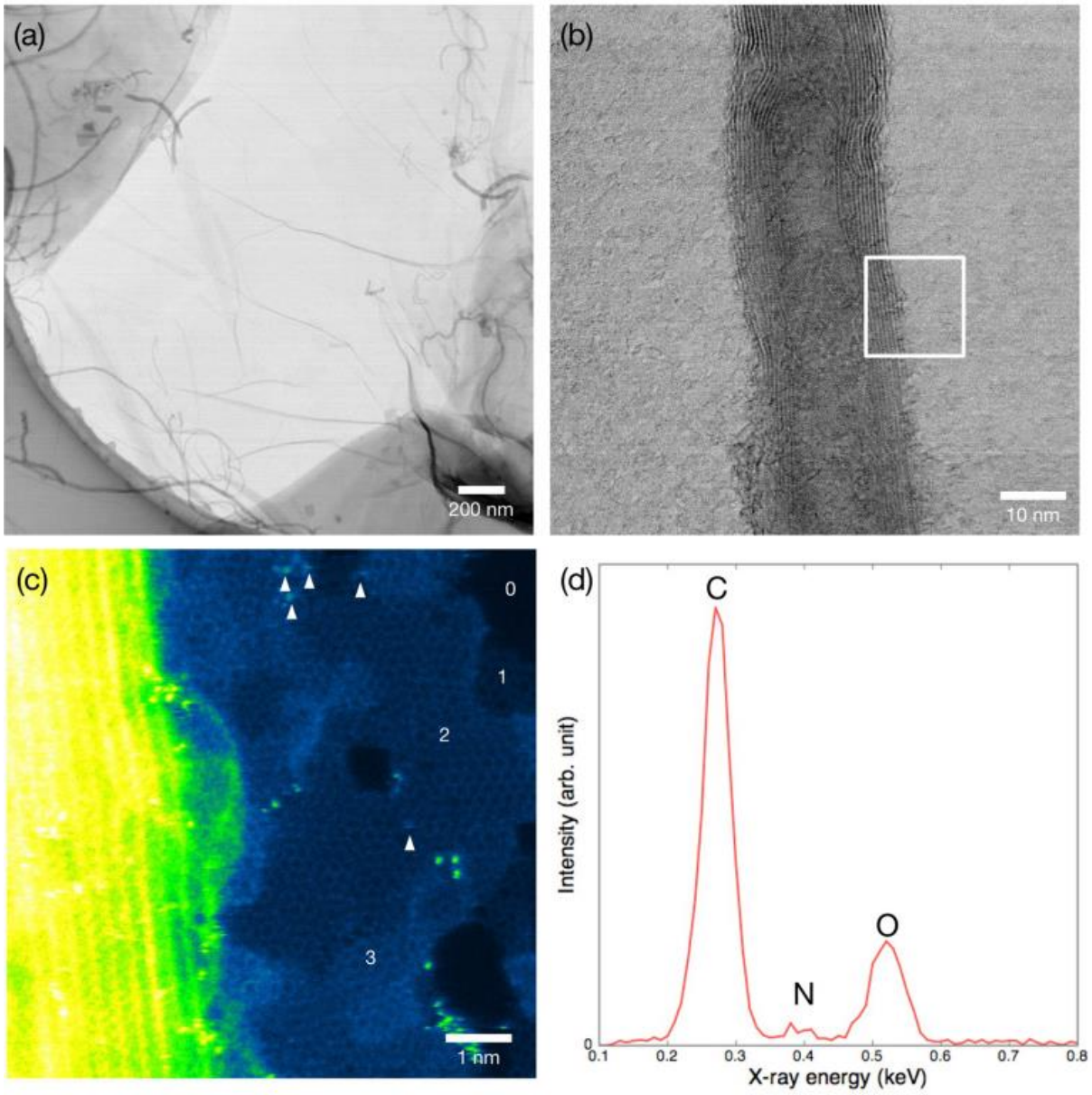

Fig. 34 (a) low-magnification BF-STEM image of GO/CNTs and (b) single CNT, (c) atomic-resolution ADF-STEM image obtained from the corresponding area in (b) (marked by white rectangle). The numbers and white arrowheads in (c) indicate the number of graphene layers and the location of single oxygen atoms, respectively. (d) EDXS spectrum acquired from GO substrate region.

Fig. 35 shows the FT IR spectra of pure HTT 1800 and resultant single-source-precursors. In the FT IR spectrum of HTT 1800, typical absorption bands related to C-H (2960 and 2965 cm^{-1}), Si-N-H (1160 cm^{-1}), and Si-N (930 cm^{-1}) groups appear [240, 254]. After amidation in the presence of the $ZnCl_2$ catalyst, new peaks located at ν= 1332 cm^{-1} (amide C-N), ν= 1646 cm^{-1} (amide C=O), ν= 1590 cm^{-1} (amide N-H) are assigned, which supports the expected reaction

between COOH groups of GO and NH groups of the polysilazane HTT 1800 [214, 250-253]. However, for the spectrum of the physically-blended-precursor PBP-hybrid-2.0, these new peaks are not detected. This result strongly indicates that the single-source-precursor was successfully synthesized by the amidation reaction between GO and HTT 1800 with the assistance of $ZnCl_2$ catalyst. Based on the findings that the esterification and dehydrogenative coupling reactions can be effectively catalyzed by Lewis acids such as $FeCl_3$ and $ZnCl_2$ [218, 255], we here propose a possible reaction mechanism for the present amidation reaction. Accordingly, $ZnCl_2$ serves as a Lewis acid catalyst and activates the carboxylic group by coordination of the Zn atom at the O atom of the C=O group. Then, N-H of the polysilazane reacts with the activated carboxylic C atom by a nucleophilic attack.

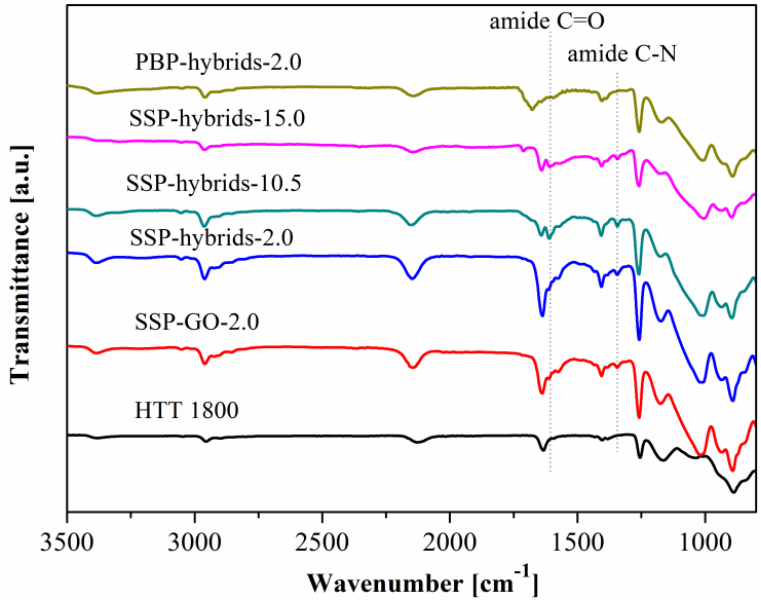

Fig. 35 FT-IR spectra of HTT 1800, single-source-precursors and physically-blended-precursor.

Representative SEM images of fracture surfaces of the formed ceramic samples are shown in Fig. 36. Fig. 36a and 36b are low magnification SEM images of HTT 1800-derived SiCN (S1) and RGO/CNTs-SiCN (S6) with 15.0 wt. % GO/CNTs hybrids in the feed. Low magnification SEM images of the resultant ceramic nanocomposites did not reveal defects in any of the specimens and confirmed a relative dense microstructure with open porosities of as low as 5.1~5.3 %. In Fig. 36b, an obvious and unique network structure (with the width of 80-100 nm) can be clearly identified in form of an interconnecting bright phase, which is considered to result from the carbon nanofillers since no such microstructural features were found inside the pure SiCN matrix. The high magnification images of RGO/CNTs-SiCN derived from samples S4 and S6 (Fig.36c-d) clearly indicate that the CNTs are uniformly

dispersed in the SiCN-matrix. Despite an increasing amount of GO/CNTs hybrids in the feed from 2.0 wt.% (S4) to 15.0 wt.% (S6), no agglomeration of the carbon nanofillers in the ceramic matrix was found.

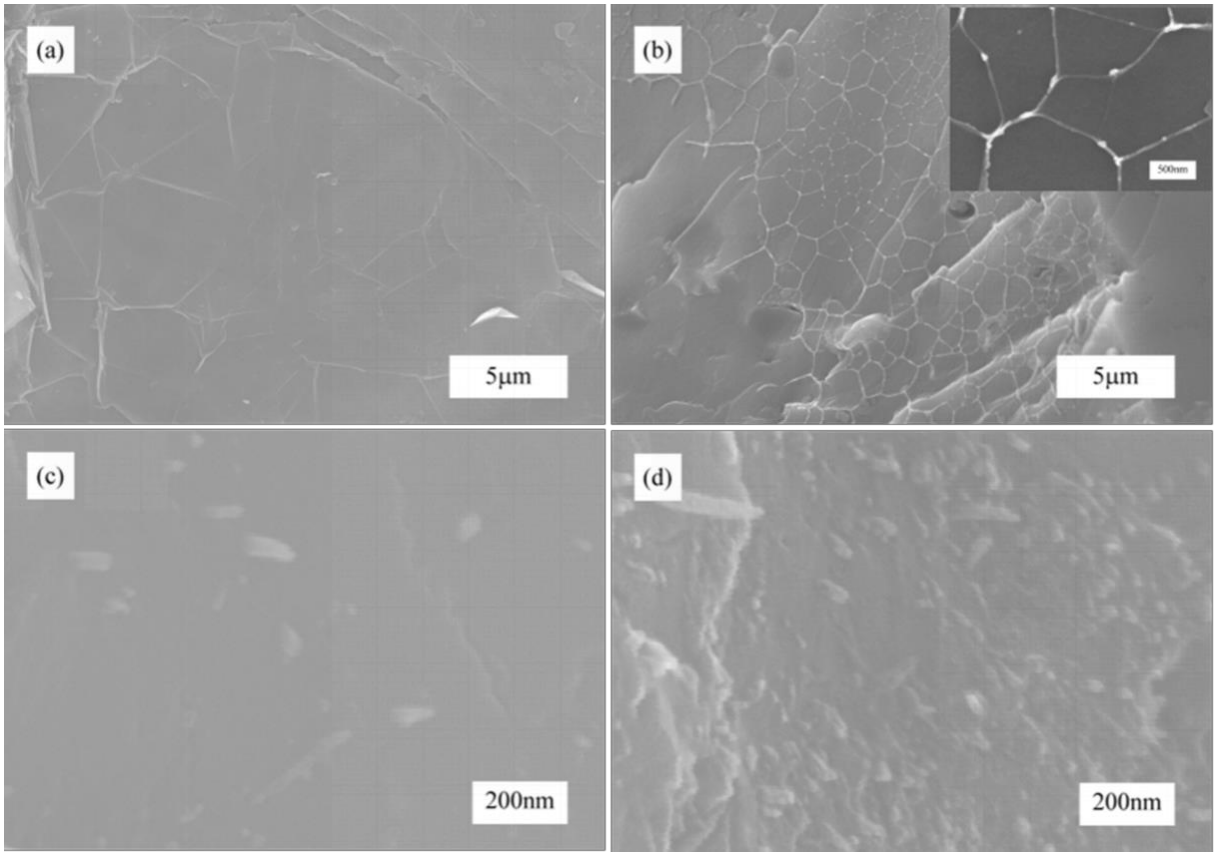

Fig. 36 SEM images of the fracture surface of densified (a) SiCN, (b) RGO/CNTs-SiCN from sample S6 (insert shows a high magnification image), (c) S4 and (d) S6.

To further investigate the morphology of the RGO/CNTs hybrids in the SiCN matrices, TEM observation was employed and the results are shown in Fig.37. Fig. 37a is a representative TEM image of the RGO/CNTs-SiCN nanocomposite, revealing that the integrity of the CNTs is retained. In the higher magnification TEM image (Fig. 37b), it is obvious, that the CNTs and RGO (2 layers) are still in contact after processing, including single-source-precursor synthesis, warm pressing and pyrolysis. This result clearly demonstrates that the integrity of the nanocarbon phase, namely RGO/CNTs, is retained after the pyrolysis procedure, which is shown by the homogeneous distribution of the CNTs in the ceramic matrix (see Fig. 37b).

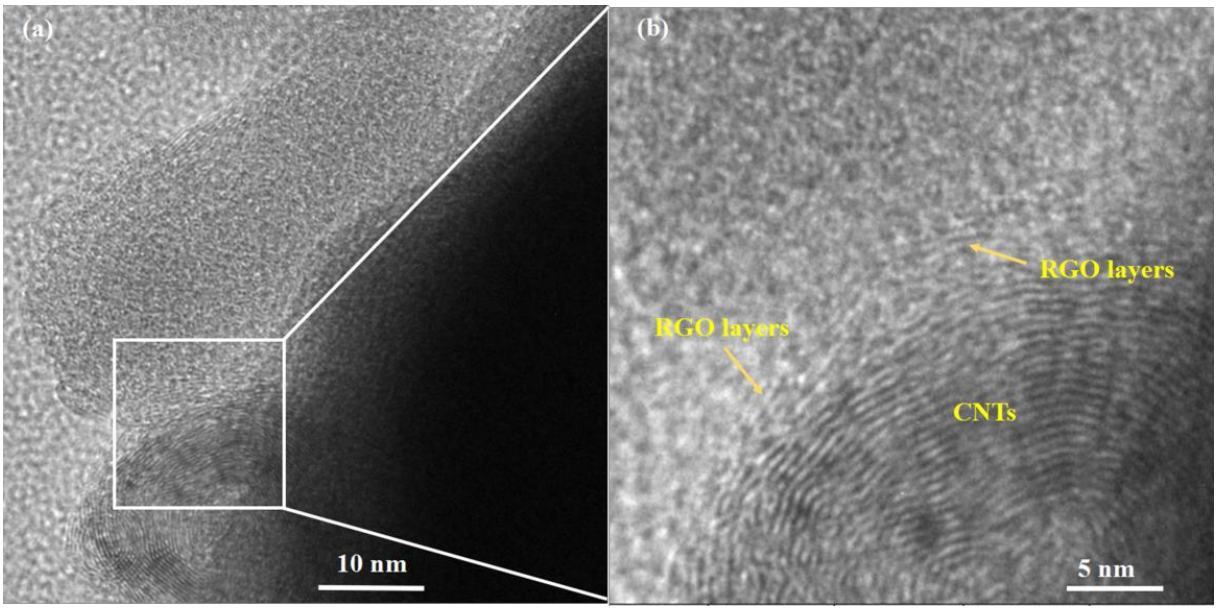

Fig. 37 (a) Typical high resolution TEM image of resultant RGO/CNTs-SiCN nanocomposites, (b) magnified image of the corresponding area in (a) (marked by white rectangle).

Fig. 38a shows the ADF-STEM image of the RGO/CNTs-SiCN (sample S6). In agreement with the SEM image, the dark-line contrast in the ADF-STEM image forms a network with the width of *ca.*100 nm. The electron diffraction pattern (Fig. 38b) shows the amorphous nature of our material. To confirm the composition of the networks, STEM-EDXS imaging was performed at the corresponding area in Fig. 38a and the EDXS maps (at.%) are given in Fig. 38c-f, where the edges of (c) Si-K, (d) C-K, (e) N-K and (f) O-K were employed, respectively. It is clear that silicon is predominantly located in the matrix and is poor in the networks, which is compatible with the dark-line contrast in ADF-STEM. On the other hand, the carbon content is rich at the ADF dark-line contrast region. Taking into account the FT IR, XRD and Raman spectroscopic results, it is reasonable to conclude that the matrix is comprised of SiCN while the interphase region (network) is a carbon-rich phase. The formation of the carbon-rich networks undoubtedly facilitate electrons to travel fast over long distances, which is expectedto enhance the electrical conductivity or dielectric properties of the final nanocomposites [81, 112].

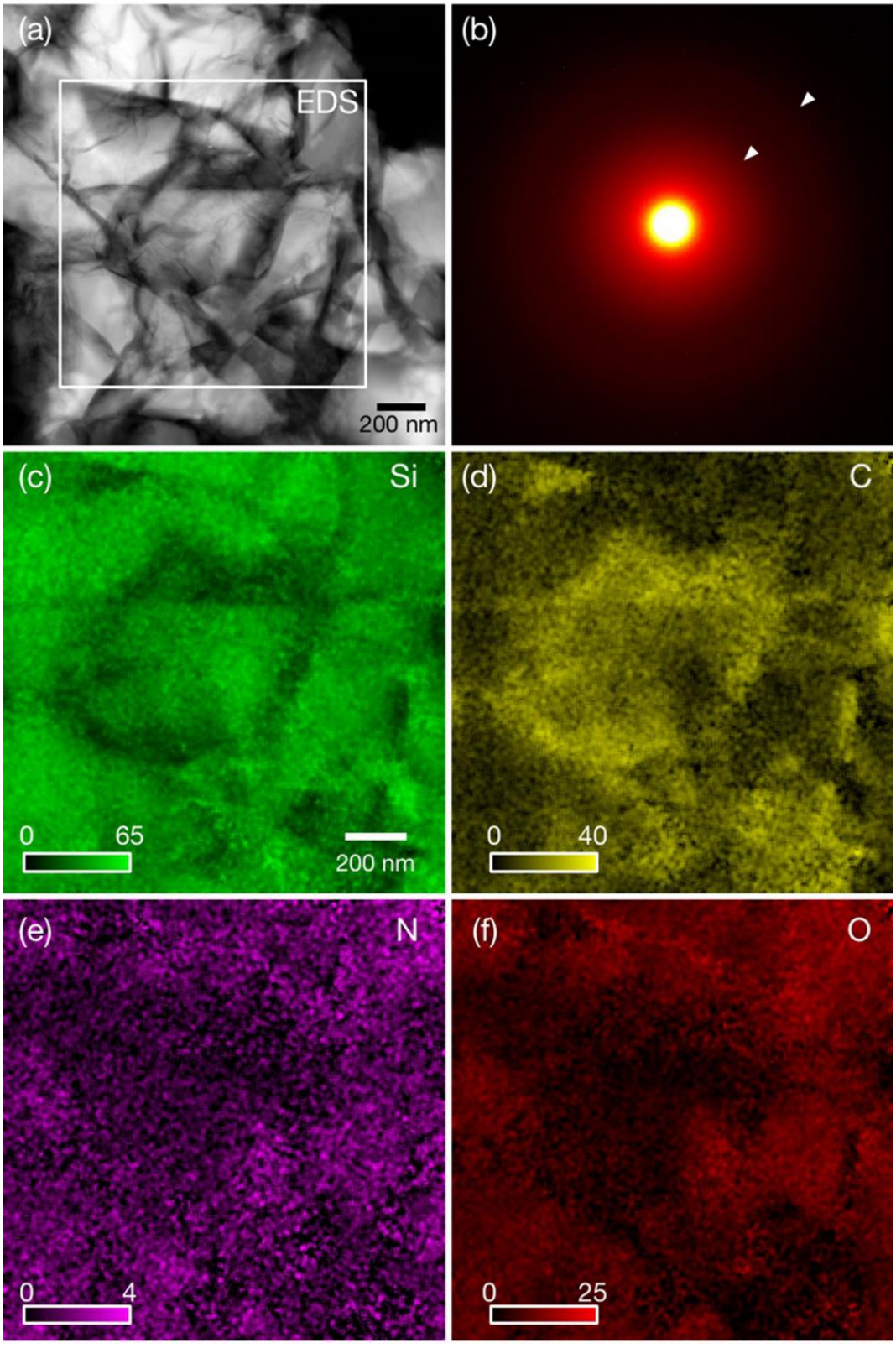

Fig. 38 (a) ADF-STEM image of the sample RGO/CNTs-SiCN (S6), and (b) the corresponding electron diffraction pattern. STEM-EDXS elemental maps (at.%) acquired from the area shown in (a): (c) Si, (d) C, (e) N, (f) O, respectively. The intensity scale bars in EDXS maps are given in each panels and the unit is at.%.

Fig. 39 shows the XRD and Raman results of the synthesized ceramic nanocomposites. According to Fig. 39a, the HTT 1800 derived SiCN shows a complete amorphous feature which agrees well with previous reports in the literature [51, 181]. As for the RGO/CNTs-SiCN ceramic (sample S6), a weak peak stemming from graphitic carbon at 2θ = 26.5° (002 plane) is found and no reflections related to the used $ZnCl_2$ catalyst occur. During the pyrolysis, reduction gaseous byproducts including CH_4, CO and H_2 can be released. So we predict that at a synthesis temperature of 1000°C, these byproducts together with the carbon nanofillers introduced into the matrix can help to reduce the $ZnCl_2$ catalyst into gaseous Zn, and the gaseous Zn finally evaporated out of the ceramic [220]. From the STEM-EDXS image we can find that no Zn atom was found in the ceramic matrix which strongly supports our prediction. Fig. 39b shows the Raman spectra of the formed RGO/CNTs-SiCN samples. The graphitization grade (G_G) of a carbon containing material can be calculated as follows: $I_G/(I_G + I_D)$, where I_G and I_D is the intensity of disorder-induced (D) and graphite-like (G) bands, respectively [234, 243]. When the content of hybrids increases from 0.0 wt.% to 15.0 wt.%, the G_G of the synthesized ceramics increases from 46.7% to 49.9%, indicating that the introduction of RGO/CNTs leads to an improvement of the degree of graphitization of the material [234, 243, 256].

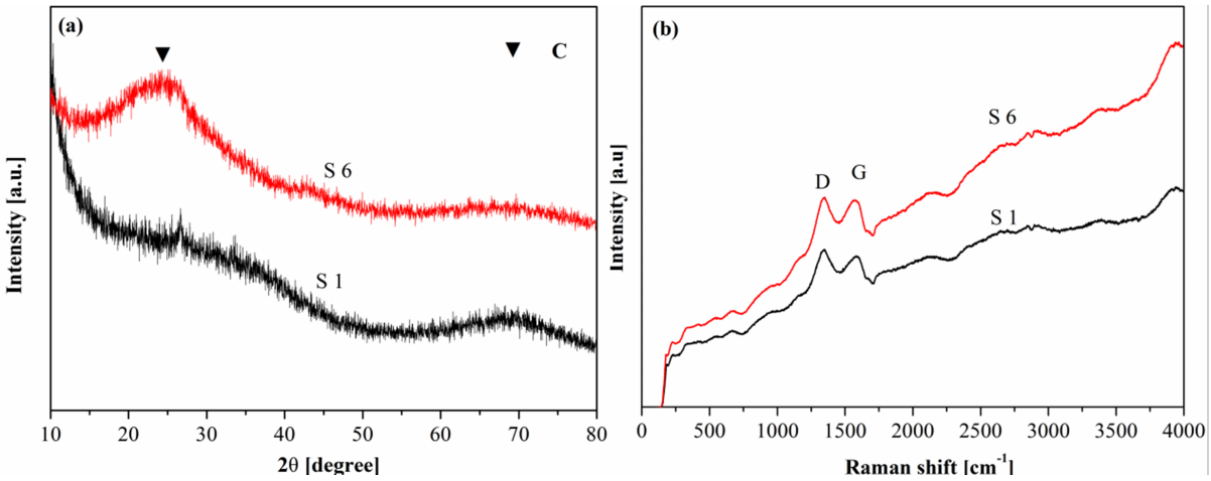

Fig. 39 (a) XRD and (b) Raman spectra of HTT1800-derived SiCN (S1) and RGO/CNTs-SiCN (S6) ceramic nanocomposites.

Electrical conductivity is an important parameter for the prediction of electromagnetic properties of non-magnetic materials [121, 243]. Based on the literature that the DC electrical conductivity of bulk graphene foam and monolithic carbon nanotubes reinforced carbon

fiber/pyrolytic carbon (CNTs-C_f/C) composites were measured with a two-probe method [243, 257], the electrical conductivity of as-prepared monolithic ceramic samples were determined by the same method and the results are shown in Fig. 40. The measured electrical conductivity of the SiCN ceramic matrix amounts ~10^{-7} S cm^{-1}, which agrees well with reference [181]. In general, with the introduction of RGO or RGO/CNTs into the SiCN matrix, the electrical conductivity of the carbon nanofiller modified SiCN nanocomposite increases significantly. With the highest GO/CNTs content (15.0 wt%) in the feed, the electrical conductivity of the final RGO/CNTs-SiCN composites reaches the maximum value (~5.7 S cm^{-1}). The increase of electrical conductivity is due to the following reasons: Firstly, the RGO and RGO/ CNTs nanofillers inside the matrix can build up pathways for the mobile charge carriers inside the ceramic matrix and with the increase of nanofiller content, the amount of pathways will increase accordingly. It is well known that the electrical conductivity of RGO and CNTs is far superior than that of the pure SiCN ceramic [258, 259]. Therefore, with the same cross section, the carbon nanofillers provide better pathway for the mobile charge carriers, leading to an improved electrical conductivity [243]. Secondly, the in-situ formed networks inside the ceramic matrix can also contribute to the improvement of electrical conductivity since the networks are composed of carbon rich phases (see Fig. 38). The establishment of these carbon rich networks provides a smooth way for the long-distance transport of the mobile charge carriers [81].

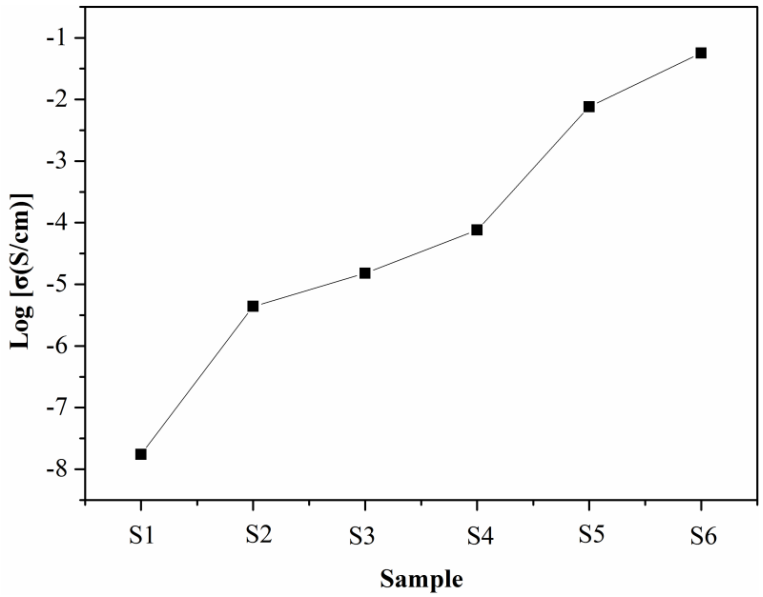

Fig. 40 Electrical conductivity of as-prepared ceramic nanocomposites.

The ε of the resultant RGO/CNTs-SiCN ceramics was measured in the frequency range of 8.2-12.4 GHz (X band). According to the Debye theory, ε' is related to the polarization relaxation and ε'' represents the dielectric loss capability, which is determined by the electrical conductivity of the materials and tan δ represents the microwave attenuation capability [21, 30, 121].

In Fig. 41a and 41b, the SiCN (sample S1) presents a low ε' (with an average value of 4.87) and ε" (9.10×10^{-3}-1.01×10^{-1}), indicating that amorphous SiCN possesses an electromagnetic wave transparent property [108, 121], which well demonstrates the role of SiCN as an impedance matching phase in the obtained RGO/CNTs-SiCN nanocomposites. By the addition of carbon-based absorbent phases into the SiCN matrix, both ε' and ε" increase gradually with increasing amount of RGO/CNTs in the SiCN matrix. The increased ε' is discussed in terms of dipole polarizations induced by the defects inside the nanofillers including RGO and RGO/CNTs hybrids [108]. Polarization relaxations induced by electron motion hysteresis under alternating EM field and increasing electrical conductivity are responsible for the increase of ε" [108,121]. As a result, the tangent loss (tan δ) obviously increases with the introduction of absorbent into the SiCN matrix (Fig. 41c). By comparing samples S2 (SSP-derived RGO-SiCN) and S4 (SSP-derived RGO/CNTs-SiCN), the pronounced enhancement in the dielectric properties (including ε', ε" and tan δ) does not only result from the unique microstructure of sample S4 but is also due to the distinguished synergistic effects obtained by the RGO/CNTs hybrids [95, 108]. Compared with sample S4, the dielectric properties of sample S3 prepared by mechanical blending are obviously lower with the same GO/CNTs content in the feed, which unambiguously proves the advantage of the SSP-derived RGO/CNTs-SiCN. This phenomenon is explained by the homogeneous dispersion of the carbon nanofillers in sample S 4.

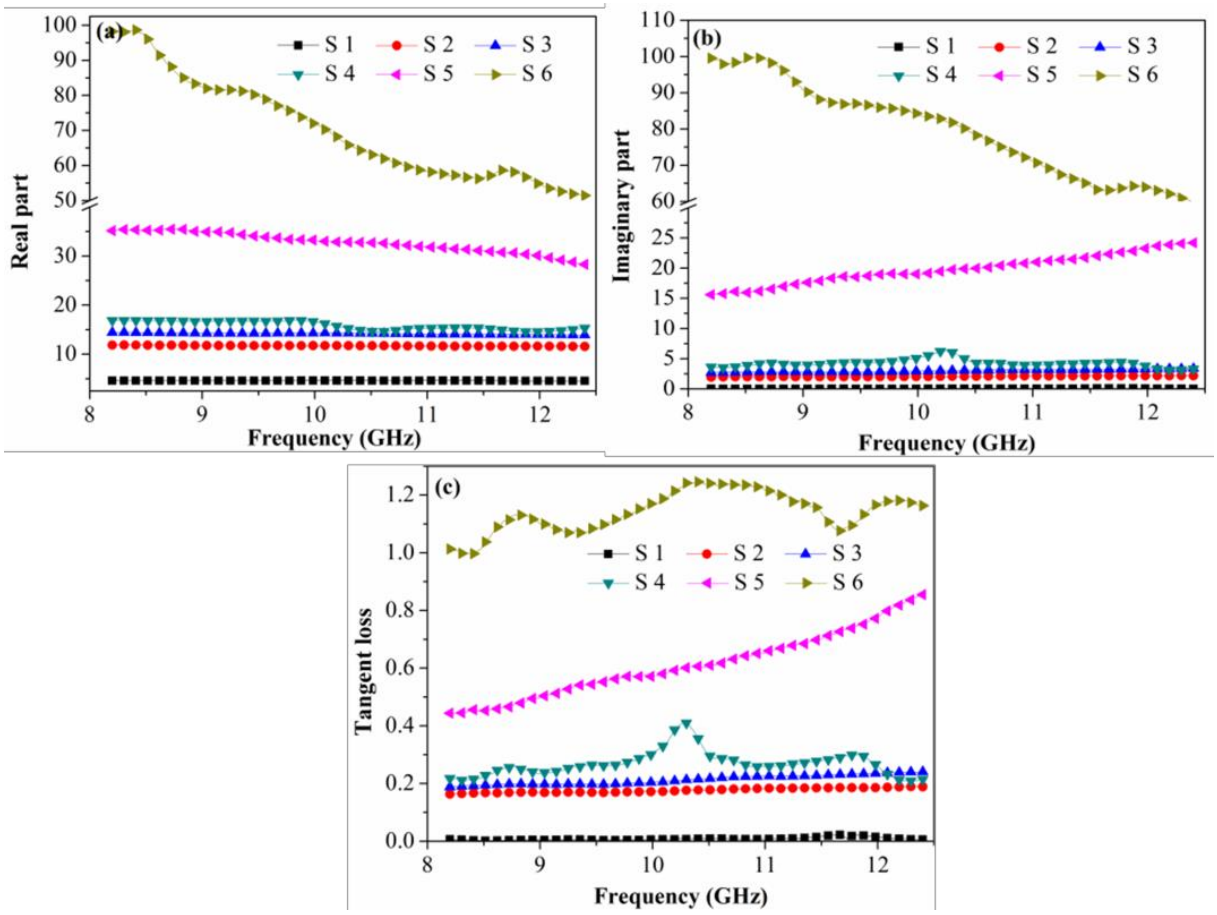

Fig. 41 (a) Real part, (b) imaginary part and (c) tangent loss of the resultant samples.

The measurement of the SE of a material is calculated from scattering parameter S_{ij}, available by the vector network analyzer [121, 244, 260]. For a transverse electromagnetic wave propagating into a sample with negligible magnetic interaction, SE of the sample is expressed as Eq. 22 in a unit of decibel (dB) [146, 244, 260].

Shielding mechanisms of a conductive shielding material include reflection, absorption and multiple reflections [121, 146, 244, 260]. Multiple reflections are the internal reflections between the internal surfaces of the shielding material. In cases where the shielding by absorption (i.e., absorption loss) is higher than 10 dB, most of the re-reflected wave will be absorbed within the shield [146, 260]. Thus, multiple reflections can be ignored in the present work. Actually, when an electromagnetic wave is incident on a shielding material, the incident power is subdivided into reflected power, absorbed power and transmitted power. The SE_T, SE_A, SE_R, R, T and A were calculated based on Eq. 20-24 [146, 260].

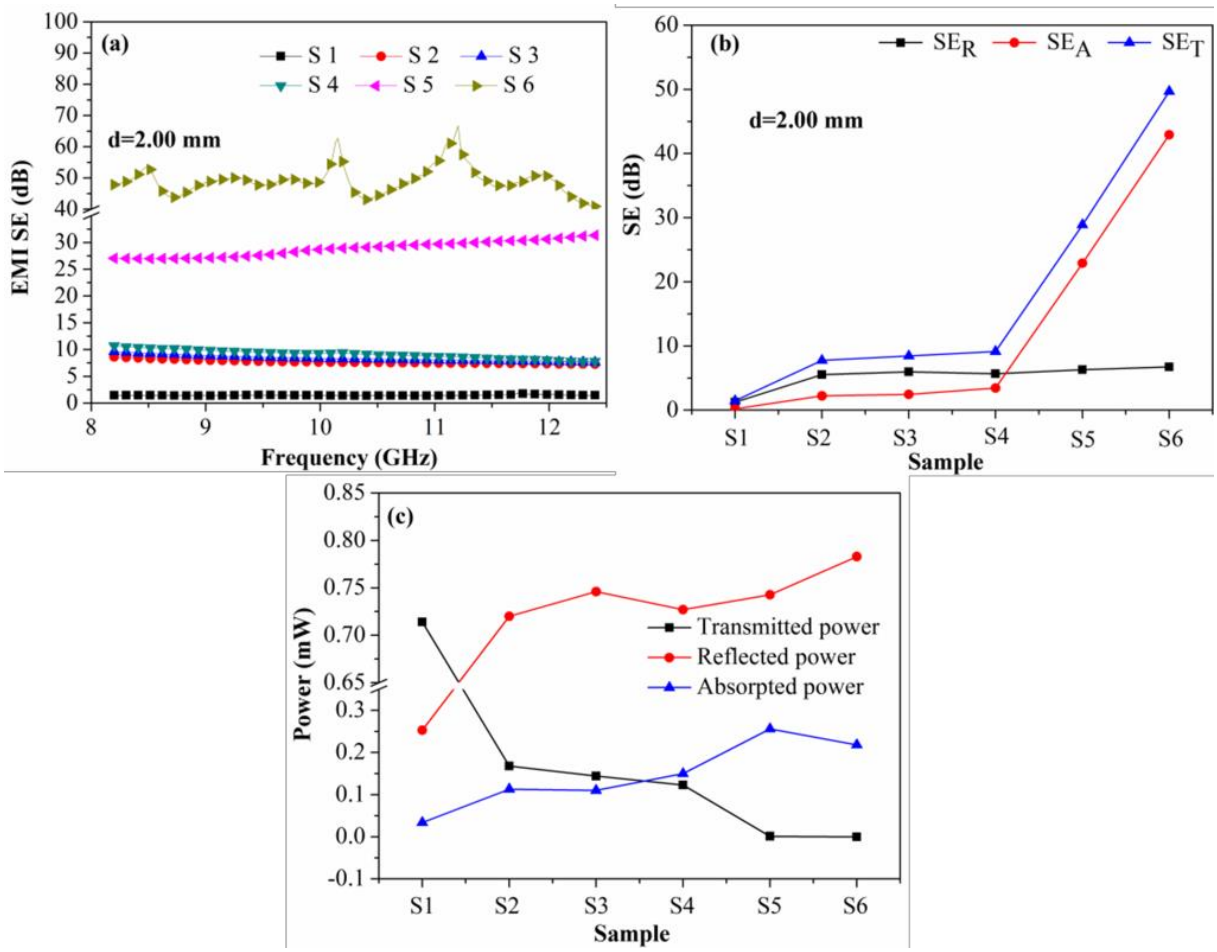

Fig. 42 (a) Total EMI SE, (b) average SE_T, SE_R and SE_A and (c) power balance of the resultant samples.

From Fig. 42a-c the electromagnetic interference shielding effectiveness and power balance of the samples can be taken. As shown in Fig. 42a and as compared with sample S1, the SE of that of S2, S3, S4, S5 and S6 increases significantly due to the introduction of conductive carbon nanofillers into the SiCN matrix. Especially, the SE is analyzed to be 67.2 dB with sample S6 (with 15.0 wt.% carbon hybrids in the feed), which is the highest among all the RGO-based composites published in the literature (Table 5). Fig. 42b shows that both values, SE_A and SE_R, increase with the increasing content of carbon nanofillers, which well agrees with the increase of SE_T. At a lower absorbent content of 2.0 wt.%, the SE_A is always lower than that of SE_R. However, with increasing absorbent content (samples S5 and S6), the SE_A is higher than that of the SE_R. As shown in Fig. 42c, the power balance reveals a remarkable increase in R and A, and a decrease in T with the increase of the absorbent content. Moreover, the value of R is always higher than that of A. In general, A, T and R represent the capability of a material to absorb, transmit and reflect the microwave when the microwave transmits a material, respectively [37, 119]. However, SE_A represents the ability of a material to attenuate microwave that comes inside of the material [37, 119]. A high SE_A is characteristic for a material possessing a high intrinsic absorption property [41, 130, 260]. Normally, a high SE_A requires high

electrical conductivity which also leads to strong reflection [41, 130, 244]. Since reflection takes place before absorption, most of the incident waves are reflected before they finally come inside of the material. Therefore, though sample S6 possesses a high SE_A, it is highly reflective, which can be confirmed from the reflection power. From the mean value of T we can see that only 0.001% waves transmitted the material, which means nearly 99.999% of the waves are shielded.

Table 5 shows the SE of various RGO-based composites. It is worth mentioning that our present RGO/CNTs-SiCN composites show the highest SE (67.2 dB) with the thickness of 2.0 mm among all the graphene-based composites with comparable thickness.

Table 5. EMI shielding performance of various RGO-based composites [146]

Filler	Filler content (wt.%)	Matrix	Thickness (mm)	Conductivity (S m^{-1})	EMI SE (dB)	Ref
RGO	7	PS	2.5	43.5	45.1	[81]
RGO	10	PEI	2.3	0.001	22	[261]
RGO	0.7	PMDS	1	180	30	[47]
RGO	20	Wax	2.0	<0.1	29	[33]
RGO	60	Wax	0.35	2500	27	[262]
RGO	7.5	WPU	1	16.8	34	[263]
RGO	15	Epoxy	/	10	21	[264]
RGO	30	PS	2.5	1.25	29	[32]
RGO	4	PI	0.073	2×10^{5}	51	[265]
RGO	33	PANI	2.8	1800	34.2	[266]
S-doped RGO	15	PS	2	33	24.5	[267]
RGO/γ-Fe_2O_3	75	PANI	2.5	80	51	[83]
RGO/Fe_2O_3	35	PVA	0.3	<1	15	[268]
RGO/Fe_2O_3	66	PANI	2.5	260	30	[269]
RGO/CF/γ-Fe_2O_3	50	Resin	0.4	1.7×10^{4}	41.8	[270]
RGO/Fe_3O_4	10	PVC	1.8	7.7×10^{-4}	13	[271]
RGO/Fe_3O_4	10	PEI	2.5	10^{-4}	18	[49]
RGO/MnO_2	Bulk	/	3	/	57	[272]
rGO/Fe_3O_4	Bulk	/	0.25	5000	24	[273]
rGO/Fe_3O_4	Bulk	/	3	700	41	[274]
rGO-$BaTiO_3$	Bulk	/	1.5	/	41.7	[275]
rGO-Ba Ferrite	Bulk	/	1.0	98	18	[47]
rGO/CNT/Fe_3O_4	Bulk	/	2.0	/	37.5	[34]
RGO/CNTs	10.0	PDMS	2.0	/	10.4	[95]
RGO/CNTs	15.0	SiCN	2.0	5.7	67.2	This work

3.3.2. Statement of personal contribution

[3] Liu X, Yu Z, Ishikawa R, et al. Single-source-precursor derived RGO/CNTs-SiCN ceramic nanocomposite with ultra-high electromagnetic shielding effectiveness. Acta Materialia, 130 (2017) 83-93.

The idea and experiment designing behind this work were developed by myself. All experimental work related to the material synthesis and preparation was carried out by myself. All applied chemical and microstructural characterization methods were performed by myself, except TEM and permittivity measurement. The TEM measurement was done by Dr. Ryo Ishikawa and Prof. Zhaoju Yu and the permittivity measurement was done by Lingqi Chen and Xiaofei Liu. The electromagnetic absorption calculation was accomplished by myself. The manuscript was written by myself and revised and approved by Prof. Zhaoju Yu and Prof. Ralf Riedel.

4. Summary

Within the scope of this thesis, carbon nanofillers including 1D CNTs, 2D RGO and 3D RGO/CNTs modified SiCN ceramic nanocomposites derived from single-source-precursors were studies as electromagnetic absorption and electromagnetic interference shielding materials. Chemical, structural and electromagnetic characterization methods were applied in order to investigate the resultant ceramic nanocomposites.

The first part of this work was focused on the synthesis, characterization and electromagnetic absorption calculation and analysis of 1D CNTs containing SiCN ceramic nanocomposites derived from commercially available poly(methylvinyl)silazane HTT 1800 modified by CNTs-COOH. Single-source-precursors of CNTs-HTT 1800 were synthesized via amidation reaction of HTT 1800 with CNTs-COOH at the assistance of $ZnCl_2$ catalyst. The -N-H groups of the molecular precursor work as functional groups reacting with the carboxylic groups on CNTs. After the reaction, a thin film of HTT 1800 with a thickness of ~3 nm was analysed to be attached on the surface of CNTs, which significantly changed the compatibility between the CNTs and host precursors and block each individual CNTs from tangling. Crack-free monolithic CNTs-SiCN nanocomposites were prepared through pyrolysis of the obtained single-source-precursor green bodies at 1000°C. Due to the strong influence of the polymer structure on the microstructure of the final ceramics, the single-source-precursor derived CNTs-SiCN nanocomposites clearly show a homogeneous distribution of the CNTs in the SiCN matrix while a physically-blended-precursor derived CNTs-SiCN nanocomposite exhibit serious aggregation and entangling of the CNTs in the SiCN matrix. With the same CNT content in the feed, the single-source-precursor derived CNTs-SiCN nanocomposites possess significant improvements of EM absorbing properties compared to those obtained from physically-blended-precursors. With the same CNT content (4.5 wt.%) in the feed, the single-source-precursor derived CNTs-SiCN nanocomposites possess a RC_{min} of -21.8 dB and an effective bandwidth of 3.7 GHz with a sample thickness of 2.2 mm while the physically-blended-precursor derived CNTs-SiCN nanocomposites show a far inferior RC_{min} of -6.4 dB with the same sample thickness. The significant improvements of EM absorbing property of single-source-precursor derived CNTs-SiCN nanocomposites is due to the microstructural feature characterized by the homogeneous distribution of the CNTs in the SiCN matrix, which is strongly dependent on the molecular precursor structure, namely, the uniform dispersion of the CNTs in the single-source-precursors.

The second part of this thesis was concerned with the study of 2D RGO modified SiCN ceramic nanocomposites. In this work, RGO-SiCN ceramic nanocomposites were synthesized through chemical modification of GO with HTT 1800 and followed by thermolysis of resultant single-source-precursor derived monolithic green bodies at 1000ºC. After pyrolysis, monolithic crack free RGO/SiCN ceramic nanocomposites were prepared. Through varying the content of GO (1.0, 2.5, 6.0 and 12.0 wt.%) in the resultant single-source-precursor, different batches of RGO/SiCN ceramic nanocomposites were obtained. Compared with physically blended precursor derived samples, the restacking of RGO in the single-source-precursor derived samples was effectively reduced due to the grafting of HTT 1800 onto the carbon backbones of GO. Successive conductive networks formed by RGO were found inside the ceramic matrix, which can contribute to improving the electrical conductivity. Through calculation, the resultant RGO-SiCN nanocomposites are found to possess versatile EM properties ranging from EM absorbing to shielding behavior. With 2.5 wt.% GO in the feed, the final RGO-SiCN nanocomposite exhibits an excellent RCmin of -62.1 dB at 9.0 GHz, and the effective absorption bandwidth reaches 3.0 GHz with a sample thickness of 2.10 mm. With the same GO content, the resultant RGO-SiCN nanocomposite prepared by mechanical blending exhibits a far inferior RC_{min} of -8.2 dB. This finding strongly supports that the advantage of the developed SSP route for the fabrication of RGO-SiCN nanocomposites with significantly enhanced EM properties. With 12.0 wt.% GO content in the feed, the obtained RGO-SiCN nanocomposite reveals an excellent shielding effectiveness of 41.2 dB with a sample thickness of 2.00 mm, which means that more than 99.99 % of electromagnetic wave is blocked.

The third part of this thesis was focused the attention on the synthesis of 3D GO/CNTs hybrids and the fabrication, microsturcture and EM properties of RGO/CNTs-SiCN ceramic nanocomposites. Hierarchically 3D GO/CNTs hybrids were prepared through amidation reaction of CNTs-NH_2 with GO at the assistance of $ZnCl_2$ catalyst. 3D RGO/CNTs hybrids modified SiCN ceramic nanocomposites were prepared through chemical modification of HTT 1800 with chemically bonded GO/CNTs hybrids and followed by thermolysis of the monolithic single-source-precursor green bodies at 1000ºC. Through varying the content of GO/CNTs hybrids (0.0, 2.0, 10.5 and 15.0 wt.%) in the resultant single-source-precursor, different batches of RGO/CNTs-SiCN ceramic nanocomposites were prepared. The SSP-derived nanocomposite exhibits significantly enhanced dielectric properties if compared with that of a physically-blended-precursor derived reference material or RGO-SiCN ceramic nanocomposite with same amount of fillers in the feed. Moreover, the SSP-derived

RGO/CNTs-SiCN composite containing 15.0 wt.% GO/CNTs in the feed possess an electromagnetic shielding effectiveness of 67.2 dB with a sample thickness of 2.00 mm, which is the highest value among all the reported graphene-based composites with comparable thickness.

In summary, for the investigation of CNFs modified SiCN ceramic nanocomposite, the incorporation of absorbent derivates within the ceramic microstructure allows for the following conclusions, hierarchically addressed by their importance: Firstly, PDC SiCN is a promising matrix for electromagnetic materials. Secondly, a highly homogeneous dispersion of nano scaled absorbent is of great importance for the improvement of electromagnetic properties. Thirdly, through varying the content of absorbent in the SiCN matrix, the electromagnetic property of the resulting nanocomposite can be varied from EM absorption to EM shielding.

5. Outlook

Besides the excellent electromagnetic shielding performance of the resultant SiCN-based nanocomposites, an obvious drawback of the material is its relatively poor EM absorption performance, especially for the low effective bandwidth. Accordingly, future work on these ceramic nanocomposites should focus on the improvement on the EM absorption property, especially improvement on the effective absorption bandwidth. One possible way is to increase the porosity of the ceramic nanocomposites. In this work, compared with the real part, the imaginary part increased too fast, which could lead to a relatively low tangent loss. It is reported that increasing porosity could lead to increasing real part [276]. Typically, there are two approaches to increase the porosity, namely by a) introduction of a foaming agent; b) decreasing the loading during warm pressing. Another possible way is to introduce magnetizable elements such as Fe, Co, Ni into the matrix, which will be beneficial for the improvement of permeability. Even though the absorbents (CNTs, RGO and RGO/CNTs) employed in this Ph.D thesis exhibit excellent electrical performance, they can not make any contribution for the improvement of magnetic property. Based on the equation of the reflection coefficient, permeanbility is also an important scientific criterion for the absorption performance. Introduction of magnetizable elements into the ceramic matrix can significantly improve their magnetic property [189-194].

Another challenge is that the oxidation resistance of the resultant material is insufficiant due to the poor oxidation resistance of the carbon absorbent, which would seriously limit the practical application in oxidizing environments. A temperature of higher than 400ºC leads to the oxidation of carbon in the matrix if the resultant materials are exposed in air or an oxidation environment. Decreasing the carbon content in the ceramic matrix could unavoidably lead to the decrease of electrical conductivity and EM property. Deposition of Si_3N_4 or SiC(N) on the surface of the resultant materials with CVD methods can not only change the impedance matching between the air and the resultant materials but also effectively prevent the carbon from oxidation [277, 278]. So in following studies, protective coatings should be applied on the surface of the SiCN-based nanocomposites.

The third drawback of the current materials is that to get a decent EM performance, especially for the EM shielding performance, a high content of absorbent should have to be employed. However, a high content of nanofiller could lead to a poor processibility and shapibility of the resultant material, which could inevitably lead to a decrease in the mechanical strength. It is

reported that in-situ formation of graphitic carbon in the matrix or CNTs and SiC nanowires in the pores could lead to the improvement of electrical conductivity and EM performance [62, 172, 205]. Typically, there are two approaches to induce the formation of graphite. For example, annealing of the matrix at a temperature of higher than 2000°C could lead to the crystallization of amorphous carbon. Moreover, in-situ formation of graphene in the matrix or carbon nanotubes or/and nanowires in the pores with the assistance of a catalyst (Fe, Co and Ni) is another effective way to improve the EM performance. Moreover, introduction of catalyst could also lead to the formation of CNTs or SiC nanowires. In the following work, the EM shielding performance could be improved by annealing the carbon conaining materials at high temperature and/or by introduction of transition metals such as Fe. In the current work, $ZnCl_2$ as a Lewis acid was employed as catalyst. If we replace $ZnCl_2$ by $FeCl_2$, the $FeCl_2$ can not only catalyze the reaction of the absorbent precursor in the synthesis of single-source-precursors, but can also catalyze the transformation of amorphous carbon into graphite or in-situ form carbon nanotubes or carbon nanowires in the pores.

Besides the aforementioned drawbacks, a significant highlight of this work is that carbon nanofillers from 1D CNTs to 3D RGO/CNTs hybrids were homogeneously introduced into the ceramic matrix by the single-source-precursor route. Especially for the 3D RGO/CNTs hybrids, even though 1D CNTs and 2D graphene layers can be homogeneously introduced through in-situ formation, by now the homogeneous introduction of 3D RGO/CNTs via the single-source-precursor route has been proved to be the only possibe way to the best of our knowledge. In the EM field, nanoscaled materials are typically employed as absorbent. The homogeneous dispersion of the nano absorbent in the matrix seems constantly to be an insurmountable challenge. The single-source-precursor route has been proved to be a promising way for the dispersion of nanofillers, which may find a new avenue for the preparation of highly advanced EM materials.

References

[1] A. Drossos, V. Santomaa, N. Kuster, IEEE Transactions on Microwave Theory and Techniques, 48 (2000) 1988-1995.

[2] E. Litvak, K.R. Foster, M.H. Repacholi, Bioelectromagnetics, 23 (2002) 68-82.

[3] P.S. Neelakanta. CRC press, 1995.

[4] K.L. Kaiser, Boca Raton, United States: CRC Press, (2006) 1-52.

[5] C.R. Paul, Hoboken, NJ: Wiley, 2006.

[6] A. Firstenberg, Brooklyn, NY, 1997.

[7] A.L. Galeev, Neuroscience and Behavioral Physiology, 30 (2000) 187-194.

[8] I. Belyaev, Microwave Review, 11 (2005) 13-29.

[9] H.P. Hutter, H. Moshammer, P.Wallner, M. Kundi, Occupational and Environmental Medicine, 63 (2006) 307-313.

[10] A. Balmori, Pathophysiology, 16 (2009) 191-199.

[11] H. Mosallaei, Y. Rahmat-Samii, IEEE Trans Antennas Propag, 48 (2000) 1594-1606.

[12] K.J. Vinoy, R.M. Jha, Boston, MA: Kluwer; 1996.

[13] S.P. Rea, D. Linton, E. Orr, J.M. Connell, IEE Proceedings-Microwaves, Antennas and Propagation, 153 (2006) 307-313.

[14] M. Liepe, B. Barstow, H. Padamsee, Proceedings of the 2003 Particle Accelerator Conference (PAC 2003), vol. 2, p. 1320-1322.

[15] R. Carlile, A. Cavalli, W. Cramer, R. Hyde, W. Seidler, IEEE Transactions on Antennas and Propagation, 27 (1979) 596-603.

[16] N. Li, Y. Huang, F. Du, X. He, X. Lin, H. Gao, et al., Nano Letters, 6 (2006) 1141-1145.

[17] C.M. Chang, J.C. Chiu, W.S. Jou, T.L. Wu, W.H. Cheng, IEEE Journal of Selected Topics in Quantum Electronics, 25 (1989) 1025-1031.

[18] C.L. Holloway, R.R. DeLyser, R.F. German, P. McKenna, M. Kanda, IEEE Transactions on Electromagnetic Compatibility, 39 (1997) 33-47.

[19] R.G. Sheffield, Radnor, Pennsylvania: Pam Williams, 1989.

[20] D. Micheli, A. Vricella, R. Pastore, et al., Carbon, 77 (2014) 756-774.

[21] R. Che, L.M. Peng, X.F. Duan, et al., Advanced Materials, 16 (2004) 401-405.

[22] X.F. Zhang, X.L. Dong, H. Huang, et al., Applied Physics Letters, 89 (2006) 053115.

[23] R.C. Che, C.Y. Zhi, C.Y. Liang, et al., Applied Physics Letters, 88 (2006) 033105.

[24] T. Wang, Z. Liu, M. Lu, et al. Journal of Applied Physics, 113 (2013) 024314.

[25] M.S. Cao, J. Yang, W.L. Song, et al., ACS Applied Materials & Interfaces, 4 (2012) 6949-6956.

[26] J. Liang, Y. Xu, D. Sui, et al., The Journal of Physical Chemistry C, 114 (2010) 17465-17471.

[27] G. Tong, J. Guan, Q. Zhang, Advanced Functional Materials, 23 (2013) 2406-2414.

[28] W. Zhu, L. Wang, R. Zhao, et al., Nanoscale, 3 (2011) 2862-2864.

[29] Q. Liu, Q. Cao, H. Bi, et al., Advanced Materials, 28 (2016) 486-490.

[30] B. Wen, M. Cao, M. Lu, et al., Advanced Materials, 26 (2014) 3484-3489.

[31] Z. Chen, C. Xu, C. Ma, et al., Advanced Materials, 25 (2013) 1296-1300.

[32] D.X. Yan, P.G. Ren, H. Pang, et al., Journal of Materials Chemistry, 22 (2012) 18772-18774.

[33] B. Wen, X.X. Wang, W.Q. Cao, et al., Nanoscale, 6 (2014) 5754-5761.

[34] A.P. Singh, M. Mishra, D. Hashim, et al., Carbon, 85 (2015) 79-88.

[35] J. Liu, H.B. Zhang, R. Sun, et al., Advanced Materials, 29 (2017).

[36] M. Albano, D. Micheli, G. Gradoni, et al. Acta Astronautica, 87 (2013) 30-39.

[37] F. Moglie, D. Micheli, S. Laurenzi, et al., Carbon, 50 (2012) 1972-1980.

[38] D. Ding, Y. Shi, Z. Wu, et al. Carbon, 60 (2013) 552-555.

[39] Y. Mu, W. Zhou, C. Wang, et al., Ceramics International, 40 (2014) 10037-10041.

[40] L. Chen, X. Yin, X. Fan, et al. Carbon, 95 (2015) 10-19.

[41] M.H. Al-Saleh, U. Sundararaj, Carbon, 47 (2009) 1738-1746.

[42] M.H. Al-Saleh, W.H. Saadeh, U. Sundararaj, Carbon, 60 (2013) 146-156.

[43] J. Liang, Y. Wang, Y. Huang, et al., Carbon, 47 (2009) 922-925.

[44] M.H. Al-Saleh, G.A. Gelves, U. Sundararaj, Composites Part A: Applied Science and Manufacturing, 42 (2011) 92-97.

[45] W.L. Song, M.S. Cao, M.M. Lu, et al., Carbon, 66 (2014) 67-76.

[46] B. Shen, W. Zhai, W. Zheng, Advanced Functional Materials, 24 (2014) 4542-4548.

[47] M. Verma, A.P. Singh, P. Sambyal, et al., Physical Chemistry Chemical Physics, 17 (2015) 1610-1618.

[48] Y. Zhang, Y. Huang, T. Zhang, et al., Advanced Materials, 27 (2015) 2049-2053.

[49] B. Shen, W. Zhai, M. Tao, et al., ACS Applied Materials & Interfaces, 5 (2013) 11383-11391.

[50] V. Eswaraiah, V. Sankaranarayanan, S. Ramaprabhu. Macromolecular Materials and Engineering, 296 (2011) 894-898.

[51] E. Ionescu, H.J. Kleebe, R. Riedel, Chemical Society Reviews, 41 (2012) 5032-5052.

[52] P. Colombo, G. Mera, R. Riedel, et al., Journal of the American Ceramic Society, 93 (2010) 1805-1837.

[53] R. Riedel, A. Kienzle, W. Dressler, L. Ruwisch, J. Bill, F. Aldinger, Nature, 382 (1996) 796-798.

[54] A. Saha, R. Raj, Journal of the American Ceramic Society, 90 (2007) 578-583.

[55] S. Modena, G. D. Soraru, Y. Blum, R. Raj, Journal of the American Ceramic Society, 88 (2005) 339-345.

[56] Y. Wang, W. Fei, L. An, Journal of the American Ceramic Society, 89 (2006) 1079-1082.

[57] T. Rouxel, G. D. Soraru, J. Vicens, Journal of the American Ceramic Society, 84 (2001) 1052-1058.

[58] L. An, R. Riedel, C. Konetschny, H.J. Kleebe, R. Raj, Journal of the American Ceramic Society, 81 (1998) 1349-1352.

[59] R. Riedel, L. M. Ruwisch, L. An, R. Raj, Journal of the American Ceramic Society, 81 (1998) 3341-3344.

[60] X. Fan, X. Yin, L. Chen, et al., Journal of the American Ceramic Society, 99 (2016) 1717-1724.

[61] Y. Mu, W. Zhou, Y. Hu, et al., Ceramics International, 41 (2015) 4199-4206.

[62] X.M. Liu, X.W. Yin, L. Kong, et al., Carbon, 68 (2014) 501-510.

[63] Z. Liu, G. Bai, Y. Huang, et al., Carbon, 45 (2007) 821-827.

[64] G. Wang, Z. Gao, S. Tang, et al., ACS Nano, 6 (2012) 11009-11017.

[65] Z. Liu, G. Bai, Y. Huang, et al., The Journal of Physical Chemistry C, 111 (2007) 13696-13700.

[66] Y. Wang, L.P. Huang, Y.Q. Liu, D.C. Wei, H.L. Zhang, H. Kajiura, Y.M. Li, Nano Research, 2 (2009) 865.

[67] Y. Wang, M. Jaiswal, M. Lin, S. Saha, B. Özyilmaz, K. P. Loh, ACS Nano, 6 (2012) 1018-1025 .

[68] A. Facchetti, M.H. Yoon, T.J. Marks, Advanced Materials, 17 (2005) 1705-1725.

[69] M.S. Cao, W.L. Song, Z.L. Hou, et al., Carbon, 48 (2010) 788-796.

[70] X. Luo, D.D.L. Chung, Composites Part B: Engineering, 30 (1999) 227-231.

[71] D.D.L. Chung, Carbon, 39 (2001) 279-285.

[72] N.C. Das, D. Khastgir, T.K. Chaki, et al., Composites part A: applied science and manufacturing, 31 (2000) 1069-1081.

[73] J.H. Oh, K.S. Oh, C.G. Kim, et al. Composites Part B: Engineering, 35 (2004) 49-56.

[74] N.C. Das, T.K. Chaki, D. Khastgir, et al., Advances in Polymer Technology, 20 (2001) 226-236.

[75] M.M.J. Treacy, T.W. Ebbesen, J.M.Gibson, Nature, 381 (1996) 678-680.

[76] M.F. Yu, O. Lourie, M.J. Dyer, et al., Science, 287 (2000) 637-640.

[77] M.F. Yu, B.S. Files, S. Arepalli, et al., Physical Review Letters, 84 (2000) 5552.

[78] R.H. Baughman, A.A. Zakhidov, W.A. De Heer. Science, 2002, 297(5582): 787-792.

[79] N. Li, Y. Huang, F. Du, et al. Nano letters, 6 (2006) 1141-1145.

[80] K.S. Novoselov, A.K. Geim, S.V. Morozov, et al., Science, 306 (2004) 666-669.

[81] D.X. Yan, H. Pang, B. Li, et al., Advanced Functional Materials, 25 (2015) 559-566.

[82] L. Kong, X. Yin, Y. Zhang, et al., The Journal of Physical Chemistry C, 117 (2013) 19701-19711.

[83] A.P. Singh, M. Mishra, P. Sambyal, et al., Journal of Materials Chemistry A, 2 (2014) 3581-3593.

[84] E. Ma, J. Li, N. Zhao, et al., Materials Letters, 91 (2013) 209-212.

[85] P.B. Liu, Y. Huang, X. Sun, ACS Applied Materials & Interfaces, 5 (2013) 12355-12360.

[86] Y. Wang, D. Chen, X. Yin, et al., ACS Applied Materials & Interfaces, 7 (2015) 26226-26234.

[87] P. Liu, Y. Huang, L. Wang, et al., Materials Letters, 107 (2013) 166-169.

[88] M.Q. Zhao, X.F. Liu, Q. Zhang, et al., ACS Nano, 6 (2012) 10759-10769.

[89] C. Tang, Q. Zhang, M.Q. Zhao, et al., Advanced materials, 26 (2014) 6100-6105.

[90] H.J. Peng, J.Q. Huang, M.Q. Zhao, et al. Advanced Functional Materials, 24 (2014) 2772-2781.

[91] S. Li, Y. Luo, W. Lv, et al., Advanced Energy Materials, 1 (2011) 486-490.

[92] Z. Fan, J. Yan, L. Zhi, et al., Advanced Materials, 22 (2010) 3723-3728.

[93] G. Zhu, Z. He, J. Chen, et al., Nanoscale, 6 (2014) 1079-1085.

[94] Y. Zhu, L. Li, C. Zhang, et al., Nature Communications, 3 (2012) 1225.

[95] L. Kong, X. Yin, X. Yuan, et al., Carbon, 73 (2014) 185-193.

[96] S.H. Lee, D. Kang, I.K. Oh, Carbon, 111 (2017) 248-257.

[97] X. Qi, Q. Hu, H. Cai, et al., Scientific Reports, 2016, 6.

[98] D. Yu, L. Dai, Journal of Physical Chemistry Letters, 1 (2009) 467-470.

[99] N. Jha, P. Ramesh, E. Bekyarova, et al., Advanced Energy Materials, 2 (2012) 438-444.

[100] Q. Cheng, J. Tang, J. Ma, et al., Physical Chemistry Chemical Physics, 13 (2011) 17615-17624.

[101] Y. Wang, Y. Wu, Y. Huang, et al., The Journal of Physical Chemistry C, 115 (2011) 23192-23197.

[102] N. Jung, S. Kwon, D. Lee, et al., Advanced Materials, 25 (2013) 6854-6858.

[103] H.R. Byon, S.W. Lee, S. Chen et al., Carbon, 49 (2011) 457-467.

[104] M. Beidaghi, C. Wang, Advanced Functional Materials, 22 (2012) 4501-4510.

[105] Y. Wu, T. Zhang, F. Zhang, et al., Nano Energy, 1 (2012) 820-827.

[106] J. Lin, C. Zhang, Z. Yan, et al., Nano Letters, 13 (2012) 72-78.

[107] L. An, W. Xu, S. Rajagopalan, et al., Advanced Materials, 16 (2004) 2036-2040.

[108] M. Han, X. Yin, W. Duan, et al., Journal of European Ceramic Society, 36 (2016) 2695.

[109] E.T. Thostenson, Z. Ren, T.W. Chou, Composite Science and Technology, 61 (2001) 1899-1912.

[110] Z. Yu, L. Yang, H. Min, et al., Journal of Materials Chemistry C, 2 (2014) 1057-1067.

[111] M. Hojamberdiev, R.M. Prasad, C. Fasel, et al., Journal of the European Ceramic Society, 33 (2013) 2465-2472.

[112] Q. Wen, Y. Xu, B. Xu, et al., Nanoscale, 6 (2014) 13678-13689.

[113] K. Hayashida, H. Tanaka, Advanced Functional Materials, 22 (2012) 2338-2344.

[114] K. Hayashida, Y. Matsuoka, Carbon, 85 (2015) 363-371.

[115] A.A. Eddib, D.D.L. Chung, Carbon 117 (2017) 427-436.

[116] A. Ishimaru, John Wiley & Sons, 2017.

[117] M.I.G. Mishchenko, 2016 Sci Tech Publishing Edison, NJ978-1-61353-221-8, 2017.

[118] D. Micheli, R. Pastore, C. Apollo, et al., IEEE Transactions on Microwave Theory and Techniques, 59 (2011) 2633-2646.

[119] D. Micheli, R. Pastore, C. Apollo, et al., IEEE Transactions on Microwave Theory and Techniques, 59 (2011) 2633-2646.

[120] D. Micheli, R.B. Morles, M. Marchetti, et al. Carbon, 68 (2014) 149-158.

[121] X. Yin, L. Kong, L. Zhang, et al., International Materials Reviews, 59 (2014) 326-355.

[122] L.B. Kong, Z.W. Li, L. Liu, et al., International Materials Reviews, 58 (2013) 203-259.

[123] T. Li, M. Huang, J. Yang, et al., Journal of Physics D: Applied Physics, 44 (2011) 325102.

[124] M.S. Cao, X.X. Wang, W.Q. Cao, et al., Journal of Materials Chemistry C, 3 (2015) 6589-6599.

[125] K. Lichtenecker, K. Rother, Phys. Z., 32 (1931) 255-260.

[126] S.J. Penn, N.M. Alford, A. Templeton, X. Wang, M. Xu, M. Reece, K. Schrapel, Journal of American Ceramic Society, 80 (1997) 1885-1888.

[127] F. Sharif, M. Arjmand, A.A. Moud, et al., ACS Applied Materials & Interfaces, 9 (2017) 14171-14179.

[128] C.R. Paul, John Wiley & Sons, 2006.

[129] V.P. Kodali, Institute of Electrical and Electronics Engineers, 2001.

[130] M.H. Al-Saleh, U. Sundararaj, Journal of Physics D: Applied Physics, 46 (2013) 035304.

[131] L. Kong, X.W. Yin, F. Ye, Q. Li, L.T. Zhang, L.F. Cheng, The Journal of Physical Chemistry C, 117 (2013) 2135–2146.

[132] M. Han, X. Yin, S. Ren, et al., RSC Advances, 6 (2016) 6467-6474.

[133] M. Han, X. Yin, H. Wu, et al., ACS Applied Materials & Interfaces, 8 (2016) 21011-21019.

[134] L. Kong, X. Yin, M. Han, et al., Ceramics International, 41 (2015) 4906-4915.

[135] Microwave absorber and method of manufacture: U.S. Patent 3, 185, 986[P]. 1965-5-25.

[136] S.K. Chiu, U.S. Patent 5, 155, 316. 1992-10-13.

[137] L. Liu, Y. Duan, Ma L, et al., Applied Surface Science, 257 (2010) 842-846.

[138] X.F. Zhang, X.L. Dong, H. Huang, et al., Journal of Physics D: Applied Physics, 40 (2007) 5383.

[139] B. Zhang, Y. Feng, J. Xiong, et al., IEEE Transactions on Magnetics, 42 (2006) 1778-1781.

[140] F.S Wen, F. Zhang, Z.Y Liu. The Journal of Physical Chemistry C 115 (2011) 14025-14030.

[141] G. Liu, L. Wang, G. Chen, et al., Journal of Alloys and Compounds, 514 (2012) 183-188.

[142] Z. Fan, G. Luo, Z. Zhang, et al., Materials Science and Engineering: B, 132 (2006) 85-89.

[143] N. Quiévy, P. Bollen, J.M. Thomassin, et al., IEEE Transactions on Electromagnetic Compatibility, 54 (2012) 43-51.

[144] M. Suman, E.M.K. Saini, A. Sharma, International Journal, 8 (2017).

[145] D.D.L. Chung, JMEPEG, 9 (2000) 350-354.

[146] F. Shahzad, M. Alhabeb, C.B. Hatter, et al., Science, 353 (2016) 1137-1140.

[147] P. Theilmann, D.J. Yun, P. Asbeck, S.H. Park, Organic Electronics, 14 (2013) 1531-1537.

[148] A.A. Eddib, D.D.L. Chung, Carbon, 117 (2017) 427-436.

[149] J. Liu, H.B. Zhang, R. Sun, et al., Advanced Materials, 29 (2017).

[150] A.P. Singh, B.K. Gupta, M. Mishra, et al., Carbon, 56 (2013) 86-96.

[151] J. Chen, D. Zhao, H. Ge, et al., Construction and Building Materials, 84 (2015) 66-72.

[152] B. Wang, Z. Guo, Y. Han, et al., Construction and Building Materials, 46 (2013) 98-103.

[153] D. Asok, Study of Si (Al) CN functionalized carbon nanotube composite as a high temperature thermal absorber coating material. 2013.

[154] M. Zaheer, T. Schmalz, G. Motz, et al., Chemical Society Reviews, 41 (2012) 5102-5116.

[155] R. J. P. Corriu, P. Gerbier, C. Guerin, et al., Journal of Materials Chemistry, 10 (2000) 2173-2182.

[156] D. Seyferth, H. Lang, C.A. Sobon, et al., Journal of Inorganic and Organometallic Polymers and Materials, 2 (1992) 59–77.

[157] G.R. Whittell, I. Manners, Advanced Materials, 19 (2007) 3439-3468.

[158] F.W. Ainger, J.M. Herbert, Special Ceramics, (1960) 168-168.

[159] P.G. Chantrell, P. Popper, Special Ceramics, (1965) 67-67.

[160] W. Verbeek, 1973, Ger. Pat. No. 2218960, U.S. Pat. No. 3853567.

[161] W. Verbeek, G. Winter, 1974, Ger. Pat. No. 2236078.

[162] G. Winter, W. Verbeek, M. Mansmann, 1974, Ger. Pat. No. 2243527.

[163] S. Yajima, J. Hayashi, M. Omori, Chemistry Letters, 4 (1975) 931-934.

[164] S. Yajima, J. Hayashi, M. Omori, K. Okamura, Nature, 261 (1976) 683-685.

[165] S. Yajima, K. Okamura, J. Hayashi, et al., Journal of the American Ceramic Society, 59 (1976) 324-327.

[166] R. West, L.D. David, P.I. Djurovich, et al., American Ceramic Society Bulletin, 62 (1983) 899-903.

[167] D. Seyferth, G.H. Wiseman, C. Prud'homme, Journal of the American Ceramic Society, 66 (1983) C13-C13.

[168] K.J. Wynne, R.W. Rice, Annual Review of Materials Science, 14 (1984) 297-334.

[169] J. Kaspar, M. Graczyk-Zajac, S. Lauterbach, et al., Journal of Power Sources, 269 (2014) 164-172.

[170] J. Kaspar, C. Terzioglu, E. Ionescu, et al., Advanced Functional Materials, 24 (2014) 4097-4104.

[171] M. Weinmann, J. Schuhmacher, H. Kummer, et al., Chemistry of Materials, 2000, 12, 623-632.

[172] W. Duan, X. Yin, Q. Li, et al., Journal of the European Ceramic Society, 36 (2016) 3681-3689.

[173] J. Bill, F. Aldinger, Advanced Materials, 7 (1995) 775-787.

[174] R. Riedel, G. Mera, R. Hauser, et al., Journal of the Ceramic Society of Japan, 114 (2006) 425-444.

[175] A.M. Wrobel, M. Kryszewski, M. Gazicki. Polymer, 17 (1976) 678-684.

[176] R.K. Iler, L. L. Hench, D. R. Ulrich, Science of Ceramic Chemical Processing. Wiley, New York, 1986.

[177] Transformation of organometallics into common and exotic materials: design and activation. 1988.

[178] L. L. Hench, D. R. Ulrich, Ultrastructure processing of ceramics, glasses, and composites. Wiley, 1984.

[179] O. Flores, T. Schmalz, W. Krenkel, et al., Journal of Materials Chemistry A, 1 (2013) 15406-15415.

[180] S. Yajima, American Ceramic Society Bulletin, 62 (1983) 893-903.

[181] E. Ionescu, A. Francis, R. Riedel, Journal of Materials Science, 44 (2009) 2055-2062.

[182] A. Geissinger, J. Oberle, W. Teschner, H. Boeder, and K.-H. Heussner, Ceramic

Electric Resistors; U.S. Patent 5, 961, 888, 1999.

[183] J. Cordelair, P. Greil, Journal of European Ceramic Society, 20 (2000) 1947-1957.

[184] C. Haluschka, C. Engel, R. Riedel, Journal of European Ceramic Society, 20 (2000) 1365-1374.

[185] S. Trassl, G. Motz, E. Rossler, et al., Journal of Non-crystalline Solids, 293 (2001) 261-267.

[186] S. Trassl, H. J. Kleebe, H. Stormer, et al., Journal of American Ceramic Society, 85 (2002) 1268-1274.

[187] S. Trassl, M. Puchinger, E. Rossler, et al., Journal of European Ceramic Society, 23 (2003) 781-789.

[188] T. Plachky, Z. Lences, L. Hric, et al., Journal of European Ceramic Society, 30 (2010) 759-767.

[189] A. Saha, S.R. Saha, R. Raj, et al., Journal of Materials Research, 18 (2003) 2549-2551.

[190] R. Hauser, A. Francis, R. Theismann, et al., Journal of Materials Science, 43 (2008) 4042–4049.

[191] B. Z. Tang, R. Petersen, D.A. Foucher, et al., Chemistry of Materials, (1993) 523-525.

[192] R. Petersen, D.A. Foucher, B.Z. Tang, et al., Chemistry of Materials, 7 (1995) 2045-53.

[193] M.J. MacLachlan, A.J. Lough, W.E. Geiger, et al., Organometallics, 17 (1998) 1873-1883.

[194] M.J. MacLachlan, M. Ginzburg, N. Coombs, et al., Science, 287 (2000) 1460-1463.

[195] L. Biasetto, A. Francis, P. Palade, et al., Journal of Materials Science 43 (2008) 4119-4126.

[196] Q. Li, X. Yin, W. Duan, et al., Journal of Alloys and Compounds, 565 (2013) 66-72.

[197] Z. Yu, H. Min, J. Zhan, et al., Ceramics International, 39 (2013) 3999-4007.

[198] Q. Li, X. Yin, W. Duan, et al., Journal of the European Ceramic Society, 34 (2014) 2187-2201.

[199] C. Luo, W. Duan, X. Yin, et al., The Journal of Physical Chemistry C, 120 (2016) 18721-18732.

[200] F. Ye, L. Zhang, X. Yin, et al., Journal of the European Ceramic Society, 33 (2013) 1469-1477.

[201] F. Ye, L. Zhang, X. Yin, et al., Journal of the European Ceramic Society, 34 (2014) 205-215.

[202] Y. Zhang, X. Yin, F. Ye, et al., Journal of the European Ceramic Society, 34 (2014) 1053-1061.

[203] Q. Li, X. Yin, W. Duan, et al., Journal of the European Ceramic Society, 34 (2014) 589-598.

[204] Q. Li, X. Yin, L. Feng, Ceramics International, 38 (2012) 6015-6020.

[205] W. Duan, X. Yin, Q. Li, et al., Journal of the European Ceramic Society, 34 (2014) 257-266.

[206] W. Duan, X. Yin, F. Cao, et al., Materials Letters, 159 (2015) 257-260.

[207] W. Duan, X. Yin, C. Luo, et al., Journal of the European Ceramic Society, 37 (2017) 2021-2030.

[208] W. Duan, X. Yin, F. Ye, et al., Journal of Materials Chemistry C, 4 (2016) 5962-5969.

[209] W. Zhao, G. Shao, M. Jiang, et al., *Journal of the European Ceramic Society*, *37* (2017), 3973-3980.

[210] M. Zaheer, G. Motz, R. Kempe, Journal of Materials Chemistry, 21 (2011) 18825-18831.

[211] M. Hamon, J. Chen, H. Hu, et al., Advanced Materials, 11 (1999) 834-840.

[212] W. Huang, Y. Lin, S. Taylor, et al., Nano Letters, 2 (2002) 231-234.

[213] W. Huang, S. Taylor, K. Fu, et al., Nano Letters, 2 (2002) 311-314.

[214] F. Pompeo, D. Resasco, Nano Letters, 2 (2002) 369-373.

[215] D. Bezier, S. Park, M. Brookhart, Organic Letters, 15 (2013) 496-499.

[216] S. Guo, S. Dong, Advanced Materials, 22 (2010)1269-1272.

[217] H. Yang, B. Li, Y. Cui, Synthetic Communications, 28 (1998)1233-1238.

[218] G. Liu, Synlett, 9 (2006)1431-1433.

[219] J. Zou, L. Liu, H. Chen, et al., Advanced Materials, 20 (2008) 2055-2060.

[220] X. Kong, X. Sun, X. Li, et al., Chemical Physics, 82 (2003) 997-1001.

[221] M. Huang, Y. Wu, H. Feick, et al., Advanced Materials, 13 (2001) 113-116.

[222] J. Qian, C. Pantea, G. Voronin, et al., Journal of Applied Physics 90 (2001) 1632-1637.

[223] Z. Zhu, Y. Lu, D. Qiao, et al., Journal of the American Chemical Society, 127 (2005) 15698-15699.

[224] C. Vakifahmetoglu, E. Pippel, J. Woltersdorf, et al., Journal of the American Ceramic Society, 93 (2010) 959-968.

[225] Vakifahmetoglu C, Colombo P, Carturan S, et al., Journal of the American Ceramic Society, 93 (2010) 3709-3719.

[226] K. Hayashida, H. Tanaka, Advanced Functional Materials, 22 (2012) 2338-2344.

[227] M. Han, X. Yin, L. Kong, et al., Journal of Materials Chemistry A, 2 (2014) 16403-16409.

[228] L. Kong, X. Yin, Q. Li, et al., Journal of the American Ceramic Society, 96 (2013) 2211-2217.

[229] J. Liu, R. Che, H. Chen, et al., Small, 8 (2012) 1214-1221.

[230] D. Micheli, C. Apollo, R. Pastore, et al., Composites Science and Technology, 70 (2010) 400-409.

[231] D. Micheli, A. Vricella, R. Pastore, et al., Carbon, 77 (2014) 756-774.

[232] D. Micheli, C. Apollo, R. Pastore, et al., Composites Science and Technology 70 (2010) 400-409.

[233] J. Liu, J. Xu, R. Che, et al., European Journal of Medicinal Chemistry, 19 (2013) 6746-6752.

[234] H.A. Becerril, J. Mao, Z. Liu, et al., ACS Nano, 2 (2008) 463-470.

[235] S. Park, R.S. Ruoff, Nature Nanotechnology, 4 (2009) 217–224.

[236] Y. Zhu, M.D. Stoller, W. Cai, et al., ACS Nano, 4 (2010) 1227-1233.

[237] P. Colombo, R. Riedel, G. D. Soraru, et al., DE Stech Publications, Inc, 2010.

[238] Y. Gao, G. Mera, H. Nguyen, et al., Journal of the European Ceramic Society , 32 (2012) 1857-1866.

[239] G. Mera, A. Navrotsky, S. Sen, et al., Journal of Materials Chemistry A, 1 (2013) 3826-3836.

[240] X. F. Wang, G. Mera, K. Morita, et al., Journal of the Ceramic Society of Japan, 124 (2016) 981-988.

[241] B. Mi, Science, 343 (2014) 740-742.

[242] S.H. Aboutalebi, M.M. Gudarzi, Q.B. Zheng, et al., Advanced Functional Materials, 21 (2011) 2978-2988.

[243] X. Liu, X. Yin, G. Zheng, et al., Ceramics International, 40 (2014) 531-540.

[244] Y. Liu, X.W. Yin, L. Kong, et al., Carbon, 64 (2013) 541–544.

[245] X.Y. Yuan, L.F. Cheng, L. Kong, et al., Journal of Alloys and Compounds, 596 (2014) 132–139.

[246] P. Theilmann, D.J. Yun, P. Asbeck, S.H. Park, Organic Electronics, 14 (2013) 1531-1537.

[247] K. Hayashida, Y. Matsuoka, Carbon, 85 (2015) 363-371.

[248] D. Micheli, C. Apollo, R. Pastore, et al., Acta Astronautica , 69 (2011) 747-757.

[249] D. Micheli, R. Pastore, G. Gradoni, et al., Acta Astronautica , 88 (2013) 61-73.

[250] J. Chen, M.A. Hamon, H. Hu, et al., Science, 282 (1998) 95-98.

[251] E.V. Basiuk, E.V. Basiuk, J.G. Banuelos, et al., Journal of Materials Chemistry B, 106 (2002) 1588-1597.

[252] J. Chen, A.M. Rao, S. Lyuksyutov, et al., Journal of Materials Chemistry B, 105 (2001) 2525-2528.

[253] S. Niyogi, E. Bekyarova, M.E. Itkis, et al., Journal of the American Chemical Society, 128 (2006) 7720-7721.

[254] M. Zaheer, G. Motz, R. Kempe, Journal of Materials Chemistry, 21 (2011) 18825-18831.

[255] H.R. Yang, B.N. Li, Y.D. Cui, Synthetic Communications, 28 (1998) 1233-1238.

[256] S. Stankovich, D.A. Dikin, G.H. Dommett, et al., Nature, 442 (2006) 282-286.

[257] Z.P. Chen, W.C. Ren, L.B. Gao, et al., Nature Materials, 10 (2011) 424-428.

[258] E. Minoux, O. Groening, K.B. Teo, et al., Nano Letters, 5 (2005) 2135-2138.

[259] X. Wang, L. Zhi, K. Müllen, Nano Letters, 8 (2008) 323-327.

[260] M. Arjmand, M. Mahmoodi, G.A. Gelves, et al., Carbon, 49 (2011) 3430-3440.

[261] J. Ling, W. Zhai, W. Feng, et al., ACS Applied Materials & Interface, 5 (2013) 2677-2684.

[262] B.H. Yuan, C.L. Bao, X.D. Qian, et al., Carbon, 75 (2014) 178-189.

[263] S.T. Hsiao, C.C. Ma, W.H. Liao, et al., ACS Applied Materials & Interface, 6 (2014) 10667-10678.

[264] J.J. Liang, Y. Wang, Y. Huang, et al., Carbon, 47 (2009) 922-925.

[265] Z.H. Zeng, H. Jin, M.J. Chen, et al., Advanced Functional Materials, 26 (2016) 303-310.

[266] B.Q. Yuan, L.M. Yu, L.M. Sheng, et al., Journal of Physics D: Applied Physics, 45 (2012) 235108.

[267] F. Shahzad, S. Yu, P. Kumar, et al., Composite Structures, 133 (2015) 1267-1275.

[268] B.B. Rao, P. Yadav, R. Aepuru, et al., Physical Chemistry Chemical Physics, 17 (2015) 18353-18363.

[269] K. Singh, A. Ohlan, V.H. Pham, R. et al., Nanoscale, 5 (2013) 2411-2420.

[270] A.P. Singh, P. Garg, F. Alam, et al., Carbon, 50 (2012) 3868-3875.

[271] K. Yao, J. Gong, N.N. Tian, et al., RSC Advances, 5 (2015) 31910-31919.

[272] T.K. Gupta, B.P. Singh, V.N. Singh, et al., Journal of Materials Chemistry A, 2 (2014) 4256-4263.

[273] W.L. Song, X.T. Guan, L.Z. Fan, et al., Journal of Materials Chemistry A, 3 (2015) 2097-2107.

[274] M. Mishra, A.P. Singh, B. Singh, et al., Journal of Materials Chemistry A, 2 (2014) 13159-13168.

[275] Y.C. Qing, Q.L. Wen, F. Luo, et al., Journal of Materials Chemistry C, 4 (2016) 371-375.

[276] S.J. Penn, N.M.N. Alford, A. Templeton, et al. Journal of the American Ceramic Society, 80(1997) 1885-1888.

[277] X. Li, L. Zhang, X. Yin, Journal of the American Ceramic Society, 95 (2012) 1038-1041.

[278] X. Li, X. Yin, L. Zhang, et al., International Journal of Applied Ceramic Technology, 8(2011) 627-636.

Publications

[1] Liu X, Yu Z, Chen L, et al. Role of single-source-precursor structure on microstructure and electromagnetic properties of CNTs-SiCN nanocomposites. **Journal of the American Ceramic Society,** 100 (2017) 4649-4660.

[2] Liu X, Yu Z, Ishikawa R, et al. Single-source-precursor synthesis and electromagnetic properties of novel RGO–SiCN ceramic nanocomposites. **Journal of Materials Chemistry C**, 5 (2017) 7950-7960.

[3] Liu X, Yu Z, Ishikawa R, et al. Single-source-precursor derived RGO/CNTs-SiCN ceramic nanocomposite with ultra-high electromagnetic shielding effectiveness. **Acta Materi**alia, 130 (2017) 83-93.

[4] Liu X, Yin X, Kong L, et al. Fabrication and electromagnetic interference shielding effectiveness of carbon nanotube reinforced carbon fiber/pyrolytic carbon composites. **Carbon**, 68 (2014) 501-510.

[5] Liu X, Yin X, Zheng G, et al. In-situ formation of carbon nanotubes in pyrolytic carbon–silicon nitride composite ceramics. **Ceramics International**, 40 (2014) 531-540.

[6] Zheng G, Yin X, Liu S, Liu X, et al. Improved electromagnetic absorbing properties of Si_3N_4–SiC/SiO_2 composite ceramics with multi-shell microstructure. **Journal of the European Ceramic Society**, 33 (2013) 2173-2180.

[7] Liu Y, Yin X, Kong L, Liu X, et al. Electromagnetic properties of SiO_2 reinforced with both multi-wall carbon nanotubes and ZnO particles. **Carbon**, 64 (2013) 541-544.

[8] Duan W, Yin X, Li Q, Liu X, et al. Synthesis and microwave absorption properties of SiC nanowires reinforced SiOC ceramic. **Journal of the European Ceramic Society**, 34 (2014) 257-266.

[9] Kong L, Yin X, Yuan X, Zhang Y, Liu X, et al. Electromagnetic wave absorption properties of graphene modified with carbon nanotube/poly (dimethyl siloxane) composites. **Carbon**, 73 (2014) 185-193.

[10] Li Q, Yin X, Duan W, Hao B, Kong L, Liu X, et al. Improved dielectric and electromagnetic interference shielding properties of ferrocene-modified polycarbosilane derived SiC/C composite ceramics. **Journal of the European Ceramic Society**, 34 (2014) 2187-2201.

[11] Liu X, Chai N, et al. Flexible, lightweight and high efficient 3D CNTs/Ti_3C_2-sodium alginate foam for electromagnetic absorption application. Submitted to **Journal of Materials Science & Technology**.

[12] Liu X, Yu Z, et al. Fabrication and electromagnetic interference shielding of the reduced graphene oxide and SiC nanowires modified SiCN. **Under preparation**.

Received: 10 February 2017 | Accepted: 24 May 2017

DOI: 10.1111/jace.15000

ORIGINAL ARTICLE

Journal of the American Ceramic Society

Role of single-source-precursor structure on microstructure and electromagnetic properties of CNTs-SiCN nanocomposites

Xingmin Liu[1] | Zhaoju Yu[2,3] | Lingqi Chen[4] | Binbin Xu[5] | Shuang Li[2,3] | Xiaowei Yin[4] | Ralf Riedel[1,3,4]

[1]Institut für Materialwissenschaft, Technische Universität Darmstadt, Darmstadt, Germany

[2]College of Materials, Key Laboratory of High Performance Ceramic Fibers (Xiamen University), Ministry of Education, Xiamen, China

[3]College of Materials, Fujian Key Laboratory of Advanced Materials (Xiamen University), Xiamen, China

[4]Science and Technology on Thermostructural Composite Materials Laboratory, Northwestern Polytechnical University, Xi'an, China

[5]College of Chemistry & Chemical Engineering, Xiamen University, Xiamen, China

Correspondence
Zhaoju Yu, College of Materials, Key Laboratory of High Performance Ceramic Fibers (Xiamen University), Ministry of Education, Xiamen, China.
Email: zhaojuyu@xmu.edu.cn

Funding information
Natural Science Foundation of China, Grant/Award Number: 50802079; Natural Science Foundation of Fujian Province of China, Grant/Award Number: 2015J01221; Creative Research Foundation of Science and Technology on Thermostructural Composite Materials Laboratory, Grant/Award Number: 6142911040114; China Scholarship Council, Grant/Award Number: 201406290019

Abstract

Novel single-source-precursors (SSPs), namely carbon nanotube modified poly (methylvinyl) silazane (CNTs-HTT 1800), were synthesized via amidation reaction of poly (methylvinyl) silazane (HTT 1800) with carboxylic acid functionalized carbon nanotubes (CNTs-COOH) at the assistance of $ZnCl_2$ catalyst, which was confirmed by means of Fourier transform infrared spectra (FT IR) and transmission electron microscopy (TEM). Besides, the TEM results unambiguously show the homogeneous distribution of the CNTs in the matrix of SSPs while serious aggregation of the CNTs in the matrix of physically-blended-precursor. Crack-free monolithic silicon carbonitride modified by carbon nanotubes ceramic nanocomposites (CNTs-SiCN) were prepared through pyrolysis of the obtained SSP green bodies at 1000°C. Due to the strong influence of polymer structure on the microstructure of final ceramics, the SSP-derived CNTs-SiCN nanocomposites clearly show the homogeneous distribution of the CNTs in the SiCN matrix while the physically-blended-precursor derived CNTs-SiCN nanocomposites exhibit serious aggregation and entangling of the CNTs in the SiCN matrix. With the same CNT content in the feed, the SSP-derived CNTs-SiCN nanocomposites possess significant improvements of electromagnetic (EM) absorbing properties compared to those from physically-blended-precursors, due to the quality of the dispersion of CNTs in the ceramic matrices.

KEYWORDS

CNTs, Single-source-precursor, Ceramic nanocomposites, Dielectric properties, Electromagnetic properties

1 | INTRODUCTION

High-efficiency and light weight are two key factors that drive practical applications of electromagnetic (EM) waves attenuation materials.[1,2] Beside these two factors, the materials possessing high thermal stability, good oxidation resistance and bearing high mechanical load are becoming increasingly attractive in some applications including in aircrafts and spacecraft,[3] where the polymer, carbon foam and carbon film based EM materials lose their superiority.[2,4-8]

Polymer derived ceramics (PDCs), owning to their excellent physical-chemical and functional properties as well as their flexible processability, have found wide applications in the fields of information technology, transport, defense, energy as well as environmental systems, biomedical components and micro- or nanoelectromechanical systems.[9-12] Recently, PDCs exhibit their excellent potential as EM materials due to their tailorable permittivity and electrical conductivity, facile moldability, and microstructure tailoring at the molecular level.[13-20] Basically, the following dielectric properties are required for the EM applications: The real part of permittivity (ε') and imaginary part of permittivity (ε'') should amount 5~20 and 1~10, respectively for the use as EM absorbing material and >20 and >10, respectively for EM shielding material.[1] However, the intrinsic low electrical conductivity and permittivity of PDCs are far inferior to the required level for practical application.[1] As reported, the PDCs-SiBCN pyrolyzed at 900°C possess a permittivity of 2.75 (ε') and 0.03 (ε''), whose imaginary part is more than 2 orders of magnitudes lower than the required values in practical application.[18] Though the PDCs-SiOC annealed at 900°C show a higher permittivity of 3.63 (ε') and 0.14 (ε''), it is still too low to be used as EM materials.[14]

Carbon nanotubes (CNTs), owning to their intrinsic advantages including excellent electrical conductivity (>10^6 S/m) and high aspect ratio (>1000), have been widely used as microwave absorbent in different matrix since their emergence.[7,18,21–23] Incorporation of CNTs into PDC matrix has been proven to be an effective way to improve their permittivity.[18] However, as an absorbent the effective utilization of CNTs in composites depends strongly on their dispersed state since agglomeration of CNTs can lead to an inferior polarization relaxation and electrical conductivity.[18] However, due to the high aspect ratio and strong Van der Waals interactions of CNTs, poor compatibility between the CNTs and precursors and poor efficiency of currently used dispersing approach, homogeneous dispersion of incorporated CNTs inside the ceramic is still a great challenge.[18,24,25] Yajun Zhang et al. incorporated multi-walled CNTs into the polyborosilazane (SiBCN precursor) with mechanical force dispersing approach.[18] However, due to the poor compatibility and wettability between the hydrophobic CNTs and viscous preceramic polymers, serious tangling is always unavoidable during the cross-linking and shaping process when the mechanical dispersion forces were removed. Linan An et al. introduced chemical functionalized CNTs into SiCN precursors through functionalization of CNTs with high concentration HNO_3 (60 wt%).[26] The dispersion of functionalized CNTs depends strongly on their functionalization degree and content of functional groups attached to the nanotubes.[27] However, an exceeding functionalization would inevitably seriously disrupt the long range π conjugation of the CNTs, which can lead to decreased electrical conductivity, diminished mechanical strength, and other undesired properties.[27] Moreover, although it is much more effective than physical blending, the dispersion of CNTs was still not satisfying.[27] In this circumstance, to make the best utilization of CNTs as a microwave absorbent inside the ceramic matrix and to fabricate a highly efficient EM material containing a low CNT content, facile and effective dispersing approach should be developed.

In this work, novel single-source-precursors (SSPs), namely CNT modified poly (methylvinyl) silazane (CNTs-HTT 1800), were synthesized via amidation reaction of poly(methylvinyl)silazane (HTT 1800) with carboxylic acid functionalized carbon nanotubes (CNTs-COOH) at the assistance of $ZnCl_2$ catalyst, in order to avoid aggregation of the CNTs in the final ceramic matrix. After pyrolysis of the as-synthesized CNTs-HTT 1800, monolithic CNTs modified SiCN (CNTs-SiCN) nanocomposites were fabricated. The microstructure of the obtained CNTs-SiCN are characterized as homogeneous distribution of CNTs in SiCN matrix, which avoids the serious aggregation and entangling of CNTs by traditional physical blending method. The influence of polymer structure on microstructure evolution and EM absorbing properties of the resultant CNTs-SiCN nanocomposites was investigated in detail.

2 | EXPERIMENTAL PROCEDURE

2.1 | Materials synthesis

The carboxylic functionalized multi-walled carbon nanotubes (MWCNTs-COOH) (Outer Diameter: 20~30 nm, Length: 10~30 μm, Special Surface Area >110 m^2/g, Electrical conductivity>100 s/m, -COOH content: 1.23 wt%, Xianfeng Nano, China) were dispersed into N, N-Dimethylformamide (DMF) (Sigma-Aldrich, Munich, Germany) with a weight ratio of 1:100 in a flask. After ultra-sonication of the obtained mixture for 4 hours, $ZnCl_2$ catalyst and poly (methylvinyl)silazane HTT 1800 (KiON Specialty Polymers) with a weight ratio of 2:98 was added. Then the reaction mixture was heated up to 70°C for 72 hours under argon flow with magnetic stirring. Subsequently, the as-synthesized SSPs were cross-linked at 120°C for 4 hours. After the evaporation of the DMF, black solid powders were isolated. After ball milling for 3 hours under the protection of Ar atmosphere, the SSP powders were warm-pressed into green bodies with a three dimensions of $50.0\times40.0\times3.0$ mm^3 under a pressure of 60 KN while maintaining the temperature at 245°C for 2 hours. The green bodies were pyrolyzed under Ar atmosphere at 1000°C under the heating program shown in Figure 1. and machined into samples with dimensions of

$22.86 \times 10.16 \times 2.00$ mm^3 with wire cutting. The synthesis procedure of monolithic CNTs-SiCN nanocomposites is shown in Figure 2.

To investigate the influence of CNT content on the EM properties of final ceramic composites, a series of CNTs-SiCN nanocomposites with different CNT content in the feed were prepared (as shown in Table 1). With 2.5 wt%, 4.5 wt% and 8.0 wt% CNTs in the feed and with $ZnCl_2$ as catalyst, the obtained SSPs were nominated as HTT 1800-2.5, HTT 1800-4.5a and HTT 1800-8.0, respectively. To make a comparison with the SSP, a control test containing 4.5 wt% CNTs without catalyst was performed under the same condition and the resultant physically-blended-precursor was denoted as HTT 1800-4.5b. After pyrolysis of preceramic precursors HTT 1800, HTT 1800-2.5, HTT 1800-4.5a, HTT 1800-4.5b and HTT 1800-8.0 under the same condition, the resultant CNTs-SiCN samples were denoted as S-0.0, S-2.5, S-4.5a, S-4.5b and S-8.0, respectively.

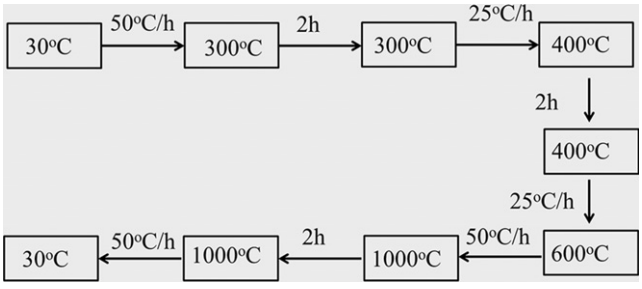

FIGURE 1 Schematic illustration of heating program

2.2 | Characterization methods

Fourier transform infrared (FT IR) spectra were collected using a Bruker Vertex 70 FT IR instrument (Bruker, Billerica, MA) in attenuated total reflectance geometry. X-ray diffraction (XRD) was employed to conduct phase analysis (X'Pert Pro; Philips, Netherlands). Raman spectra were recorded from 100 to 4000 cm^{-1} employing a micro-Raman HR8000 spectrometer (Horiba Jobin Yvon, Bensheim, Germany) using a laser wavelength of 514.5 nm. The microstructure of the samples was observed by scanning electron microscopy (SEM; S-4799, Hitachi, Tokyo, Japan). TEM studies were conducted on ground powder samples using a JEM-2100 microscope (JEOL Ltd., Tokyo, Japan) at an acceleration voltage of 200 kV (wavelength l52.51 pm). The density and open porosity of final ceramics were measured using Archimedes method. The values of scattering parameters (S-parameters; S11, S12, S21 and S22) of the as-prepared samples with dimensions of $22.86 \times 10.16 \times 2.00$ mm^3 were measured by waveguide method using a vector network analyzer (VNA, MS4644A; Anritsu, Japan) from 8.2 to 12.4 GHz (X-band). To diminish the influence of the air-gap, at least three samples for

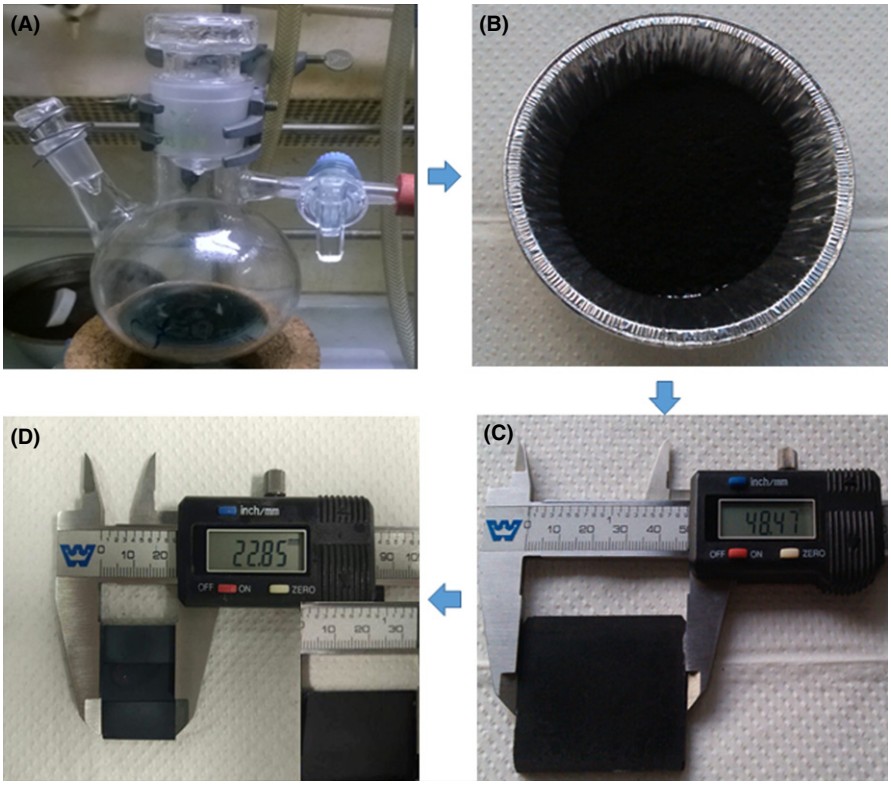

FIGURE 2 (A) As-synthesized single-source-precursor in DMF, (B) single-source-precursor powders after removal of DMF, (C) green body of single-source-precursor after warm-pressing at 245°C and (D) CNTs-SiCN ceramic sample after machining by wire cutting (insert shows the monolithic CNTs-SiCN ceramic after pyrolysis at 1000°C) [Color figure can be viewed at wileyonlinelibrary.com]

each CNT content were prepared, and the measured values of S-parameters were compared to confirm that the errors caused by sample measurement are less than 3%.

3 | RESULTS AND DISCUSSION

3.1 | Single-source-precursor characterization

In this study, a series of preceramic precursors were synthesized by adjusting the CNT content in feed. The CNT contents are 0.0 wt%, 2.5 wt%, 4.5 wt% and 8.0 wt%, and the resultant polymers are abbreviated as HTT 1800-0.0, HTT 1800-2.5, HTT 1800-4.5a, HTT 1800-4.5b (physically-blended-precursor), and HTT 1800-8.0, respectively. The FT IR spectra of the SSPs and physically-blended-precursor crossed-linked at 120°C were measured and the results are shown in Figure 3. In the FT IR spectrum of HTT 1800-0.0, typical absorption bands related to C–H (2960 and 2965 cm^{-1}), Si–N–H (1160 cm^{-1}), and Si–N (930 cm^{-1}) groups were observed.[28,29] With the spectra of the SSPs, additional absorption bands at ν=1332 cm^{-1} (amide C–N), ν=1646 cm^{-1} (amide C=O), ν=1590 cm^{-1} (amide C–N) appeared, due to the formed amide groups derived from the amidation reaction between -COOH groups of CNTs and -N-H groups of HTT 1800.[30–34] However, for the spectrum of HTT 1800-4.5b prepared by physical blending without catalyst, no absorption bands from amide groups were found, indicating that the amidation reaction did not take place in the absence of $ZnCl_2$ catalyst.[35,36] Based on the literatures that the esterification and dehydrogenative coupling reactions can be effectively catalyzed by Lewis acid such as $FeCl_3$ and $ZnCl_2$,[37,38] we propose a possible reaction mechanism for the present amidation reaction. Accordingly, the $ZnCl_2$ serves as a Lewis acid catalyst and activates the carboxylic group by the coordination of the Zn atom at the O atom of the C=O group. Then, the -NH groups of polysilazane reacts with the activated carboxylic C by a nucleophilic attack.

TABLE 1 Content of catalyst and CNTs in the feed

Ceramics	Precursors	CNT content (wt%)	$ZnCl_2$ content (wt%)
S-0.0	HTT 1800-0.0	0.0	0.0
S-2.5	HTT 1800-1.0	1.0	2.0
S-4.5b[a]	HTT 1800-4.5b	4.5	0.0
S-4.5a	HTT 1800-4.5a	4.5	2.0
S-8.0	HTT 1800-8.0	8.0	2.0

[a]S-4.5b was obtained by pyrolysis of physically blended CNTs/HTT 1800 mixture.

To observe the morphology of CNTs before and after reaction with HTT 1800, TEM observation was employed and the results are shown in Figure 4. Figure 4A-B are the TEM images of original CNTs-COOH. The diameter of CNTs is about 15~30 nm. From the high-resolution TEM image (Figure 4B), we can clearly observe that the number of CNT walls in this area is about 10~15 and the outside walls of carbon backbones were seriously disrupted (white arrows) due to the attachment of -COOH groups.[27] Figure 4C is the low resolution TEM image of SSP, which shows that the CNTs were separated by the hosting HTT 1800 matrix. To make a comparison, for the physically blended CNTs/HTT 1800 sample, the serious agglomeration and entangling of CNTs did occur inside the HTT 1800 matrix (Figure 4E). From the high-resolution TEM image of SSP (Figure 4D), an amorphous film with a thickness of ~3 nm was found to attach on the surface of

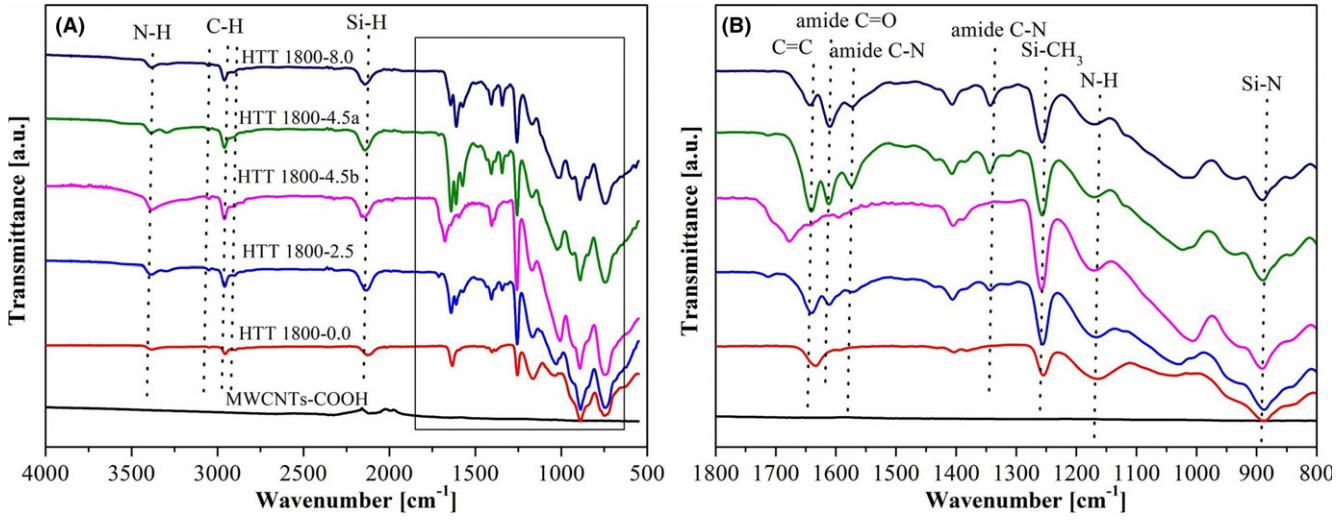

FIGURE 3 (A) FT IR spectra of physically-blended-precursor, MWCNTs-COOH and single-source-precursors with different CNT content in the feed, and the region from 800 to 1800 cm^{-1} is shown magnified in (B) [Color figure can be viewed at wileyonlinelibrary.com]

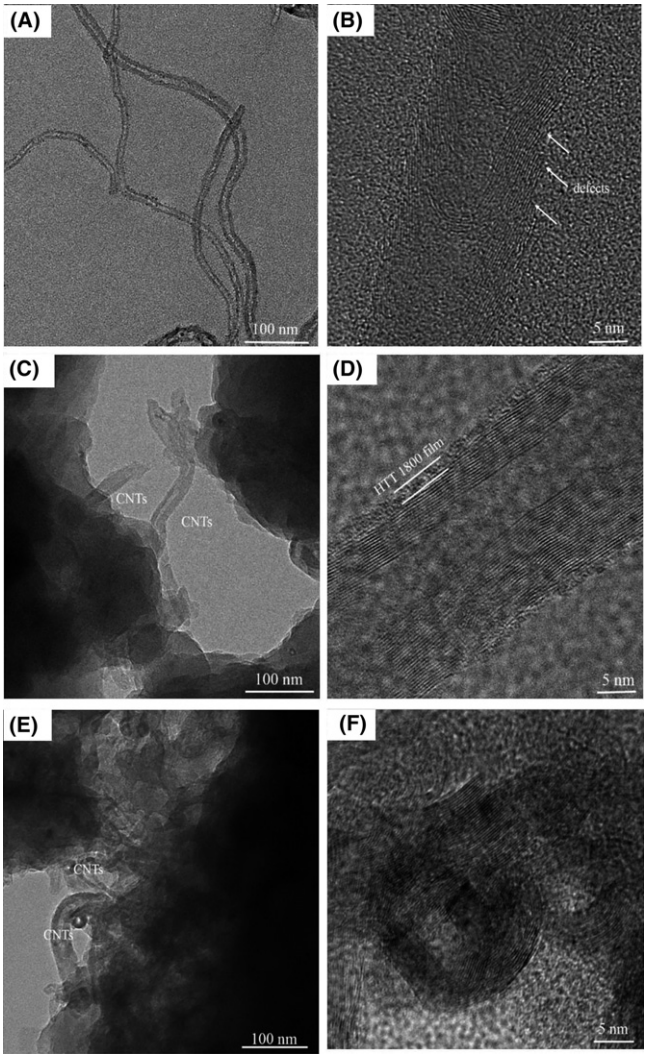

FIGURE 4 Low resolution TEM images of (A) original CNTs, (C) single-source-precursor, (E) physically-blended-precursor, and high-resolution TEM images of (B) original CNTs, (D) single-source-precursor, (F) physically-blended-precursor

CNTs. However, the high-resolution TEM image of physically-blended-precursor unambiguously shows that, no amorphous film was attached on the surface of CNTs (Figure 4F), which is consistent with the reported literature that during the functionalization of CNTs, the amorphous carbon layer of CNTs was removed by the strong attack of HNO_3 before the attachment of -COOH groups on the graphite layers.[26] Based on the findings shown in Figure 4D, F, we assume that the amorphous film on the surface of CNTs is due to HTT 1800 polymers attached on the CNTs after amidation reaction.

Therefore, the TEM results are consistent with the FT IR results, which further confirm the successful formation of SSPs. Based on the FT IR and TEM results, Figure 5 shows the chemical reaction between the CNTs-COOH and the HTT 1800.

3.2 | Microstructure characterization

Figure 6A shows the XRD patterns of HTT 1800-derived SiCN and CNTs-SiCN ceramic nanocomposites. The pristine SiCN shows a complete amorphous feature which agrees well with the previous reports.[9] As for the CNTs-SiCN ceramic nanocomposites, only a weak characteristic peak of C (0 0 2) plane from graphitic carbon at 2θ of 26.5 is observed. Though $ZnCl_2$ was used as catalyst of chemical synthesis, no signal from Zn was finally found in the XRD pattern. As reported, at the temperature of 1000°C, the $ZnCl_2$ catalyst can be reduced into gaseous Zn by carbon (CNTs) or CO and H_2 released by the decomposition of precursors and evaporates out of the ceramic nanocomposites.[39,40] Figure 6B shows the Raman spectra of pristine SiCN and CNTs-SiCN samples, indicating the presence of both disorder-induced (D) and graphite-like (G) bands. The graphitization grade (G_G) of a carbon-based material can be calculated as follows: $I_G/(I_G+I_D)\times 100\%$, where I_G and I_D represent the intensity of G and D-bands, respectively.[41,42] The graphitization grade of resultant CNTs-SiCN (sample S-4.5a) with 4.5 wt% CNT content in the feed amounts

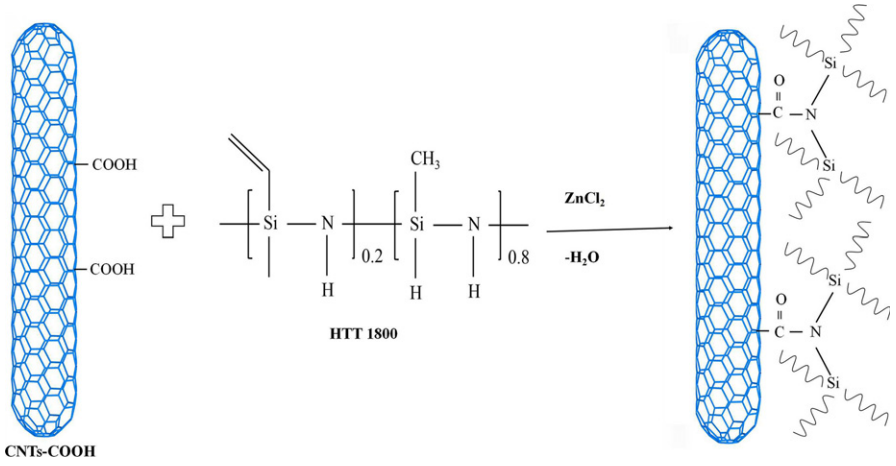

FIGURE 5 Reaction between CNT-COOH and HTT 1800 to synthesize single-source-precursors [Color figure can be viewed at wileyonlinelibrary.com]

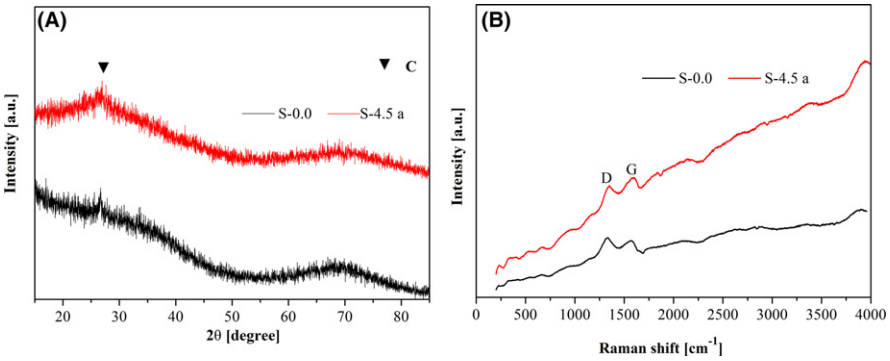

FIGURE 6 (A) XRD patterns and (B) Raman spectra of pristine SiCN (sample S-0.0) and CNTs-SiCN nanocomposites (sample S-4.5a) [Color figure can be viewed at wileyonlinelibrary.com]

51.6%, higher than that of pristine SiCN (46.7%), due to the introduction of CNTs into the SiCN matrix.

As shown in Figure 2, the obtained monolithic CNTs-SiCN ceramic sample shows a totally crack free morphology though it suffered from ca. 30% linear and ca. 50% volume shrinkage. With the CNT content increasing from 2.5 wt% to 8.0 wt% in the feed, the open porosity of resultant CNTs-SiCN composites increased from 4.22% to 4.53% while the density of final ceramic samples decreased from 2.10 g/cm^3 to 2.02 g/cm^3. To further investigate morphology of ceramic samples, the fracture surface of monolithic CNTs-SiCN ceramics derived from SSP and physically-blended-precursor was observed with SEM. In general, representative SEM images reveal relatively dense microstructure and no obvious pores were found on the fracture surface. For the SSP-derived sample S-4.5a exhibits uniform distribution of CNT tips in the ceramic matrix (Figure 7A, D). To make a comparison, in the case of the physically-blended-precursor derived ceramic sample S-4.5b, Figure 7B (low magnification) and Figure 7E (high magnification) images both show serious aggregation and entangling of CNTs in the ceramic matrix. Despite

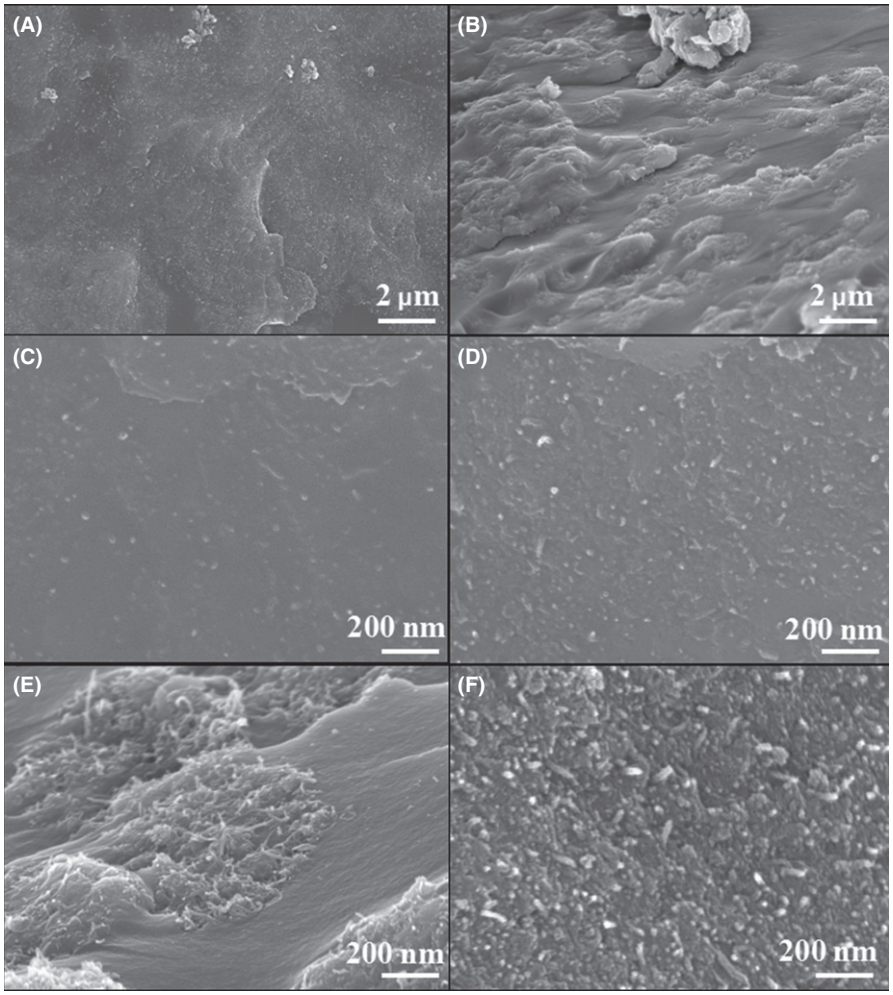

FIGURE 7 Low magnification SEM images of (A) S-4.5a and (B) S-4.5b and high magnification SEM images of (C) S-2.5, (D) S-4.5a, (E) S-4.5b and (F) S-8.0

increasing amount of CNTs in the feed from 2.5 wt% (S-2.5) to 8.0 wt% (S-8.0), no obvious agglomeration of the carbon nanofillers in the ceramic matrix was found (as shown in Figure 7C, D, F), which further confirms that the CNTs are homogeneously distributed in the SiCN matrix. The SEM results show significant difference in the morphology of the SSP and physically-blended-precursor derived ceramics.

Figure 8 shows the TEM images of CNTs-SiCN ceramic nanocomposites derived from SSP and physically-blended-precursor. After pyrolysis of SSP at 1000°C, each individual CNT is well separated by the SiCN matrix, which means the agglomeration of CNTs is effectively prevented (as shown in Figure 8A). However, for the physically-blended-precursor derived sample (Figure 8C), serious agglomeration and entangling of CNTs was observed. Figure 8B, D are the high-resolution TEM images of CNTs-SiCN ceramics. Regardless of dispersing approach, the seriously disrupted carbon backbones of CNTs-COOH (shown in Figure 4B) were found to get recovered after the pyrolysis (Figure 8B, D), resulting from the self-catalytic behavior of CNTs.[43] As reported,[43] defected carbon nanotubes themselves can absorb and install free C_n species at their opening edges or sidewalls and thus to grow axially and "fat" radially. The structural defects on the tube walls can serve as proper sites for the nucleation and development of new graphene layers. During the polymer-to-ceramic conversion, gaseous by-products including CH_4, CO and other hydrocarbon gases (C_n) evaporated out of precursor.[14,44,45] When the gaseous hydrocarbon evaporating out of precursor passed over the CNTs, they were decomposed and installed on the defected CNTs.[43] The recovery of carbon backbones can lead to the improvement of electrical conductivity,[27] which is expected to improve the utilization of CNTs in this work.

Based on the FT IR results (Figure 3) and TEM observation (Figure 4 and 8), Figure 9 shows microstructural evolution of CNTs-SiCN nanocomposites derived from SSP and single-source-precursor, respectively. Due to the strong Van der Waals interactions between each individual CNT and poor compatibility and wettability between the CNTs and HTT 1800, the CNTs exhibit serious agglomeration in the matrix of physically-blended-precursor (Figure 9A),[27,46] directly leading to the inhomogeneous distribution of CNTs in the SiCN matrix after polymer-to-ceramic transformation (Figure 9C). However, Figure 9B illustrates that agglomeration of CNTs was avoided, instead, a homogeneous dispersion of CNTs were successfully achieved throughout the polymer matrix, which may be due to that (i) the attachment of precursor film effectively changed the compatibility and wettability between the CNTs and hosting HTT 1800 and imparted CNTs solubility and (ii) the HTT

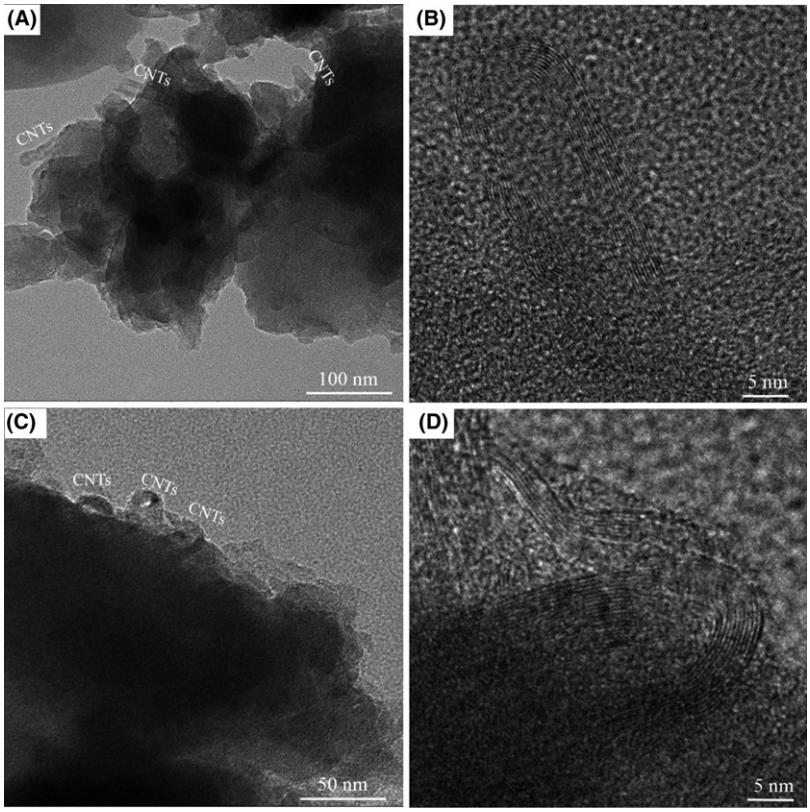

FIGURE 8 (A) Low resolution and (B) high-resolution TEM images of single-source-precursor derived CNTs-SiCN, (C) low resolution and (D) high-resolution TEM images of physically-blended-precursor derived CNTs-SiCN

1800 bonded on the surface of CNTs physically blocked the tangling of CNTs.[27,30–33,46] Due to the formation of SSP, the agglomeration of CNTs is effectively prevented during the cross-linking, warm-pressing and polymer-to-ceramic conversion. Therefore, a homogeneous dispersion is finally obtained in the CNTs-SiCN ceramics (Figure 9D). Moreover, Figure 9 shows that the recovery of carbon backbones of pristine CNTs-COOH during the polymer-to-ceramic transformation.

3.3 | Dielectric permittivity

The relative complex permittivity ($\varepsilon = \varepsilon' - j\varepsilon''$) of ceramics was measured in the frequency range of 8.2-12.4 GHz (X band). Figure 10 shows the real (ε') and imaginary (ε'') parts of the effective complex permittivity, and the tangent loss ($\tan\delta = \varepsilon''/\varepsilon'$) of pure SiCN and CNTs-SiCN with different CNT content as a function of frequency. As shown in Figure 10A, the HTT 1800-derived SiCN ceramic (S-0.0) presents a relatively low ε' with an average value of 4.87. With the introduction of CNTs into SiCN ceramic matrix, the ε' value of S-2.5 shows significant enhancement from 4.87 to 9.62. With the increase in CNT content in ceramics, the value of ε' increases gradually. Especially, with the 8.0 wt% CNTs in the feed, the ε' value of the obtained S-8.0 increases to 23.35. Meanwhile, as shown in Figure 10B, the ε'' value of SiCN is as low as 1.1×10^{-1}. However, for the samples S-2.5, S-4.5b, S-4.5a and S-8.0, the values of ε'' are significantly improved, which are in the range of 1.23~1.27, 1.26~1.30, 4.98~7.08, and 9.18~16.17, respectively. The polarization relaxations induced by the electron motion hysteresis in the dipole under alternating electromagnetic field enhance the dielectric loss,[47,48] leading to the increasing of ε''. In addition, to the contribution of polarizations, the conductive loss is another factor for the increasing imaginary part, which is caused by the conductive networks constructed by the carbon nanophase.[20] In Figure 10C, the tangent loss shows an obviously increasing tendency with the increasing of CNT content in SSP-derived ceramics. When the CNT content increases from 0.0 to 8.0 wt%, the tangent loss increases from 0.02 to 0.72. It is worth mentioning that both the ε'' and the tangent loss of S-4.5b are significantly lower than those of S-4.5a, due to the decreasing interface polarization and relaxation as well as inferior electrical conductivity in the physically-blended-precursor derived sample S-4.5b compared to the SSP-derived S-4.5a. In conclusion, the dielectric permittivity results indicate the significant advantages of SSP approach over physical blending method to preparing CNTs-SiCN nanocomposites, which is strongly influenced by the microstructure of the CNTs-SiCN such as distribution status of CNTs in the SiCN matrix.

3.4 | Electromagnetic absorption

The electromagnetic absorbing property was determined by calculating the reflection coefficient (*RC*).[49–51] Based on the model of metal backplane, *RC* of the sample is determined from the measured relative complex permeability

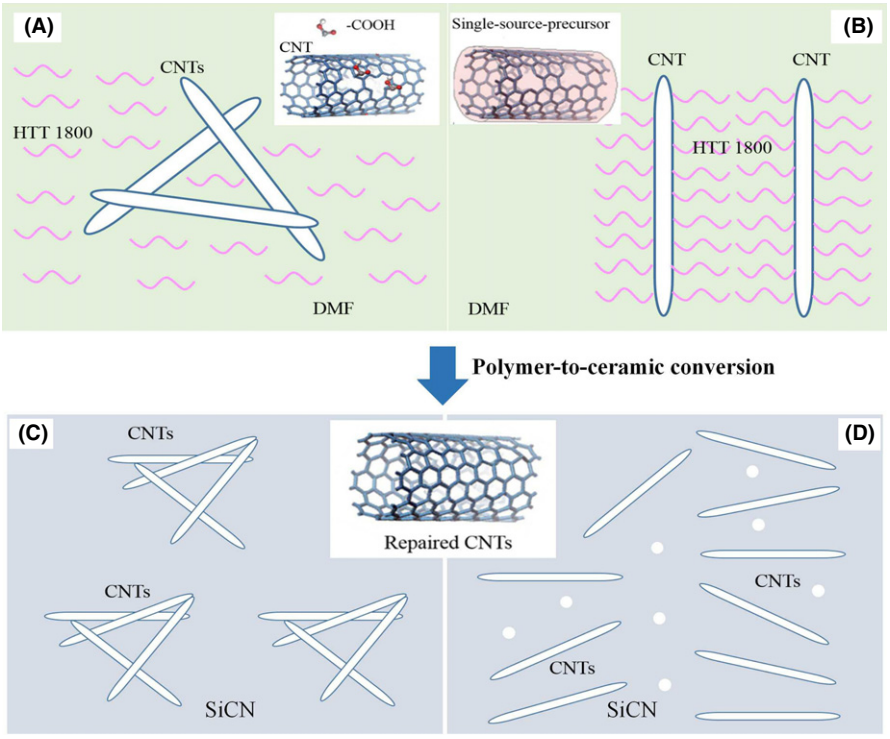

FIGURE 9 Schematic illustration of microstructural evolution of (A) physically-blended-precursor and (B) single-source-precursor derived CNTs-SiCN ceramics (C) and (D), respectively [Color figure can be viewed at wileyonlinelibrary.com]

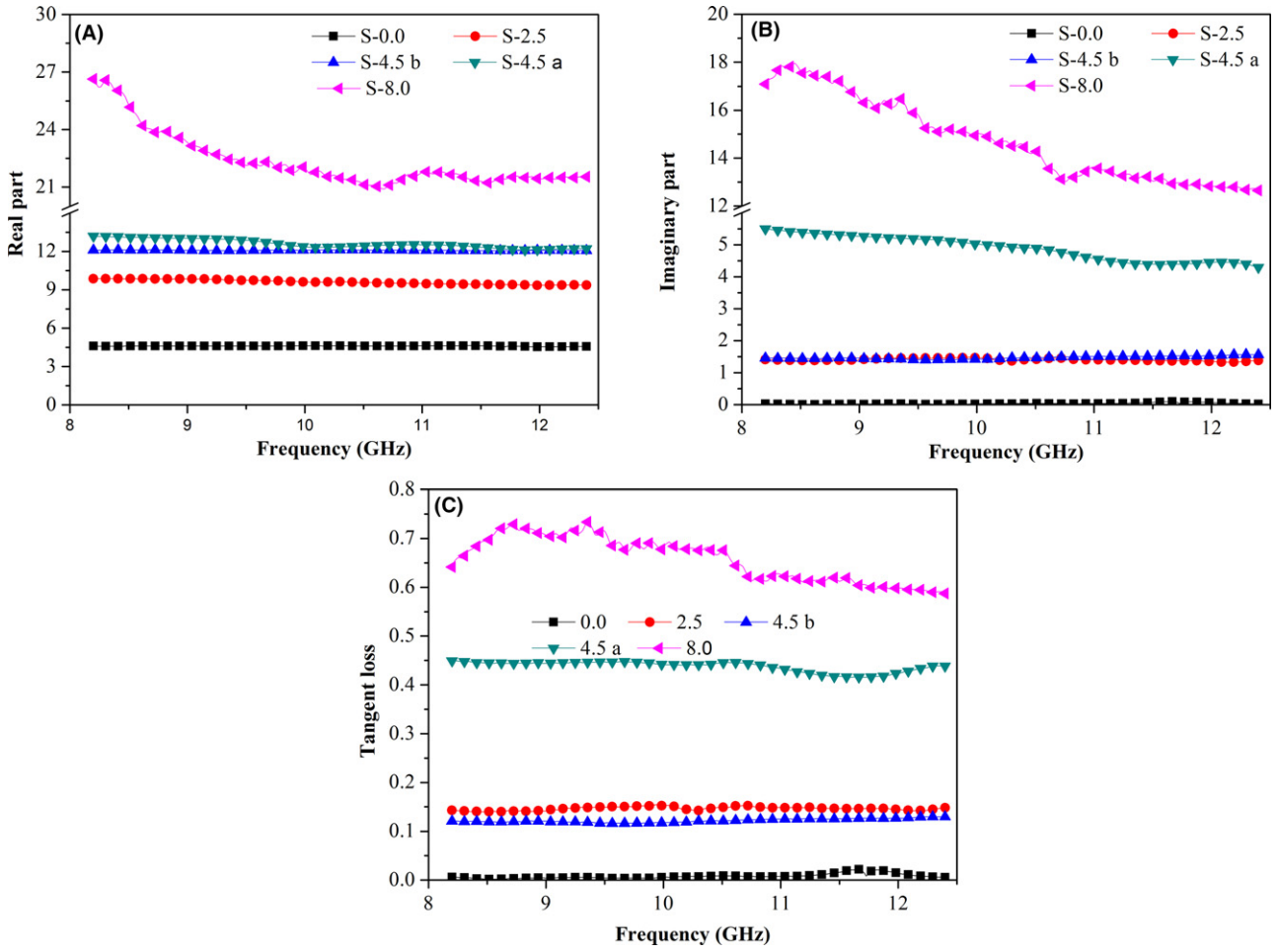

FIGURE 10 Real part (A), imaginary part (B) and tangent loss (C) of resultant SiCN and CNTs-SiCN ceramics [Color figure can be viewed at wileyonlinelibrary.com]

and permittivity according to the following equations[49–53]:

$$RC(\mathrm{dB}) = 20 \cdot \log_{10}|(Z_{in} - 1)/(Z_{in} + 1)| \quad (1)$$

$$Z_{in} = \sqrt{\frac{\mu}{\varepsilon}} \tanh(j2\pi\sqrt{\mu\varepsilon}\, fd/c) \quad (2)$$

where Z_{in}, d, and μ are the normalized input impedance, thickness and permeability of the material, c is the light velocity in vacuum, and f is the microwave frequency.

Figure 11 shows RC of resultant samples as a function of frequency in X-band. The absorption capability of sample S-2.5 is weak at every sample thickness due to the low ε'' (Figure 11A). With the sample thickness of 3.0 mm, it exhibits a minimal RC (RC_{min}), corresponding to the maximum absorption of −9.1 dB at the frequency of 8.75 GHz. In contrast, the RC_{min} value was significantly improved when the CNT content increases to 4.5 wt%. It can be seen that the RC_{min} of the sample S-4.5a shifts towards a higher frequency with the decreasing sample thickness (Figure 11B). The peak shift was attributed to the phenomena of quarter-wavelength attenuation, in which the absorption meets the phase match conditions.[20] The RC_{min} of the S-4.5a reaches −21.8 dB at 10.2 GHz, and the effective bandwidth (the bandwidth of RC values lower than −10 dB, namely, more than 90% microwaves are attenuated) amounts 3.7 GHz (from 8.7 to 12.4 GHz) with a thickness of 2.2 mm. With the decrease in sample thickness, the RC_{min} exhibits an improved tendency while the effective bandwidth shows a decreased trend. When the sample thickness decreased to 2.0 mm, the RC_{min} decreased to −26.1 dB with the effective bandwidth of 2.8 GHz (from 9.6 to 11.2 GHz). In contrast, for the sample S-4.5b derived from physically-blended-precursor, the RC_{min} is only −6.4 dB with a sample thickness of 2.2 mm, which is far inferior to that of the SSP-derived sample S-4.5a. This inferior EM property resulted from the low ε'' and tangent loss, which is strongly dependent on the poor dispersion of CNTs in the SiCN ceramic matrix.[18] Based on the findings that the ε' and ε'' should amount 5~20 and 1~10, respectively for the use as EM absorbing material,[1] the EM absorbing performance of the sample S-8.0 is very poor due to the high ε'>20 and ε''>10 and the result is not shown.

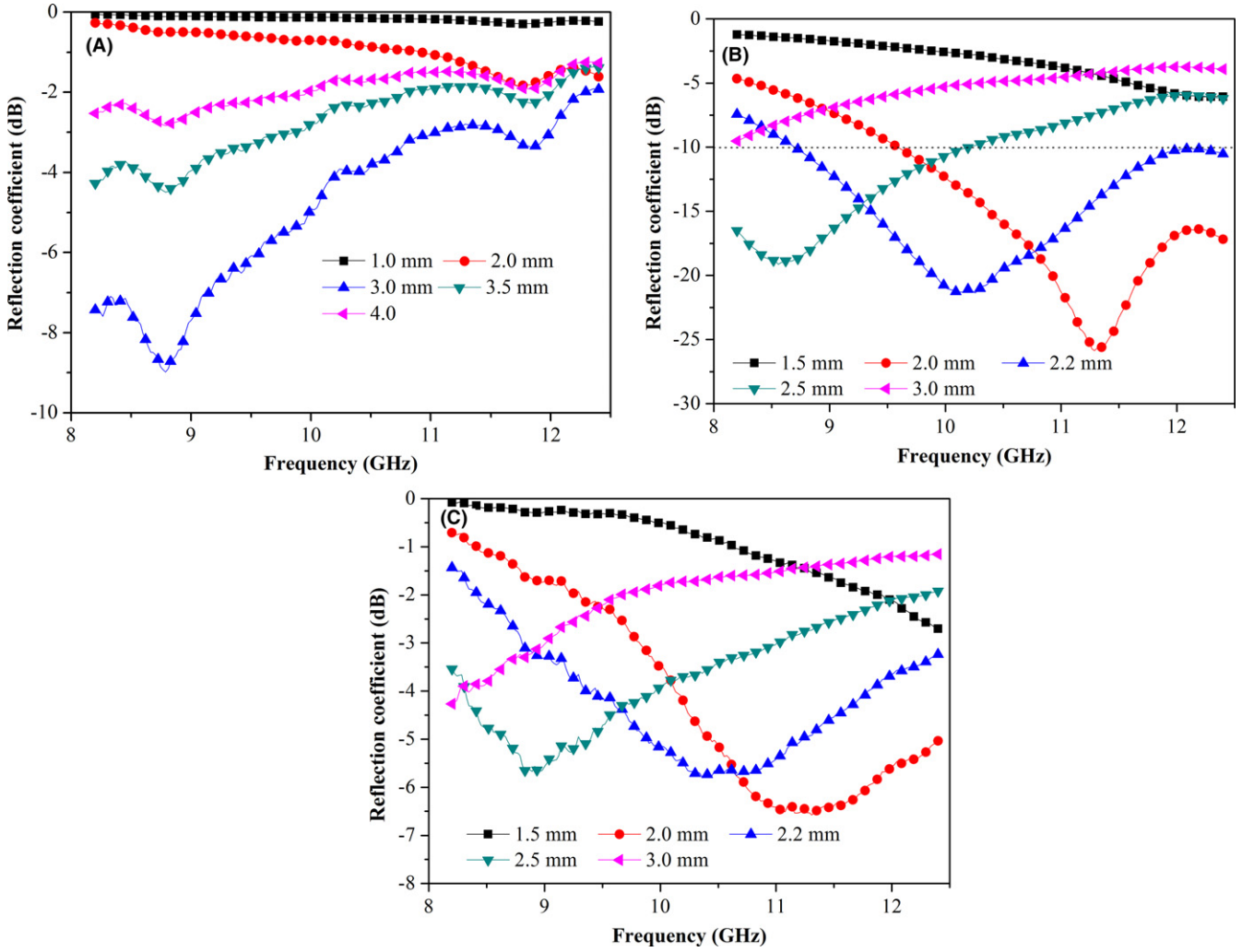

FIGURE 11 Reflection coefficient of resultant CNTs-SiCN nanocomposites S-2.5 (A), S-4.5a (B) and S-4.5b (C) [Color figure can be viewed at wileyonlinelibrary.com]

4 | CONCLUSIONS

In summary, novel SSPs were prepared through amidation reaction of poly (methylvinyl) silazane HTT 1800 with carboxylic groups functionalized CNTs at the assistance of $ZnCl_2$ catalyst, which was confirmed by the FT IR measurement. TEM images of the as-synthesized SSPs reveal that an HTT 1800 film with a thickness of ~3 nm was always attached on the surface of CNTs, which further indicates the successful formation of the SSPs. Crack-free monolithic CNTs-SiCN ceramic nanocomposites were prepared through pyrolysis of the obtained SSP green bodies at 1000°C. With the same CNT content (4.5 wt%) in the feed, the SSP-derived CNTs-SiCN nanocomposites possess a minimal reflection coefficient (RC_{min}) of −21.8 dB and an effective bandwidth of 3.7 GHz with a sample thickness of 2.2 mm while the physically-blended-precursor derived CNTs-SiCN nanocomposites show a far inferior RC_{min} of −6.4 dB with the same sample thickness. The significant improvements of EM absorbing property of SSP-derived CNTs-SiCN nanocomposites is due to the microstructural feature characterized by the homogeneous distribution of the CNTs in the SiCN matrix, which is strongly dependent on the precursor molecular structure, namely, the uniform dispersion of the CNTs in the SSPs.

ACKNOWLEDGEMENTS

Zhaoju Yu thanks the Natural Science Foundation of China (No. 50802079), Natural Science Foundation of Fujian Province of China (No. 2015J01221) and Creative Research Foundation of Science and Technology on Thermostructural Composite Materials Laboratory (No. 6142911040114) for financial support. Xingmin Liu acknowledges the financial support from China Scholarship Council (No. 201406 290019).

REFERENCES

1. Yin X, Kong L, Zhang L, et al. Electromagnetic properties of Si-C-N based ceramics and composites. *Inter Mater Rev*. 2014;59:326-355.
2. Wen B, Cao M, Lu M, et al. Reduced graphene oxides: light-weight and high-efficiency electromagnetic interference shielding at elevated temperatures. *Adv Mater*. 2014;26:3484-3489.
3. Albano M, Micheli D, Gradoni G, et al. Electromagnetic shielding of thermal protection system for hypersonic vehicles. *Acta Astronaut*. 2013;87:30-39.
4. Zeng Z, Jin H, Chen M, et al. Lightweight and anisotropic porous MWCNT/WPU composites for ultrahigh performance electromagnetic interference shielding. *Adv Funct Mater*. 2016;26:303-310.
5. Sun H, Che R, You X, et al. Cross-stacking aligned carbon-nanotube films to tune microwave absorption frequencies and increase absorption intensities. *Adv Mater*. 2014;26:8120-8125.
6. Zhang Y, Huang Y, Zhang T, et al. Broadband and tunable high-performance microwave absorption of an ultralight and highly compressible graphene foam. *Adv Mater*. 2015;27:2049-2053.
7. Kong L, Yin X, Han M, et al. Macroscopic bioinspired graphene sponge modified with in-situ grown carbon nanowires and its electromagnetic properties. *Carbon*. 2017;111:94-102.
8. Chen Z, Xu C, Ma C, et al. Lightweight and flexible graphene foam composites for high-performance electromagnetic interference shielding. *Adv Mater*. 2013;25:1296-1300.
9. Ionescu E, Kleebe H, Riedel R. Silicon-containing polymer-derived ceramic nanocomposites (PDC-NCs): preparative approaches and properties. *Chem Soc Rev*. 2012;41:5032-5052.
10. Seifollahi Bazarjani M, Hojamberdiev M, Morita K, et al. Visible light photocatalysis with c-WO_3–x/WO_3× H_2O nanoheterostructures in situ formed in mesoporous polycarbosilane-siloxane polymer. *J Am Chem Soc*. 2013;135:4467-4475.
11. Graczyk-Zajac M, Mera G, Kaspar J, et al. Electrochemical studies of carbon-rich polymer-derived SiCN ceramics as anode materials for lithium-ion batteries. *J Eur Ceram Soc*. 2010;30:3235-3243.
12. Colombo P, Mera G, Riedel R, et al. Polymer-derived ceramics: 40 years of research and innovation in advanced ceramics. *J Am Ceram Soc*. 2010;93:1805-1837.
13. Li Q, Yin X, Duan W, et al. Electrical, dielectric and microwave-absorption properties of polymer derived SiC ceramics in X band. *J Alloy Compd*. 2013;565:66-72.
14. Duan W, Yin X, Li Q, et al. Synthesis and microwave absorption properties of SiC nanowires reinforced SiOC ceramic. *J Eur Ceram Soc*. 2014;34:257-266.
15. Li Q, Yin X, Duan W, et al. Dielectric and microwave absorption properties of polymer derived SiCN ceramics annealed in N_2 atmosphere. *J Eur Ceram Soc*. 2014;34:589-598.
16. Wang X, Mera G, Morita K, et al. Synthesis of polymer-derived graphene/silicon nitride-based nanocomposites with tunable dielectric properties. *J Ceram Soc Jpn*. 2016;124:981-988.
17. Li Q, Yin X, Duan W, et al. Improved dielectric and electromagnetic interference shielding properties of ferrocene-modified polycarbosilane derived SiC/C composite ceramics. *J Eur Ceram Soc*. 2014;34:2187-2201.
18. Zhang Y, Yin X, Ye F, et al. Effects of multi-walled carbon nanotubes on the crystallization behavior of PDCs-SiBCN and their improved dielectric and EM absorbing properties. *J Eur Ceram Soc*. 2014;34:1053-1061.
19. Ye F, Zhang L, Yin X, et al. Dielectric and EMW absorbing properties of PDCs-SiBCN annealed at different temperatures. *J Eur Ceram Soc*. 2013;33:1469-1477.
20. Han M, Yin X, Duan W, et al. Hierarchical graphene/SiC nanowire networks in polymer-derived ceramics with enhanced electromagnetic wave absorbing capability. *J Eur Ceram Soc*. 2016;36:2695-2703.
21. Liu X, Yin X, Kong L, et al. Fabrication and electromagnetic interference shielding effectiveness of carbon nanotube reinforced carbon fiber/pyrolytic carbon composites. *Carbon*. 2014;68:501-510.
22. Liu Y, Yin X, Kong L, et al. Electromagnetic properties of SiO_2 reinforced with both multi-wall carbon nanotubes and ZnO particles. *Carbon*. 2013;64:541-544.
23. Wen B, Cao M, Hou Z, et al. Temperature dependent microwave attenuation behavior for carbon-nanotube/silica composites. *Carbon*. 2013;65:124-139.
24. Thostenson E, Ren Z, Chou T. Advances in the science and technology of carbon nanotubes and their composites: a review. *Compos Sci Technol*. 2001;61:1899-1912.
25. Ma P, Mo S, Tang B. Dispersion, interfacial interaction and re-agglomeration of functionalized carbon nanotubes in epoxy composites. *Carbon*. 2010;48:1824-1834.
26. An L, Xu W, Rajagopalan S, et al. Carbon-nanotube-reinforced polymer-derived ceramic composites. *Adv Mater*. 2004;16:2036-2040.
27. Zou J, Liu L, Chen H, et al. Dispersion of pristine carbon nanotubes using conjugated block copolymers. *Adv Mater*. 2008;20:2055-2060.
28. Yuan J, Hapis S, Breitzke H, et al. Single-source-precursor synthesis of hafnium-containing ultrahigh-temperature ceramic nanocomposites (UHTC-NCs). *Inorg Chem*. 2014;53:10443-10455.
29. Zaheer M, Motz G, Kempe R. The generation of palladium silicide nanoalloy particles in a SiCN matrix and their catalytic applications. *J Mater Chem*. 2011;21:18825-18831.
30. Chen J, Hamon M, Hu H, et al. Solution properties of single-walled carbon nanotubes. *Science*. 1998;282:95-98.
31. Hamon M, Chen J, Hu H, et al. Dissolution of single-walled carbon nanotubes. *Adv Mater*. 1999;11:834-840.
32. Huang W, Lin Y, Taylor S, et al. Sonication-assisted functionalization and solubilization of carbon nanotubes. *Nano Lett*. 2002;2:231-234.
33. Huang W, Taylor S, Fu K, et al. Attaching proteins to carbon nanotubes via diimide-activated amidation. *Nano Lett*. 2002;2:311-314.
34. Pompeo F, Resasco D. Water solubilization of single-walled carbon nanotubes by functionalization with glucosamine. *Nano Lett*. 2002;2:369-373.
35. Bézier D, Park S, Brookhart M. Selective reduction of carboxylic acids to aldehydes catalyzed by $B(C_6F_5)_3$. *Org Lett*. 2013;15:496-499.
36. Guo S, Dong S, Wang E. Constructing carbon nanotube/Pt nanoparticle hybrids using an imidazolium-salt-based ionic liquid as a linker. *Adv Mater*. 2010;22:1269-1272.
37. Yang H, Li B, Cui Y. Preparation of salicylic acid resin supported $FeCl_3$ Lewis acid catalyst and its application in organic synthesis. *Synth Commun*. 1998;28:1233-1238.

38. Liu G. Preparation of silyl esters by $ZnCl_2$-catalyzed dehydrogenative crosscoupling of carboxylic acids and silanes. *Synlett*. 2006;9:1431-1433.
39. Kong X, Sun X, Li X, et al. Catalytic growth of ZnO nanotubes. *Chem Phys*. 2003;82:997-1001.
40. Huang M, Wu Y, Feick H, et al. Catalytic growth of zinc oxide nanowires by vapor transport. *Adv Mater*. 2001;13:113-116.
41. Ionescu E, Francis A, Riedel R. Dispersion assessment and studies on AC percolative conductivity in polymer-derived Si–C–N/CNT ceramic nanocomposites. *J Mater Sci*. 2009;44:2055-2062.
42. Qian J, Pantea C, Voronin G, et al. Partial graphitization of diamond crystals under high-pressure and high-temperature conditions. *J Appl Phys*. 2001;90:1632-1637.
43. Zhu Z, Lu Y, Qiao D, et al. Self-catalytic behavior of carbon nanotubes. *J Am Chem Soc*. 2005;127:15698-15699.
44. Vakifahmetoglu C, Pippel E, Woltersdorf J, et al. Growth of one-dimensional nanostructures in porous polymer-derived ceramics by catalyst-assisted pyrolysis. Part I: iron catalyst. *J Am Ceram Soc*. 2010;93:959-968.
45. Vakifahmetoglu C, Colombo P, Carturan S, et al. Growth of one-dimensional nanostructures in porous polymer-derived ceramics by catalyst-assisted pyrolysis. Part II: cobalt catalyst. *J Am Ceram Soc*. 2010;93:3709-3719.
46. Hayashida K, Tanaka H. Ultrahigh electrical resistance of poly (cyclohexyl methacrylate)/carbon nanotube composites prepared using surface-initiated polymerization. *Adv Funct Mater*. 2012;22:2338-2344.
47. Han M, Yin X, Kong L, et al. Graphene-wrapped ZnO hollow spheres with enhanced electromagnetic wave absorption properties. *J Mater Chem A*. 2014;2:16403-16409.
48. Kong L, Yin X, Li Q, et al. High-temperature electromagnetic wave absorption properties of $ZnO/ZrSiO_4$ composite ceramics. *J Am Ceram Soc*. 2013;96:2211-2217.
49. Liu J, Che R, Chen H, et al. Microwave absorption enhancement of multifunctional composite microspheres with spinel Fe_3O_4 cores and anatase TiO_2 shells. *Small*. 2012;8:1214-1221.
50. Micheli D, Apollo C, Pastore R, et al. X-Band microwave characterization of carbon-based nanocomposite material, absorption capability comparison and RAS design simulation. *Compos Sci Technol*. 2010;70:400-409.
51. Micheli D, Vricella A, Pastore R, et al. Synthesis and electromagnetic characterization of frequency selective radar absorbing materials using carbon nanopowders. *Carbon*. 2014;77:756-774.
52. Che R, Peng L, Duan X, et al. Microwave absorption enhancement and complex permittivity and permeability of Fe encapsulated within carbon nanotubes. *Adv Mater*. 2004;16:401-405.
53. Liu J, Xu J, Che R, et al. Hierarchical $Fe_3O_4@TiO_2$ yolk shell microspheres with enhanced microwave-absorption properties. *Chem Eur J*. 2013;19:6746-6752.

How to cite this article: Liu X, Yu Z, Chen L, et al. Role of single-source-precursor structure on microstructure and electromagnetic properties of CNTs-SiCN nanocomposites. *J Am Ceram Soc*. 2017;100:4649–4660. https://doi.org/10.1111/jace.15000

Journal of Materials Chemistry C

PAPER

View Article Online
View Journal | View Issue

Cite this: J. Mater. Chem. C, 2017, 5, 7950

Single-source-precursor synthesis and electromagnetic properties of novel RGO–SiCN ceramic nanocomposites†

Xingmin Liu,[b] Zhaoju Yu,*[ac] Ryo Ishikawa,[d] Lingqi Chen,[e] Xiaowei Yin,[e] Yuichi Ikuhara[d] and Ralf Riedel[bce]

Received 23rd January 2017,
Accepted 11th July 2017

DOI: 10.1039/c7tc00395a

rsc.li/materials-c

Single-source-precursors (SSPs) have been synthesized through chemical modification of poly(methylvinyl)-silazane (HTT 1800) with graphene oxide (GO) *via* an amidation reaction catalyzed by $ZnCl_2$. With the formation of an SSP, the restacking of GO was effectively prevented by the HTT 1800 grafted at the surface of GO. After pyrolysis of warm-pressed green bodies comprising the SSP, GO-HTT 1800, monolithic silicon carbonitride (SiCN) ceramic nanocomposites containing *in situ* thermally reduced graphene oxide (RGO), namely RGO–SiCN, were successfully prepared. The resultant RGO–SiCN nanocomposites possess versatile electromagnetic (EM) properties ranging from EM absorbing to shielding behavior. With 2.5 wt% GO in the feed, the final RGO–SiCN nanocomposite exhibits an outstanding minimal reflection coefficient (RC_{min}) of −62.1 dB at 9.0 GHz, and the effective absorption bandwidth reaches 3.0 GHz with a sample thickness of 2.10 mm. With the same GO content, the resultant RGO–SiCN nanocomposite prepared by mechanical blending exhibits a far inferior RC_{min} of −8.2 dB. This finding strongly supports the advantage of the developed SSP route suitable for the fabrication of RGO–SiCN nanocomposites with significantly enhanced EM properties. With 12.0 wt% GO content in the feed, the obtained RGO–SiCN nanocomposite reveals an excellent shielding effectiveness of 41.2 dB with a sample thickness of 2.00 mm.

1. Introduction

With the rapid development of wireless communication and stealth technology, considerable attention has been paid to theoretical and experimental research on effective electromagnetic (EM) shielding and absorbing materials.[1–5] For an excellent radar-absorbing material, a low reflection coefficient (RC) (in cases where the RC value is lower than −10 dB, more than 90% of the EM wave is attenuated) and a wide effective absorption bandwidth (EAB, the corresponding frequency range with RC lower than −10 dB) are required.[1] For a qualified EM shielding material, shielding effectiveness of at least 30–60 dB is required for civil and military use.[1] High efficiency is the fundamental factor for the preparation of EM materials.[2] Single-layer reduced graphene oxide (RGO), as the thinnest material in the carbon family, which possesses extremely high specific surface areas and carrier mobilities coupled with abundant defects, is reported to be a promising candidate for high loss tangent and high-efficiency EM materials.[2,6,7] Generally, RGO-based foam and films have been reported as electromagnetic interference shielding (EMI) materials due to their strong reflections, which resulted from high electrical conductivity.[8,9] However, in some applications EM materials are also required to show appropriate oxidation resistance, high thermal stability and (or) withstand high mechanical loads,[1,10,11] which is far beyond the capability of currently reported RGO-based foams and films.[6–9] Therefore, the search for EM shielding and absorbing materials with advanced efficiency for high temperature applications in harsh environments is still a challenging task.

Polymer derived ceramics (PDCs), owing to their intrinsic advantages including reasonable permittivity, oxidation resistance and improved mechanical strength at elevated temperatures, are considered as excellent candidate matrix EM materials.[1,12–15] However, due to the relatively low permittivity, PDC-based materials are mostly used as EM absorption materials.[1,3] As a highly conductive phase and an excellent microwave absorbent, RGO can build up effective conductive networks at a low content inside the

[a] College of Materials, Key Laboratory of High Performance Ceramic Fibers (Xiamen University), Ministry of Education, Xiamen 361005, China. E-mail: zhaojuyu@xmu.edu.cn; Tel: +86 0592-2181898
[b] Institut für Materialwissenschaft, Technische Universität Darmstadt, D-64287, Darmstadt, Germany
[c] College of Materials, Fujian Key Laboratory of Advanced Materials (Xiamen University), Xiamen 361005, China
[d] Institute of Engineering Innovation, University of Tokyo, Bunkyo, Tokyo, 113-8656, Japan
[e] Science and Technology on Thermostructural Composite Materials Laboratory, Northwestern Polytechnical University, Xi'an, 710072, China

† Electronic supplementary information (ESI) available. See DOI: 10.1039/c7tc00395a

ceramic matrix, which significantly improves the permittivity and electrical conductivity of the resulting composites.[1] However, the effectiveness of the absorbent strongly requires a homogeneous dispersion of the RGO phase. Agglomeration of RGO will lead to low polarization and relaxation and poor electrical conductivity, and thus result in unsatisfactory absorption and inferior shielding performance.[16–18] Unfortunately, due to the limitations of the currently used mechanical blending approach, serious agglomeration of the nano-scaled absorbents in the dispersion medium is found to be unavoidable when the mechanical dispersing forces are removed. As a result, a decent EM performance is achieved only with a high absorbent content.[17,18] However, a high loading of carbon nanofillers may decrease the mechanical properties and processibility of the composite due to severe agglomeration and poor filler-matrix bonding.[9]

Solubilization of graphene oxide (GO) through chemical reactions with dispersion assistants has been reported to be an effective method to prevent their agglomeration.[19,20] The organic dispersion agent grafted onto the surface of GO not only imparts solubility to GO in the organic solvent but also sterically hinders restacking.[21] Taking this concept into the PDC approach, agglomeration of the GO in the preceramic polymers is expected to be facilely prevented by grafting preceramic macromolecules onto the GO surface through chemical reactions, namely *via* a single-source-precursor (SSP) route. However, the SSP related to a chemically bonded GO/preceramic polymer has never been reported so far despite Wang *et al.* recently described the synthesis and dielectric properties of polymer-derived graphene/silicon nitride-based nanocomposites prepared by the mechanical blending of GO and a Si_3N_4 precursor.[22] Meikang Han *et al.*[16] investigated the EM absorbing properties of RGO-incorporated in SiOC ceramics with *in situ* grown SiC nanowires. The materials were synthesized *via* pyrolysis of physically blended GO/polysiloxane mixtures. Finally, to our best knowledge, the SSP derived materials based on RGO-modified PDCs and their EM properties derived therefrom have not been reported yet.

Therefore, in this work, we demonstrate the successful synthesis of a SSP obtained by the chemical reaction of poly(organo)silazane (HTT 1800) to GO *via* amidation with the assistance of $ZnCl_2$ as a catalyst. This procedure avoids aggregation of RGO in the final PDC matrix. After the pyrolysis of the obtained SSP at 1000 °C in Ar, *in situ* thermally reduced GO modified SiCN (RGO–SiCN) ceramic nanocomposites were obtained. The structural characterization of the SSP and the influence of the GO content on the microstructure and dielectric properties were investigated in detail. Furthermore, we successfully tailored the EM performances of the obtained RGO–SiCN ceramic nanocomposites from EM absorbing to shielding behavior just by varying the content of RGO.

2. Experimental section

2.1 Materials synthesis

Poly(organo)silazane HTT 1800 (KiON Specialty Polymers) was used as a precursor for SiCN. The graphene oxide flakes (Xianfeng Nano, China) were firstly blended with *N*,*N*-dimethylformamide (DMF) (Sigma-Aldrich, Germany) with a weight ratio of 1 : 500 in a flask. After ultra-sonication for 4 h, the $ZnCl_2$ catalyst (Sigma-Aldrich, Germany) with a weight ratio of 2 : 98 with respect to the precursor HTT 1800 was added. After ultra-sonication for another 2 h, the HTT 1800 was dropped into the flask. Then the resultant mixture was heated up to 70 °C for 72 h under argon flow and magnetic stirring. Subsequently, the as-synthesized SSP was cross-linked at 120 °C under an Ar atmosphere before the DMF was finally removed under vacuum. After ball milling for 3 h, the black GO–HTT 1800 powders were warm pressed into green bodies with the dimensions of 50 × 40 × 3 mm^3 under a pressure of 60 kN. Then, the as-prepared green bodies were pyrolyzed under an Ar atmosphere at 1000 °C and machined into samples with dimensions of 22.86 × 10.16 × 2.00 mm^3 by wire cutting.

To investigate the influence of the RGO content on the EM properties of the ceramic composites, a series of GO-HTT 1800 precursors with different GO contents (0.0 wt%, 1.0 wt%, 2.5 wt%, 6.0 wt% and 12.0 wt%) in the feed were prepared (Table 1). With 2.5 wt% GO in the feed, a control test based on the physical blending method as the reference sample was also performed under the same conditions but no $ZnCl_2$ was added.

2.2 Characterization methods

FT IR spectra were collected using a Bruker Vertex 70 FT-IR instrument (Bruker, USA) in attenuated total reflectance geometry. X-ray diffraction (XRD) was employed to conduct phase analysis (X'Pert Pro; Philips, Netherlands). Raman spectra were recorded from 100 cm^{-1} to 4000 cm^{-1} employing a micro-Raman HR8000 spectrometer (Horiba Jobin Yvon, Bensheim, Germany) using a laser wavelength of 514.5 nm. The microstructure of the samples was observed by scanning electron microscopy (SEM; S-4799, Hitachi, Tokyo, Japan). Transmission electron microscopy (TEM) studies were conducted on ground ceramic powder samples using a JEM-2100 (JEOL Ltd, Tokyo, Japan) microscope at an acceleration voltage of 200 kV (wavelength 152.51 pm). Electron diffraction patterns on the bulk ceramic samples were acquired by transmission electron microscopy (JEOL JEM 2010HC). The annular dark-field (ADF) imaging and elemental mapping with energy-dispersive X-ray spectroscopy (EDXS) were performed by scanning transmission electron microscopy (STEM) using a JEOL ARM300CF. The values of scattering parameters (S-parameters; S11, S12, S21 and S22) of the as-prepared samples with dimensions of 22.86 × 10.16 × 2.00 mm^3 were measured by

Table 1 Content of catalyst and graphene oxide in the feed

Ceramics	Precursors	GO (wt%)	$ZnCl_2$ (wt%)
S-1	HTT 1800	0.0	0.0
S-2	HTT 1800-1.0	1.0	2.0
S-3[a]	Physically blended HTT 1800-2.5	2.5	0.0
S-4	HTT 1800-2.5	2.5	2.0
S-5	HTT 1800-6.0	6.0	2.0
S-6	HTT 1800-12.0	12.0	2.0

[a] S-3 was obtained by pyrolysis of physically blended GO/HTT 1800 mixture.

the waveguide method using a vector network analyzer (VNA, MS4644A; Anritsu, Japan) from 8.2 to 12.4 GHz (X-band). To diminish the influence of the air-gap, at least three samples for each measurement were prepared, and the measured values of S-parameters were compared to confirm that the errors are less than 3%.

3. Results and discussion

3.1 Characterization of the single-source-precursor GO–HTT 1800

In the present work, a series of SSPs were synthesized by adjusting the GO content in the feed. The amount of GO was adjusted to 1.0 wt%, 2.5 wt%, 2.5 wt% without the catalyst, 6.0 wt% and 12.0 wt%. The resultant preceramic precursors are denoted as HTT 1800-1.0, HTT 1800-2.5, physically blended HTT 1800-2.5, HTT 1800-6.0 and HTT 1800-12.0 (as shown in Table 1), respectively. In the following, the FT IR spectra of the synthesized SSPs crossed-linked at 120 °C are discussed and shown in Fig. 1.

In the FT IR spectrum of the sample HTT 1800, typical absorption bands related to C–H (2960 and 2965 cm^{-1}), Si–N–H (1160 cm^{-1}), and Si–N (930 cm^{-1}) groups were analyzed.[23,24] In the spectra of the GO containing samples HTT 1800-1.0, HTT 1800-2.5, HTT 1800-6.0 and HTT 1800-12.0, additional new absorption bands at ν = 1332 cm^{-1} (amide C–N), ν = 1646 cm^{-1} (amide C═O), ν = 1590 cm^{-1} (amide N–H) appeared,[25–28] which are due to the formed amide groups derived from the amidation reaction between –COOH groups of GO and –N–H groups of HTT 1800. In contrast, the spectrum of the sample physically blended HTT 1800-2.5 does not show these new absorption bands, indicating that the amidation reaction did not occur without the presence of $ZnCl_2$. Therefore, the FT IR results confirm that the –COOH groups of GO react with the –N–H groups of HTT 1800 *via* an amidation reaction to form the SSP, which is shown in Fig. 2. We propose a possible reaction mechanism for the present amidation reaction,

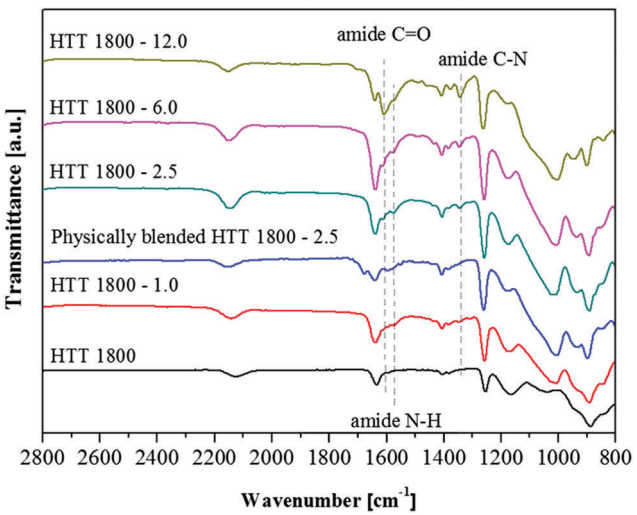

Fig. 1 FT IR spectra of pristine GO, physically blended HTT 1800/GO mixture and the synthesized SSPs with different GO contents.

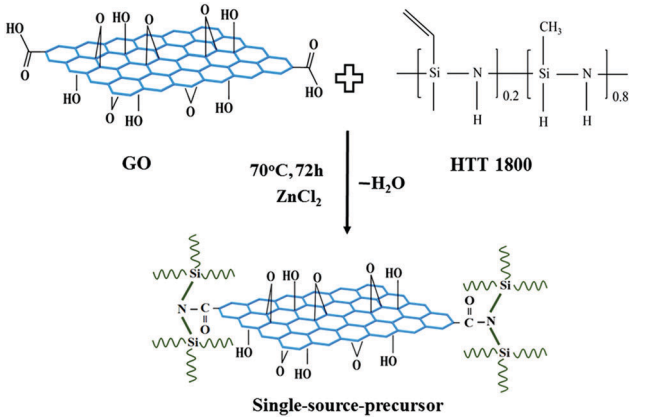

Fig. 2 Synthesis of SSP (GO–HTT 1800) by amidation reaction between GO and HTT 1800.

as follows: $ZnCl_2$ serves as a Lewis acid catalyst and activates the carboxylic group by the coordination of the Zn atom at the O atom of the C═O group. Then, the –NH group of polysilazane reacts with the activated carboxylic C by a nucleophilic attack.

3.2 Microstructure characterization

Raman spectroscopy is a non-destructive method for characterizing carbon-containing materials like graphite, carbon black-based materials, amorphous carbon films, or carbon nanotubes and their composites. Fig. 3a shows the Raman spectra of the HTT 1800-derived SiCN and the resultant RGO–SiCN ceramic nanocomposites. All spectra clearly indicate the presence of both, disorder-induced D and graphite-like G bands. The D-band at 1352 cm^{-1} corresponds to the presence of amorphous carbonaceous products, disordered carbon or defects in graphite and the G-band at 1580 cm^{-1} is related to the signal from graphite.[29,30] The graphitization grade (G_G) of a carbon containing material can be calculated as follows: $I_G/(I_G + I_D) \times 100\%$, where I_G and I_D are the intensity of the G and D-bands, respectively.[29,30] As reported, GO begins to decompose with the desorption of CO, CO_2 and other oxygenated carbon species when the temperature is higher than 200 °C, which is known as thermal reduction.[31] During the thermal reduction process, parts of the defective carbon backbones of GO are restored and a higher graphitization grade of the *in situ* formed RGO should be achieved.[30–33] Based on the findings that the ceramic yield of HTT 1800 is about 70.0 wt%[23] and the GO experiences a mass loss of more than 70.0 wt% with a thermal reduction temperature as high as 1000 °C,[31] the RGO content in the resultant RGO–SiCN nanocomposite (with 12.0 wt% GO in the feed) is roughly determined to be less than 5.5 wt%, which accounts for the slight increase of G_G of the resultant ceramic nanocomposites from 46.7% to 53.8% with the GO content increasing from 0.0 wt% to 12.0 wt% in the feed. This finding supports that GO was *in situ* thermally reduced to RGO during the polymer-to-ceramic transformation of the SSP.

Fig. 3b shows the XRD patterns of pristine SiCN and the obtained RGO–SiCN ceramic nanocomposite. Pure SiCN shows a complete amorphous state which agrees well with the

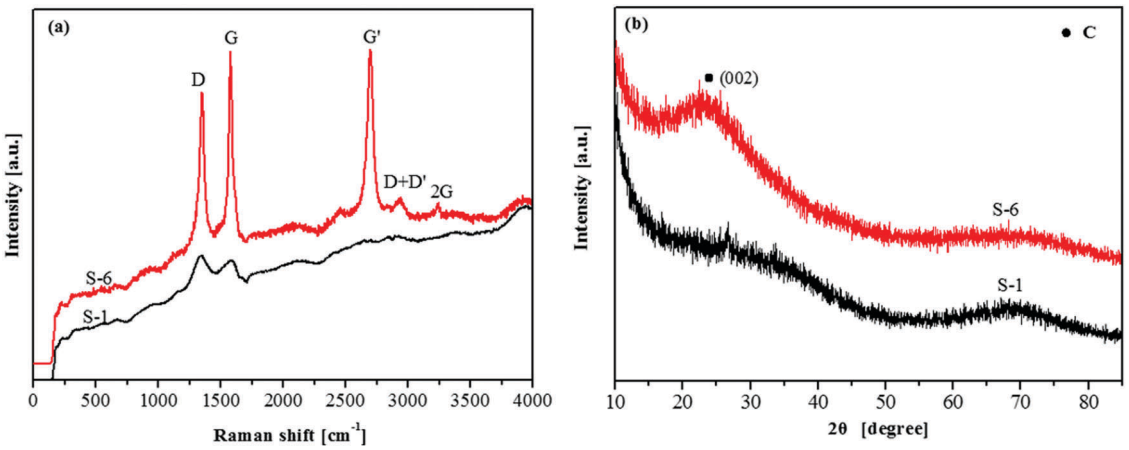

Fig. 3 (a) Raman spectra and (b) XRD patterns of resultant SiCN (sample S-1) and RGO–SiCN ceramic nanocomposite (sample S-6) (according to the Bragg diffraction equation, the interlayer spacing of RGO is calculated as 0.366 nm).

findings reported in the literature.[14,29] In the pattern of the RGO–SiCN nanocomposite, a weak characteristic peak of C (002) at 2θ of 24.29° refers to the RGO since that of graphite appears at 2θ = 26.5 °C. However, no signals related to Zn or Zn compounds were found though $ZnCl_2$ was used as the catalyst. According to the literature,[34,35] this observation is explained by the reduction of $ZnCl_2$ to metallic Zn by carbon species (thermally reduced GO or H_2, CO released by the decomposition of polysilazane) and metallic Zn evaporates out of the ceramic nanocomposites during the pyrolysis. Therefore, Zn cannot be found in the final nanocomposites, which is also confirmed by the STEM-EDXS elemental images of RGO–SiCN nanocomposites since only Si, C, N and O atoms were found while no Zn atom was detected (shown in Fig. 6).

As shown in Fig. 4, the obtained ceramic sample exhibits a linear shrinkage of *ca.* 30% and a volume shrinkage of more than 50% after pyrolysis. However, the monolithic ceramic sample shows a totally crack free morphology though it suffered from large linear and volume shrinkage.

To investigate the morphology of the ceramic samples, the fracture surface of monolithic SiCN (Fig. 5a and c) and RGO–SiCN nanocomposites (Fig. 5b and d) was analyzed by SEM. In general, representative SEM observation images reveal a relatively dense microstructure. In Fig. 5b and d, an obvious and unique network structure (with the width of 50–100 nm) can be clearly identified in the form of a 3D interconnected

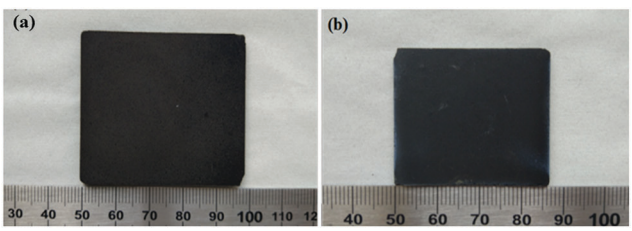

Fig. 4 (a) Optical images of the green body derived from warm pressing of the resultant SSP GO–HTT 1800 at 245 °C and (b) monolithic RGO–SiCN nanocomposites obtained after pyrolysis at 1000 °C in Ar.

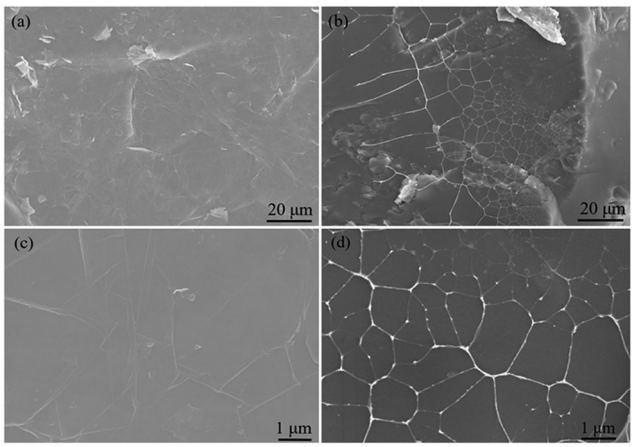

Fig. 5 Low magnification SEM images of fracture surface of (a) SiCN (S-1) and (b) RGO–SiCN (S-6), and high magnification SEM images of fracture surface of (c) S-1 and (d) S-6.

bright (inter)phase, which was also found in the case of RGO/polymer composites.[8] The formed networks are discussed to result from the *in situ* formed RGO since such microstructural features were not found inside the pure SiCN matrix.

To confirm the chemical composition and microstructure, the bulk SiCN and RGO–SiCN samples were investigated by transmission electron microscopy (TEM). Fig. 6a shows a selected-area diffraction pattern obtained from the network area (Fig. 6b) of the RGO–SiCN sample (GO content is 12.0 wt%). No Bragg reflections but several ring patterns as marked by arrowheads are found, suggesting that both the matrix and the grain boundary interphase (networks) are not crystallized but amorphous. Fig. 6b shows the ADF-STEM image obtained from the network (interphase) regions. The width of the interphase is less than 100 nm and the region exhibits dark-contrast, suggesting that the region consists of light elements. It is noteworthy that the bright contrast in the matrix of Fig. 6b (marked by arrowheads) originates from the supporting carbon thick film of the TEM grid. This carbon grid shows local carbon

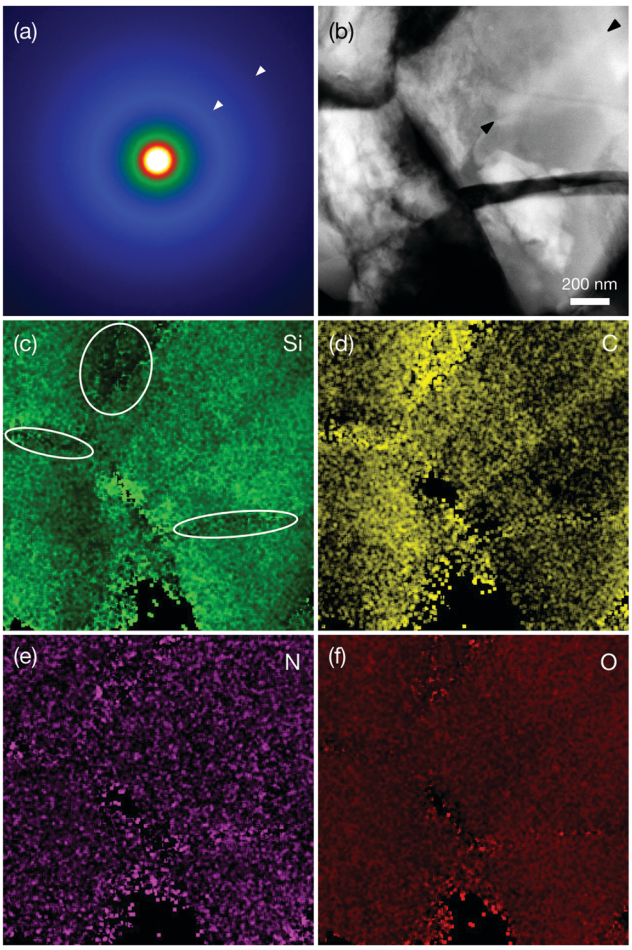

Fig. 6 (a) Electron diffraction pattern obtained from the sample RGO–SiCN (S-6), and (b) ADF-STEM image at the same area of (a). The bright contrast marked with dark arrowheads in (b) refers to the supporting carbon film of the TEM grid. STEM-EDXS elemental images are obtained from the same area of (b), and the images are formed by using the following edges: (c) Si–K, (d) C–K, (e) N–K, (f) O–K, respectively.

enrichment (see Fig. 6d). To investigate the elemental distribution in the matrix and the interphase (network), we performed STEM-EDXS mapping and the results are given in Fig. 6c–f, where the used edges are (c) Si–K, (d) C–K, (e) N–K, and (f) O–K, respectively. The Si is basically distributed in the matrix and it becomes poor in the network structure, while carbon has the opposite distribution. The carbon rich phase is segregated in the grain boundary interphase, denoted as the network. In our observation, the segregated networks will be covered by the matrix, and therefore it is difficult to discuss the accurate composition of the matrix and the segregated phase. It is well accepted that the HTT 1800 precursors were transformed into amorphous SiCN after pyrolysis at 1000 °C.[23] Characteristic peaks of graphite are identified by Raman spectra and XRD patterns. Therefore, combining other methods such as Raman and XRD we conclude that the matrix is composed of SiCN and the carbon-rich phase is segregated in the analyzed networks. As reported in the literature, upon pyrolysis at 1000 °C, the nanostructure of polysilazane-derived amorphous SiCN ceramics can be generally described as a random network of Si–C–N atoms.[36–38] No segregated carbon was observed by HRTEM in the amorphous SiCN obtained after annealing at 1100 °C.[37] With the increase of annealing temperatures to 1400 °C, the amorphous SiCN ceramics experienced phase separation with the formation of Si_3N_4, SiC and graphene-like carbon.[37] In the present work, the carbon-rich phase can only be considered as the *in situ* formed RGO since no other segregated carbon is formed in the SiCN matrix after heat treatment at a low temperature of 1000 °C. The RGO networks form electrically conductive pathways and, therefore, improve the electrical conductivity and dielectric properties.[1]

To observe the morphology of the *in situ* formed RGO in the SiCN matrix, representative TEM images of powdered RGO–SiCN nanocomposites derived from a physically-blended-precursor (Fig. 7a) and SSP (Fig. 7c) are shown in Fig. 7. From Fig. 7b, it can be concluded that the RGO layers are seriously restacked in the physically-blended-precursor derived RGO–SiCN. The interlayer distance of the adjacent RGO layers was determined to be *ca.* 0.551 nm, which is larger than that of graphite (*i.e.*, 0.335 nm) and the number of stacked RGO varies from 8 to 12, which is correlated with the results obtained in the literature related to rGO/Si_3N_4 nanocomposites prepared by physical blending of GO and a Si_3N_4 precursor.[22] However, for the sample derived from the SSP (Fig. 7d), the restacking of RGO was significantly reduced since the number of stacked RGO varies between 2 and 3 layers and even single layer RGO (the distance between the adjacent RGO is larger than 1 nm) can be found in some areas. In general, the significantly reduced restacking of RGO is attributed to a physical (steric hindrance) blocking by HTT 1800 grafted on the surface of GO (Fig. 7c), which is consistent with the reported literature.[21] As reported, the layered GO is derived from the exfoliation of graphite with strong chemical attack.[31,39] During the chemical attack, functional groups including hydroxyl, epoxy groups are attached on their basal planes and carboxyl groups on their edges, which destroys the van der Waals bonds between the adjacent layers. As a result, the interlayer distance of GO is enlarged and is much larger than that of graphite.[31,39] After thermal reduction, the obtained RGO still shows a larger interlayer distance than graphite. With respect to the physically-blended-precursor, the GO layers were dispersed into the HTT 1800 precursor with the assistance of ultrasonication. Due to the strong van der Waals interactions between each adjacent GO layers, they tend to restack when the ultrasonication disappeared (Fig. 7a). However, as shown in Fig. 7c, the HTT 1800 molecules were grafted onto the surface of GO through chemical modification, which blocked GO from restacking and further enlarged their interlayer distance. Therefore, the interlayer distance of RGO in Fig. 7d is even larger than that of RGO in Fig. 7b. After the polymer-to-ceramic conversion, the HTT 1800 transformed into SiCN and inserted into the adjacent RGO, which is strongly supported by the nano/micro-structure shown in Fig. 7d.

3.3 Dielectric properties

The relative complex permittivity ($\varepsilon = \varepsilon' - j\varepsilon''$) of the obtained ceramics was measured in the frequency range of 8.2–12.4 GHz

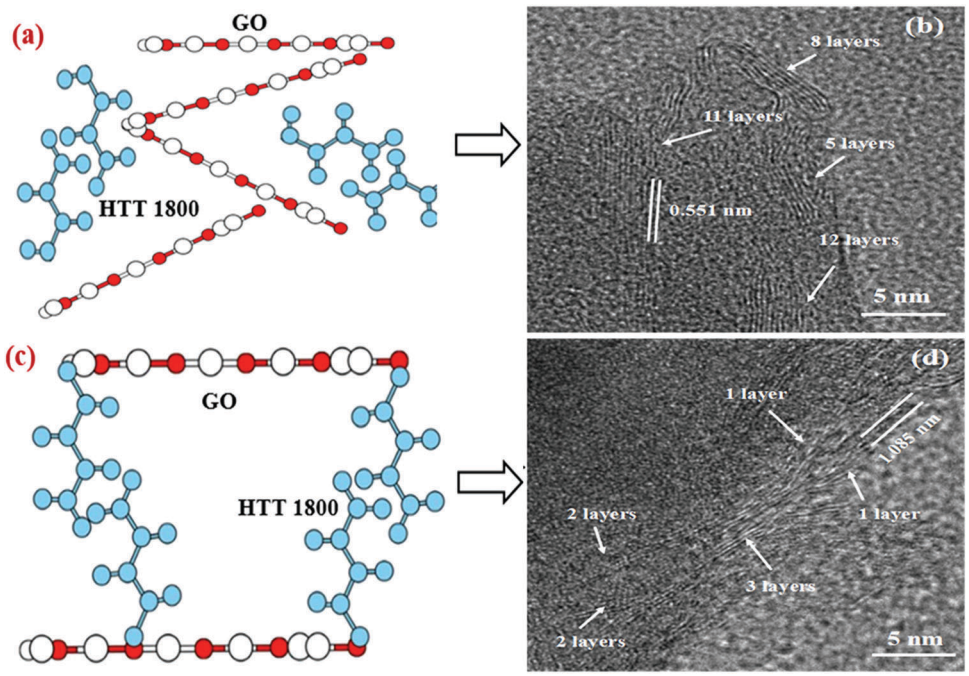

Fig. 7 Schematic illustration of (a) physically-blended-precursor and (c) SSP. TEM images of RGO–SiCN ceramic nanocomposites derived from (b) physically-blended-precursor and from (d) SSP.

(X band). According to the Debye theory, the real part of the permittivity (ε') is related to the polarization relaxation and the imaginary part of the permittivity (ε'') represents the dielectric loss capability.[40–42]

Fig. 8 shows the ε' and ε'' values of the effective complex permittivity of the resultant SiCN and RGO–SiCN nanocomposites in the X band. The HTT 1800-derived SiCN (S-1) sample exhibits a relatively low ε' with an average value of 4.87. With increasing amount of RGO (corresponding to the increasing amount of GO in the feed), the value of ε' increases gradually as shown in Fig. 8a, which is consistent with the reported literature.[16] Fig. 8b shows that ε'' also increases with increasing RGO content as follows: the ε'' of SiCN is in the range of 0.01–0.02, while those of RGO–SiCN samples S-2, S-3, S-4, S-5 and S-6 are 1.23–1.27, 1.72–1.98, 4.98–7.08, 8.49–10.62 and 9.18–16.17, respectively. An increasing fraction of RGO increases the volume of charge carriers inside the material and improves their electrical conductivity.[16] In addition to the contribution of polarizations, the conductive loss is another factor causing an increasing imaginary part, which originates from the conductive carbon network formed by RGO.[16] The polarization relaxation induced by the electron motion hysteresis in the dipole under an alternating electromagnetic field enhances the dielectric loss.[43,44] It is worth mentioning that with the same content of GO in the feed, both the ε' and ε'' values of sample S-4 derived from the SSP are significantly higher than those of sample S-3

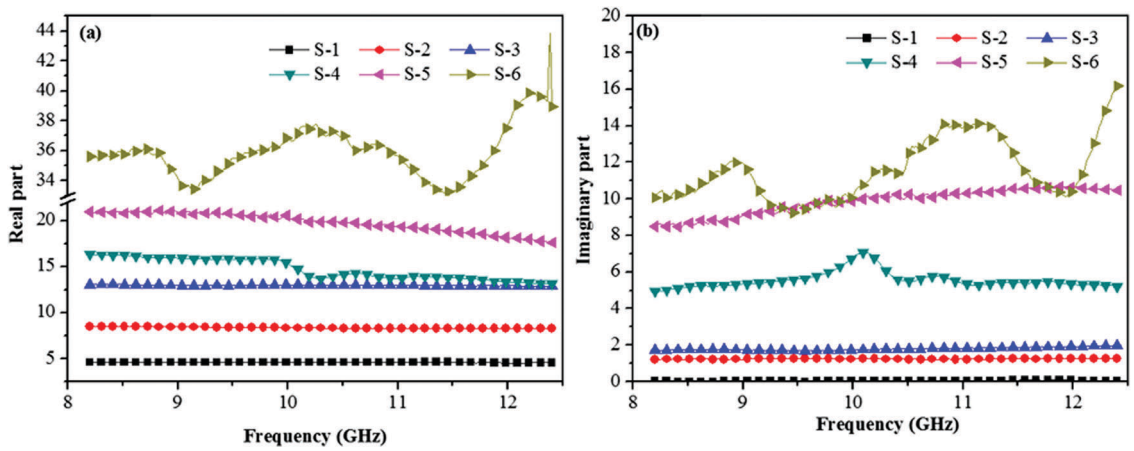

Fig. 8 (a) Real part and (b) imaginary part of the resultant SiCN (S-1) and RGO–SiCN ceramic nanocomposite samples S-2 to S-6 as a function of frequency.

obtained by physical blending. With respect to the dielectric performance this result clearly indicates the significant advantage of the SSP approach as compared to that of the physical blending method.

3.4 Electromagnetic absorption properties

The reflection coefficient (RC) is a comprehensive parameter to evaluate the absorption properties of an EM material. Based on the transmission-line theory and the metal back-panel model, the reflection coefficient (RC) can be calculated from the relative complex permeability and permittivity:[45,46]

$$\mathrm{RC(dB)} = 20 \cdot \log\left|\frac{(Z_{\mathrm{in}} - 1)}{(Z_{\mathrm{in}} + 1)}\right| \quad (1)$$

$$Z_{\mathrm{in}} = \sqrt{\frac{\mu}{\varepsilon}}\tanh\left(\frac{\mathrm{j}2\pi\sqrt{\mu\varepsilon}fd}{c}\right) \quad (2)$$

where Z_{in}, d, and μ are the normalized input impedance, thickness and permeability of the material, c is the light velocity in a vacuum, and f is the microwave frequency.

Fig. 9 shows the RC of the obtained ceramic samples as a function of frequency in the X-band. The absorption capability of S-2 with 1.0 wt% GO in the feed is weak at every sample thickness since it exhibits a minimal RC ($\mathrm{RC_{min}}$) of −7 dB. In contrast, the RC value of sample S-4 is significantly improved when the GO content increases to 2.5 wt%. It is worth pointing out that the $\mathrm{RC_{min}}$ reaches −61.9 dB at 9.0 GHz and the effective absorption bandwidth (RC values lower than −10 dB) amounts to about 3.0 GHz (from 8.2 to 11.2 GHz). By a comparison of the RC values between samples S-3 and S-4, it unambiguously shows again the significant advantage of the SSP approach over the physical blending method regarding the EM absorption properties: the $\mathrm{RC_{min}}$ of the sample S-3 is even higher than −9 dB while the sample S-4 reaches −61.9 dB. The huge difference in the $\mathrm{RC_{min}}$ of the samples S-3 and S-4 can be explained by the quality of the dispersion of RGO in the ceramic matrix as shown in Fig. 7. However, with the GO content in the feed increasing to 6.0 wt%, the value of $\mathrm{RC_{min}}$ of the sample S-5 decreases significantly (Fig. 9d). When the RGO content exceeds a certain limit, the impedance mismatching between the sample and air occurs, which could lead to a strong reflection. As a result, sample S-4 shows the most excellent absorption capability among all the RGO–SiCN samples.

As can be seen from each curve calculated from different sample thicknesses, the RC varies with varying frequency and reaches its minimal value only at a certain frequency point. This behavior is explained by the fact that if the sample thickness is the odd multiple of a quarter-wavelength, a sharp destructive interference takes place, which is caused by the inverse phase angle of the reflection EM wave from the upper and bottom surfaces. With decreasing sample thickness, the $\mathrm{RC_{min}}$ decreases while the effective bandwidth increases. To better

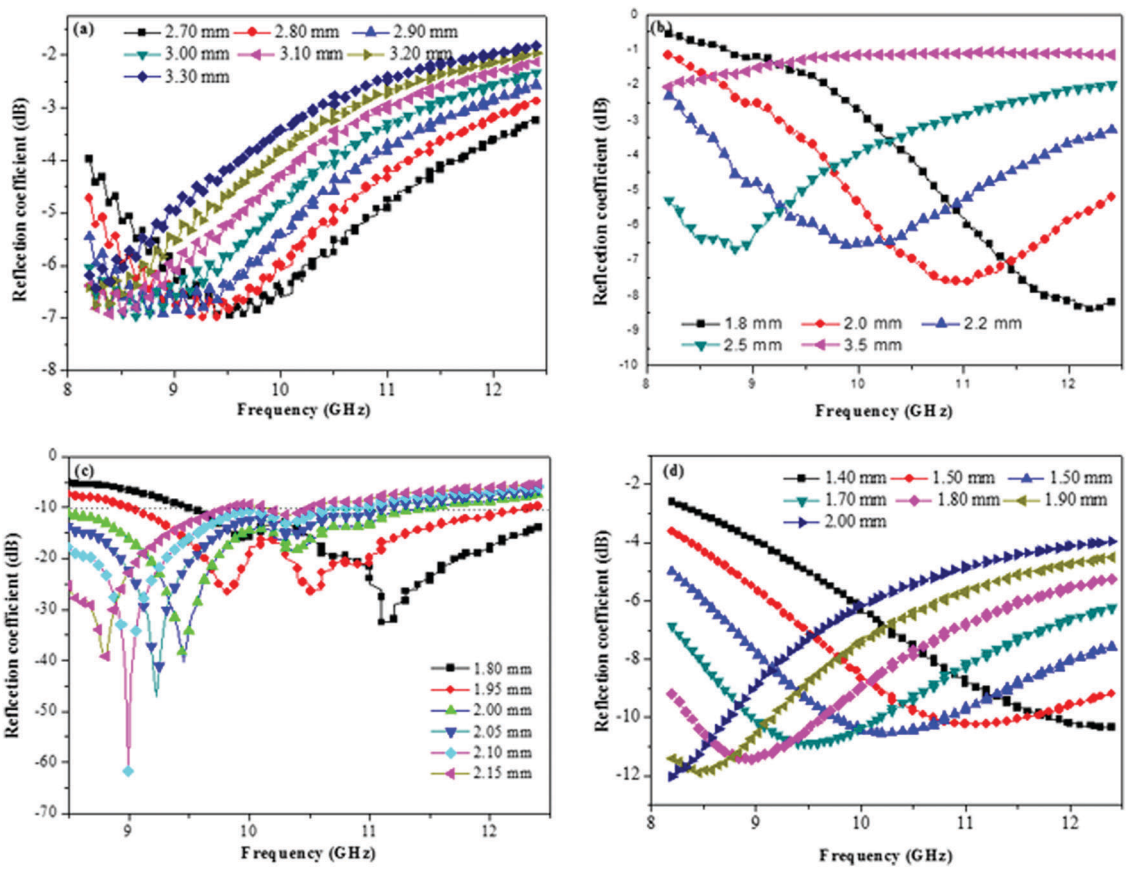

Fig. 9 Reflection coefficients of RGO–SiCN ceramic nanocomposites of the samples (a) S-2, (b) S-3, (c) S-4 and (d) S-5.

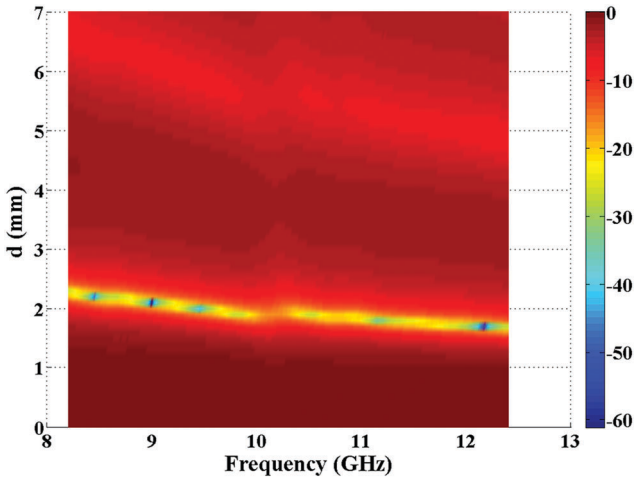

Fig. 10 Two dimensional colorful map of reflection coefficient of sample S-4.

understand the variation of RC as a function of the sample thickness, a two-dimensional colorful map of RC based on sample S-4 is shown in Fig. 10. With the sample thickness of *ca.* 2.10 mm, the corresponding RC value is much lower than that of their adjacent, indicating better EM absorbing abilities. At above the sample thickness of 2.10 mm, the reflected EM waves by the upper surface has a phase opposite to that EM wave coming from the back reflection, resulting in the total cancellation of the two waves at the air–material interface.[47] In this case, the thicknesses of the EM absorbing materials are satisfied using the quarter-wavelength law:

$$d = \left(\frac{n}{4}\right)\lambda = \left(\frac{n}{4}\right)\frac{\lambda_0}{\left(|\varepsilon_r||\mu|_r\right)^{\frac{1}{2}}} \quad (3)$$

where λ_0 is the free space wavelength and n can be assumed to be 1, 3, 5, 7...

3.5 Electromagnetic interference shielding effectiveness

The capability of a shielding material can be expressed by the electromagnetic interference shielding effectiveness or efficiency (EMI SE), indicating how many incident waves are blocked by the shielding material.[1] Theoretically, the EMI SE can be computed using Simon formalism;[48]

$$\mathrm{SE} = 50 + 10\log\left(\frac{\sigma}{f}\right) + 1.7d\sqrt{\sigma f} \quad (4)$$

where, σ [S cm^{-1}] is the electrical conductivity, f [MHz] is the frequency, and d [cm] is the thickness of the shield. The AC conductivity (σ_{AC}) of the nanocomposites can be calculated based on the imaginary part of permittivity and the frequency as follows:[44]

$$\sigma_{AC}\ (\mathrm{S\ m^{-1}}) = 2\pi f\varepsilon_o\varepsilon'' \quad (5)$$

where f is the frequency in Hz and ε_o is the permittivity of free space ($\varepsilon_o = 8.854 \times 10^{-12}$ F m^{-1}).

From the Simon formalism, the EMI SE of shielding materials strongly depends on their electrical conductivity. However, the electrical conductivity is not the scientific criterion for the EMI shielding materials since the shielding behavior requires mobile electrons inside the materials to interact with incident EM waves instead of the electrical conductive network.[49–51] When EM waves are incident into shielding materials, mobile electrons inside the absorbent interact with incident EM waves, which blocks EM waves from transmitting. To make a comparison between the σ_{AC} calculated using eqn (5) and DC conductivity (σ_{DC}) measured using a four-pin probe method, the results showed that the σ_{AC} was remarkably higher than σ_{DC}.[44] Based on the abovementioned drawbacks of Simon formalism, in the present work, the EMI SE is calculated by S-parameters which can be directly measured by the waveguide method using a vector network analyzer (see eqn (6)–(11)).[1–3]

Shielding mechanisms of a conductive shielding material include reflection, absorption and multiple reflections.[44,46] Multiple reflections are the internal reflections between the internal surfaces of the shielding material. In the case where the shielding by absorption (*i.e.*, absorption loss) is higher than 10 dB, most of the re-reflected wave will be absorbed within the shield.[44,46] Thus, multiple reflections can be ignored. Actually, when an electromagnetic wave is incident on a shielding material, the incident power is divided into reflected power (R), absorbed power (A) and transmitted power (T). The total shielding effectiveness (SE_T), absorption shielding effectiveness (SE_A), reflection shielding effectiveness (SE_R), R, T and A were calculated based on the following equations:[52,53]

$$\mathrm{SE_T} = \mathrm{SE}_R + \mathrm{SE}_A \quad (6)$$

$$\mathrm{SE_R} = -10\cdot\log(1 - R) \quad (7)$$

$$\mathrm{SE_A} = -10\cdot\log\left(\frac{T}{1-R}\right) \quad (8)$$

$$R = |S_{11}|^2 = |S_{22}|^2 \quad (9)$$

$$T = |S_{12}|^2 = |S_{21}|^2 \quad (10)$$

$$A = 1 - T - R \quad (11)$$

where S_{ij} represents the power transmitting from port i to port j.

Fig. 11 shows the EMI SE and power balance of SiCN and RGO–SiCN ceramic nanocomposites over the frequency range of 8.2–12.4 GHz. As shown in Fig. 11a, the pristine SiCN shows a low SE value of around 1.7 dB, which further demonstrates its role as an impedance matching material. With respect to the RGO–SiCN nanocomposites, the SE value increases gradually with the increasing amount of GO in the feed. The introduction of carbon nanofillers is expected to enhance the electrical conductivity. The fact that the improvement of the electrical conductivity leads to the improvement of the EMI SE has been proven and reported in the literature.[54,55] In particular, with the 12.0 wt% GO content in the feed, the maximum EMI SE value of the resultant sample S-6 reaches 41.2 dB, which means that more than 99.99% EM waves are shielded. Fig. 11b shows the change in the mean value of SE_A, SE_R and SE_T of the SiCN and RGO–SiCN nanocomposites. The SE_A increases with increasing GO content in the starting material. When the GO content in the feed is lower than 2.5 wt%, the SE_A is always lower than the

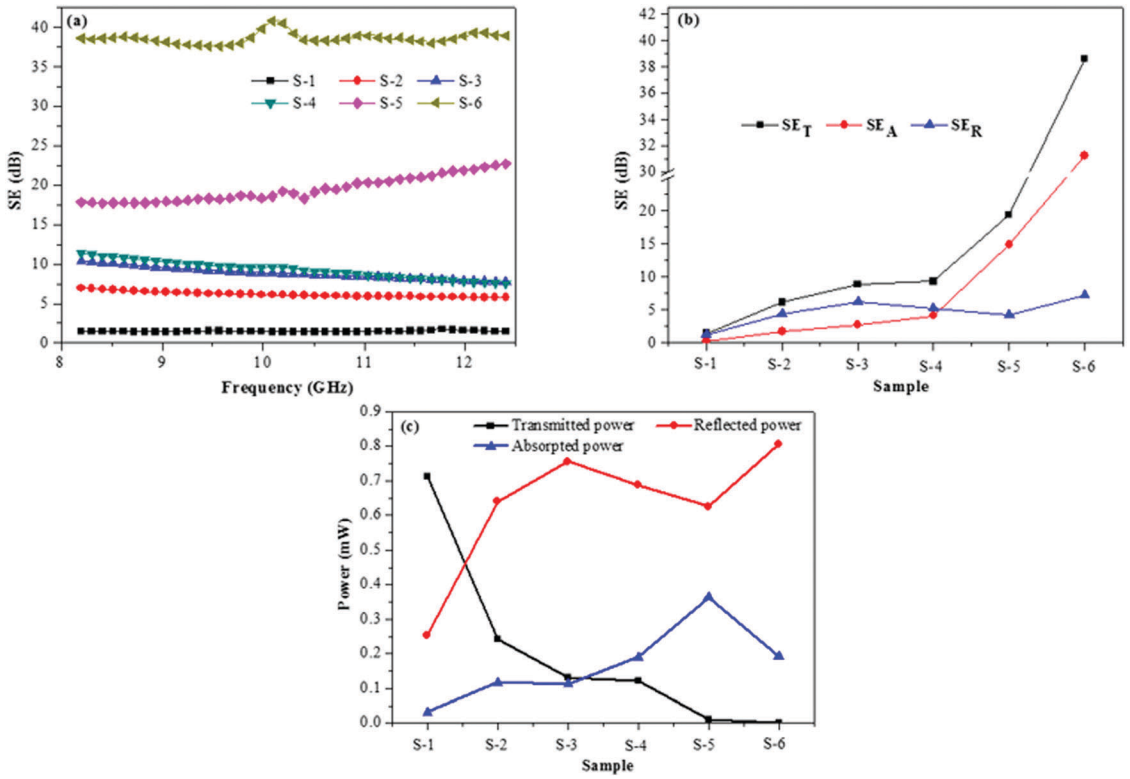

Fig. 11 (a) EMI SE and (b) average SE_T, SE_R and SE_A and (c) power balance of the resultant samples.

SE_R for samples S-2, S-3 and S-4. However, with increasing GO contents, the SE_A of S-5 becomes higher than that of the SE_R of samples S-5 and S-6. In particular, the SE_A of the material S-6 increases to 35.2 dB compared to 9.0 dB of SE_R. As can be seen from eqn (8), the SE_A represents the absorbed ratio of the microwave that reaches the interior part of the material. A high SE_A represents a material possessing a high intrinsic absorption ability. However, a high intrinsic absorption ability is always accompanied by strong reflection[52,53] which can be proven by its power balance in Fig. 11c. Actually, the reflected power (R), the absorbed power (A) and the transmitted power (T) represent the capability of a material to reflect, absorb and transmit a microwave, respectively.[44,46] As shown in Fig. 11c, the power balance reveals a remarkable increase in the reflected power and absorbed power and a decrease in the transmitted power with increasing absorbent content. With the increasing amount of GO in the starting material, the absorbed power exhibits an increasing tendency. However, when the GO content is increased to 12.0 wt%, the absorbed power of sample S-6 is decreased as compared with that of sample S-5. This phenomenon is due to the strong reflection of the material S-6. As reflection occurs before absorption, the microwaves are reflected before they reach the inner part of the material, leading to a decrease of the absorption power. Therefore, the obtained RGO–SiCN nanocomposites (S-6) are not suitable for applications requiring low reflection. However, our materials are useful for applications requiring high thermal resistance and/or high mechanical loads at elevated temperatures.[1] In order to decrease the reflection of a material, a multilayered composite material of graded electrical conductivity has to be designed in future.

4. Conclusion

Novel SSPs were synthesized *via* an amidation reaction between GO and the poly(organo)silazane HTT 1800 with the assistance of $ZnCl_2$ as a catalyst. Monolithic RGO–SiCN ceramic nanocomposites were fabricated by warm pressing of the SSP and subsequent pyrolysis of the resultant green bodies. In the case of the sample with 2.5 wt% GO content in the feed, the RC_{min} of the formed RGO–SiCN nanocomposites reaches −61.9 dB and an effective absorption bandwidth of about 3.0 GHz with a sample thickness of 2.10 mm. With the same GO content, the obtained RGO–SiCN nanocomposite derived from a physically-blended precursor as a reference sample exhibits a far inferior RC_{min} of −8.2 dB. This result unambiguously demonstrates the outstanding effectiveness of the SSP approach over the physical blending method. The sample comprising 12.0 wt% GO exhibits an EMI SE of the as-prepared RGO–SiCN of 41.2 dB at a sample thickness of 2.00 mm. The findings reported here clearly show that the SSP-derived RGO–SiCN nanocomposites possess not only exceptional but also versatile EM performance ranging from electromagnetic absorbing to shielding behavior.

Acknowledgements

Z. Y. thanks the Alexander von Humboldt Foundation, the Natural Science Foundation of China (No. 50802079), the Natural Science Foundation of Fujian Province of China (No. 2015J01221) and Creative Research Foundation of Science and Technology on Thermostructural Composite Materials

Laboratory (No. 6142911040114) for financial support. X. L. acknowledges the financial support from China Scholarship Council (No. 201406290019). R. I. and Y. I. acknowledge support from the Joint Research Project between Japan and Germany through JSPS Bilateral Program and the Exploratory Research program of MEXT, Core-to-Core Program of JSPS.

References

1 X. W. Yin, L. Kong, L. T. Zhang, L. F. Cheng, N. Travitzky and P. Greil, *Int. Mater. Rev.*, 2014, **59**, 326–355.
2 M. S. Cao, X. X. Wang, W. Q. Cao and J. Yuan, *J. Mater. Chem. C*, 2015, **3**, 6589–6599.
3 M. K. Han, X. W. Yin, H. Wu, C. Q. Song, X. L. Li, L. T. Zhang and L. F. Cheng, *ACS Appl. Mater. Interfaces*, 2016, **8**, 21011–21019.
4 N. Li, Y. Huang, F. Du, X. B. He, X. Lin, H. J. Gao, Y. F. Ma, F. F. Li, Y. S. Chen and P. C. Eklund, *Nano Lett.*, 2006, **6**, 1141–1145.
5 Y. L. Yang, M. C. Gupta, K. L. Dudley and R. W. Lawrence, *Nano Lett.*, 2005, **5**, 2131–2134.
6 B. Shen, W. Zhai and W. Zheng, *Adv. Funct. Mater.*, 2014, **24**, 4542–4548.
7 N. Yousefi, X. Y. Sun, X. Y. Lin, X. Shen, J. J. Jia, B. Zhang, B. Z. Tang, M. S. Chan and J.-K. Kim, *Adv. Mater.*, 2014, **26**, 5480–5487.
8 D. X. Yan, H. Pang, B. Li, R. Vajtai, L. Xu, P. G. Ren, J. H. Wang and Z. M. Li, *Adv. Funct. Mater.*, 2015, **25**, 559–566.
9 Z. P. Chen, C. Xu, C. Q. Ma, W. C. Ren and H. M. Cheng, *Adv. Mater.*, 2013, **25**, 1296–1300.
10 D. H. Ding, Y. M. Shi, Z. H. Wu, W. C. Zhou, F. Luo and J. Chen, *Carbon*, 2013, **60**, 552–555.
11 M. Albano, D. Micheli, G. Gradoni, R. B. Morles, M. Marchetti, F. Moglie and V. M. Primiani, *Acta Astronaut.*, 2013, **87**, 30–39.
12 R. Riedel, A. Kienzle, W. Dressler, L. Ruwisch, J. Bill and F. Aldinger, *Nature*, 1996, **382**, 796–798.
13 R. Riedel, G. Passing, H. Schönfelder and R. Brook, *Nature*, 1992, **355**, 714–717.
14 E. Ionescu, H. J. Kleebe and R. Riedel, *Chem. Soc. Rev.*, 2012, **41**, 5032–5052.
15 L. An, W. Xu, S. Rajagopalan, C. Wang, H. Wang, Y. Fan, L. Zhang, D. Jiang, J. Kapat, L. Chow, B. Guo, J. Liang and R. Vaidyanathan, *Adv. Mater.*, 2004, **16**, 2036–2040.
16 M. K. Han, X. W. Yin, W. Y. Duan, S. Ren, L. T. Zhang and L. F. Cheng, *J. Eur. Ceram. Soc.*, 2016, **36**, 2695–2703.
17 B. Wen, M. S. Cao, M. M. Lu, W. Q. Cao, H. L. Shi, J. Liu, H. B. Jin, X. Y. Fang, W. Z. Wang and J. Yuan, *Adv. Mater.*, 2014, **26**, 3484–3489.
18 Y. J. Zhang, X. W. Yin, F. Ye and L. Kong, *J. Eur. Ceram. Soc.*, 2014, **34**, 1053–1061.
19 S. Niyogi, E. Bekyarova, M. E. Itkis, J. L. McWilliams, M. A. Hamon and R. C. Haddon, *J. Am. Chem. Soc.*, 2006, **128**, 7720–7721.
20 Y. Matsuo, T. Komiya and Y. Sugie, *Carbon*, 2009, **47**, 2782–2788.
21 B. Mi, *Science*, 2014, **343**, 740–742.
22 X. F. Wang, G. Mera, K. Morita and E. Ionescu, *J. Ceram. Soc. Jpn.*, 2016, **124**, 981–988.
23 J. Yuan, S. Hapis, H. Breitzke, Y. Xu, C. Fasel, H. J. Kleebe, G. Buntkowsky, R. Riedel and E. Ionescu, *Inorg. Chem.*, 2014, **53**, 10443–10455.
24 M. Zaheer, G. Motz and R. Kempe, *J. Mater. Chem.*, 2011, **21**, 18825–18831.
25 J. Chen, M. A. Hamon, H. Hu, Y. Chen, A. M. Rao, P. C. Eklund and R. C. Haddon, *Science*, 1998, **282**, 95–98.
26 W. Huang, Y. Lin, S. Taylor, J. Gaillard, A. M. Rao and Y. P. Sun, *Nano Lett.*, 2002, **2**, 231–234.
27 W. Huang, S. Taylor, K. Fu, Y. Lin, D. Zhang, T. W. Hanks, A. M. Rao and Y.-P. Sun, *Nano Lett.*, 2002, **2**, 311–314.
28 F. Pompeo and D. E. Resasco, *Nano Lett.*, 2002, **2**, 369–373.
29 E. Ionescu, A. Francis and R. Riedel, *J. Mater. Sci.*, 2009, **44**, 2055–2062.
30 J. Qian, C. Pantea, G. Voronin and T. Zerda, *J. Appl. Phys.*, 2001, **90**, 1632–1637.
31 H. A. Becerril, J. Mao, Z. Liu, R. M. Stoltenberg, Z. Bao and Y. Chen, *ACS Nano*, 2008, **2**, 463–470.
32 S. Park and R. S. Ruoff, *Nat. Nanotechnol.*, 2009, **4**, 217–224.
33 Y. Zhu, M. D. Stoller, W. Cai, A. Velamakanni, P. D. Piner, D. Chen and R. S. Ruoff, *ACS Nano*, 2010, **4**, 1227–1233.
34 X. H. Kong, X. M. Sun, X. L. Li and Y. D. Li, *Mater. Chem. Phys.*, 2003, **82**, 997–1001.
35 M. H. Huang, Y. Wu, H. Feick, N. Tran, E. Weber and P. Yang, *Adv. Mater.*, 2001, **13**, 113–116.
36 P. Colombo, R. Riedel, G. D. Sorarù and H. J. Kleebe, *Polymer derived ceramics: from nano-structure to applications*, DE Stech Publications, Inc, 2010.
37 Y. Gao, G. Mera, H. Nguyen, K. Morita, H. J. Kleebe and R. Riedel, *J. Eur. Ceram. Soc.*, 2012, **32**, 1857–1866.
38 G. Mera, A. Navrotsky, S. Sen, H. J. Kleebe and R. Riedel, *J. Mater. Chem. A*, 2013, **1**, 3826–3836.
39 S. H. Aboutalebi, M. M. Gudarzi, Q. B. Zheng and J. K. Kim, *Adv. Funct. Mater.*, 2011, **21**, 2978–2988.
40 X. M. Liu, X. W. Yin, L. Kong, Q. Li, Y. Liu, W. Y. Duan, L. T. Zhang and L. F. Cheng, *Carbon*, 2014, **68**, 501–510.
41 Y. Liu, X. W. Yin, L. Kong, X. M. Liu, F. Ye, L. T. Zhang and L. F. Cheng, *Carbon*, 2013, **64**, 541–544.
42 L. Kong, X. W. Yin, F. Ye, Q. Li, L. T. Zhang and L. F. Cheng, *J. Phys. Chem. C*, 2013, **117**, 2135–2146.
43 F. Shahzad, M. Alhabeb, C. B. Hatter, B. Anasori, S. M. Hong, C. M. Koo, C. M. Koo and Y. Gogotsi, *Science*, 2016, **353**, 1137–1140.
44 M. H. Al-Saleh, W. H. Saadeh and U. Sundararaj, *Carbon*, 2013, **60**, 146–156.
45 R. C. Che, L. M. Peng, X. F. Duan, Q. Chen and X. Liang, *Adv. Mater.*, 2004, **16**, 401–405.

46 J. W. Liu, R. C. Che, H. J. Chen, F. Zhang, F. Xia, Q. S. Wu and M. Wang, *Small*, 2012, **8**, 1214–1221.
47 X. Y. Yuan, L. F. Cheng, L. Kong, X. W. Yin and L. T. Zhang, *J. Alloys Compd.*, 2014, **596**, 132–139.
48 M. Arjmand, M. Mahmoodi, G. A. Gelves, S. Park and U. Sundararaj, *Carbon*, 2011, **49**, 3430–3440.
49 D. D. L. Chung, *Carbon*, 2001, **39**, 279–285.
50 P. Theilmann, D. J. Yun, P. Asbeck and S. H. Park, *Org. Electron.*, 2013, **14**, 1531–1537.
51 K. Hayashida and Y. Matsuoka, *Carbon*, 2015, **85**, 363–371.
52 D. Micheli, C. Apollo, R. Pastore, R. B. Morles, S. Laurenzi and M. Marchetti, *Acta Astronaut.*, 2011, **69**, 747–757.
53 K. L. Kaiser, *Electromagnetic shielding*, CRC Press, Boca Raton, United States, 2006, pp. 1–52.
54 D. Micheli, R. Pastore, G. Gradoni, V. M. Primiani, F. Moglie and M. Marchetti, *Acta Astronaut.*, 2013, **88**, 61–73.
55 F. Moglie, D. Micheli, S. Laurenzi, M. Marchetti and V. M. Primiani, *Carbon*, 2012, **50**, 1972–1980.

Acta Materialia 130 (2017) 83–93

Contents lists available at ScienceDirect

Acta Materialia

journal homepage: www.elsevier.com/locate/actamat

Full length article

Single-source-precursor derived RGO/CNTs-SiCN ceramic nanocomposite with ultra-high electromagnetic shielding effectiveness

Xingmin Liu [b], Zhaoju Yu [a, c, *], Ryo Ishikawa [d], Lingqi Chen [e], Xiaofei Liu [e], Xiaowei Yin [e], Yuichi Ikuhara [d], Ralf Riedel [b, c, e]

[a] College of Materials, Key Laboratory of High Performance Ceramic Fibers (Xiamen University), Ministry of Education, Xiamen, 361005, China
[b] Institut für Materialwissenschaft, Technische Universität Darmstadt, D-64287, Darmstadt, Germany
[c] College of Materials, Fujian Key Laboratory of Advanced Materials (Xiamen University), Xiamen, 361005, China
[d] Institute of Engineering Innovation, University of Tokyo, Bunkyo, Tokyo, 113-8656, Japan
[e] Science and Technology on Thermostructural Composite Materials Laboratory, Northwestern Polytechnical University, Xi'an, 710072, China

ARTICLE INFO

Article history:
Received 22 January 2017
Received in revised form
11 March 2017
Accepted 13 March 2017
Available online 15 March 2017

Keywords:
Single-source-precursor
Ceramic nanocomposite
RGO/CNTs hybrids
Dielectric properties
Electromagnetic shielding

ABSTRACT

For the first time, single-source-precursors (SSPs) were synthesized through chemical modification of a commercial poly(methylvinyl)silazane with chemically bonded graphene oxide and carbon nanotube hybrids (GO/CNTs). After pyrolysis of warm-pressed and consolidated SSP-powders at 1000 °C in Ar, monolithic SiCN ceramic nanocomposites modified with in-situ thermally reduced GO/CNTs, namely RGO/CNTs-SiCN, were successfully obtained. The SSP-derived nanocomposite exhibits significantly enhanced dielectric properties if compared with that of a physically-blended-precursor derived reference material. Moreover, the SSP-derived RGO/CNTs-SiCN composite containing 15.0 wt% GO/CNTs in the feed possesses an electromagnetic shielding effectiveness of 67.2 dB with a sample thickness of 2.00 mm, which is the highest value among all the reported graphene-based composites with comparable thickness.

1. Introduction

High frequency electromagnetic (EM) waves with wavelengths varying from 2.4×10^{-2} to 3.7×10^{-2} m are widely used in various environments, especially for critical electronic equipment in wireless communication, medical and aerospace applications, indicating the increasing demands for high efficient EM shielding materials [1,2]. Besides high efficiency, in some applications EM materials have to be operated in high temperature and oxidizing environments and/or under high mechanical load, where polymer, carbon foam and carbon film based EM materials lose their superiority [2–4]. Polymer-derived ceramics (PDCs) are considered to be promising candidate materials for EM applications due to their intrinsic advantages including tunable permittivity, excellent oxidation resistance, high thermal stability and high temperature mechanical properties [1,5]. Basically, the real part of permittivity ε' and imaginary part of permittivity ε'' should amount >20 and > 10, respectively for EM shielding applications [1]. However, due to their intrinsic low permittivity, high temperature resistant ceramics in general cannot be applied as EM shielding materials [1,6].

Nano carbon phases such as carbon nanotubes (CNTs) and reduced graphene oxide (RGO) have been widely used as absorbent in EM materials because of their activated carrier hopping associated with defect states [7–10]. As for their use in ceramic-based EM materials, at least two different architectures can be conceived: a) carbon nanofillers can be used as absorbent to improve the permittivity [11,12], b) ceramic matrices can adjust the impedance matching and protect the carbon fillers from harsh environment [11–13]. However, due to the strong Van der Waals interactions between each individual nanofiller, a homogeneous distribution of carbon nanofillers in PDC matrices by blending or mechanical mixing is still challenging since agglomeration of nanofillers will unavoidably occur during the polymer-to-ceramic transformation

* Corresponding author. College of Materials, Key Laboratory of High Performance Ceramic Fibers (Xiamen University), Ministry of Education, Xiamen, 361005, China.
E-mail address: zhaojuyu@xmu.edu.cn (Z. Yu).

http://dx.doi.org/10.1016/j.actamat.2017.03.031
1359-6454/

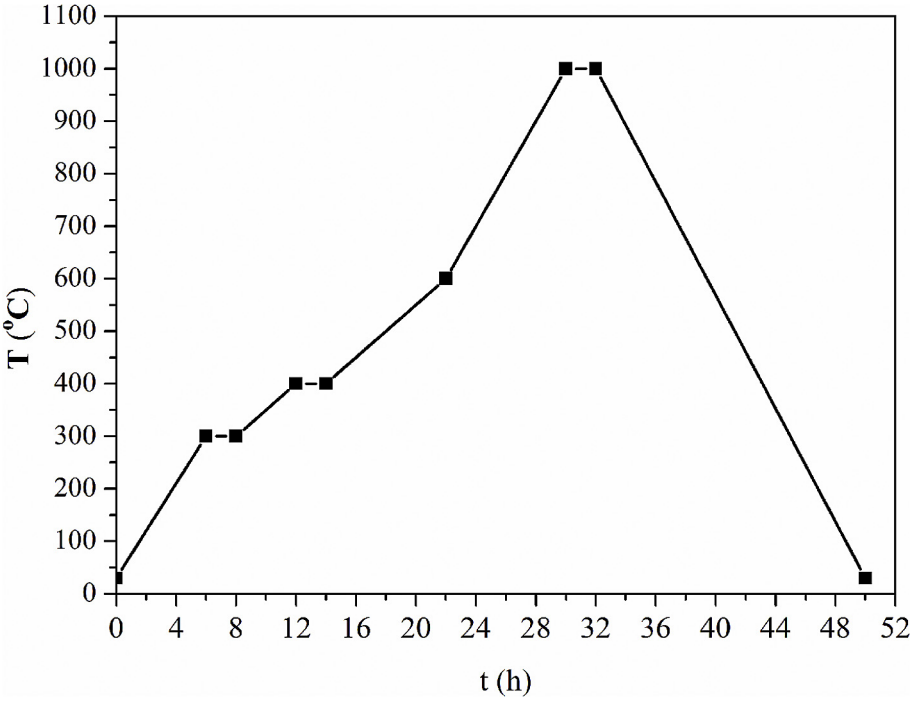

Fig. 1. Heating program on synthesis of RGO/CNTs-SiCN nanocomposites.

from liquid to solid when the mechanical force is removed [14]. The agglomeration of nanofillers leads to a decreased interface polarization and relaxation, and thus results into an inferior EM performance [12].

An assembly of RGO with CNTs can yield RGO/CNTs hybrids with enhanced functional properties as compared to their individual components due to synergistic effects [15–17]. In our previous work based on RGO/CNTs-modified poly(dimethylsiloxane) (PDMS) composites prepared by mechanical blending, a significant synergistic effect was analyzed by the fact that the minimal reflection coefficient (RC_{min}) of CNTs-PDMS, RGO-PDMS and RGO/CNTs-PDMS amounts −10, −14 and −55 dB, respectively [18]. However, EM properties of RGO/CNTs-modified PDCs never have been reported yet, due to the aforementioned limitation of homogeneous dispersion of carbon nanofillers in PDC matrices. In this report, for the first time, we successfully fabricated nanocomposites containing SiCN modified by three dimensional (3D) hierarchical RGO/CNTs hybrids (RGO/CNTs-SiCN) synthesized by a single-source-precursor (SSP) route in order i) to take advantage of outstanding EM absorption properties of RGO/CNTs hybrids and ii) to avoid aggregation of carbon nanofillers in a PDC matrix. The micro/nanostructure, dielectric properties and EM shielding performance of the obtained RGO/CNTs-SiCN nanocomposites were investigated in detail.

2. Experimental

2.1. Materials synthesis

Commercially available amino functionalized multi-walled carbon nanotubes (MWCNTs-NH_2) and GO powders employed in this study were purchased from Xianfeng Nano, China. Polysilazane HTT 1800 (KiON Specialty Polymers) was used as precursor for SiCN. The GO and MWCNTs-NH_2 were separately dispersed in anhydrous ethanol by a weight ratio of 1:1000 in an ultrasonication bath for 4 h before they were blended together with the weight ratio of GO/CNTs of 4:1. Then $ZnCl_2$ (Sigma-Aldrich, Germany) catalyst by a weight percentage of 2.0 wt% to GO/CNTs/ethanol reaction mixture was added. After ultrasonication at 50 °C for 4 h, the obtained GO/CNTs hybrids were separated with the assistance of centrifugation (5000 r/min) and washed with anhydrous ethanol for 5 times. The obtained GO/CNTs hybrids were chosen as the derivative of microwave absorbent and blended into DMF with a weight ratio of 1:500 in a flask. After ultra-sonication for 2 h, the $ZnCl_2$ catalyst was introduced into the GO/CNTs-DMF mixture with a weight ratio of catalyst/HTT 1800 of 2:98. After the reaction solution was heated up to 70 °C for 72 h under argon flow and magnetic stirring, the as-synthesized single-source-precursor was crosslinked at 120 °C before the solvent was removed under vacuum. After ball milling for 3 h, the GO/CNTs-HTT 1800 single-source-precursor powders were warm pressed to rectangular green bodies with dimensions of 50.0 × 40.0 × 2.5 mm^3 under a pressure of 60 KN. After pyrolysis in Ar atmosphere under the heating program shown in Fig. 1, the obtained RGO/CNTs-SiCN nanocomposites were machined into samples with dimensions of 22.86 × 10.16 × 2.00 mm^3 by wire cutting for the measurement of dielectric properties. The synthesis procedure of RGO/CNTs-SiCN nanocomposites by the SSP approach is shown in Fig. 2.

Moreover, Table 1 summarizes the starting compositions used to prepare the carbon nanofiller-free SiCN ceramic (sample S1), SiCN-based nanocomposites derived from SSPs and from a physically-blended-precursor (PBP) GO/CNTs/HTT 1800 mixture (sample S3).

2.2. Characterization methods

FT IR spectra were collected using a Bruker Vertex 70 FT-IR instrument (Bruker, USA) in attenuated total reflectance geometry. TGA was carried out with a thermal analysis device (STA 449C Jupiter, Netzsch, Germany). The thermal analysis included heating under flowing argon with a rate of 5 °C/min up to 1000 °C and free cooling down to room temperature. X-ray diffraction (XRD) was

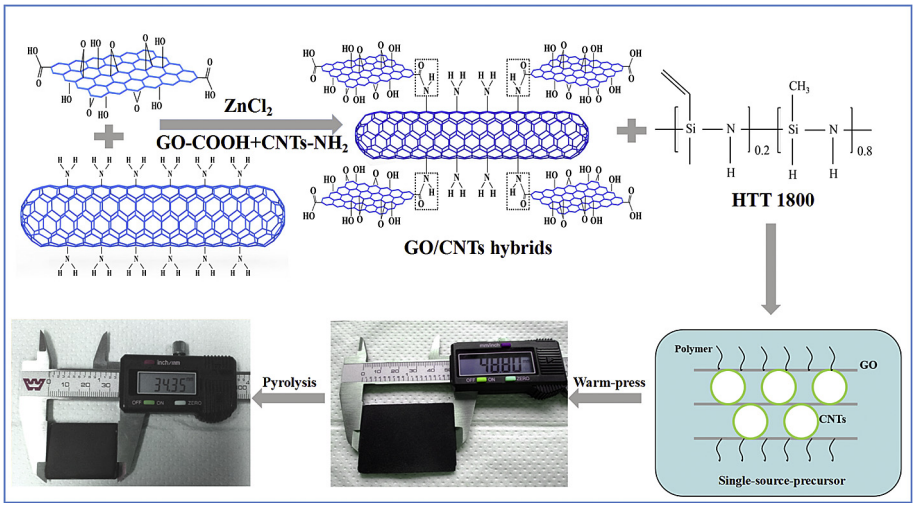

Fig. 2. Synthesis procedure of RGO/CNTs-SiCN nanocomposites.

Table 1
Content of catalyst and carbon nanofiller in the feed.

Ceramic sample	Precursor	Type of carbon nanofiller	GO: CNTs (Weight ratio)	Carbon nanofiller (wt.%)	$ZnCl_2$ (wt.%)
S1	HTT 1800	none	/	0.0	0.0
S2	SSP-GO-2.0	GO	/	2.0	2.0
S3[a]	PBP-hybrids-2.0	GO/CNTs	4:1	2.0	0.0
S4	SSP-hybrids-2.0	GO/CNTs	4:1	2.0	2.0
S5	SSP-hybrids-10.5	GO/CNTs	4:1	10.5	2.0
S6	SSP-hybrids-15.0	GO/CNTs	4:1	15.0	2.0

[a] S3 was obtained by pyrolysis of physically blended GO/CNTs/HTT 1800 mixture.

employed to conduct phase analysis (X0Pert Pro; Philips, Netherlands). The microstructure of the samples was observed by scanning electron microscopy (SEM; S-4799, Hitachi, Tokyo, Japan). Transmission electron microscopy (TEM) studies were conducted on ground ceramic powder samples using a JEM-2100 (Japan) microscope at an acceleration voltage of 200 kV (wavelength l52.51 p.m.). The BF/DF TEM observations and electron diffraction patterns on the GO/CNTs hybrids and on the bulk ceramic samples were taken by a JEOL 2010HC, operated at 200 kV. The ADF/BF-STEM images were acquired with a JEOL ARM300CF, equipped with JEOL COSMO aberration corrector, a cold field emission gun, and an EDXS silicon drift detector. The microscope is operated at 80 and 300 kV and the illumination angles are 27 and 24 mrad, respectively. Electrical conductivity was measured by two-wire probe using a current source (Keithley 6220 DC; Ohio, USA). The open porosities were measured using Archimedes method according to ASTM C-20 standard. The scattering parameters (S-parameters) were measured by waveguide method using a vector network analyzer (VNA, MS4644A; Anritsu, Japan) from 8.2 to 12.4 GHz (X-band).

3. Results and discussion

3.1. Characterization of single-source-precursor GO/CNTs-HTT 1800

The pristine GO, CNT-NH_2 and GO/CNTs hybrids were characterized with FT IR (Fig. 3). Fig. 3a shows the FT IR spectra of pristine GO, CNT-NH_2 and GO/CNTs hybrids starting from the CNT-NH_2 with an amino content of 0.45 wt%. It is worth mentioning that the absorption band corresponding to the C═O of carboxylic groups (1730 cm^{-1}) in GO is partially replaced by new absorption bands (1646 cm^{-1}, assigned to C═O of amide groups) due to the

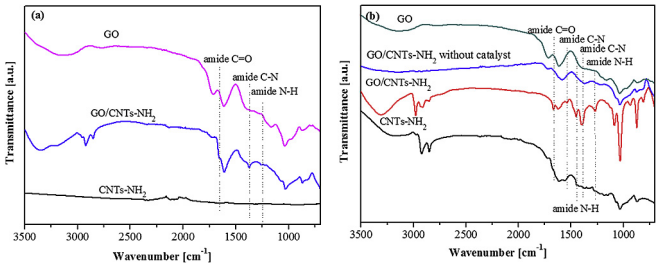

Fig. 3. (a) FT IR spectra of pristine GO, CNTs-NH_2 and GO/CNTs hybrids starting from the CNTs-NH_2 with an amino content of 0.45 wt%, (b) FT IR spectra of pristine GO, CNTs-NH_2 and GO/CNTs hybrids starting from the CNTs-NH_2 with an amino content of 2–3 wt%.

amidation reaction [19,20]. Besides, the new bands at 1332 cm^{-1} and 1454 cm^{-1} are assigned to the stretching vibrations of amide C–N and N–H bonds, respectively [19–23]. The partial replacement of COOH groups by amide (–CONH–) groups indicates that the amidation reaction between GO-COOH and CNTs-NH_2 did take place. Regardless of the CNT ratio in the feed, remaining COOH groups can always be found in the obtained GO/CNTs hybrids, which can be used to further react with the polysilazane precursor. Fig. 3b is the FT IR spectra of GO, CNTs-NH_2 with a higher amino content of 2–3 wt%, and the obtained GO/CNTs hybrids with and without $ZnCl_2$ as catalyst. Due to the increase of the amino content in the CNTs from 0.45 to 2–3 wt%, the intensities of the as-formed amide bands of the GO/CNTs hybrids synthesized with the catalyst significantly increase as compared to those shown in Fig. 3a. However, the FT IR spectrum of GO/CNTs hybrids without $ZnCl_2$ as catalyst shows no changes as compared to that of pristine GO. Again, this finding strongly indicates that $ZnCl_2$ catalyst is

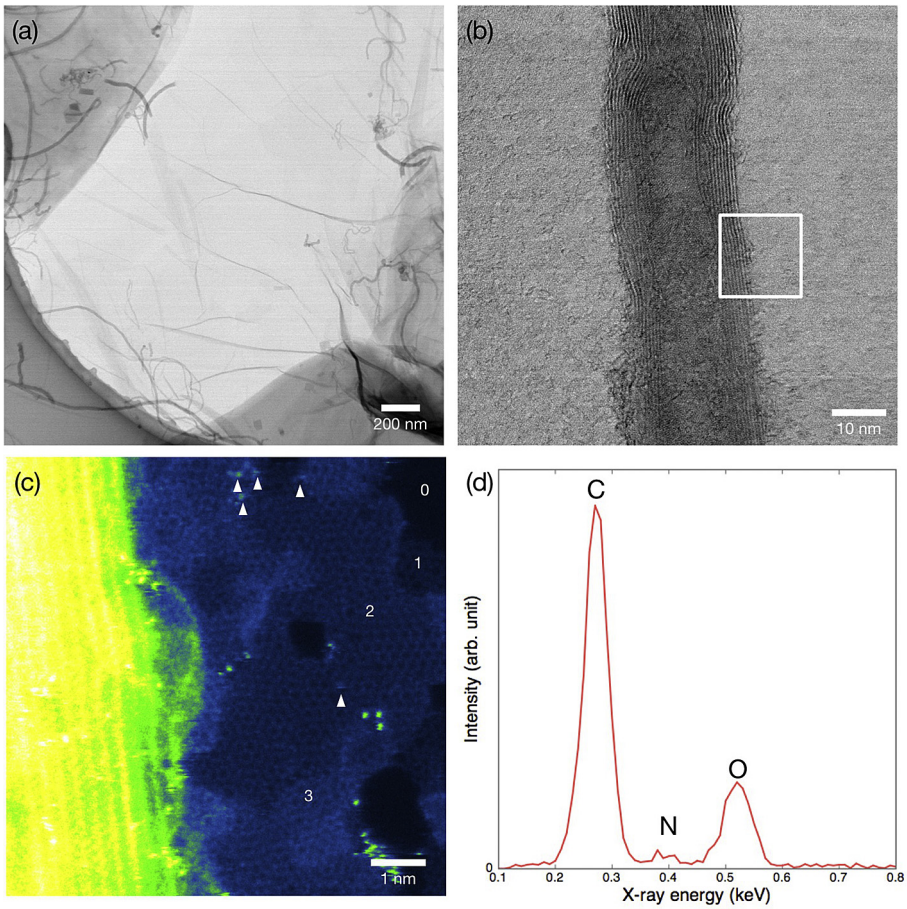

Fig. 4. (a) Low-magnification BF-STEM image of GO/CNTs and (b) single CNT, (c) atomic-resolution ADF-STEM image obtained from the corresponding area in (b) (marked by white rectangle). The numbers and white arrowheads in (c) indicate the number of graphene layers and the location of single oxygen atoms, respectively. (d) EDXS spectrum acquired from GO substrate region.

necessary for the successful amidation reaction between GO-COOH and CNTs-NH_2. It is worth mentioning that the COOH groups disappear completely, indicating the complete reaction of COOH groups on GO. Since no carboxylic groups were remained after the amidation reaction, the further reaction of GO/CNTs hybrid with the polysilazane HTT 1800 is impossible. Therefore, in the present work, CNTs-NH_2 with lower amino content (0.45 wt%) are employed to fabricate GO/CNTs hybrids.

Fig. 4 shows the TEM image and EDXS spectrum of resultant chemically bonded GO/CNTs hybrids. Fig. 4a is a low magnification bright-field scanning transmission electron microscopy (BF-STEM) image of the obtained GO/CNTs hybrids. Though the GO is difficult to identify because of its weak scattering power (and thin structure), the tubular contrast of CNTs can be seen not isolated but always on the substrate of GO. It is noteworthy that, for the preparation of electron transparent thin specimens, we used ultrasonic sonication method in ethanol (exposed by 1 h), but CNTs seem to be still well attached onto GO. Fig. 4b shows a high magnification BF-STEM image of single CNT with GO, where the CNT consists of multi-wall nanotubes. We observed a number of different regions, but basically all the CNTs are well attached onto GO, which is most evident in the atomic-resolution ADF-STEM image (annular dark field), as shown in Fig. 4c. Though the used electron probe has a relatively large depth of field (>5 nm), the observed flat regions are well focused on both CNT edge and GO substrate over the large areas. Therefore, CNTs and GO are chemically bonded between each other. Moreover, we performed energy dispersive x-ray spectroscopy (STEM-EDXS) at few-layer-graphene regions and the spectrum is given in Fig. 4d. The EDX spectrum shows strong oxygen intensity (due to the COOH and OH groups of GO) and weak nitrogen intensity (due to amide groups of chemically bonded GO/CNTs). Therefore, we identify that our starting material is characterized by the presence of GO/CNTs hybrids and that the constituents are well-bonded between each other, which agrees well with the FT IR results shown in Fig. 3.

Fig. 5 shows the FT IR spectra of pure HTT 1800 and resultant single-source-precursors. In the FT IR spectrum of HTT 1800, typical absorption bands related to C–H (2960 and 2965 cm^{-1}), Si–N–H (1160 cm^{-1}), and Si–N (930 cm^{-1}) groups appear [24,25]. After amidation in the presence of the $ZnCl_2$ catalyst, new peaks located at ν = 1332 cm^{-1} (amide C–N), ν = 1646 cm^{-1} (amide C=O), ν = 1590 cm^{-1} (amide N–H) are assigned, which supports the expected reaction between COOH groups of GO and NH groups of the polysilazane HTT 1800 [19–23]. However, for the spectrum of the physically-blended-precursor PBP-hybrid-2.0, these new peaks are not detected. This result strongly indicates that the single-source-precursor was successfully synthesized by the amidation reaction between GO and HTT 1800 with the assistance of $ZnCl_2$ catalyst. Based on the findings that the esterification and dehydrogenative coupling reactions can be effectively catalyzed by Lewis acids such as $FeCl_3$ and $ZnCl_2$ [26,27], we here propose a possible reaction mechanism for the present amidation reaction. Accordingly, $ZnCl_2$ serves as a Lewis acid catalyst and activates the carboxylic group by coordination of the Zn atom at the O atom of

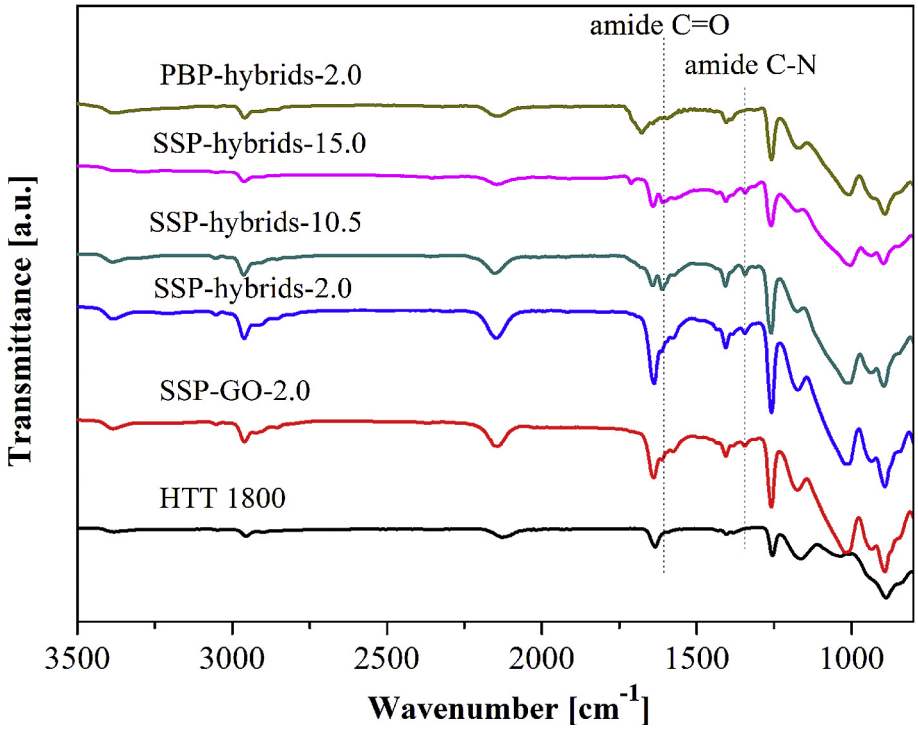

Fig. 5. FT IR spectra of HTT 1800, single-source-precursors and physically-blended-precursor.

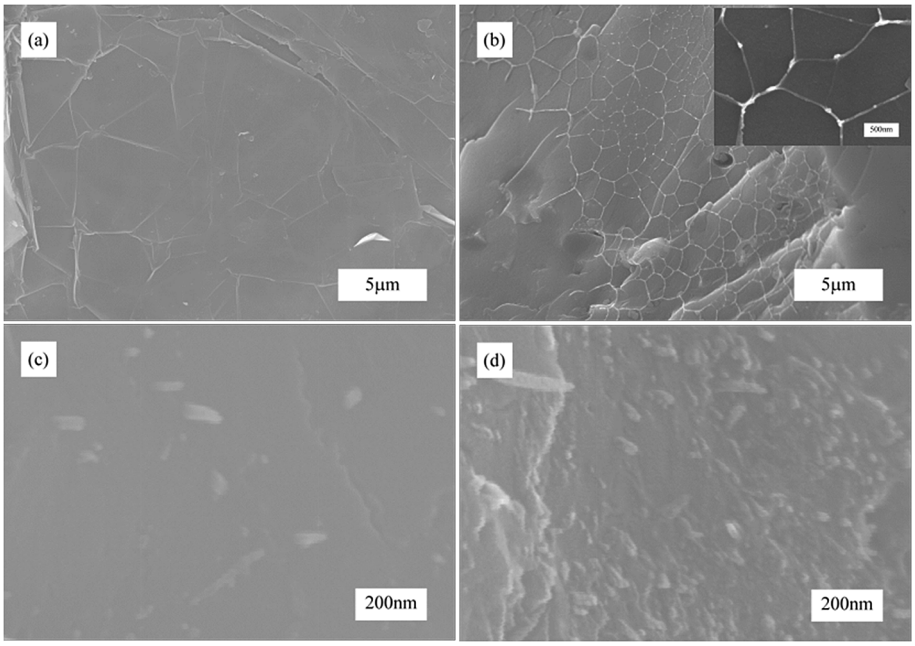

Fig. 6. SEM images of the fracture surface of densified (a) SiCN, (b) RGO/CNTs-SiCN from sample S6 (insert shows a high magnification image), (c) S4 and (d) S6.

the C═O group. Then, NH– of the polysilazane reacts with the activated carboxylic C atom by a nucleophilic attack.

3.2. Morphology and microstructure

Representative SEM images of fracture surfaces of the formed ceramic samples are shown in Fig. 6. Fig. 6a and b are low magnification SEM images of HTT 1800-derived SiCN (S1) and RGO/CNTs-SiCN (S6) with 15.0 wt % GO/CNTs hybrids in the feed. Low magnification SEM images of resultant ceramic nanocomposites did not reveal defects in any of the specimens and confirmed a relatively dense microstructure with open porosities of as low as 5.1–5.3%. In Fig. 6b, an obvious and unique network structure (with the width of 80–100 nm) can be clearly identified in form of an interconnecting bright phase, which is considered to result from the carbon nanofillers since no such microstructural features were found inside the pure SiCN matrix. The high magnification images of RGO/CNTs-SiCN derived from samples S4 and S6 (Fig. 6c–d) clearly indicate that the CNTs are uniformly dispersed in the SiCN-matrix. Despite increasing amount of GO/CNTs hybrids in the feed from 2.0 wt% (S4) to 15.0 wt% (S6), no agglomeration of the carbon nanofillers in the ceramic matrix was found.

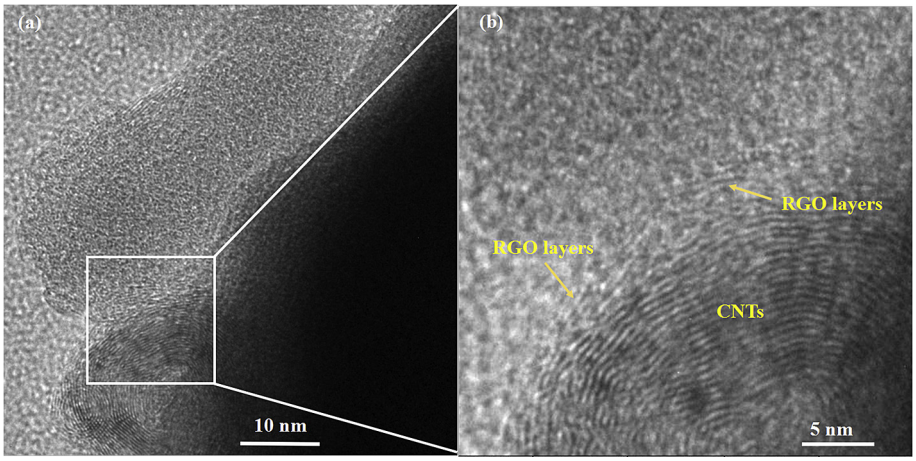

Fig. 7. (a) Typical high resolution TEM image of resultant RGO/CNTs-SiCN nanocomposites, (b) magnified image of the corresponding area in (a) (marked by white rectangle).

To further investigate the morphology of the RGO/CNTs hybrids in the SiCN matrices, TEM observation was employed and the results are shown in Fig. 7. Fig. 7a is a representative TEM image of the RGO/CNTs-SiCN nanocomposite, revealing that the integrity of the CNTs is retained. In the higher magnification TEM image (Fig. 7b), it is obvious, that the CNTs and RGO (2 layers) are still in contact after processing, including single-source-precursor synthesis, warm pressing and pyrolysis. This result clearly demonstrates that the integrity of the nanocarbon phase, namely RGO/CNTs, is retained after the pyrolysis procedure, which is shown by the homogeneous distribution of the CNTs in the ceramic matrix (see Fig. 6d).

Fig. 8a shows the ADF-STEM image of the RGO/CNTs-SiCN (sample S6). In agreement with the SEM image, the dark-line contrast in the ADF-STEM image forms a network with the width of *ca.*100 nm. The electron diffraction pattern (Fig. 8b) shows the amorphous nature of our material. To confirm the composition of the networks, we performed STEM-EDXS imaging at the corresponding area in Fig. 8a and the EDXS maps (at.%) are given in Fig. 8c–f, where we use the edges of (c) Si-K, (d) C-K, (e) N-K and (f) O-K, respectively. It is clear that silicon is predominantly located in the matrix and is poor in the networks, which is compatible with the dark-line contrast in ADF-STEM. On the other hand, the carbon content is rich at the ADF dark-line contrast region. Taking into account the FT IR, XRD and Raman spectroscopic results, it is reasonable to conclude that the matrix is comprised of SiCN while the interphase region (network) is a carbon-rich phase. The formation of the carbon-rich networks undoubtedly facilitates electrons to travel fast over long distances, which is expected to enhance the electrical conductivity or dielectric properties of the final nanocomposites [8,28].

Fig. 9 shows the XRD and Raman results of the synthesized ceramic nanocomposites. In Fig. 9a, the HTT 1800 derived SiCN shows a complete amorphous feature which agrees well with previous reports in the literature [29,30]. As for the RGO/CNTs-SiCN ceramic (sample S6), a weak peak stemming from graphitic carbon at $2\theta = 26.5^{\circ}$(002 plane) is found and no reflections related to the used $ZnCl_2$ catalyst occur. During the pyrolysis, reduction gaseous byproducts including CH_4, CO and H_2 can be released [29]. These byproducts together with the carbon nanofillers introduced into the matrix can reduce the $ZnCl_2$ catalyst into gaseous Zn, and the gaseous Zn finally evaporated out of the ceramic [31]. Fig. 9b shows the Raman spectra of the formed RGO/CNTs-SiCN samples. The graphitization grade (G_G) of a carbon containing material can be calculated as follows: $I_G/(I_G + I_D)$, where I_G and I_D is the intensity of disorder-induced (D) and graphite-like (G) bands, respectively [32,33]. When the content of hybrids increases from 0.0 wt% to 15.0 wt%, the G_G of the synthesized ceramics increases from 46.7% to 49.9%, indicating that the introduction of RGO/CNTs can lead to an improvement of the degree of graphitization of the material [32–34].

3.3. Electrical conductivity

Electrical conductivity is an important parameter for the prediction of electromagnetic properties of non-magnetic materials [1]. Based on the literature that the DC electrical conductivity of bulk graphene foam and monolithic carbon nanotubes reinforced carbon fiber/pyrolytic carbon (CNTs-C_f/C) composites were measured with a two-probe method [32,35], the electrical conductivity of as-prepared monolithic ceramic samples were determined by the same method and the results are shown in Fig. 10. The measured electrical conductivity of the SiCN ceramic matrix amounts ~10^{-7} S cm^{-1}, which agrees well with reference [30]. In general, with the introduction of RGO or RGO/CNTs into the SiCN matrix, the electrical conductivity of the carbon nanofiller modified SiCN nanocomposite increases significantly. With the highest GO/CNTs content (15.0 wt%) in the feed, the electrical conductivity of the final RGO/CNTs-SiCN composites reaches the maximum value (~5.7 S cm^{-1}). The increase of electrical conductivity is due to the following reasons: Firstly, the RGO and RGO/CNTs nanofillers inside the matrix can build up flowing paths for the mobile charge carriers inside the ceramic matrix and with the increase of nanofiller content, the amount of flowing paths will increase accordingly. It is well known that the electrical conductivity of RGO and CNTs is far superior than that of SiCN ceramic [36,37]. Therefore, with the same cross section, the carbon nanofillers provide better flowing path for the mobile charge carriers, leading to an improved electrical conductivity [32]. Secondly, the in-situ formed networks inside the ceramic matrix can also contribute to the improvement of electrical conductivity since the networks are composed of carbon rich phase (see Fig. 8). The establishment of these carbon rich networks provide a smooth way for the long-distance transport of the mobile charge carriers [8].

3.4. Dielectric properties

The relative complex permittivity ($\varepsilon = \varepsilon' - j\varepsilon''$) of resultant RGO/CNTs-SiCN ceramics was measured in the frequency range of 8.2–12.4 GHz (X band). According to the Debye theory, the real part of the permittivity (ε') is related to the polarization relaxation and the imaginary part of the permittivity (ε'') represents the dielectric loss capability, which is determined by the electrical conductivity of the materials and tangent loss ($\tan\delta = \varepsilon''/\varepsilon'$) represents the microwave attenuation capability [1,2,7].

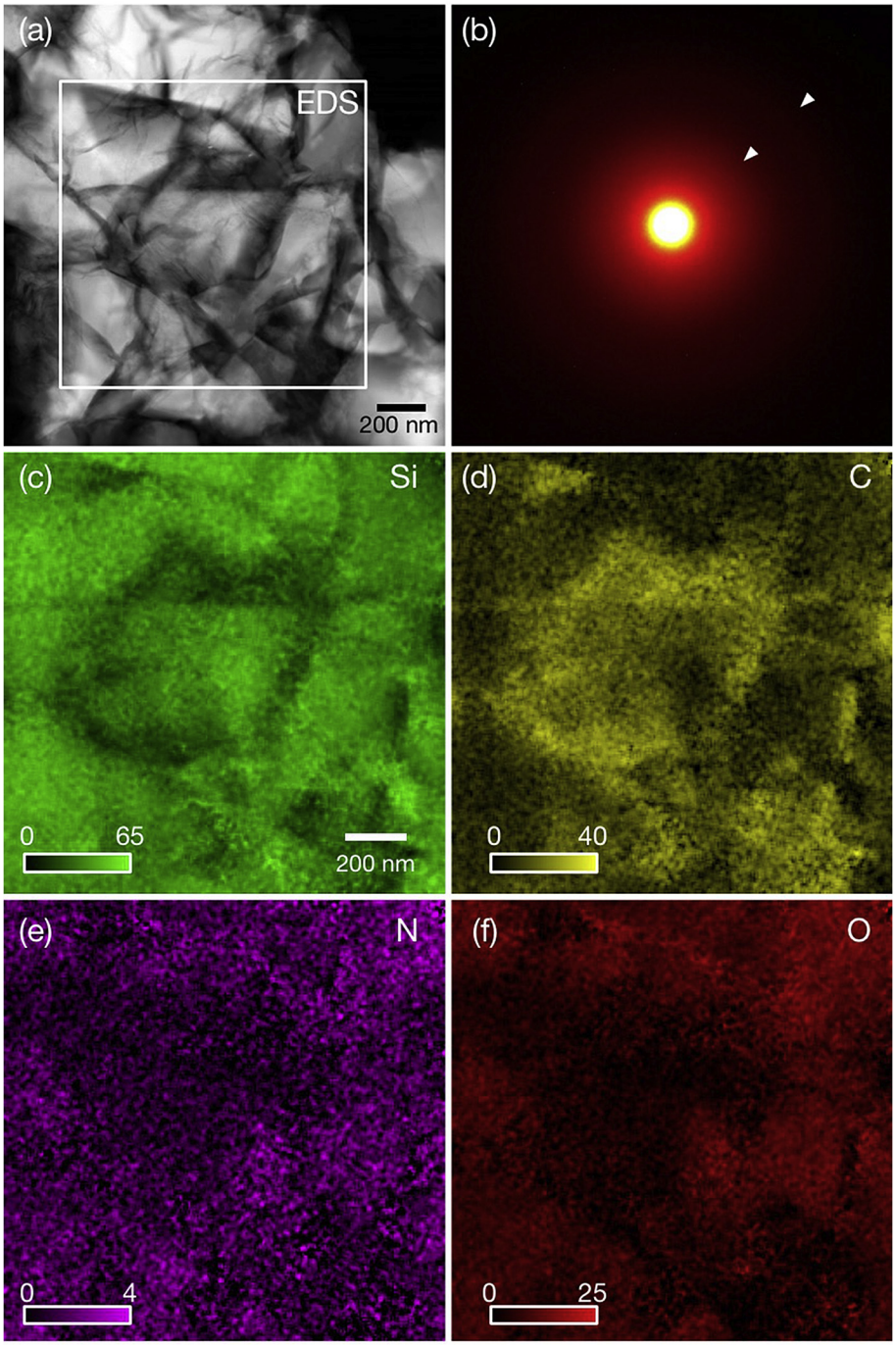

Fig. 8. (a) ADF-STEM image of the sample RGO/CNTs-SiCN (S6), and (b) the corresponding electron diffraction pattern. STEM-EDXS elemental maps (at.%) acquired from the area shown in (a): (c) Si, (d) C, (e) N, (f) O, respectively. The intensity scale bars in EDXS maps are given in each panels and the unit is at.%.

In Fig. 11a and b, the SiCN (sample S1) presents a low ε' (with an average value of 4.87) and ε'' (9.10×10^{-3}-1.01×10^{-1}), indicating that amorphous SiCN possesses an electromagnetic wave transparent property [1], which well demonstrates the role of SiCN as an impedance matching phase in the obtained RGO/CNTs-SiCN nanocomposites. By the addition of carbon-based absorbent phases into the SiCN matrix, both ε' and ε'' increase gradually with increasing amount of RGO/CNTs in the SiCN matrix. The increased ε' is discussed in terms of dipole polarizations induced by the defects inside the nanofillers including RGO and RGO/CNTs hybrids [12]. Polarization relaxations induced by electron motion hysteresis under alternating EM field and

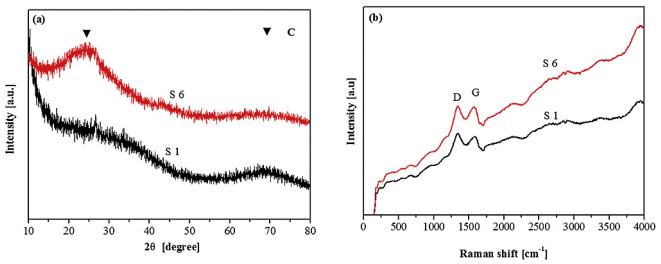

Fig. 9. (a) XRD and (b) Raman spectra of HTT1800-derived SiCN (S1) and RGO/CNTs-SiCN (S6) ceramic nanocomposites.

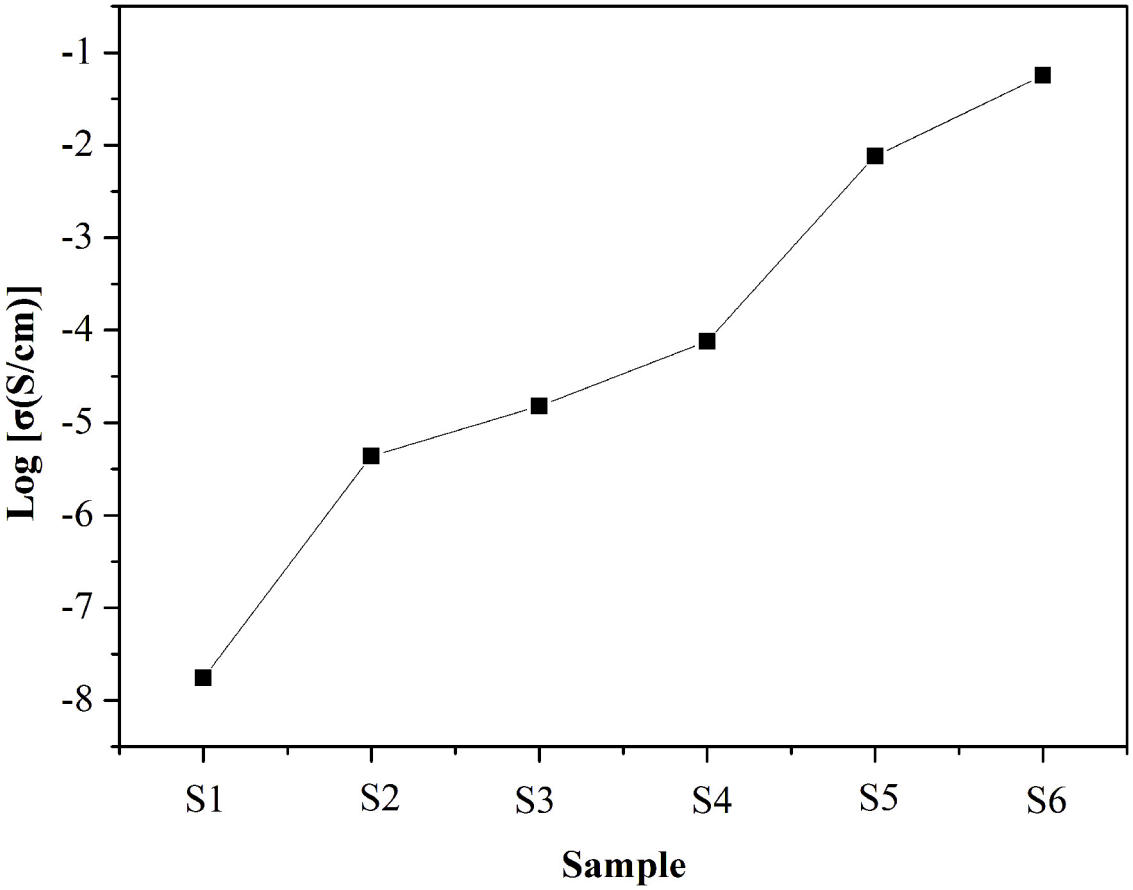

Fig. 10. Electrical conductivity of as-prepared ceramic nanocomposites.

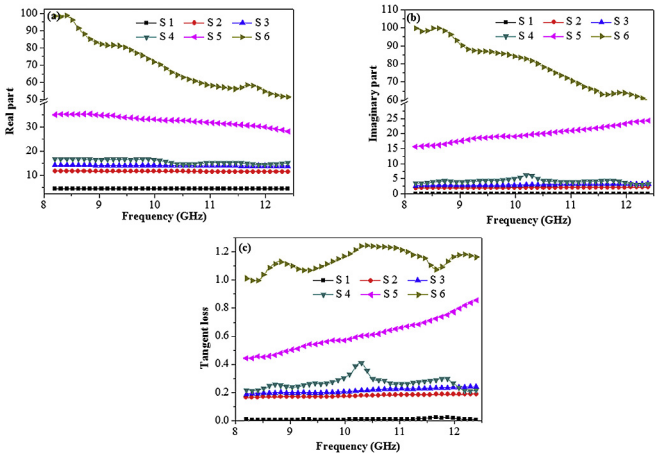

Fig. 11. (a) Real part, (b) imaginary part and (c) tangent loss of the resultant samples.

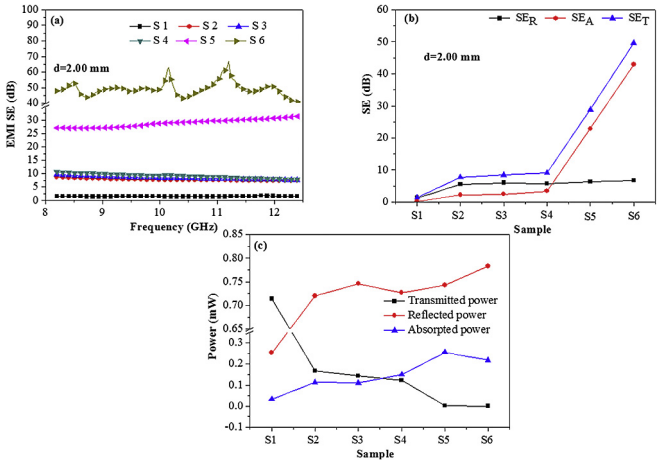

Fig. 12. (a) Total EMI SE, (b) average SE_T, SE_R and SE_A and (c) power balance of the resultant samples.

increasing electrical conductivity are responsible for the increase of ε″ [1,12]. As a result, the tangent loss (tan δ) obviously increases with the introduction of absorbent into the SiCN matrix (Fig. 11c). By comparing samples S2 (SSP-derived RGO-SiCN) and S4 (SSP-derived RGO/CNTs-SiCN), the pronounced enhancement in the dielectric properties (including ε′, ε″ and tan δ) does not only result from the unique microstructure of sample S4 but also is due to the distinguished synergistic effects obtained by the RGO/CNTs hybrids [12,18]. Compared with sample S4, the dielectric properties of sample S3 prepared by mechanical blending are obviously lower with the same GO/CNTs content in the feed, which unambiguously proves the advantage of the SSP-derived RGO/CNTs-SiCN. This phenomenon is explained by the homogeneous dispersion of the carbon nanofillers in sample S4.

3.5. Electromagnetic interference shielding effectiveness (EMI SE)

Measurement of SE of a material is calculated from scattering parameter S_{ij}, available by the vector network analyzer [1,32,38].

Table 2
EMI shielding performance of various RGO-based composites [39].

Filler	Filler content (wt.%)	Matrix	Thickness (mm)	Conductivity (S m^{-1})	EMI SE (dB)	Ref
RGO	7	PS	2.5	43.5	45.1	[8]
RGO	10	PEI	2.3	0.001	22	[44]
RGO	0.7	PMDS	1	180	30	[45]
RGO	20	Wax	2.0	<0.1	29	[46]
RGO	60	Wax	0.35	2500	27	[47]
RGO	7.5	WPU	1	16.8	34	[48]
RGO	15	Epoxy	/	10	21	[49]
RGO	30	PS	2.5	1.25	29	[50]
RGO	4	PI	0.073	2×10^5	51	[51]
RGO	33	PANI	2.8	1800	34.2	[52]
S-doped RGO	15	PS	2	33	24.5	[53]
RGO/γ-Fe_2O_3	75	PANI	2.5	80	51	[54]
RGO/Fe_2O_3	35	PVA	0.3	<1	15	[55]
RGO/Fe_2O_3	66	PANI	2.5	260	30	[56]
RGO/CF/γ-Fe_2O_3	50	Resin	0.4	1.7×10^4	41.8	[57]
RGO/Fe_3O_4	10	PVC	1.8	7.7×10^{-4}	13	[58]
RGO/Fe_3O_4	10	PEI	2.5	10^{-4}	18	[59]
RGO/MnO_2	Bulk	/	3	/	57	[60]
rGO/Fe_3O_4	Bulk	/	0.25	5000	24	[61]
rGO/Fe_3O_4	Bulk	/	3	700	41	[62]
rGO-$BaTiO_3$	Bulk	/	1.5	/	41.7	[63]
rGO-Ba Ferrite	Bulk	/	1.0	98	18	[64]
rGO/CNT/Fe_3O_4	Bulk	/	2.0	/	37.5	[65]
RGO/CNTs	10.0	PDMS	2.0	/	10.4	[18]
RGO/CNTs	15.0	SiCN	2.0	5.7	67.2	This work

For a transverse electromagnetic wave propagating into a sample with negligible magnetic interaction, SE of the sample is expressed as Eq. (1) in a unit of decibel (dB) [32,38]:

$$SE = 10 \log\left[\frac{1}{|S_{ij}|^2}\right] \quad (1)$$

where S_{ij} represents the power transmitting from port i to port j.

Shielding mechanisms of a conductive shielding material include reflection, absorption and multiple reflections [1,32,38,39]. Multiple reflections are the internal reflections between the internal surfaces of the shielding material. In cases where the shielding by absorption (i.e., absorption loss) is higher than 10 dB, most of the re-reflected wave will be absorbed within the shield [38,39]. Thus, multiple reflections can be ignored in the present work. Actually, when an electromagnetic wave is incident on a shielding material, the incident power is divided into reflected power (R), absorbed power (A) and transmitted power (T). Total shielding effectiveness (SE_T), absorption shielding effectiveness (SE_A), reflection shielding effectiveness (SE_R), R, T and A were calculated based on the following equations [38,39]:

$$SE_T = SE_R + SE_A \quad (2)$$

$$SE_R = -10 \cdot \log(1 - R) \quad (3)$$

$$SE_A = -10 \cdot \log\left(\frac{T}{1 - R}\right) \quad (4)$$

$$R = |S_{11}|^2 = |S_{22}|^2 \quad (5)$$

$$T = |S_{12}|^2 = |S_{21}|^2 \quad (6)$$

$$A = 1 - T - R \quad (7)$$

Again, where S_{ij} represents the power transmitting from port i to port j.

From Fig. 12a–c the EMI SE and power balance of the samples can be taken. As shown in Fig. 12a and as compared with sample S1, the SE of that of S2, S3, S4, S5 and S6 increases significantly due to the introduction of conductive carbon nanofillers into the SiCN matrix. Especially, the SE is analyzed to be 67.2 dB with sample S6 (with 15.0 wt% carbon hybrids in the feed), which is the highest among all the RGO-based composites published in the literature (Table 2). Fig. 12b shows that both values, SE_A and SE_R, increase with the increasing content of carbon nanofillers, which well agrees with the increase of SE_T. At a lower absorbent content of 2.0 wt%, the SE_A is always lower than that of SE_R. However, with increasing absorbent content (samples S5 and S6), the SE_A is higher than that of the SE_R. As shown in Fig. 12c, the power balance reveals a remarkable increase in R and A and a decrease in T with the increase of the absorbent content. Moreover, the value of R is always higher than that of A. In general, A, T and R represent the capability of a material to absorb, transmit and reflect the microwave when the microwave transmits a material, respectively [40,41]. However, SE_A represents the ability of a material to attenuate microwave that comes inside of the material [40,41]. A high SE_A is characteristic for a material possessing a high intrinsic absorption property [38,42,43]. Normally, a high SE_A requires high electrical conductivity which also leads to strong reflection [32,42,43]. Since reflection takes place before absorption, most of the incident waves are reflected before they finally come inside of the material. Therefore, though sample S6 possesses a high SE_A, it is highly reflective, which can be confirmed from the reflection power. From the mean value of T we can see that only 0.001% waves transmitted the material, which means nearly 99.999% of the waves are shielded.

Table 2 shows the EMI shielding performance of various RGO-based composites. It is worth mentioning that our present RGO/CNTs-SiCN composites show the highest SE (67.2 dB) with the thickness of 2.0 mm among all the graphene-based composites with comparable thickness.

4. Conclusion

A novel strategy to synthesize RGO/CNTs-SiCN ceramic nanocomposites by an SSP approach is reported. A unique network

microstructure composed of conductive carbon nanophase, namely RGO/CNTs, in the SiCN matrices is clearly identified, which accounts for the significant enhancement of the electrical conductivity, dielectric properties and EM shielding performance of final RGO/CNTs-SiCN nanocomposites. The common features of our novel materials are summarized as follows: i) concerning the dielectric properties, the developed SSP route exhibits significant advantage over the physical blending method; ii) due to the increased dielectric properties, the sample containing 15.0 wt% GO/CNTs in the feed shows an outstanding SE value of the formed RGO/CNTs-SiCN in the amount of 67.2 dB, which is the highest value among all the reported RGO-based composites.

Acknowledgment

Z. Y. thanks the Natural Science Foundation of Fujian Province of China (No. 2015J01221) for financial support. X. L. acknowledges the financial support from China Scholarship Council (CSC) (201406290019). R. I. and Y. I. acknowledge support from the Joint Research Project between Japan and Germany through JSPS Bilateral Program and the Exploratory Research program of MEXT, Core-to-Core Program of JSPS.

References

[1] X.W. Yin, L. Kong, L.T. Zhang, L.F. Cheng, N. Travitzky, P. Greil, Electromagnetic properties of Si–C–N based ceramics and composites, Int. Mater. Rev. 59 (2014) 326–355.
[2] B. Wen, M. Cao, M. Lu, W. Cao, H. Shi, J. Liu, X. Wang, H. Jin, X. Fang, W. Wang, Reduced graphene oxides: light-weight and high-efficiency electromagnetic interference shielding at elevated temperatures, Adv. Mater. 26 (2014) 3484–3489.
[3] M. Albano, D. Micheli, G. Gradoni, R.B. Morles, M. Marchetti, F. Moglie, V.M. Primiani, Electromagnetic shielding of thermal protection system for hypersonic vehicles, Acta Astronaut. 87 (2013) 30–39.
[4] Z. Chen, C. Xu, C. Ma, W. Ren, H.M. Cheng, Lightweight and flexible graphene foam composites for high-performance electromagnetic interference shielding, Adv. Mater. 25 (2013) 1296–1300.
[5] R. Riedel, A. Kienzle, W. Dressler, L. Ruwisch, J. Bill, F. Aldinger, A silicoboron carbonitride ceramic stable to 2,000 °C, Nature 382 (1996) 796–798.
[6] L. Kong, X.W. Yin, F. Ye, Q. Li, L.T. Zhang, L.F. Cheng, Electromagnetic wave absorption properties of ZnO-based materials modified with $ZnAl_2O_4$ nanograins, J. Phys. Chem. C 117 (2013) 2135–2146.
[7] R. Che, L. Peng, X. Duan, Q. Chen, X. Liang, Microwave absorption enhancement and complex permittivity and permeability of Fe encapsulated within carbon nanotubes, Adv. Mater. 16 (2004) 401–405.
[8] D. Yan, H. Pang, B. Li, R. Vajtai, L. Xu, P. Ren, J. Wang, Z. Li, Structured reduced graphene oxide/polymer composites for ultra-efficient electromagnetic interference shielding, Adv. Funct. Mater. 25 (2015) 559–566.
[9] M. Cao, X. Wang, W. Cao, J. Yuan, Ultrathin graphene: electrical properties and highly efficient electromagnetic interference shielding, J. Mater. Chem. C 3 (2015) 6589–6599.
[10] M. Arjmand, M. Mahmoodi, G. Gelves, A.S. Park, U. Sundararaj, Electrical and electromagnetic interference shielding properties of flow-induced oriented carbon nanotubes in polycarbonate, Carbon 49 (2011) 3430–3440.
[11] Y.J. Zhang, X.W. Yin, F. Ye, L. Kong, Effects of multi-walled carbon nanotubes on the crystallization behavior of PDCs-SiBCN and their improved dielectric and EM absorbing properties, J. Eur. Ceram. Soc. 34 (2014) 1053–1061.
[12] M. Han, X. Yin, W. Duan, S. Ren, L. Zhang, L. Cheng, Hierarchical graphene/SiC nanowire networks in polymer-derived ceramics with enhanced electromagnetic wave absorbing capability, J. Eur. Ceram. Soc. 36 (2016) 2695–2703.
[13] L. An, W. Xu, S. Rajagopalan, C. Wang, H. Wang, Y. Fan, L. Zhang, D. Jiang, J. Kapat, L. Chow, Carbon-nanotube-reinforced polymer-derived ceramic composites, Adv. Mater. 16 (2004) 2036–2040.
[14] E.T. Thostenson, Z. Ren, T.W. Chou, Advances in the science and technology of carbon nanotubes and their composites: a review, Comp. Sci. Technol. 61 (2001) 1899–1912.
[15] F. Tristán-López, A. Morelos-Gómez, S.M. Vega-Díaz, M.L. García-Betancourt, N. Perea-López, A.L. Elías, H. Muramatsu, R. Cruz-Silva, S. Tsuruoka, Y.A. Kim, Large area films of alternating graphene–carbon nanotube layers processed in water, ACS Nano 7 (2013) 10788–10798.
[16] C.Z. Yuan, L. Yang, L.R. Hou, J.Y. Li, Y.X. Sun, X.G. Zhang, L.F. Shen, X.J. Lu, S.J. Xiong, X.W. Lou, Flexible hybrid paper made of monolayer Co_3O_4 microsphere arrays on rGO/CNTs and their application in electrochemical capacitors, Adv. Funct. Mater. 22 (2012) 2560–2566.
[17] P. Xiao, C.J. Wan, J.C. Gu, Z.Z. Liu, Y.H. Men, Y.J. Huang, J.W. Zhang, L.Q. Zhu, T. Chen, 2D janus hybrid materials of polymer-grafted carbon nanotube/graphene oxide thin film as flexible, miniature electric carpet, Adv. Funct. Mater. 25 (2015) 2428–2435.
[18] L. Kong, X.W. Yin, X.Y. Yuan, Y.J. Zhang, X.M. Liu, L.F. Cheng, L.T. Zhang, Electromagnetic wave absorption properties of graphene modified with carbon nanotube/poly (dimethyl siloxane) composites, Carbon 73 (2014) 185–193.
[19] J. Chen, M.A. Hamon, H. Hu, Y.S. Chen, A.M. Rao, P.C. Eklund, R.C. Haddon, Solution properties of single-walled carbon nanotubes, Science 282 (1998) 95–98.
[20] F. Pompeo, D.E. Resasco, Water Solubilization of single-walled carbon nanotubes by functionalization with glucosamine, Nano Lett. 2 (2002) 369–373.
[21] E.V. Basiuk, E.V. Basiuk, J.G. Bañuelos, J.M. Saniger-Blesa, V.A. Pokrovskiy, T.Y. Gromovoy, A.V. Mischanchuk, B.G. Mischanchuk, Interaction of oxidized single-walled carbon nanotubes with vaporous aliphatic amines, J. Mater. Chem. B 106 (2002) 1588–1597.
[22] J. Chen, A.M. Rao, S. Lyuksyutov, M.E. Itkis, M.A. Hamon, H. Hu, R.W. Cohn, P.C. Eklund, D.T. Colbert, R.E. Smalley, Dissolution of full-length single-walled carbon nanotubes, J. Mater. Chem. B 105 (2001) 2525–2528.
[23] S. Niyogi, E. Bekyarova, M.E. Itkis, J.L. McWilliams, M.A. Hamon, R.C. Haddon, Solution properties of graphite and graphene, J. Am. Chem. Soc. 128 (2006) 7720–7721.
[24] X.F. Wang, G. Mera, K. Morita, E. Ionescu, Synthesis of polymer-derived graphene/silicon nitride-based nanocomposites with tunable dielectric properties, J. Ceram. Soc. Jpn. 124 (2016) 981–988.
[25] M. Zaheer, G. Motz, R. Kempe, The Generation of palladium silicide nanoalloy particles in a SiCN matrix and their catalytic applications, J. Mat. Chem. 21 (2011) 18825–18831.
[26] H.R. Yang, B.N. Li, Y.D. Cui, Preparation of salicylic acid resin supported $FeCl_3$ Lewis acid catalyst and its application in organic synthesis, Synth. Commun. 28 (1998) 1233–1238.
[27] G.B. Liu, Preparation of silyl esters by $ZnCl_2$-catalyzed dehydrogenative cross-coupling of carboxylic acids and silanes, Synlett 2006 (2006) 1431–1433.
[28] Q.B. Wen, Q.,Y. Feng, Z.J. Yu, D.L. Peng, N. Nicoloso, E. Ionescu, R. Riedel, Microwave absorption of $SiC/HfC_xN_{1-x}/C$ ceramic nanocomposites with HfC_xN_{1-x}Carbon core–shell particles, J. Am. Ceram. Soc. 99 (2016) 2655–2663.
[29] E. Ionescu, H.J. Kleebe, R. Riedel, Silicon-containing polymer-derived ceramic nanocomposites (PDC-NCs): preparative approaches and properties, Chem. Soc. Rev. 41 (2012) 5032–5052.
[30] E. Ionescu, A. Francis, R. Riedel, Dispersion assessment and studies on AC percolative conductivity in polymer-derived Si–C–N/CNT ceramic nanocomposites, J. Mater. Sci. 44 (2009) 2055–2062.
[31] X.H. Kong, X.M. Sun, X.L. Li, Y.D. Li, Catalytic growth of ZnO nanotubes, Mater. Chem. Phys. 82 (2003) 997–1001.
[32] X.M. Liu, X.W. Yin, L. Kong, Q. Li, Y. Liu, W.Y. Duan, L.T. Zhang, L.F. Cheng, Fabrication and electromagnetic interference shielding effectiveness of carbon nanotube reinforced carbon fiber/pyrolytic carbon composites, Carbon 68 (2014) 501–510.
[33] H.A. Becerril, J. Mao, Z. Liu, R.M. Stoltenberg, Z. Bao, Y. Chen, Evaluation of solution-processed reduced graphene oxide films as transparent conductors, ACS Nano 2 (2008) 463–470.
[34] S. Stankovich, D.A. Dikin, G.H. Dommett, K.M. Kohlhaas, E.J. Zimney, E.A. Stach, R.D. Piner, S.T. Nguyen, R.S. Ruoff, Graphene-based composite materials, Nature 442 (2006) 282–286.
[35] Z.P. Chen, W.C. Ren, L.B. Gao, B.L. Liu, S.F. Pei, H.M. Cheng, Three-dimensional flexible and conductive interconnected graphene networks grown by chemical vapour deposition, Nat. Mater. 10 (2011) 424–428.
[36] E. Minoux, O. Groening, K.B. Teo, S.H. Dalal, L. Gangloff, J.P. Schnell, L. Hudanski, I.Y. Bu, P. Vincent, P. Legagneux, G.A. Amaratunga, W.I. Milne, Achieving high-current carbon nanotube emitters, Nano Lett. 5 (2005) 2135–2138.
[37] X. Wang, L. Zhi, K. Müllen, Transparent, conductive graphene electrodes for dye-sensitized solar cells, Nano Lett. 8 (2008) 323–327.
[38] M. Arjmand, M. Mahmoodi, G.A. Gelves, S. Park, U. Sundararaj, Electrical and electromagnetic interference shielding properties of flow-induced oriented carbon nanotubes in polycarbonate, Carbon 49 (2011) 3430–3440.
[39] F. Shahzad, M. Alhabeb, C.B. Hatter, B. Anasori, S.M. Hong, C.M. Koo, Y. Gogotsi, Electromagnetic interference shielding with 2D transition metal carbides (MXenes), Science 353 (2016) 1137–1140.
[40] D. Micheli, R. Pastore, C. Apollo, M. Marchetti, G. Gradoni, V. Primiani, M.F. Moglie, Broadband electromagnetic absorbers using carbon nanostructure-based composites, IEEE T. Microw. Theory 59 (2011) 2633–2646.
[41] F. Moglie, D. Micheli, S. Laurenzi, M. Marchetti, V.M. Primiani, Electromagnetic shielding performance of carbon foams, Carbon 50 (2012) 1972–1980.
[42] M.H. Al-Saleh, U. Sundararaj, Electromagnetic interference shielding mechanisms of CNT/polymer composites, Carbon 47 (2009) 1738–1746.
[43] M.H. Al-Saleh, U. Sundararaj, X-band EMI shielding mechanisms and shielding effectiveness of high structure carbon black/polypropylene composites, J. Phys. D. Appl. Phys. 46 (2012) 035304.
[44] J. Ling, W. Zhai, W. Feng, B. Shen, J. Zhang, W.G. Zheng, Facile preparation of lightweight microcellular polyetherimide/graphene composite foams for electromagnetic interference shielding, ACS Appl. Mater. Inter 5 (2013) 2677–2684.

[45] Z.P. Chen, C. Xu, C.Q. Ma, W.C. Ren, H.M. Cheng, Lightweight and flexible graphene foam composites for high-performance electromagnetic interference shielding, Adv. Mater. 25 (2013) 1296–1300.
[46] B. Wen, X.X. Wang, W.Q. Cao, H.J. Shi, M.M. Lu, G. Wang, H.B. Jin, W.Z. Wang, J. Yuan, M.S. Cao, Reduced graphene oxides: the thinnest and most lightweight materials with highly efficient microwave attenuation performances of the carbon world, Nanoscale 6 (2014) 5754–5761.
[47] B.H. Yuan, C.L. Bao, X.D. Qian, L. Song, Q.L. Tai, K.M. Liew, Y. Hu, Design of artificial nacre-like hybrid films as shielding to mitigate electromagnetic pollution, Carbon 75 (2014) 178–189.
[48] S.T. Hsiao, C.C. Ma, W.H. Liao, Y.S. Wang, S.M. Li, Y.C. Huang, Y.R.B. Yang, W.F. Liang, Lightweight and flexible reduced graphene oxide/water-borne polyurethane composites with high electrical conductivity and excellent electromagnetic interference shielding performance, ACS Appl. Mater. Inter 6 (2014) 10667–10678.
[49] J.J. Liang, Y. Wang, Y. Huang, Y.F. Ma, Z.F. Liu, J.M. Cai, C.D. Zhang, H.J. Gao, Y.S. Chen, Electromagnetic interference shielding of graphene/epoxy composites, Carbon 47 (2009) 922–925.
[50] D.X. Yan, P.G. Ren, H. Pang, Q. Fu, M.B. Yang, Z.M. Li, Efficient electromagnetic interference shielding of lightweight graphene/polystyrene composite, J. Mater. Chem. 22 (2012) 18772–18774.
[51] Z.H. Zeng, H. Jin, M.J. Chen, W.W. Li, L.C. Zhou, Z. Zhang, Lightweight and anisotropic porous MWCNT/WPU composites for ultrahigh performance electromagnetic interference shielding, Adv. Funct. Mater 26 (2016) 303–310.
[52] B.Q. Yuan, L.M. Yu, L.M. Sheng, K. An, X.L. Zhao, Comparison of electromagnetic interference shielding properties between single-wall carbon nanotube and graphene sheet/polyaniline composites, J. Phys. D. Appl. Phys. 45 (2012) 235108.
[53] F. Shahzad, S. Yu, P. Kumar, J.W. Lee, Y.H. Kim, S.M. Hong, C.M. Koo, Sulfur doped graphene/polystyrene nanocomposites for electromagnetic interference shielding, Compos. Struct. 133 (2015) 1267–1275.
[54] A.P. Singh, M. Mishra, P. Sambyal, B.K. Gupta, B.P. Singh, A. Chandra, S. Dhawan, Encapsulation of γ-Fe_2O_3 decorated reduced graphene oxide in polyaniline core–shell tubes as an exceptional tracker for electromagnetic environmental pollution, J. Mater. Chem. A 2 (2014) 3581–3593.
[55] B.B. Rao, P. Yadav, R. Aepuru, H. Panda, S. Ogale, S. Kale, Single-layer graphene-assembled 3D porous carbon composites with PVA and Fe_3O_4 nano-fillers: an interface-mediated superior dielectric and EMI shielding performance, Phys. Chem. Chem. Phys. 17 (2015) 18353–18363.
[56] K. Singh, A. Ohlan, V.H. Pham, R. Balasubramaniyan, S. Varshney, J. Jang, S.H. Hur, W.H. Choi, M. Kumar, S.K. Dhawan, B.S. Kong, J.S. Chung, Nanostructured graphene/Fe_3O_4 incorporated polyaniline as a high performance shield against electromagnetic pollution, Nanoscale 5 (2013) 2411–2420.
[57] A.P. Singh, P. Garg, F. Alam, K. Singh, R. Mathur, R. Tandon, A. Chandra, S. Dhawan, Phenolic resin-based composite sheets filled with mixtures of reduced graphene oxide, γ-Fe_2O_3 and carbon fibers for excellent electromagnetic interference shielding in the X-band, Carbon 50 (2012) 3868–3875.
[58] K. Yao, J. Gong, N.N. Tian, Y.C. Lin, X. Wen, Z.W. Jiang, H. Na, T. Tang, Flammability properties and electromagnetic interference shielding of PVC/graphene composites containing Fe_3O_4 nanoparticles, RSC Adv. 5 (2015) 31910–31919.
[59] B. Shen, W.T. Zhai, M.M. Tao, J.Q. Ling, W.G. Zheng, Lightweight, multifunctional polyetherimide/graphene@ Fe_3O_4 composite foams for shielding of electromagnetic pollution, ACS Appl. Mater. Inter 5 (2013) 11383–11391.
[60] T.K. Gupta, B.P. Singh, V.N. Singh, S. Teotia, A.P. Singh, I. Elizabeth, S.R. Dhakate, S. Dhawan, R. Mathur, MnO_2 decorated graphene nanoribbons with superior permittivity and excellent microwave shielding properties, J. Mater. Chem. A 2 (2014) 4256–4263.
[61] W.L. Song, X.T. Guan, L.Z. Fan, W.Q. Cao, C.Y. Wang, Q.L. Zhao, M.S. Cao, Magnetic and conductive graphene papers toward thin layers of effective electromagnetic shielding, J. Mater. Chem. A 3 (2015) 2097–2107.
[62] M. Mishra, A.P. Singh, B. Singh, V. Singh, S. Dhawan, Conducting ferrofluid: a high-performance microwave shielding material, J. Mater. Chem. A 2 (2014) 13159–13168.
[63] Y.C. Qing, Q.L. Wen, F. Luo, W.C. Zhou, D.M. Zhu, Graphene nanosheets/$BaTiO_3$ ceramics as highly efficient electromagnetic interference shielding materials in the X-band, J. Mater. Chem. C 4 (2016) 371–375.
[64] M. Verma, A.P. Singh, P. Sambyal, B.P. Singh, S. Dhawan, V. Choudhary, Barium ferrite decorated reduced graphene oxide nanocomposite for effective electromagnetic interference shielding, Phys. Chem. Chem. Phys. 17 (2015) 1610–1618.
[65] A.P. Singh, M. Mishra, D. Hashim, P.T. Narayanan, M. Hahm, G. Hahm, P. Kumar, J. Dwivedi, G. Kedawat, A. Gupta, B.P. Singh, Probing the engineered sandwich network of vertically aligned carbon nanotube–reduced graphene oxide composites for high performance electromagnetic interference shielding applications, Carbon 85 (2015) 79–88.